MEASUREMENT AND ANALYSIS OF AEROSOLS, CIRRUS-CONTRAILS, WATER VAPOR AND TEMPERATURE IN THE UPPER TROPOSPHERE WITH THE JUNGFRAUJOCH LIDAR SYSTEM

THÈSE N^{O} 2975 (2004)

PRÉSENTÉE À LA FACULTÉ ENVIRONNEMENT NATUREL, ARCHITECTURAL ET CONSTRUIT

Institut des sciences et technologies de l'environnement

SECTION DES SCIENCES ET INGÉNIERIE DE L'ENVIRONNEMENT

ÉCOLE POLYTECHNIQUE FÉDÉRALE DE LAUSANNE

POUR L'OBTENTION DU GRADE DE DOCTEUR ÈS SCIENCES TECHNIQUES

PAR

Ioan BALIN

licence en physique, Université A.I. Cuza, Iasi, Roumanie
et de nationalité roumaine

acceptée sur proposition du jury:

Prof. H. van den Bergh, directeur de thèse
Prof. B. Calpini, rapporteur
Prof. C. Comninellis, rapporteur
Prof. M. Parlange, rapporteur
Dr V. Simeonov, rapporteur

Lausanne, EPFL
2004

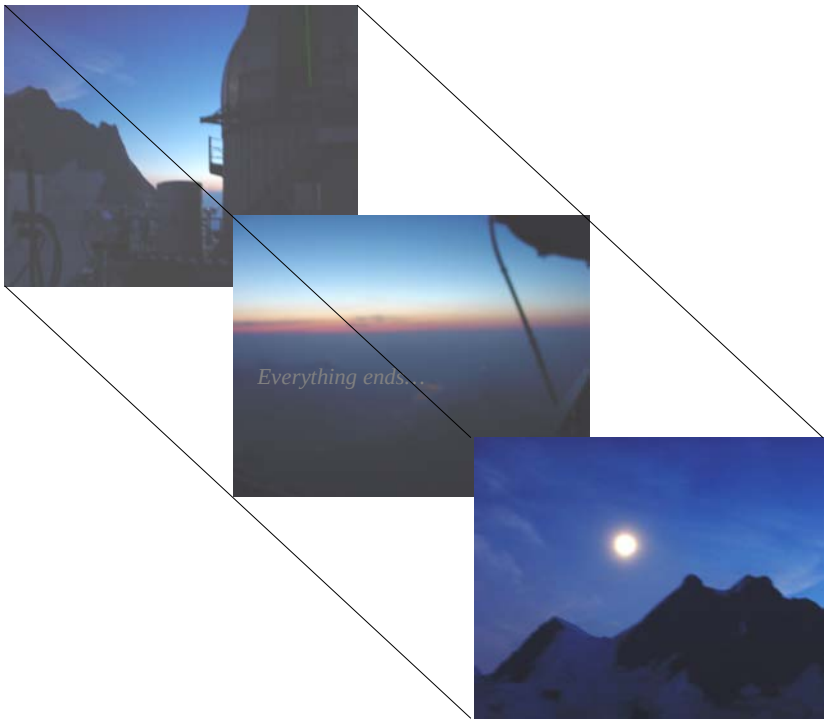

À la science mon 1er hobby
à ma femme unique, Daniela
à ma famille
à mes amis
à ceux qui m'aiment et croient en moi
à mes ennemis si ça se trouve

Ioan

ABSTRACT

The impact of human activities on the global climate may lead to large disruptions of the economic, social and political *status quo* in the middle and long term. Understanding the dynamics of the Earth's climate is thus of paramount importance and one of the major scientific challenges of our time. The estimation of the relative contribution of the many components (interacting each other) of the Earth's climate system requires observation and continuous monitoring of various atmospheric physical and chemical parameters. Temperature, water vapor and greenhouse gases concentration, aerosol and clouds loads, and atmospheric dynamics are parameters of particular importance in this respect. The quantification of the anthropogenic influence on the dynamics of these above-mentioned parameters is of crucial importance nowadays but still affected by significant uncertainties.

In the present context of these huge uncertainties in our understanding of how these different atmospheric compounds contribute to the radiative forcing, the research presented in this report is related to the following topics:

- Development of lidar-based remote sensing techniques for monitoring atmospheric compounds and processes
- Aerosols – cirrus – contrails optical properties up to the tropopause
- Water vapor mixing ratio and relative humidity estimation in the upper troposphere
- Temperature profiling in the upper troposphere-lower stratosphere
- Characterization of the long-range transported mineral aerosols (i.e. Saharan dust outbreaks)
- Planetary boundary layer-upper troposphere exchanges (i.e. August 2003 heatwave effect)

In the above research frames, the development and application of measurement techniques for the monitoring of climate-change parameters, this work refers to the implementation of a multi-wavelength LIDAR[1] system (JFJ - LIDAR)[2] at the International Scientific Station of Jungfraujoch (ISSJ, 46°33' N, 7°59' E, at 3580 m ASL- above sea level). The JFJ[3] station is situated above the planetary boundary layer (PBL) almost all year long and is located in a mountain pass linking the Swiss plateau to the North with the Rhone Valley to the South through the Aletsch glacier corridor.

[1] LIDAR – **LI**ght **D**etection **A**nd **R**anging
[2] JFJ-LIDAR is the acronym used here for Jungfraujoch multi-wavelength LIDAR system
[3] JFJ is the abbreviation for Jungfraujoch

- Measurements with the JFF-LIDAR system provide regular vertical and horizontal remote sensing of water vapor, temperature, and optical properties (backscatter and extinction coefficients) of aerosols, cirrus clouds and contrails in the upper troposphere (UT)[4]. The lidar system is based on the laser emission at 355, 532 and 1064 nm and on subsequent detection of both elastic (Mie) and inelastic (Raman) atmospheric backscatter light. The backscattering collected radiation is precisely: the elastic at 355, 532 and 1064 nm; the rotational-vibrational Raman radiation from nitrogen at ~ 387 nm, and from water vapor at ~ 407 nm as well as the pure rotational nitrogen/oxygen Raman excited at ~ 532 nm. The depolarization of the initially linearly polarized radiation was also detected at 532 nm and it was use to distinguish between water and ice contents in cirrus clouds, but also it may reveal long-range transported mineral aerosols such as Saharan dust.
- Profiles of backscatter and extinction coefficients of aerosols-cirrus-contrails, needed for estimation of the radiative balance of the atmosphere, are derived from elastic and Raman light scattering processes, or through a combination of both, using devoted algorithms and software developed within this research. Data gathered from routine measurements are statistically analyzed and interpreted in comparison with similar measurements obtained from co-located techniques. Optical and microphysical properties of a typical contrail were studied.
- The UT water vapor mixing ratio profiles are estimated from the ratio of ~ 407 nm and ~387 nm Raman radiation excited by 355 nm. Upon appropriate calibration, real time water vapor mixing ratio profiles derived from LIDAR measurements are found in good agreement with the closest radiosounding techniques, and co-located measurements such as the GPS[5] and sun photometer based measurements. The water vapor profiles, combined with simultaneous temperature profiles taken from atmospheric models, radiosounding or, more realistically, based on the pure rotational Raman technique, were used for the estimation of relative humidity profiles which allow the identification of UT super-saturation regions.
- Air temperature profiles were obtained up to the lower stratosphere using the backscatter of pure rotational Raman radiation excited by 532 nm. These first results compare well to simultaneous regional radiosounding measurements, and follow standard atmospheric models. The pure rotational Raman

[4] UT will be used as abbreviation for upper troposphere (from ~ 3600 m ASL to the tropopause atmospheric region)
[5] GPS is the acronym for Global Positioning System

backscatter was also used for determining absolute extinction and the lidar ratio for cirrus clouds.
Based on the JFJ-LIDAR measurements, supported by co-located and regional measurements, the research presents also in detail two case studies related to climate problematic:

- The first concerns the tracking of a Saharan dust outbreak (SDO) and the derivation of its optical properties.
- The second study refers to the analysis of the evolution and consequences of the high altitudes planetary boundary layer (PBL)[6] convection during the August 2003 heat - wave episode.

The results presented within this research provide a promising basis for extending these JFJ-LIDAR observations from the upper troposphere into the *stratosphere* by using the existent astronomic telescope (~15 times increased sensitivity) and a new (~ 3 times more powerful) laser source. Consequently DIAL[7] technique for measuring the *stratospheric ozone* will be developed and implemented in the near future at JFJ. Future challenges include also JFJ-LIDAR *remote control* operation and the ability of *real time* obtained atmospheric calibrated profiles (i.e. optical properties of aerosols-cirrus-contrails, water vapor, temperature and ozone).

KEYWORDS

LIDAR, Jungfraujoch, upper troposphere, aerosols, cirrus-contrails, water vapor mixing ratio, temperature, Rayleigh, Raman, Mie, backscattering, extinction, depolarization, Saharan dust, planetary boundary layer, Ångstrom coefficients, heatwave

[6] PBL - planetary boundary layer – its top is usually situated under the altitude of the JFJ station (i.e. 3600m ASL)
[7] DIAL - is the acronym coming from **DI**fferential **A**bsorption **L**idar

RÉSUMÉ

L'impact des activités humaines sur le climat peut conduire à des perturbations économiques, sociales et politiques à court et long terme. La compréhension des dynamiques du climat sur Terre est à présent une préoccupation majeure de la communauté scientifique mondiale.
L'estimation de la contribution relative des facteurs actifs sur le climat nécessite de nouvelles observations réalisées à long – terme (i.e. du monitoring) des nombreux paramètres physico-chimiques de l'atmosphère terrestre.
La température, la concentration de la vapeur d'eau et des autres gaz à effet de serre, les aérosols, les nuages et les différents échanges entre les couches de l'atmosphère sont des paramètres déterminants du climat.
Dans le contexte actuel, de larges incertitudes subsistent quant à la contribution des composants atmosphériques à l'effet de serre (peu d'estimations quantitatives des différentes contributions dans le bilan radiatif du système Soleil – Atmosphère – Terre). Dans ce contexte le travail présenté par ce rapport est relié aux problématiques suivantes:

- L'élaboration des outils basée sur la technique lidar pour l'observation systématique des composants et processus atmosphériques
- L'estimation des propriétés optiques des aérosols – cirrus – « contrails »
- L'estimation de la vapeur d'eau et de l'humidité relative dans la haute troposphère
- L'estimation de la température atmosphérique jusqu'à la basse stratosphère
- Caractérisation des aérosols minéraux transportés à l'échelle globale (i.e. les poussières de Sahara)
- Echanges entre la couche limite planétaire et haute troposphere (i.e. l'effet de la canicule d'août 2003)

Dans le contexte du développement et de l'application des techniques mesurant des paramètres atmosphériques à forte vocation climatique, ce travail rapporte l'implémentation d'un système LIDAR multi - longueur d'onde (JFJ - LIDAR) à la station scientifique de Jungfrajoch (ISSJ, 46°33' N, 7°59' E, 3580 m ASL). La station est située au-dessus de la couche limite planétaire (excepté quelques jours en été). L'observatoire est construit au sommet d'une proéminence rocheuse de type permafrost (Sphynx) en plein milieu du col de Jungfraujoch. Ce col relie le bassin du

Rhin (au Nord) avec la vallée du glacier d'Aletsch qui appartient au bassin hydrographique du Rhône (au Sud).

- Le JFJ - LIDAR est en mesure de fournir systématiquement des profils (horizontaux et verticaux) de la concentration de la vapeur d'eau, de la température et des propriétés optiques (i.e. coefficients de rétro-diffusion et d'extinction) des aérosols et des cirrus dans la haute troposphère. Le système lidar est basé sur l'émission de faisceaux laser à trois longueurs d'onde (i.e. 355, 532 et 1064 nm) et la détection des radiations rétro – diffusées : élastiques (Mie, 355, 532 et 1064 nm) ou inélastiques (Raman, 387, 407, 607, et 532 rotationnel). La dépolarisation de la lumière rétro-diffusée à 532 nm à été aussi mesurée et utilisée pour analyser le degré de composition des nuages en eau et glace ou pour l'analyse de la poussière saharienne.
- Des profils de coefficients de rétro-diffusion et d'extinction des aérosols - cirrus « contrails », en vue des calculs de bilan radiatif, sont dérivés à partir des signaux Mie et Raman en utilisant des algorithmes développés en MatLab, LabView, Delphi, etc. Ce rapport contient une analyse statistique des mesures réalisées entre mai 2000 et mai 2002. Ces valeurs sont comparées aux mesures similaires obtenues par d'autres instruments installés à la station. Les propriétés optiques et microphysiques (très peu connues) d'un « contrail » typique ont été analysée et sont rapportées dans ce document. L'analyse de la dépolarisation à 532 nm a permis de faire la distinction entre eau-glace ou mélange de deux dans les nuages ainsi que de détecter les aérosols minéraux transportés à l'échelle globale comme les poussières sahariennes.
- Le rapport de mélange de la vapeur d'eau dans la troposphère libre par la technique du Raman lidar a été dérivé systématiquement (i.e. profils verticaux à haute résolution spatio-temporelle) considérant le rapport de la radiation Raman de l'eau à 407 nm et celle de l'azote à 387 nm. Les estimations absolues, basées sur une calibration in situ, comparées à d'autres mesures à la station (i.e GPS) ou régionales (i.e radiosondage de Payerne) montrent des corrélations réalistes. Des profils d'humidité relative ont été calculés en considérant d'abord les profiles de température des modèles et à partir de juin 2002 ceux mesurés par le lidar même. Sur les profiles d'humidité relative on a pu identifier systématiquement des régions de super-saturation dans la haute troposphère.
- Des profiles de température ont été aussi obtenus jusqu'en basse stratosphère en utilisant la technique Raman rotationnel à 532 nm. Les premiers résultats sont en très bonne corrélation avec les modèles et le radiosondage de Payerne. Les signaux du Raman rotationnel ont été aussi utilisés pour la détermination absolue de la rétro - diffusion, de

l'extinction et du rapport extinction/rétro-diffusion correspondant aux cirrus.

Sur la base des mesures du système lidar à Jungfraujoch et d'autres observations faites à Jungfraujoch ou à caractère régional deux études de cas sont proposées, due à leur importance vis-à-vis de la problématique climatique.

- La 1ère est dédiée à la caractérisation optique et microphysique des poussières sahariennes lors de la tempête de poussière désertique du 02 août 2001
- La 2ème se penche sur l'interprétation des mesures obtenues lors de la vague de chaleur extrême d'août 2003.

Les résultats de ce travail constituent une base prometteuse pour l'extension des *mesures lidar à la stratosphère* en utilisant le télescope astronomique (~ 15 fois plus sensible) et une nouvelle source lidar (~ 3 fois plus puissante). Avec ces améliorations en émission et en détection la mesure de *l'ozone stratosphérique* doit être possible à court terme.

Pour des mesures systématiques à long terme, *l'opération à distance* du système ainsi que la réalisation des *mesures en temps réel* sont envisagés.

MOTS CLÉS

LIDAR haute troposphère, aérosols, cirrus, contrails, vapeur d'eau, température, Rayleigh, Raman, Mie, rétro-diffusion, extinction, dépolarisation, poussières sahariennes, couche limite planétaire, coefficients d'Ångstrom, vague de chaleur.

ACKNOWLEDGEMENTS

Prof. H. van den Bergh made possible this work by accepting me in the LPAS laboratory advising me to reorient my career from fundamental physics to environmental research including geophysical experiments related to air quality or climate change and mainly using lidar-based applications. I strongly thank him for the confidence and the opportunity he offered me to work on such original, unique, actual and worth research as the Jungfraujoch EPFL-LIDAR project.
I thank the examiners Prof. M. Parlange, Prof. C. Comninellis, Prof. B. Calpini and Dr. V. Simeonov for accepting to be in my thesis jury.
The work here presented, and in a general manner the results obtained during my LPAS lifetime (May 1998 - March 2004) were not possible without a strong collaboration, mutual help, critical discussions, scientific confrontations, participation to many international measurement field campaigns and data interpretation within the LIDAR team formed by colleagues of quite different personalities, cultures and nationalities (many of them remaining friends for life): Bertrand, Valentin, Rodrigo, Gilles, Remo, Philippe, Francois, Benoit, Pablo, Marian and many other shorter lifetime passengers in the LIDAR team e.g. Adriana, Mathieu, Fernando, Manuel, Alfonso, Robert, Todor, Minko, Luca, Jerôme, David, etc . I'll add here Veronique, Carine and Flavio who were also within LIDAR spirit helping us a lot.

I thank them all for all.
Any emphasis doesn't make sense as I always considered all in a team spirit.

Besides my colleagues from atmospheric measurements group I want to thank also the modeling team: Erika, Olivier, Frank, Alain, Martin, Yves-Alain, Clive, Sylvain, Jerôme, Alberto, and many others for the fruitful collaboration in putting together measurement and model outputs for answering complex regional questions in air quality studies. I am also generally grateful to all LPAS members with whom I had useful and positive collaborations.
I especially acknowledge the Jungfraujoch foundation members (Prof. Fluckiger, Mrs Louise Wilson, Mr and Ms: Jenni, Staub and Ficher. I'll never forget the common time spent at the JFJ station and interesting discussions with various member of JFJ research teams (e.g. particularly Prof Delbouille, Dr. Roland, Dr. Cervais, P. Demoulin, Pierre Duchatelet, and many other scientists who I had the opportunity to meet or even to cohabite at the JFJ station).
For the external collaboration I want to mention the PSI institute team (Dr. Ernest Weingartner and Dr. U. Baltensperger), the IAP team (e.g. Dr. Daniel Gerber and Dr. June Morland,), EMPA (Daniel Schaub), Swissmeteo (Mr P. Jeannet, M. G. Levrat, Dr. M. Collaud, Dr. S. Nyeki and Dr. L. Vuillemeyer), Neuchatel Observatory (Dr. R. Matthey and Dr. V. Mitev), Rusian Academy –

Applied Optics Institute from Tomsk (Dr. Y. Arshinov, Dr. S. Brobovnikov and Dr. I. Serikov), from Johns Hopkins University (Prof. M. Parlange, Mrs. M. Adam and C Higgins), ETH (Dr. Stefan Bojinsky) and many many others.
Thanks to undergraduate and high school students and visitors at JFJ for their patience, understanding and interest on my various presentations.
I am grateful to the EPFL direction (communication department) for our positive collaboration. I remember also well the initial support of A. Jaccard and K. Vinckenbosch, from the EPFL social service, which made possible the start of my EPFL adventure in 1997. I also thank the support from the EPFL technical service mainly via Mlle Mercier.
Prof Tarradellas, Sonja Desplos and their collaborators are thanked for the excellent organization and the quality of the postgraduate cycle in environmental sciences, which in fact opened my mind of fundamentally involved physicist to what was, is and has to be done in environmental research and its usefulness.
I am also thanking all my former students and many colleagues spread all worldwide because they achieved to convince me that a scientist has to have a Dr. title. I am grateful to all my colleagues from UAIC University and particularly to those from the Optics and Spectroscopy Department from the time when I was there.
For the improvement of the written English of this manuscript I am pleased to thank the great help given by Marry Parlange and Daniela Balin-Talamba.
Finally I thank all members of my family from Maramures (North of Transylvania) and all my friends wherever they are and I hope they keep on accepting my way, principles and scale of values during our Earth's biological but rational lifetime. Within my Swiss family I thanks Cosinsky and Moldovan families for their moral and personal support as well as the Parintele Diaconu.
This work was financially supported within EARLINET (European Aerosols Research Lidar Network) project, the SNF (Swiss National Fundation), the EPFL (Federal Institute of Technology from Lausanne) and it benefits from the endorsement of the Jungfraujoch Foundation.
I am particularly grateful to my wife Daniela, who understood, allowed, supported, and helped me in this complex task.
My gratification will come in fact sincerely from everybody who will take time to read this thesis manuscript

Yours,

Lausanne-Switzerland,
April 2004

PS: I express my humble gratitude to ??? … we still do not know very well who, how, where, when and he is (e.g God) for the force, the courage and the necessary health to start, to continue and to finish this work.

TABLE OF CONTENTS

Chapter IV Water vapor retrieval based on Raman lidar technique

Chapter V Temperature and other atmospheric retrievals based on pure rotational Raman technique

Contents Scheme

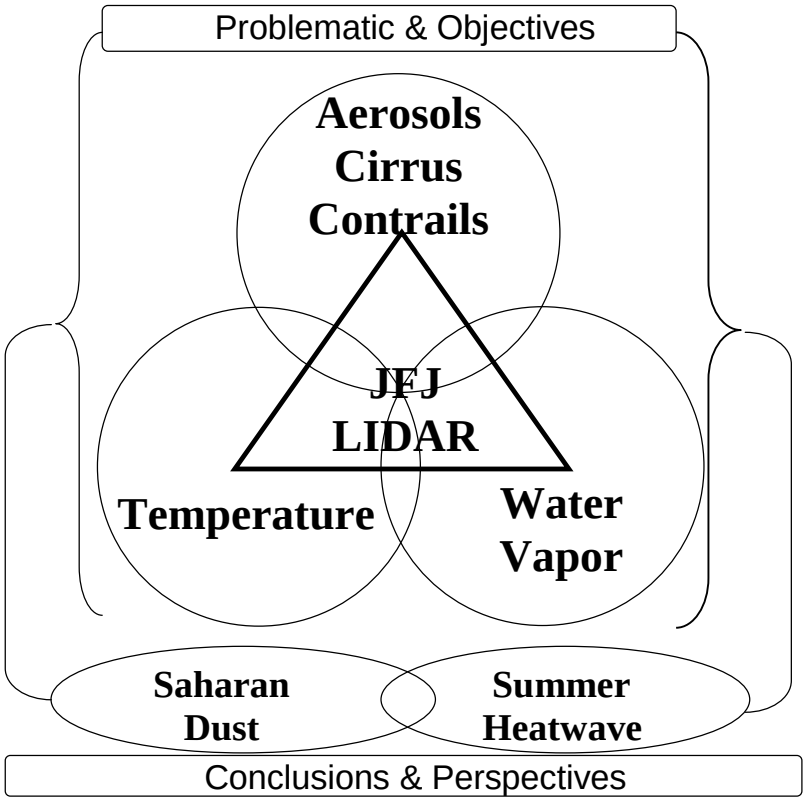

Chapter I

Introduction

1. Research context

The Earth *atmosphere*[1] is a vital global environmental segment together with the water and soil. The air-water-soil natural cycles drive transport and exchanges of energy and matter and they define in time and space the life-related processes on the Earth. The carbon and hydrologic cycles, for example, are fundamental for life on Earth. There is a growing body of evidence showing that the natural equilibrium of these dynamic cycles is sensitive to human activities. Human activities have a negative feedback that ultimately affects human life itself. These anthropogenic perturbations are of short duration compared to geological time scales and superpose over the long-term natural variability of the natural cycles.

The increase in the magnitude of the anthropogenic perturbations seems to start with the industrialized era (i.e. 1850). In fact the environmental entropy concerning the natural distribution of substances began to be strongly affected by the intensive exploitation of natural resources, by fabrication of new products and by their use. Thus the environment is under an anthropogenic pressure with involving subsequent perturbations during four phases: (a) exploitation of natural resources, (b) production processes, (c) products utilization and (d) hazardous waste in environment. The general result of this anthropogenic chain is the space-time redistribution (i.e. decreasing entropy) of the natural concentrations within the air-water-soil system, which ultimately changes the corresponding natural cycles. The effects occur on both the short (i.e. acute) and long (i.e. chronic) terms. Obviously the short-time effects are immediately discovered and the human community rapidly activates necessary solutions while the long-term effects are more subtle and complex, and solutions more difficult to obtain.

The atmosphere is intimately involved in this general environmental problem in all its processes and across all its time-space scales. The short-term (at the local scale) concerns the acute problem of air quality, while the long-term (at the global scale) concerns the Earth-Sun radiation budget perturbation. Between these two time-space scales, for the atmosphere in particular, many important meteorological processes have to be taken into account because they drive

[1] Derived from the Greek ατμοζ (for vapor) and σφαιρα (for sphere), the word *atmosphere* describes the layer, essentially gaseous, that envelopes the Earth (more details in annex A1)

regional air pollution effects and themselves may be subsequently influenced in magnitude and frequency by potential climatic scale changes.
The present regional air pollution problem concerns the emissions of gases (e.g. CO, CO_2, NO, NO_2, SO_2, VOC,….) and particles (i.e. aerosols) and their subsequent transport and photochemical transformations (i.e. O_3 as secondary pollutant)). Industry is likely the main culprit for volatile organic carbons (VOC), while automobile traffic is responsible for NOx emissions. In the United States, air pollution may be responsible for 50,000 deaths annually, more than 2% of all deaths and similar health risks have been reported in France, United Kingdom and elsewhere [1]. In Western Europe legislation and measures that have been taken last years have started to show positive effects (e.g. SO_2 completely reduced), but the regional summer photochemical smog of tropospheric ozone and other related photochemical products are still a challenge. In addition, the emissions reductions based on the use of new automobile catalytic converters were counterbalanced by an increase in the numbers of cars owned in Europe. In developing countries in Asia, Eastern Europe and Latin America, the primary emission of gases and particles or even heavy metals seems to outweigh the secondary photochemical pollution due to ozone [1]. Furthermore, regional air pollution has, in addition to its clear direct effects on human health, wide-ranging indirect effects on humans through vegetation (e.g crops, forests) and materials (e.g. buildings, historical monuments) via direct oxidation/reduction processes.
The regional air quality problem is concerning the first atmospheric layer (e.g. < 3 Km and even higher) strongly influenced thermodynamically by the Earth's surface processes, the planetary boundary layer (i.e. PBL). The magnitude of the pollution effects depends on the intensity, type and distribution of the emissions sources while the transport and secondary photo-chemical transformations are driven by the regional dynamics of the PBL, the local topography, the meteorological conditions and are influenced by the geographical context (i.e. the larger surrounding continental domain) [2]. For example, during the August 2003 heat-wave, the air pollution high ozone episode (i.e. O_3 averaged ~ 200 $\mu g/m^3$ in 23 countries in Europe when the present legal threshold for health effects is considered 180 µg/m3) reinforced the need for new consideration of the role that tropospheric ozone plays in pollution particularly taking into account the potential for repeatability of the event in the near future [3]. In the above context there is a crucial need for both air measurements and modeling studies that would help to set the groundwork for establishing abatement strategies.
The first recognized long-term atmospheric problem at the global scale was the *depletion of the stratospheric ozone layer* by halogenated anthropogenic compounds (CFCs). The ozone "hole" and the concomitant increase of the UV radiation on the Earth surface have led to a significant effect both on human health (e.g skin cancer, eyes diseases) and public awareness of large-scale

atmospheric processes. What is not generally known is that scientists had, since 1974, been warning the world that the ozone layer would deplete rapidly unless we stopped the use of ozone depleting chemicals [4]. It took 11 years of assessment, research, and negotiations to promote the first general ozone agreement in 1985. Finally in 1985 the Vienna convention established an international legal framework for action and in 1987 the Montreal Protocol officially required industrialized countries and later developing ones to stop the production and use of ozone depleting substances (i.e. CFCs, halons, methyl-chloroform, carbon tetrachloride, hydro-CFCs).
The implementation of this protocol has led to a dramatic drop in the consumption of ozone depleting chemicals in the last ten years. Due to the relatively long lifetime of these chemicals, the stabilization and then decrease in concentration of ozone depleting substances in the stratosphere was observed only 15-20 years later. Thus ozone depletion remains a current problem and an increase in the ozone layer is expected only around ~2050 [5].
A second major global scale and long-term atmospheric related problem is the anthropogenic perturbation of the Earth's natural *greenhouse effect* due to the warming/cooling effect of gases, aerosols and induced clouds in the atmosphere. The Earth's natural greenhouse effect assures an average temperature on the Earth of ~ 12-15°C, a range that allows life to develop and flourish. This value is the result of the Sun-Earth radiation budget through the Earth's atmosphere, which is playing the role of the "planetary greenhouse roof". The radiation transfer within Sun-Earth-Atmosphere system is based on the Stefan-Boltzmann law cf. Eq. (1)

$$S = e \cdot \sigma \cdot \left(T^4 - T_a^4 \right) \qquad \text{Eq. (1)}$$

where S [Wm^{-2}] is the mean energy in radiated by a blackbody, e is its emissivity (e.g 1 for ideal case), σ = 5.6703 10^{-8} $Wm^{-2}K^{-4}$ is the Stefan-Boltzmann constant, T is the temperature of the radiator and the T_a is the temperature of its surroundings. Calculations based on Eq. (1) show that in the case when the Earth was considered as an ideal blackbody without atmosphere, the surface mean temperature would be ~278.6K (5.5 ^oC).
As in reality the Earth reflects ~30 % of the long-wave solar radiation (mean *albedo*[2] ωo ~ 0.3) only 70 % of the incoming radiation will be absorbed by the Earth and converted to infrared radiation, which corresponds to a surface temperature of 254.8 K (-18.3 ^oC). Although the *albedo* drastically influences surface temperature, it is not enough to explain the Earth's surface temperature; the effect of the atmosphere has to be taken into account. In fact the atmosphere allows the penetration of short wave solar radiation to the Earth, which will absorb a fraction of this UV_A-VIS-NIR (0.3 - 4 μm) radiation and will reconvert internally in thermal energy, which in turn is reemitted as long wave radiation

[2] *albedo* is the ratio of scattered to incident light (i.e. ~1 for negligible light absorption)

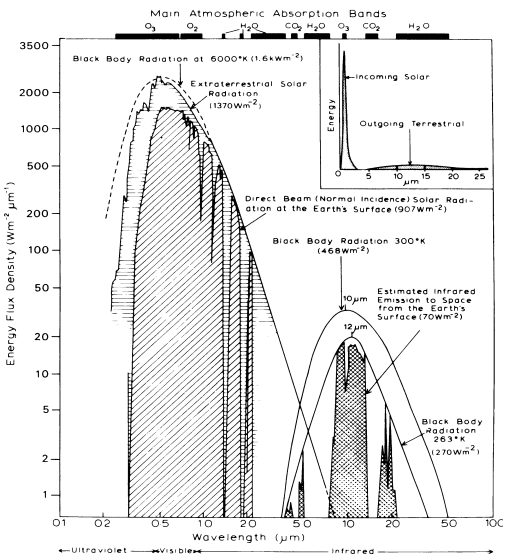

(IR ~ 4-100 μm, maximum peak ~10 μm) back to the atmosphere. The spectral distribution of the incoming (short-wave) and outgoing (long-wave) radiations is shown in Figure 1. Atmospheric gases such as water vapor (H_2O), carbon dioxide (CO_2) methane (CH_4), nitrous oxide (N_2O), chlorofluorocarbons (CFCs), ozone (O_3), absorb the Earth emitted IR radiation. They influence the radiative budget and contribute to an increase in the Earth's surface temperature.

Figure 1 Spectral distribution of solar and terrestrial radiation (from [6])

Taking into account the atmosphere effect as a blackbody absorbing and reemitting the received infrared radiation from the Earth, the calculations show an enhancement of the Earth surface temperature to ~ 303 K (30 °C), due to the downward emissions, which is clearly an overestimation compared to 12-15° C [7]. In fact the atmosphere is not completely absorbing the IR radiation. Other phenomena such as sensible (i.e. convection - turbulence) and latent (i.e. evaporation – transpiration -- phase transitions) heat transfer have to be taken into account and thus the Earth temperature is determined as expressed cf. Eq. (2)

$$S\frac{(2-f)(1-\omega_0-a_s)+a_s}{2-a_l}=\sigma T_e^4 \qquad \text{Eq. (2)}$$

where S is the mean solar energy , f is the fraction transformed in latent and sensible heat, a_s is the short wave and a_l is the long-wave atmospheric absorbance fractions, ω_0 is the surface *albedo* and T_e is the Earth surface temperature [7]. An estimative overview of the global mean radiation budget is schematically shown in the Figure 2. An average of 28 % of the incoming radiation is returned into space due to the backscattering from clouds (19 %), air molecules and particles (6%), and by the Earth surface (3%). Almost 25% is absorbed within the atmosphere, mostly by stratospheric ozone (3%), clouds (5%) and tropospheric water vapor (17%). The Earth absorbs finally the

remaining of 47%. A little bit more than half of the solar radiation absorbed at the surface is transformed into latent heat (24%) and sensible heat (5%). Only 5% is lost by radiation and thus only the remaining ~ 15% of the incoming solar radiation is trapped in the atmosphere by the greenhouse gases [8].

To estimate the relative impact of these different atmospheric compounds, their *radiative forcing* has to be calculated. From the definition given by (IPCC[3] 2001, [9]), the radiative forcing (ΔF) of the surface-troposphere climate system due to perturbation or the introduction of an agent (e.g. a change in greenhouse gas concentrations) is the change in net (down minus up) irradiance (solar plus long-wave, in Wm^{-2}) at the tropopause after allowing for stratospheric temperatures to readjust to radiative equilibrium, but with surface and tropospheric temperatures and states held fixed at the unperturbed values.

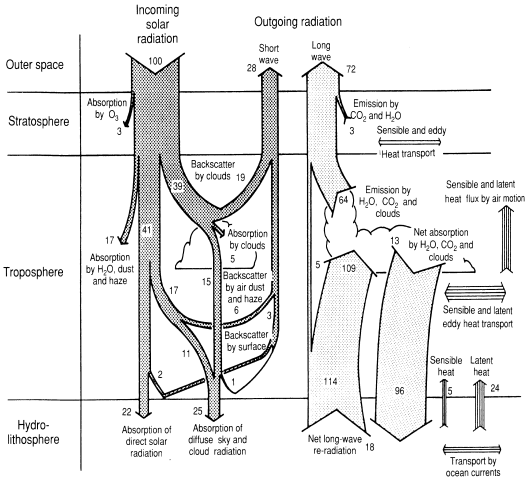

Figure 2 Annual mean of the global energy mean balance of the Atmosphere-Earth system (from ([8])

The above-cited definition does not take into consideration any feedbacks (e.g. water vapor positive feedback). The temperature change (ΔT_e) is related to the radiative forcing ΔF by the climate sensitivity factor λ_0 [K $(Wm^{-2})^{-1}$] as below.

$$\Delta F = S_{\downarrow} - S^{\uparrow} = \lambda_0 \Delta T_e \qquad \text{Eq. (3)}$$

A positive radiative forcing, such as that produced by increasing concentration of greenhouse gases, tends to warm the surface (greenhouse effect) whereas a negative radiative forcing, which can arise from an increase in some types of aerosols or clouds, tends to cool the surface (whitehouse effect). The estimates

[3] The Intergovernmental Panel on Climate Change (**IPCC**) has been conjointly established by World Meteorological Organization (**WMO**) and the United Nations Environmental Program (**UNEP**) to deal with: scientific, technical and socio - economic information relevant for the understanding of climate changes, potential impacts options and solutions for adaptation and mitigation.

of the radiative forcing due to an increase of well-mixed greenhouse gases are: +1.46 Wm^{-2} for CO_2, +0.48 Wm^{-2} for CH_4, +0.34 Wm^{-2} for halocarbons, and +0.15 Wm^{-2} for N_2O. The depletion of stratospheric ozone is estimated to cause a negative radiative forcing of -0.15Wm^{-2}, whereas the radiative forcing of tropospheric ozone is +0.35 Wm^{-2}. Ozone forcing varies considerably by region and responds much more quickly to changes in emission than the long-lived greenhouse gases (CO_2, CH_4, N_2O and CFCs) [10].

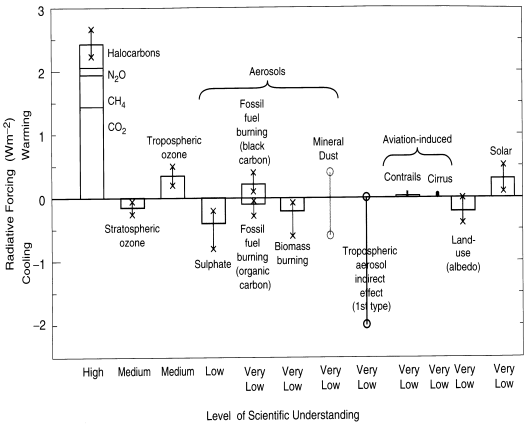

Radiative forcing has a high, medium and low level of scientific understanding. The infrared absorption and radiative transfer of the well-mixed greenhouse gases are well quantified. The short time life greenhouse gases, pose more problem because they are highly variable in space and time [11].

Figure 3 IPCC synthesis on the radiative forcing, level of understanding and uncertainties

Figure 3 shows the present estimation given by **IPCC** of the global mean radiative forcing of the climate system for the year 2000, relative to 1750 [9]. The majority of the world's scientific community estimates that a significant climatic change of anthropogenic source is as a growing body of evidence [12-15]. A clear evidence is, for example, the exponential increase in atmospheric concentrations, since the beginning of the industrial era (~1860) and particularly after 1945-1950, of CO_2, N_2O, CH_4, CFC (i.e. CO_2: ~ 280 baseline in 1850 to ~360 ppmv[4] nowadays). This increase is clearly correlated with anthropogenic activity (fuel consumption, energy production, refrigeration). For this reason the reduction of greenhouse gases was the primary objective of the United Nations Framework Convention on Climate Change (UNFCCC) protocol launched in Kyoto-Japan in December 11, 1997 and to which more and more countries are adhering.

Although it is clear that the ensemble of the greenhouse gases mentioned above are increasing the surface temperature of the planet, the effects of atmospheric

[4] ppmv- parts per million by volume i.e. 10^{-6}

aerosols either directly or through the formation of clouds are still subject of scientific debate. Uncertainties about the aerosols' effects are particularly high, for example, for mineral dust (e.g. Saharan dust) and for cirrus clouds and contrails. Another key aspect of this problem is the difficulty in characterizing the global basic aerosol properties as their number concentration, size distribution and optical parameters. The positive feedback of water vapor is expected to lead to an increase in the upper troposphere (UT) water vapor concentrations and even transport to the tropopause (TP) and lower stratosphere (LS) regions. The main contribution to the natural greenhouse effect is in fact due to atmospheric water vapor but its exact contribution is still a subject of various and controversial opinions and ranges from 35-40 % to 95-98 % [9]. The large uncertainty in our present understanding of the effect of water vapor is due to its high space-time variability, the positive feedback precise quantification and its involving in the cloud related processes. The IPCC reports that, despite non-uniform effects and difficulties in assessing the quality of the data, a tropospheric increase in water vapor was noticed over the 20th century.
For the assessment of the above-described problematic it is necessary to improve the set of well-calibrated instruments (both *in situ* and remote sensing) so that they have the ability to measure changes in atmospheric aerosol amounts and radiative properties, changes in atmospheric water vapor and temperature distributions, and changes in cloud cover and cloud interaction with solar radiation [15, 16].
As it is impossible to make full-scale experiments in the atmosphere and even on a regional scale such an endeavor would hardly make sense because of the complexity of the involved phenomena, we rely on numerical models to provide detailed estimates of climate responses and regional features. Such models cannot yet simulate all aspects of the climate and there are particular uncertainties associated with clouds and their interactions with radiation and aerosols [9, 11, 13, 16-20]. A common approach using the measurements for calibration and checking out of the model performances and then combining measurements with model results at different scales is the present adopted research solution.

2. Research presentation

In the above-described context, the present work implements new atmospheric measurements in order to address the lack of information and to take part via various global networks in the general effort to understand the effects of the atmospheric compounds on radiative forcing and climate. These relatively new measurements concern the upper troposphere (UT)[5] region between 3600 and

[5] UT will be used as abbreviation for upper troposphere (i.e. atmospheric layer between 3600 m ASL and tropopause); The abbreviation ASL will be used for altitude above see level

the tropopause (i.e. 12-15.000 m ASL) and are based on a multi-wavelength LIDAR technique (JFJ-LIDAR)[6] implemented at the International Scientific Station of Jungfraujoch (JFJ)[7]. The LIDAR[8] (**LI**ght **D**etection and **R**anging) technique is based on the interaction of a laser beam with atmospheric compounds (molecules, gases, clouds) via elastic-inelastic or resonant-non-resonant processes (scattering, absorption, fluorescence) relative to the radiation of the laser beam. By analyzing the detected backscattered radiation, suitable at many wavelengths, one may retrieve: optical properties of the atmosphere (e.g. backscatter-extinction coefficients of aerosols and clouds), atmospheric concentrations (e.g. ozone, water vapor) and atmospheric parameters (e.g. temperature, wind) with relatively high space-time resolution (e.g. ~ tens of minutes/hours - ten/hundred m).

The results presented in this thesis report are structured in chapters as follows:

Chapter II presents briefly the atmospheric related measurements at the JFJ station[9] and introduces the principle of the lidar technique and its implementation at the JFJ. Then the fundamental processes (i.e. light-atmospheric compounds interactions) on which the lidar method is based and the lidar-associated equations are reviewed. The JFJ-LIDAR system configuration (i.e. setup and optical layouts) is presented in detail. Examples of lidar signals and results from two comparisons made at JFJ with two other lidar systems are also shown.

Chapter III begins with a short description of the upper troposphere aerosols and cirrus clouds significance for the Earth radiative forcing. Then the lidar – based algorithms used for the retrieval of their optical (i.e. extinction and backscatter coefficients) and their microphysical properties (i.e. radius, refractive index, *albedo*, number-surface-volume size distributions) are described. These algorithms involve the use of elastic (Rayleigh and Mie), inelastic (Raman) and their combination for retrieving the upper troposphere optical properties (i.e. backscatter - extinction coefficients, optical depth) in three distinct cases: a quasi-aerosol-free upper troposphere, a medium aerosol loading, and in the presence of cirrus/contrails. The results obtained using the

[6] JFJ-LIDAR will be used as abbreviation for the multi-wavelength lidar system
[7] JFJ abbreviation will be used for Jungfraujoch, Jungfraujoch observatory, station, etc
[8] For simplification the LIDAR acronym will be written lidar as the LIDAR method starts to become a more known and common measurement technique nowadays
[9] The Jungfraujoch observatory (3580 m ASL, 46°33' N, 7°59' W) is geographically located in Switzerland, in the Berner Oberland region, in the area of Aletsch glacier and the Jungfrau – Mönch - Eiger Mountains.

elastic signals at 355, 532 and 1064 nm extracted from regular measurements[10] concerning the backscatter-extinction vertical profiles are presented. The integrated columns of lidar extinction vertical profiles are compared with similar measurements obtained from a co-located sun-photometer instrument. The use of the elastic-inelastic signals combination for determining the absolute optical properties of the cirrus clouds is demonstrated. Examples of atmospheric depolarization measurements at 532 nm, used to discriminate between water and ice crystal content clouds are shown. Finally a pure contrail is studied in detail in terms of its backscatter-extinction coefficients and also preliminary calculations of its microphysical properties (i.e. refractive index, *albedo* and effective radius) are illustrated.

Chapter IV is devoted to the water vapor. It contains a brief introduction of water vapor climatic significance, measurements efforts and the specificities of UT water vapor. Then the Raman lidar method, based on the ratio of water vapor at 407 and nitrogen at 387 Raman backscatter radiation excited by 355 nm, for determination of the water vapor mixing ratio is described together with the corresponding lidar layout. The retrieval procedure and typical nighttime UT profiles of water vapor are presented. Systematic estimations, based on *in situ* one-point calibration, of the water vapor column above JFJ are shown. These columns are compared with those obtained from the co-located GPS receiver data. Two typical vertical profiles (for winter and for summer) are compared with the closest space-time radiosounding and the results are discussed. Integrated water vapor columns from regular measurements, between 2000 and 2003, are also compared with those obtained from regional radiosoundings.

Chapter V is built around the implementation of a double grating polychomator module allowing the detection of backscattering radiation corresponding to parts of the atmospheric pure rotational Raman spectra excited at 532 nm. These signals are used to obtain nighttime UTLS (upper troposphere – lower stratosphere) temperature profiles but also to determine absolute extinction of cirrus clouds at 532 nm. The first calibration efforts led to temperature profiles in good agreement with US 1976 atmospheric model and the closest space-time radiosounding profile. The estimation of the relative humidity based on temperature and water vapor profile simultaneously with absolute backscatter-extinction coefficients are also exemplified both on vertical and horizontal paths.

Chapter VI is a case study concerning the characterization of the long-range transport mineral dust often occurring over Europe. A dust plume from the

[10] Regular measurements (2000-2003) in the framework of the **EARLINET** (**E**uropean **A**erosols **R**esearch **LI**dar **NET**work) project

August 2nd, 2001 Saharan dust outbreak (SDO) over the Western Europe is analyzed by combining the lidar observations with co-located *in situ* and total column aerosol-related measurements. After introducing climatic significance of the Saharan dust, the measurement techniques are briefly described. Then the SDO patterns are evidenced based on lidar, *in situ* and sun–photometer observations. The results of backward trajectory simulations are presented and they prove the African origin of this mineral dust. Furthermore the dust's optical properties are discussed based on measurements taken in three different situations: dust-free UT, dust and dust mixture with clouds. Preliminary results of dust microphysics calculations are also presented.

Chapter VII is another case study, which concern planetary boundary layer (PBL) air mass intrusions in the UT. The analysis focuses on the particular case, during the August 2003 heat wave, when a very high PBL convection (i.e. ~ 5000 m ASL) covering the Swiss Alps was observed. Lidar, sonic anemometers and other complementary observations (i.e. regional radiosoundings, glacier discharge, aerosol measurements in situ) are discussed on this context. Nighttime observations show also a persistent residual layer above the Swiss Alps characterized by relatively high humidity, aerosol load and temperature. The measurements are also compared with reference measurements taken in springtime when the PBL air masses were trapped below the JFJ altitude.

The main conclusions as well as the salient perspectives of this work are presented in **chapter VIII.**
The **Annexes** referred in the text, as $\mathbf{A}_{number}$, are grouped in chapter **IX**.

Summary*: In the local atmospheric research context at JFJ this work may be seen as a complementary relatively recent implemented tool (i.e. lidar technique) for high spatial-temporal resolution measurements (i.e. aerosols-cirrus optical properties, water vapor mixing ratio and temperature --- vertical and horizontal profiles) in the UT regions. In the global atmospheric research, it may be placed in the context of: aerosols-mineral dust-cirrus/contrails radiative forcing estimation, UT water vapor positive feedback monitoring, PBL – UT - LS exchanges, monitoring of changes in the profile of atmospheric temperature, and characterization and tracking of long range global aerosol transport. The achievements of this work are forming a promising foundation for their extension to stratosphere. A further step will be to add in the near future new observations as for example the stratospheric ozone measurement.*

A schematic overview resuming the main features of the present work is depicted in Figure 4.

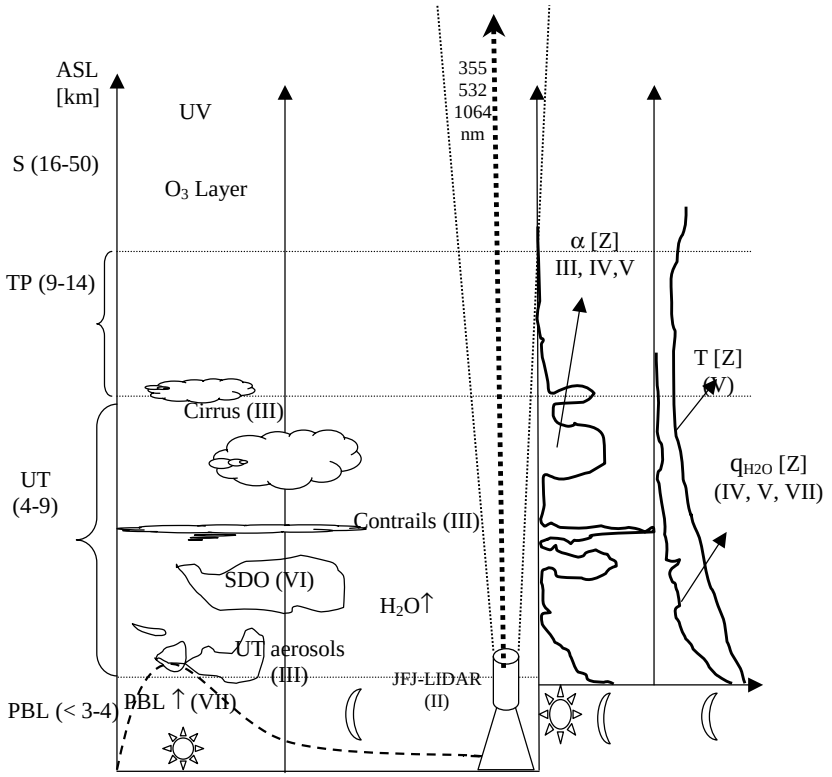

Figure 4 Simplified representation of the topics and achievements of the present work. Note: the Arabic numbers are indicating the related chapters

References

1. Earthwatch, U.N.S.-W., *Air pollution and health*. 2004, UNEP/GRID- Geneva.
2. Couach, O., I. Balin, R. Jimenez, P. Ristori, S. Perego, F. Kirchner, V. Simeonov, B. Calpini, and H. van den Bergh, *An investigation of ozone and planetary boundary layer dynamics over the complex topography of Grenoble combining measurements and modeling.* Atmospheric Chemistry and Physics, 2003. **3**: p. 549-562.
3. EEA, *Air pollution by ozone in Europe in summer 2003 - Overview of exceedances of EC ozone threshold values during the summer season April–August 2003 and comparisons with previous years*. 2004, European Environment Agency.

4. Molina, M.J. and F.S. Rowland, *Stratospheric sink for chlorofluoromethanes-chlorine atom catalyzed destruction of ozone.* Nature, 1974. **249**: p. 810.
5. UNEP-WMO, *Scientific Assesement of Ozone Depletion*. 2002.
6. Barry, R.G., Chorley, R. J., *Atmosphere, Weather & Climate*. Seventh Edition ed. 1998, New-York: Routledge.
7. Harrison, R.M., and van Grieken, R. E., *Atmospheric particles*. IUPAC series on analytical and physical chemistry of environmental systems, ed. J. Buffle, and van Leeuwen H. P. Vol. Volume 5. 1998, New-York: John Wiley & Sons. Ltd.
8. Graedel, T.E., and Crutzen, P.J., *Atmospheric Change: an Earth system perspective.* 1993, New-York: W. H. Freeman and Compagny.
9. Houghton, J.T., Y. Ding, D.J. Griggs, M. Noguer, P.J. van der Linden, and D. Xiaosu, *Climate Change 2001: The Scientific Basis: Contribution of Working Group I to the Third Assessment Report of the Intergovernmental Panel on Climate Change (IPCC)*. 2001, Cambridge University Press, UK. p. 944.
10. IPCC, *Climate change 1994*. 1995, Cambridge: Press Syndicate of the University of Cambridge.
11. Seinfeld, J.H. and S.N. Pandis, *Atmospheric Chemistry and Physics*, ed. J.W.S. ed. 1998: Wiley Interscience. 1326.
12. Santer, B., and al., *Towards the detection and attribution of an anthropogenic effect on climate.* Climate Dynamics, 1995. **12**: p. 77-100.
13. Houghton, J., *Global Warming: the complete briefing*. 1997: Cambridge University Press.
14. Shine, K.P., de Forster, P.M., *The effect of human activity on radiative forcing of climate change: a review of recent developments.* Global and Planetary Change, 1999. **20**: p. 205-225.
15. Ramanathan, V., P.J. Crutzen, J.T. Kiehl, and D. Rosenfeld, *Aerosols, Climate, and the Hydrological Cycle.* Science, 2001. **294**: p. 2119-2124.
16. Charlson, R.J., and Heintzenberg, J. (Eds.), *Aerosol forcing of climate*. Dahlem Workshop Reports, ed. R.J. Charlson, and Heintzenberg, J. Vol. Environmental Sciences Research Report 17. 1995, New-York: John Wiley & Sons, Ltd.
17. Jennings, S.G., *Aerosol Effects on Climate*, ed. S.G. Jennings. 1993: The University of Arizona Press.
18. Kondratyev, K.Y., *Climatic effects of aerosols and clouds*. Atmospheric physics & climatology, ed. J.M.B. Sc. 1999, Berlin: Springer-Verlag.
19. Finlayson-Pitts, B.J., and Pitts, J.N., *Upper and lower atmosphere: theory, experiments, and applications*. 2000, San Diego: Academic Press.
20. de Félice, P., *L'effet de serre: un changement climatique annoncé*. 2001, Paris: L'Harmattan.

Chapter II

LIDAR-based methodology: lidar technique and the JFJ-LIDAR

In the last 20-30 years, environmental research at the Jungfraujoch observatory (3580 m ASL, 46°33' N, 7°59' E) has been focused more on the atmosphere. The station is an outstanding research facility that is capable of monitoring many atmospheric parameters, including trace gases and aerosols as well as solar and cosmic radiation. These measurements are obtained using techniques such as infrared and microwave spectroscopy, gas chromatography, mass spectrometry, instruments for *in situ* determination of aerosol properties, sun photometer, GPS receivers, meteorological sensors, and many others.
Since January 2000, a multi-wavelength LIDAR system developed at EPFL/LPAS has been installed at the Jungfraujoch station. The goal of a lidar implementation at JFJ was to provide atmospheric profiles of aerosol-cirrus optical properties, water vapor mixing ratio and air temperature with high temporal and spatial resolution.
This chapter briefly introduces the measurement techniques that exist at the station and explains the basic principles of the lidar technique. The fundamentals concerning the lidar methodology are reviewed. The latest configuration of the JFJ lidar system is described in detail. Finally, examples of typical LIDAR signals and of results from two inter-comparisons with other lidar systems, installed temporarily at JFJ station, are illustrated.

1. Introduction

1.1 Atmospheric research at the Jungfraujoch station

The Jungfraujoch[1] observatory (3580 m ASL, 46°33' N, 7°59' E) is located in the Berner Oberland region of central Switzerland, in the Jungfrau-Mönch-Eiger mountain chain (Figure 1). The scientific station itself is built on the top of a rock ("Sphinx") located on the dividing line between the Rhine and Rhone watersheds.

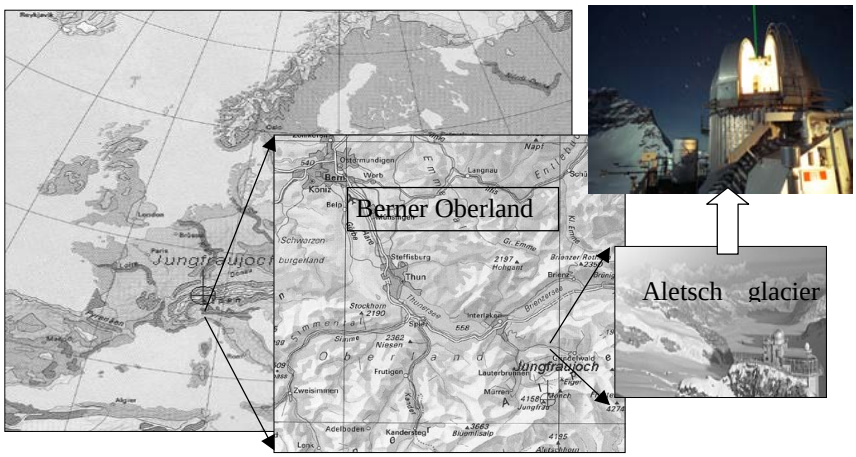

Figure 1 Geographical location of the JJF station ([1]) and a picture taken during the nighttime operation of the JFJ-LIDAR system.

The scientific interest of the region was appreciated as early as 1838-1845, by naturalist-alpinist L. Agassiz. The first scientific experiments were performed here in 1912, when Jungfraujoch became the highest railway station in Europe. The first experiments were related to astronomy (E. Schar, 1922-1927), meteorology (1925), cosmic radiation (W.Kolhorster and G. von Salis, 1926), and ozone (D. Chalonge, 1928). A big leap in scientific research came with the construction of the Sphinx observatory (1930-1937). This facility grew steadily, including the construction of the astronomic cupola (1950-1951), the installation of the first solar spectrograph (M. Migeotte, L. Neven and J. Swensson), and the construction of a large Wilson chamber for cosmic radiation detection (P.M.S.

[1] Jungfraujoch means the "young lady pass" (literal German translation)

Blackett and J.G. Wilson). Further developments included the installation of a new solar spectrograph (L. Delbouille, L. Neven, G. Roland and M. Migeotte, 1957-1958), and the addition of a ϕ 40 cm telescope (M. Golay, 1960), followed by a ϕ 76 cm telescope for systematic astronomic observations (1965-1967). These efforts set the foundation for the existing scientific instrumentation and measurement at Jungfraujoch, including long term monitoring [1].
During the last 20-30 years the research projects on climate change, including monitoring of greenhouse gases, aerosols and solar radiation, have been the main research priority at the station, and the new measurements presented in this research are part of this effort

High resolution, solar Fourier Transform Infrared Spectroscopy (FTIR) has been used for long-term monitoring since the 1950s. Using the Sun as light source, the FTIR technique measures atmospheric absorption bands/lines in the infrared [2]. These high resolution measurements enable the routine detection of column abundances of more than 20 atmospheric constituents, including stratospheric ozone depleting gases (e.g. HCl, $ClONO_2$, HNO_3, NO, NO_2, HF, COF_2, …), greenhouse gases (e.g. N_2O, CH_4, CO_2, SF_6, CCl_2F2, $CHClF_2$, HCFC, …), and species that determine the oxidization capacity of the troposphere (CO, C_2H_2, C_2H_6, OCS, HCN, H_2CO). The column density of water vapor (H_2O) is also measured. FTIR measurements at Jungfraujoch are part of global monitoring networks, such as NDSC (Network for Detecting of Stratospheric Changes [3]).

Radiation Measurements (GAW-Global Atmospheric Watch program) cover a series of UV-visible -IR detectors that measure direct and diffuse solar radiation as part of the Swiss Atmospheric Radiation Monitoring program (CHARM, [4]). This program includes broadband shortwave (solar spectrum, also UV broadband measurements) and long-wave (Earth and atmosphere spectrum) measurements. Short and long-wave measurement time series are important components of climate research, whereas UV measurements are of particular interest from a public health standpoint, as they are linked to the evolution of the ozone layer [5]. Broadband radiation is measured both as global downward hemispheric irradiance and as direct sun irradiance. In addition, the direct spectral irradiance is also measured, allowing a determination of the total column of several atmospheric constituents. Daytime aerosol optical depth [6] and water vapor column [7] are routinely estimated using a 9-wavelength-band (UV-VIS-NIR) sun track photometer (Precision Filter Radiometer – PFR, [8]). UV - irradiance and actinic flux are also measured through regular and intensive campaigns [9].

Halogenated greenhouse gases (CFCs) monitoring has also been performed from January 2000 using gas chromatography-mass spectrometry (GCMS).

These measurements address central European emissions of a wide range of halogenated greenhouse and ozone depletion related gases (as defined by the Kyoto and Montreal protocols). The instrument is part of a network (EU-project SOGE) that includes similar instruments (Monte Cimone, Italy; Spitsbergen, Norway; Jungfraujoch, Switzerland; Mace Head, Ireland). Measurements at Jungfraujoch are usually analyzed using backward trajectory techniques that can identify potential source regions [10].

Air pollutant monitoring at Jungfraujoch station provides representative background air pollution measurements for Central Europe. These measurements are part of the Swiss national 16-stations air pollution monitoring network (NABEL-BUWAL [11]) and measure Ozone (O3), carbon monoxide (CO), nitric oxide (NO), and nitrogen dioxide (NO2). In addition, selected Volatile Organic Compounds (VOCs - alkanes, aromatics) are measured with a time resolution of 4 hours. Daily samples are taken for determination of gaseous SO2 and for particulate sulphur. Finally, 48-h samples of total suspended particles (TSP) are collected and analyzed for total mass as well as for lead (Pb) and cadmium (Cd) concentrations. Annual averages are derived from these measurements.

In situ monitoring of aerosols is carried out with a set of dedicated instruments, most of which operate continuously for the measurement of aerosol properties at relative humidity (RH) of ~10% and at temperatures (T) of ~25°C. Aerosol optical properties such as the scattering coefficient are also obtained with a 3-wavelength (UV-VIS) nephelometer. Other aerosol instruments used include an aethalometer for soot determination (7 _ UV-VIS-NIR wavelengths), an epiphaniometer for aerosol surface determination, and a real time condensation particlecounter (< 1 μm) [12]. Aerosol-dedicated experiments and campaigns are systematically organized (e.g. CLACE 1, 2, and 3 [13]) with the goal of studying ambient properties of aerosols, such as hygroscopic properties and cloud processes [14, 15].

Microwave radiometry is used to determine atmospheric concentrations of water vapor and ozone based on the microwave (~180-200 GHz) emission (rotational transitions) of stratospheric water vapor (H_2O), ozone (O_3), and ClO radical. Inversion methods permit the determination of low resolution profiles [16].

Cosmic radiation measurements are important for climate related research. Neutron counting monitors provide key information about the interactions of the galactic cosmic radiation with the plasma and the magnetic fields in the heliosphere, about the Sun’s production of energetic cosmic rays and about

theinteraction of these cosmic rays with various geomagnetic, atmospheric, and environmental phenomena [17].

A **GPS** receiver that belongs to the Swiss Institute of Topography and it is part of the Automated GPS Network for Switzerland (AGNES, since 1998) is used for evaluating the atmospheric zenith total delay (ZTD). Measurements of the wet delay (WZD) enable derivation of the water vapor integrated column (IWV), which is used for monitoring the upper troposphere water vapor and for adjusting and improving weather forecast models [18, 19].

Glaciological observations of the 25 km – length Aletsch glacier (the longest alpine glacier in Europe), provide information about short - and long - term weather changes, including extreme events and climate trends. These measurements are designed to predict times of break up of large ice masses from mother glaciers [1], and to reveal paleo-atmospheric chemistry using high-altitude glacier firn and ice cores [20].

Carbon balance, ^{14}C and N_2/O_2 monitoring. Long-term observations of $^{14}CO_2$ at Jungfraujoch make it possible to distinguish between CO_2 from fossil fuel combustion and from recent biogenic emissions [21]. CO_2 and N_2/O_2 measurements reveal spatial and temporal variations of CO_2 sources and sinks over the European continent [22].
In addition to the above-mentioned experiments, other systematic observations are taken, including detection of radical species, radioactivity, materials testing under various radiation conditions, solar energy, and periodic medical tests [1].

1.2 Basics of the LIDAR technique

It is within this rich scientific context that a **LIDAR**[2] system was installed and has operated since January 2000 (see Figure 2, left) at the Jungfraujoch observatory. Data from this lidar system (i.e. JFJ-LIDAR[3]) provides various atmospheric profiles with high spatial and temporal resolution. Profiles of the optical properties of aerosols, clouds and contrails, upper troposphere water vapor mixing ratio and air temperature are obtained on a regular basis. The ultimate goal is to provide continuous monitoring using a remote controlled system.

[2] **LIDAR** is the acronym from **LI**ght **D**etection **A**nd **R**anging
[3] JFJ-LIDAR –abbreviation for the multi-wavelength Jungfraujoch LIDAR system

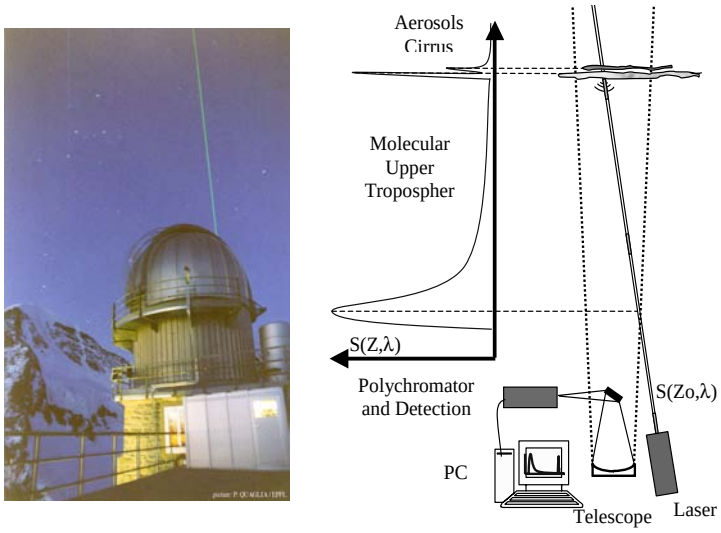

Figure 2 Green (532 nm) laser beam at nighttime pointing from the Jungfraujoch observatory (left) and a schematic setup of a lidar system (right)

The combination of LIDAR observations with the existing measurements at the JFJ station provides a unique opportunity to conduct long-term inter-calibrations and complementary or simultaneous monitoring of different atmospheric parameters over various space-time scales.

The LIDAR technique[4] is based on the detection and analysis of backscatter light that results from the interaction of a laser beam with atmospheric constituents. Probing the atmosphere with a laser is similar to using radar, with the difference that the lidar uses electromagnetic radiation (light) from the optical domain instead of radio waves. The LIDAR technique is an active method because it uses an artificial light source for the retrieval of atmospheric parameters. This contrasts with passive methods, which use light emission from natural light sources (sun, moon) or thermal emission. A typical LIDAR system (see Figure 2, right) consists of a transmitter and a receiver. The transmitter emits short-time laser pulses into the atmosphere. The laser emission is *specific* -- it has a small spatial divergence light beam, and it is quasi-monochromatic and coherent -- and it can emit very high power density, short time pulses (e.g. 100 mJ at 532 nm, pulse width ~3 ns, laser repetition rate at 50 Hz). The laser beam interacts with the atmospheric constituents as it propagates through a multitude of phenomena such as elastic light scattering (molecular-Rayleigh, aerosols-

[4] Brief historical in annex A2

Mie), and inelastic (molecular – Raman) light scattering, fluorescence and absorption. A receiving telescope collects a very small fraction of the backscattered light. In addition to the telescope, the receiver usually contains a polychromatic filter for the spectral separation, high sensitivity photodetectors, and fast sampling rate analog-to-digital converters. The magnitude of the received signal is proportional to the number density of the atmospheric diffusers (molecules or aerosols), their intrinsic properties (i.e. probability of interaction with the electromagnetic radiation at the laser wavelengths, called cross–section value) and with the laser incident energy. The detected light backscatter power S (Z, λ) at the wavelength λ from a distance Z can be expressed by the so-called lidar equation cf. Eq. (1) as follows:

$$S(\lambda_D,Z)=S(\lambda_L,Z_0)\cdot K_S(Z)\frac{A_0}{Z^2}\delta Z\cdot\beta_{atm}(\lambda_D,\lambda_L Z)\cdot T_{\rightarrow}(\lambda_L,Z)\cdot T_{\leftarrow}(\lambda_D,Z) \quad \text{Eq. (1)}$$

where $S_L(\lambda_L,Z_o)$ represents the mean power emitted by the laser source at wavelength λ_L. The λ_D is the wavelength at which the backscattered radiation is detected by the lidar receiver. The radiation is usually detected at the laser wavelength (λ_L, elastic processes) but the shifted in wavelength radiation due to inelastic processes as the Raman effect may be also detected. K_s (Z) is the instrument function that takes into account the transmitter and receiver efficiencies, the overlap function (the degree of spatial recovering between the emitted beam and the receiver field of view). A_0 is the effective receiver area (i.e. area of the telescope collector mirror) and δz is the spatial resolution expressed as:

$$\delta Z=\frac{c\left(\tau_D+\tau_L+\tau_P\right)}{2} \qquad \text{Eq. (2)}$$

where c [$m.s^{-1}$] is the light speed, τ_D [s] is the detection response time (i.e. digitizer and detector's response), τ_L [s] is the laser pulse width, and τ_P [s] is the optical interaction process lifetime. Generally the digitizer response time, $\tau_{D,}$ (typically ~ 10^{-7} s) limits the spatial resolution (e.g. ~tens of m). Both the laser pulse width, τ_L (typically ~ 3 - 10 x 10^{-9} s), and the optical interaction lifetime τ_P (typically within ~10^{-9}-10^{-12} s) have negligible contributions.

The altitude (Z_i) from which the light is scattered may be determined as: Zi = i x δZ, where i = 1 to number of acquisition channels of the laser triggered analog to digital converter (ADC). For example, the use of an acquisition sampling rate of ~ 20 MHz (e.g. τ ~ 5 x 10^{-8} s) will provide lidar backscatter signals with high spatial resolution (e.g. δZ ~7.5 m). As the repetition rate of the lasing is some ~100 Hz assuring between two laser shots to sample signals corresponding from remote distances (e.g. 100 km and more). The limitation is usually due to

the increase in the signal to noise ratio because of weak detection capacity or low laser power or intrinsically due to the involved process (e.g. magnitude of the cross section).

$T_{\rightarrow}$ is the atmospheric transmittance from the transmitter to the probed volume and $T_{\leftarrow}$ is the atmospheric transmittance from the probed volume to the receiver, and they are calculated as follows:

$$T_{\rightarrow}(\lambda_L, Z) = \exp\left[-\int_{Zo}^{Z} \alpha_{atm}(\lambda_L, z)dz\right] \quad T_{\leftarrow}(\lambda_D, Z) = \exp\left[-\int_{Z}^{Zo} \alpha_{atm}(\lambda_D, z)dz\right] \qquad \text{Eq. (3)}$$

where α_{atm} (λ, Z) is the atmospheric extinction coefficient and may be different on the two directions of the laser pulses, as is the case of the Raman backscatter radiation ($\lambda_R \neq \lambda_L$). The atmospheric backscattering coefficient, β_{atm} (λ, Z), is a key element of the lidar equation Eq. (1), and is proportional to the cross-section of the involved physical process σ_{atm} (λ_L,λ_D, Z) and to the number density n (Z) of the atmospheric active diffusers (i.e. atoms, molecules, particles, clouds) in the probed volume. The subscript[5] "$_{atm}$" encompasses all possible physical interactions within the atmosphere (main processes illustrated in Figure 3). Another often-used form of the lidar equation is given cf. Eq. (4) as follows:

$$RCS(\lambda_D, Z) = C_S(Z) \cdot \beta_{atm}(\lambda_D, \lambda_L, Z) \cdot T_{\rightarrow}(\lambda_L, Z) \cdot T_{\leftarrow}(\lambda_D, Z) \qquad \text{Eq. (4)}$$

where RCS[6] is the range corrected signal (i.e. detected signal multiplied by the square of the altitude) and Cs (Z) is the instrument function.

When the LIDAR equation is adapted to the specific process involved (i.e. Rayleigh, Mie, Raman), various atmospheric properties and parameters can be retrieved. An ideal lidar that can explore all these processes is obviously a multi-wavelength system.

Section 2 is devoted to a brief description of these light-atmosphere interaction processes upon which the lidar methodology used in this work is based. Section 3 includes a description of the latest configuration of the JFJ-LIDAR system (i.e. layout and technical specifications), signal examples and the results of two lidar inter - comparison campaigns. Section 4 will include a brief conclusion and some ideas for future perspectives.

[5] Notations: atm = atmosphere, a = aerosol, m = molecular, R = Raman, L = Laser, ext = extinction, scat =scattering, abs = absorption, d = diameter, r = radius, z, Z – altitudes and C, K = constants

[6] RCS (λ, Z) = S (λ, Z) x Z^2, range (or solid angle) corrected signal

2. LIDAR related light - atmosphere interaction processes

The description of the laser beam interaction with atmospheric constituents (i.e. molecules, particles, clouds) is based on the fundamental theory of electromagnetic wave propagation in various media. The atmosphere contains a wide range of constituents extending from atoms and molecules (Angstrom range d ~ 10^{-3}-10^{-4} μm) to aerosols (d ~10^{-2}- 5 μm), cloud water droplets and ice crystals (d ~1 –15 μm and even larger).
The mixture of these different components results in a series of complex atmospheric interactions that take place with a laser beam. The intensity of the light resulting from these processes is proportional with the initial intensity *Io*, the number density of the active diffusers *n* and the differential angular cross – section σ.
If a quasi-parallel, monochromatic, coherent and linearly polarized light (i.e. a laser beam) is sent to the atmosphere, different processes may take place with different probabilities determined by their correspondent cross-sections, σ = f (λ, process, atmospheric diffuser). The interaction may lead to elastic (Rayleigh and Mie) and inelastic (Raman) scattering, absorption, reflection, and/or diffraction. Based on these processes, various spectroscopic and non-spectroscopic measurement techniques have been developed for monitoring the atmosphere [23]. The interactions may be “non-selective", like Rayleigh, Mie or Raman scattering, and more or less important depending on the atmospheric composition (e.g. aerosol loading in the case of Mie scattering). Absorption, for example, is a selective process, and is dependent on the absorption cross section at the laser wavelength. The resonant processes (Rayleigh or Raman) are also selective, meaning that the laser wavelength radiation matches specific electronic transitions of the molecule.
Two important microscopic scattering parameters, in addition to backscatter and extinction coefficients, are used to express aerosol-atmosphere interactions; the dimensionless size parameter (χ), with $\chi = 2\pi$ r m λ^{-1} (where d is the geometric dimension of the diffuser), and the complex refractive index (m) with m (λ) = n(λ) + i k(λ). The real and the complex part of the refraction index provide information about non-absorbing and absorbing aerosol capacity. For χ << 1, Rayleigh or molecular scattering prevails; at χ ~1, Mie-aerosol scattering begins to increase in importance, and for χ >> 1, scattering is purely geometric (e.g. reflection by clouds).

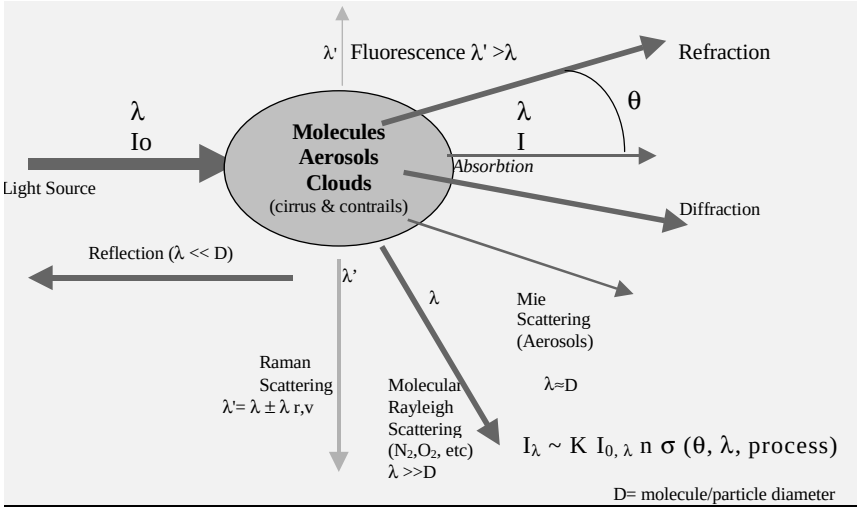

Figure 3 Main atmosphere-light interaction processes lidar related

The molecular and aerosol elastic/inelastic processes involved in the use of the LIDAR method are the following:

(a) N_2, O_2 molecular elastic ($\lambda_D = \lambda_L$) light scattering; i.e. Rayleigh diffusion ($\lambda_L >> d$, where d is the molecular diameter)
(b) Aerosol elastic ($\lambda_D = \lambda_L$) light scattering; i.e. Mie scattering ($\lambda_L \sim d$, where d is the diameter of the particle)
(c) N_2, O_2 and H_2O molecular inelastic ($\lambda_D \neq \lambda_R$) light scattering; i.e. Raman scattering ($\lambda_L >> d$, with d the molecular dimension)
(d) Gas and aerosol absorption (if the radiation at λ_L is absorbed by atmospheric molecules or by compounds forming the aerosols)
(e) Cloud/contrail light scattering ($\lambda_D = \lambda_L$, with $\lambda_L << d$, if d is the droplet/ice crystal geometrical dimension)

2.1 Elastic (Rayleigh) scattering

In the case of the elastic light scattering process, also called Rayleigh scattering, the atmospheric molecules scatter the incident radiation elastically (i.e. $\lambda_D = \lambda_L$). The electromagnetic incident wave induces a dipolar moment ($\vec{P}$) within the molecular system. $\vec{P} = \overline{\overline{\alpha}} \cdot \vec{E}$. $\vec{E}$ is the intensity of the electric field of the incident

electromagnetic wave and $\overline{\overline{\alpha}}$ is the polarisability[7] tensor of the molecule. For the atmospheric diffusers, such as nitrogen and oxygen molecules, $\overline{\overline{\alpha}}$ has a constant and isotropic component, which explains the re-emission of the radiation at the same frequency as the incident electromagnetic wave. For one incoming photon, one photon is re-emitted with the same energy. The elastic contribution always superposes itself on other non-elastic effects (e.g. Raman, absorbtion,…). If the excitation wavelength is much higher than the dimension of the atoms and molecules, the Rayleigh scattering condition is fulfilled. The Rayleigh backscatter is proportional to the diffusers' number density and to the Rayleigh differential cross section. The air differential (angular) Rayleigh cross-section, $d\sigma_m/d\Omega$ [cm^2 $molecule^{-1}sr^{-1}$], may be expressed as given by [24] and expressed by Eq. (5) :

$$\frac{d\sigma_m(\phi,\theta,\lambda)}{d\Omega} = \frac{9\pi^2\left(m_{air}^2-1\right)^2}{\lambda^4 n_{air}^2\left(m_{air}^2+2\right)^2}\left(\frac{6+3\rho}{6-7\rho}\right)\left\{\cos^2\phi\cos^2\theta+\sin^2\phi\right\} \quad \text{Eq. (5)}$$

where λ [cm] is the wavelength, n_{air} [molecules cm^{-3}] is the air molecule number density, m_{air} [-] is the air complex refraction index, ρ_{air} [-] is the depolarization ratio, ϕ [rad] is the polarization angle, and θ [rad] is the scattering angle (see Figure 4).

The Rayleigh scattering phase function is isotropic (i.e. ratio of one direction/all directions backscatter powers) and is $3/8\pi$ leading to:

$$\sigma_m(\lambda) = \frac{8\pi}{3}{}^{\pi}\sigma_m(\lambda) \quad \text{Eq. (6)}$$

where ${}^{\pi}\sigma_m$ is the backscatter (at 180°) molecular (correspondent to the sum of N_2 and O_2) cross - sections. The scattered light intensity pattern is symmetric in the forward and backward directions, and totally polarized at 90° [25].

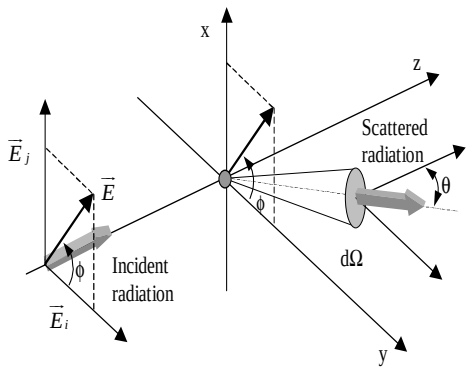

Figure 4 Schematic of the incident and scattered light waves [26]

Calculations of molecular cross-sections as expressed by Eq. (5) were amply addressed in [26] and [27]. For this work, a simpler but realistic semi-empirical

[7] The polarisability expresses the capacity of a molecule to change the distribution of its electrical charges under an external electromagnetic field.

formula for the estimation of the differential backscattering cross section given by [28] was proposed as given cf. Eq. (7) below:

$$\frac{^{\pi}d\sigma_{m}}{d\Omega} = 5.45 \text{ x } 10^{-32} \left(\frac{550}{\lambda}\right)^{4.09} \qquad \text{Eq. (7)}$$

with $d\sigma/d\Omega$ expressed in m^2 $molec^{-1}$ and λ in nm. The backscatter coefficient, β_m, is obtained by multiplying Eq. (7) with the air number density n_{air} *(Z)*. Then by multiplication with the inverse of Rayleigh phase function, the molecular extinction coefficient α_m *(Z)* is obtained

$$\alpha_m(Z) = \frac{8\pi}{3}\beta_m(Z) = \frac{8\pi}{3} n_{air}(Z) \frac{^{\pi}d\sigma_m}{d\Omega} \qquad \text{Eq. (8)}$$

with α_m expressed in m^{-1} and β_m in $m^{-1}sr^{1}$. The air number density n_{air} *(Z)* is determined from the air pressure and temperature profiles as measured by radiosondes or estimated using atmospheric models such as the US1976 model ([29], see A3).

The formula above indicates a Rayleigh cross-section that follows a $\sim \lambda^{-4}$ wavelength dependency, and for this reason, the shorter the wavelength, the more scattered the corresponding radiations. The scattering cross-section is relatively small, on the order of $\sim 10^{-28}$ $cm^2.molec^{-1}$, but the air concentration number i.e. $\sim 10^{19}$ $molec.cm^{-3}$ partially compensates for the inefficiency of this process. The LIDAR equation for the molecular–Rayleigh backscattering is:

$$RCS_m(\lambda_L, Z) = C_s(Z) \cdot \beta_m(\lambda, Z) \cdot \exp\left[-2\int_{Zo}^{Z} \alpha_m(\lambda, z)dz\right] \qquad \text{Eq. (9)}$$

The UT above the JFJ station may be often considered, in wintertime in cloud-free days, as very good approximation for a pure molecular atmosphere.

2.2 Elastic (Mie) scattering

2.2.1 Aerosol (particle) light scattering and correspondent lidar equation

In the presence of particles of size comparable to the excitation wavelength (> 0.1 μm), Mie scattering processes becomes important. Thus the laser radiation is elastically scattered ($\lambda_D = \lambda_L$) by small atmospheric particles (i.e. aerosols) of size comparable to the radiation wavelength. The Mie backscatter usually dominates the Rayleigh scattering, exhibiting high cross-section values ranging from 10^{-26} to 10^{-8} cm^2molec^{-1} (e.g. 10^{-10} cm^2molec^{-1} in the visible spectra at ~500 nm for particles with size around 0.1 μm) [30].

The angular characteristics of Mie scattering (i.e. cross-section) for all particle sizes and wavelengths are expressed by two intensity distribution functions. These functions are fundamental for all the subsequent definitions of the scattering cross sections and volume coefficients [31].
Light scattered by a particle that is observed at angle θ may be treated as consisting of two components of intensities i_c and i_p, i.e. perpendicular (polarized) and parallel to the plane of observation, respectively:

$$i_c(\chi, m, \theta) = \left[\sum_{n=1}^{\infty} \frac{2n+1}{n(n+1)}\left(a_n \pi_n + b_n \tau_n\right)\right]^2$$
$$i_p(\chi, m, \theta) = \left[\sum_{n=1}^{\infty} \frac{2n+1}{n(n+1)}\left(a_n \tau_n + b_n \pi_n\right)\right]^2 . \qquad \text{Eq. (10)}$$

where n are positive integers. The values of a_n and b_n result from Ricatti-Bessel functions, the arguments of which are the size parameter χ, and the complex refractive index, m. The functions π_n and τ_n depend only on the angle θ and involve the first and second derivatives of the Legendre polynomials of order *n* and argument cos(θ). The intensity of the light scattered by the particles is:

$$I(\theta, \phi) = E_\phi \frac{\lambda^2}{4\pi^2}\left(i_c \sin^2\phi + i_p \cos^2\phi\right) \qquad \text{Eq. (11)}$$

where E_ϕ is the irradiance of the incident light. The differential cross-section $d\sigma/d\Omega$ [$cm^2 sr^{-1}$ $molec^{-1}$] is given by:

$$\frac{d\sigma_a(\theta, \phi)}{d\Omega} = \frac{I(\theta, \phi)}{E_\phi} = \frac{\lambda^2}{4\pi^2}\left(i_c \sin^2\phi + i_p \cos^2\phi\right) \qquad \text{Eq. (12)}$$

Based on cross-section values the asymmetry parameter, g, is defined as:

$$g = \frac{\int_0^{\pi} \sigma_a(\theta)\cos(\theta)\sin(\theta)\,d\theta}{\int_0^{\pi} \sigma_a(\theta)\sin(\theta)\,d\theta} \qquad \text{Eq. (13)}$$

For isotropic or symmetric scattering (e.g. Rayleigh or spherical particle scattering), the asymmetry parameter is zero, while for a purely forward scattering the parameter is 1. The asymmetry parameter of the cloudless atmosphere ranges from 0.1 (very clean) to 0.75 (polluted). For a cloudy atmosphere, asymmetry parameter values vary between 0.8 and 0.9 [32]. The total scattering cross section σ_a [$cm^2 molec^{-1}$] may be calculated cf. Eq. (14) by integrating over the 4π sr

$$\sigma_a = \int_0^{4\pi} \frac{d\sigma_a(\theta,\phi)}{d\Omega} d\omega = 2\pi \int_0^{\pi} \sigma_a(\theta) \sin\theta d\theta \qquad \text{Eq. (14)}$$

The total scattering cross section values cover a wide range and are larger than the diffusers' geometric cross sections. The ratio of the scattering to geometric cross sections is defined as the efficiency factors as follows:

$$Q_{scat} = \frac{\sigma_a}{\pi r^2} = \frac{2}{r^2} \int_0^{\pi} \sigma_a(\theta) d\theta \quad and \quad Q_{\pi} = \frac{\sigma_a(\theta = \pi)}{\pi r^2} \qquad \text{Eq. (15)}$$

where r is the radius of the aerosol particle and the complex part of the refractive index is not taken into account. The link between the extinction α, backscatter β coefficients and the efficiency factors Q_{scat} and Q_{π} is given by

$$\alpha_a = \pi \int_0^{\infty} r^2 Q_{ext} n(r) dr \qquad and \qquad \beta_a = \pi \int_0^{\infty} r^2 Q_{\pi} n(r) dr \qquad \text{Eq. (16)}$$

where *n(r)* is the aerosol size distribution and in the calculation of Q_{ext} the complex part of the refractive index is taken into account (i.e. $Q_{ext} = Q_{scat} + Q_{abs}$). The ratio of the scattering (Q_{scat}) to extinction efficiency factors is called *single scattering albedo* (ω_0), which represents the fraction of scattered light with respect to the total light. For a non-absorbing particle, the *single scattering albedo* is 1. The lidar equation for aerosol scattering (Mie) is based on the Rayleigh lidar equation (index m) at which the Mie terms (index a) are added as follows:

$$RCS(\lambda_L, Z) = C_S(Z) \cdot \left[\beta_m(\lambda, Z) + \beta_a(\lambda, Z)\right] \cdot \exp\left[-2 \int_{Zo}^{Z} \left[\alpha_m(\lambda, z) + \alpha_a(\lambda, z)\right] dz\right] \qquad \text{Eq. (17)}$$

where β_a and α_a are the aerosol backscatter and extinction coefficients and may be determined by inverting Eq. (17) as it is explained in detail in chapter III section 2.1.

2.2.2 Aerosol extinction wavelength dependency: Angstrom turbidity law

Important parameters are also the *Angstrom coefficients* A and B that describe the wavelength dependency of the extinction coefficient:

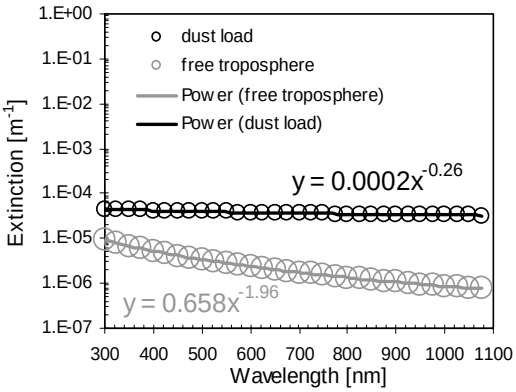

$$\alpha_a = B\lambda^{-A} \quad \text{Eq. (18)}$$

The above power law wavelength dependency cf. Eq. (18) is known as the empirical Angstrom turbidity low [33].

Figure 5 The Angstrom turbidity law exemplifications for dust load and free troposphere situations

This wavelength dependence (i.e. power law) of the aerosols' extinction (α_a) is a valid approximation to the Mie theory [34]. *B* is an index proportional to the aerosol concentration while the wavelength exponent *A* varies from 0 to 4 and is related to the size distribution.

In the almost molecular Rayleigh regime (i.e., low aerosol loading), the extinction coefficient varies with wavelength according to a power law with an exponent A ranging ~ 3 - 4, whereas in large-particle regime, this exponent ranges between 1 and 0.

An optically thick and dense cloud will have $A \rightarrow 0$ (i.e. no wavelength dependency), and A values smaller than 1 are typical for sea salt or mineral dust particles (~1-3 μm) and values larger than 1 are typical for smaller aerosol sizes (< 1μm) [31, 35, 36].

The Angstrom coefficients are good indicators of particle size (A) and number concentration (B) but do not provide precise information on the aerosol size distribution or the shape of the particles.

2.2.3 Aerosol shape: depolarization studies

The diffuser shape may be identified measuring the *depolarization* of the initial plane polarized laser light. The depolarization ratio may be used to distinguish between spherical (e.g. water droplets, with low depolarization ratios) or non-spherical (e.g. ice crystals, with high depolarization ratios).

The depolarization ratio φ (z) is calculated as the ratio of cross (c) to parallel (p) polarization states of the backscatter radiation relative to the initial linear polarization plan of the emitted laser light [37] :

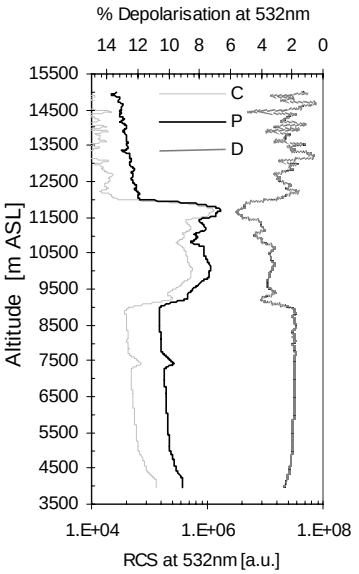

$$\varphi_{atm}(Z) = C_S(Z)\frac{S_c(Z)}{S_p(Z)} \quad \text{Eq. (19)}$$

where C_s is a calibration function taking into account the whole system depolarization effects and the differential detection on the two channels at 532 nm [38]. Generally the molecular atmosphere and spherical particles do not significantly contribute to the depolarization (only ~1-2%), while cirrus clouds composed of ice crystal cause strong depolarization of the light (usually ~10 - 40%) [38] [39, 40].

Figure 6 Depolarization (curve D) and cross (C) and parallel (P) RCS at 532 nm: a cirrus ice – water mixed phases case example

Finally, the measurement of the light depolarization degree (φ) by aerosols/clouds offers information concerning: their shape (spherical or non-spherical) and indirectly about their hydration rate (humid or dry) or even about their lifetime (aged or fresh) and their physical composition (water or ice content).

The JFJ-LIDAR is equipped with a light depolarization detection module (see latter section 3.1.). This module is able to detect separately the cross (perpendicular) and parallel polarization states of the backscattered radiation at 532 nm. The depolarization ratio φ_{atm} (z) is determined from the ratio of perpendicular to parallel corresponding lidar signals

2.2.4 Aerosol microphysics based on lidar determined aerosol optical properties

The lidar-determined values of aerosol extinction and backscatter coefficients may be used via various methods [41, 42] to determine the microphysical aerosol properties such as number-surface-volume size distributions, complex refractive index and single scattering *albedo*. The problem of determining those properties by multi-spectral lidar measurements belongs to a class of inverse ill-posed problems.

Several methods were developed to solve this problem: the singular value decomposition method [43], the iterative method [44] the regularization method [45] and finally the hybrid regularization method [41]. The extinction and

backscatter coefficients at a given altitude can be expressed by two Fredholm equations:

$$\alpha_a = \int_{r_{min}}^{r_{max}} \pi r^2 Q_{ext}(r,\lambda,m)\, n(r) dr \; ; \; \beta_a = \int_{r_{min}}^{r_{max}} \pi r^2 Q_{\pi}(r,\lambda,m)\, n(r) dr \qquad \text{Eq. (20)}$$

where n(r) is the volume concentration distribution [aerosols cm^{-3}], r_{min} and r_{max} are the minimum and maximum radius of the particles, m is the complex refractive index and Q is the extinction and backscatter efficiency (i.e. ratio of scattering and geometric cross-sections). Basically α_a and β_a are calculated cf. Eq. (20) iterating on a matrix of particle radius and complex refractive index, up to values that minimize the difference with the lidar observed values. To choose ranges for the radius, it should be noticed that only particles with radii of the order of the magnitude of the measurement wavelengths (355 to 1064 nm) possess particle-size-dependent scattering efficiencies and therefore are suitable for inversion. The key parameter that best describes the radiative properties of a given size distribution is the surface-area weighted effective radius r_e which is defined as:

$$r_e(Z) = \frac{\int n(r,Z) r^3 dr}{\int n(r,Z) r^2 dr} \qquad \text{Eq. (21)}$$

where r_e [μm] is the effective radius and *n (r, Z)* [$cm^{-3}\mu m^{-1}$] is the aerosol number concentration distribution. The total surface-area concentration a_t [$\mu m^2 cm^{-3}$], the total volume concentration v_t [$\mu m^3 cm^{-3}$], and the total number concentration n_t of particles [cm^{-3}] are given, respectively, by

$$a_t = 4\pi \int n(r) r^2 dr \; ; \; v_t = \frac{4\pi}{3} \int n(r) r^3 dr \; ; n_t = \int n(r) dr \qquad \text{Eq. (22)}$$

The JFJ-LIDAR allows obtaining the extinction and backscatter coefficients at three different wavelengths: 355, 532 and 1064 nm which are considered as solutions and thus criteria of stopping iterations on the hybrid-regularization method used in this work. Using this method one can perform the inversion with three-backscatter coefficients and one-extinction values up to 10 % of noise. In general, it was found that inversion errors increase with the reduction of measurement data and that higher accuracy of the reduced data set is required for a successful inversion. Simulations showed that for [41] noiseless data, the mean and integral parameters of the particle size distribution, (effective radius, total surface-area concentration, total volume concentration and number concentration of particles), with the exception of the number concentration, can be limited to 7 % error in the case of three backscatter and two extinction coefficients [42], which is the case for the JFJ-LIDAR system. The

microphysics calculated within this work is using a program-software developed at the Institute of Mathematics of the University of Postdam (IMP) based on the hybrid regularization method. This method uses variable projection dimension and variable B-spline order as well as truncated singular-value decomposition (TSVD) simultaneously for ill-posed inversion with a known or an unknown refractive index. In the latter case, it performs a set of solutions for a suitable refractive index grid and selects the one that minimizes the errors between the input extinction and backscatter coefficients, and the coefficients calculated using Mie theory. The minimizations are based on the absolute and the relative error of the lidar-calculated data [41, 42].

2.3 Inelastic (Raman) scattering

The Raman effect occurs when the laser radiation is inelastically ($\lambda_D = \lambda_R = \lambda_L \pm \Delta\lambda_R$) scattered from molecules, and the resulting frequency shift ($\Delta\lambda_R$) is characteristic of the molecule involved. Two types of Raman scattered radiation are observed: Stokes, $\lambda_R = \lambda_L + \Delta\lambda_R$, and anti-Stokes, $\lambda_R = \lambda_L - \Delta\lambda_R$. The interaction between the electric dipole moment of the molecule and the excitation radiation induces a change in the rotational and/or vibrational states of the molecule [46]. In this process, quanta of energy $hc/\Delta\lambda_R$ is exchanged, where $h\nu_R = E_{1,v,r} - E_{2,\,v,\,r}$ is the energy difference between two stationary states E_1 and E_2 of the molecule (for example, two vibrational or rotational energy levels).
The Raman frequency shift $\Delta\nu_R$ is completely independent of the incident light frequency, *v*. Raman spectra are studied using light sources in the visible or ultraviolet due to the λ^{-4} dependency of the Raman cross-section. Raman and Infrared (IR) absorption spectra are often complementary, since vibrations and rotations that are not observable in the IR may be active in Raman. Raman scattering is linked to molecular polarizability ($\bar{\bar{\alpha}}$). The changes in the polarizability due to the vibration-rotation motion will contribute to Raman transitions. In order for a vibration or rotation to be Raman-active, the polarizability must change during the rotation or vibration causing the molecule to get an induced dipole moment. Any non-spherical molecule can change its polarizability and thus they are Raman active. Homeopolar molecules, such as O_2, and N_2, which are not infrared active in terms of absorption, are thus Raman-active. The Raman spectra of N_2 and O_2 molecules (~99 % of atmosphere) and of water vapor (H_2O) are addressed within this work via the Raman-based lidar applications.
N_2 and O_2 (class of symmetry $D_{\infty h}$) have a single symmetrical elongation vibration mode $\leftarrow N—N \rightarrow$ and the selection rules for vibrational Raman transition are $\Delta v = 0, \pm 1, \pm 2..$, where v denotes the vibrational quantum number. For each vibrational band, the rotational Raman selection rules conduct to three

spectral bands called O (for $\Delta J = -2$), Q (for $\Delta J = 0$) and S (for $\Delta J = +2$), where J denotes the rotational quantum number.
Water vapor (class of symmetry C_{2h}) is a tri-atomic plane molecule (see Figure 7) with 3 degrees of freedom. The three corresponding normal vibrational modes are: symmetrical elongation (ν_1), deformation of bond angle (ν_2) and anti-symmetrical elongation (ν_3).

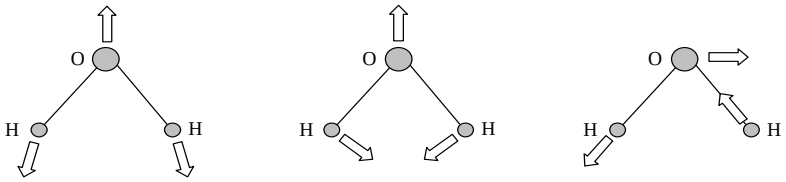

ν_1 =3657.05 cm $^{-1}$ (rel.int. 0.07)	ν_2 =1594.75 cm^{-1} (rel.int.1.47)	ν_3 =3755.93 cm^{-1} (rel.int.1)

Figure 7 The three normal vibration modes of the water vapor molecule

The selection rules are $\Delta v_i = 0,\pm1,\pm2,..$, where v_i denotes the vibrational quantum number, and i =1,2, … the ν_i vibrational modes. The most probable and important mode (i.e. intense) is the oscillation ν_2. For $\Delta v = 0$ and $\Delta J = 0$ the Cabanne scattering line is obtained. For $\Delta v = 0$ but $\Delta J = \pm 2$, the pure rotational O and S Raman spectral bands are obtained. At normal atmospheric temperatures most molecules are in their vibrational ground state v = 0. Thus Stokes bands will be much more important than anti-Stokes ones.
In addition, there is a sharp decrease of intensity as the vibrational quantum number v increases, due to the relative population of states as defined by the Boltzmann distribution. The laser excitation of O_2, N_2, and H_2O atmospheric molecules will give essentially Stokes type transitions. For illustration, the Raman spectra of a diatomic molecule is shown in Figure 8 [26]. Stokes and anti-Stokes branches of the rotational-vibrational structure are shown as well as the pure rotational one.
The first Stokes band is shown in detail. The rotational structure of the Q-branch is also shown. Often the Q branch is considered as a "single" line because its rotational lines are much less widely spaced than in the O - or S - branches. Typically the width of the Q-branch ranges from tenths of cm^{-1} to tens of cm^{-1}.
The intensity of a Raman line is determined by the scattering cross-section value of the transition between the energy levels. In the case of vibrational-rotational transitions, according to the polarizability theory [47], the scattering cross-section of a transition can then be expressed through the matrix elements of the polarizability tensor.

The expression for the total (sum of cross-sections of Q, O and S branches) Raman backscattering cross-section of a shifted vibrational-rotational Raman band ν_j is given after [48] as follows:

$$\frac{d\sigma}{d\Omega}(\upsilon_j,\upsilon_0)=\frac{(2\pi)^4}{45}\frac{(\upsilon_0-\upsilon_j)^4 b_j^2}{1-\exp\left(-\frac{hc\upsilon_j}{k_B T}\right)} g_j\left(45a_j^2+7\gamma_j^2\right) \qquad \text{Eq. (23)}$$

where ν_j [cm^{-1}] is the frequency of the j^{th} vibrational mode of the molecule, b_j is the zero amplitude of the j^{th} vibrational mode, T [K] is the temperature, g_j is the degeneracy of the j^{th} vibrational mode, a_j and γ_j are the isotropic and anisotropic components of the polarizability tensor derived with respect to the normal coordinates, and k_B is the Boltzmann constant.

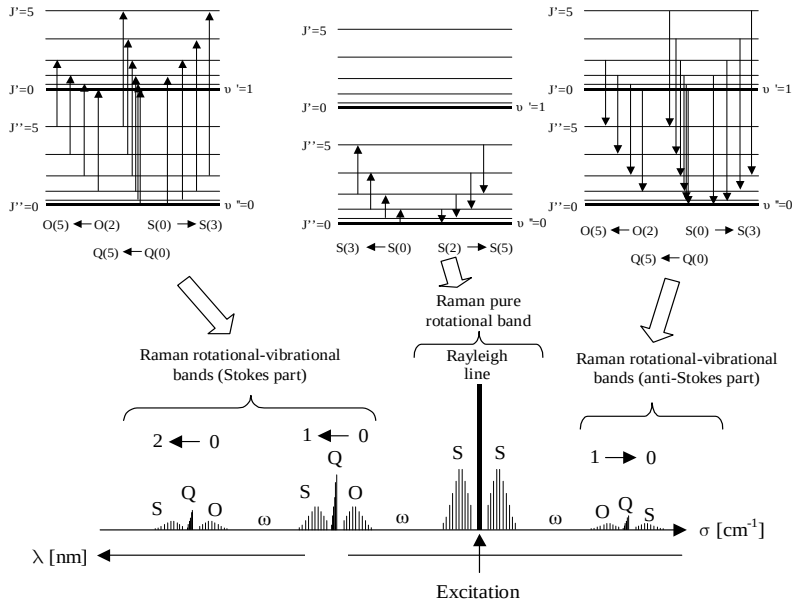

Figure 8 Energy levels diagrams and the correspondent Raman spectra for a diatomic molecule [26]

The Raman processes have relatively low efficiency (cross-sections ranges from 10^{-32} to 10^{-28} cm^2.$molec^{-1}$) compared with Rayleigh scattering which is ~3-5 orders of magnitude higher. The efficiency of this process is higher in the UV, at

shorter wavelengths, since the Raman differential cross-section follows a λ^{-4} law. The choice of the excited wavelength is a key factor and a compromise has to be found between skipping the trace gases (i.e. ozone) molecular absorption in the solar - blind UV regions, avoiding the strong solar radiation influence in the VIS spectral range and accommodating the complexity of the laser source. The Raman lidar techniques based on pure rotational spectra are suitable because of the higher intensity of the pure rotational lines (~10^2-10^3 greater than the rotational-vibrational ones [48]). The choice of the exciting wavelength has to be made carefully in order to avoid coincidences with the absorption wavelengths of the atmospheric components or with resonant molecular transitions. Possible interferences with fluorescence are generally negligible. The fluorescence process is efficient, due to cross-sections around 10^{-20} $cm^2.molec^{-1}$, but the lifetime of the excited levels, from 10^{-6} to 1 s, is in general much longer than the time between two collisions. Quenching by collision reduces drastically the efficiency of the fluorescence at least in the troposphere. The Raman spectrum of molecule-dependent specific lines, shifted with respect to the excitation wavelength, is produced during the very short interaction lifetime (~10^{-14} s) between the molecule and the electromagnetic exciting wave. One of the main advantages of Raman based techniques is the fact that using a single wavelength of the excitation radiation one may induce simultaneously Raman radiation from different molecules which are present in the sampled volume.

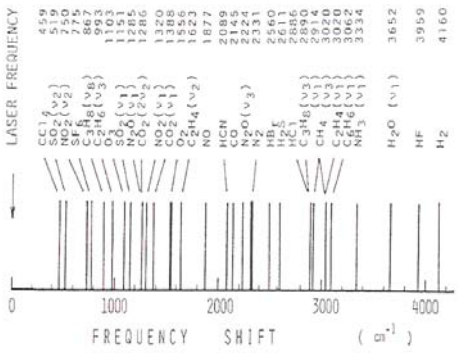

In Figure 9 Q-branch Raman shifts for typical atmospheric molecules are shown. The study of such a spectrum allows simultaneous measurements of a wide range of components, and absolute determination of their mixing ratio.

Figure 9 Raman frequency shifts of Q branch of the atmospheric molecules (from [49])

In this work, rotational-vibrational Raman spectra of N_2 at 387 nm, H_2O at 407 nm excited by 355 nm and the pure rotational Raman spectra of N_2 and O_2 excited at 532 nm are examined.
The lidar equation [50] for the Raman process may be written as:

$$S(\lambda_R, Z) = C_S(Z)\beta_R(\lambda, Z)\cdot\exp\left[-\int_{Zo}^{Z}\left[\alpha_{atm}(\lambda_L, z)+\alpha_{atm}(\lambda_R, z)\right]dz\right] \qquad \text{Eq. (24)}$$

where the Raman backscatter and extinction coefficients are given by

$$\beta_R(\lambda_{L,}\lambda_R,Z)=n_R(Z)\frac{^{\pi}d\sigma_R(\lambda_L,\lambda_R,Z)}{d\Omega}$$
$$\alpha_{atm}(\lambda_{L,R},Z)=\alpha_m(\lambda_{L,R},Z)+\alpha_a(\lambda_{L,R},Z) \qquad \text{Eq. (25)}$$

where R denotes a "Raman" processes, n_R (z) is the atmospheric profile number density of Raman active scattering molecules, $^{\pi}d\sigma_R/d\Omega$ is the differential Raman backscatter cross-section, and α_{atm} is the total (molecular - m plus aerosol - a) atmospheric extinction coefficient.
The advantage of the Raman lidar approach is the use of one laser line for sensing a number of molecular species (different Raman shifts). The main disadvantage is its reduced sensitivity as the Raman cross sections are very low (e.g. ~10^{-29} $cm^{-2}sr^{-1}$ for nitrogen [49]) compared with Rayleigh cross-sections which are 10^3 greater or with Mie cross-sections which are at least 10^3 up to 10^{20} greater. The suppression of the Rayleigh and Mie interferences in the Raman lidar detection channels is crucial for properly recording the Raman atmospheric backscatters.
Powerful laser sources, large telescopes, high performance optical filtering, and long integration times are requirements for the application of the Raman technique.

2.4 Inelastic-resonant light absorption

The absorption processes, and resonant inelastic interactions, occur when the incident photons have wavelengths corresponding to the absorption spectrum of the molecular system. In the atmosphere, light may be absorbed both by trace gases and by aerosols. The absorption coefficient, α_{abs} corresponds to cumulative absorption effects and may be expressed as:

$$\alpha_{abs}(\lambda,z)=\alpha_{abs}^{m}(\lambda,z)+\alpha_{abs}^{a}(\lambda,z)=\sum_i n_i(r)\sigma_{abs}^{i}(\lambda,r) \qquad \text{Eq. (26)}$$

where the index *i* denotes an absorber species (i.e. molecules or aerosols), n_i their concentrations, and σ_i their cross section. Cross-sections usually range from 10^{-22} - 10^{-17} cm^2 $molec^{-1}$ for typical tropospheric trace gas molecules absorbing in UV-VIS, such as NO_2, O_3, NO_3, N_2O_4. Generally, the contribution of well-mixed atmospheric gases is constant at a given laser wavelength while the aerosols' contribution may be highly variable.

Even though the atmospheric absorption is a limitation for the Raman lidar technique and has to be corrected, there are nonetheless many techniques that use the absorption process to determine atmospheric compound concentrations, such as the LIDAR DIAL and the DOAS techniques.
LIDAR DIAL (differential absorption LIDAR) technique uses the differential trace gas absorption of two very close wavelengths emitted in the atmosphere. The choice of the two wavelengths is critical for the LIDAR DIAL technique and is generally a result of a compromise. The main factors determining the ON (strongly absorbed) and OFF (less absorbed) wavelengths are the molecule absorption cross-section and the available laser wavelength. The two wavelengths are chosen in order to maximize the differential absorption. They have to be spectrally close in order to avoid the influence of the differential and highly variable aerosol backscatter and extinction. The DIAL technique is auto-calibrated and successfully applied e.g. for the detection of O_3 [51-54]. Ozone molecules display cross-sections that vary slowly with wavelength and which enable detection with lasers of comparatively broader line widths [53-55].
DOAS (differential optical absorption spectroscopy) [56] is based on the differential atmospheric absorption in relatively large spectral windows. It uses broadband light sources and exploits differences between slow and fast variations with wavelength from which path-averaged concentration can be derived [57-59].
In this work, molecular absorption of trace gases at the laser used wavelengths is considered negligible in the upper troposphere (UT: 3.5-15 km ASL). This has already been discussed and demonstrated in various reports [27, 60]. Aerosol absorption (i.e. complex part of the refractive index) is taken into account indirectly through estimation of the extinction coefficient, which includes the absorption contribution.

3. Jungfraujoch multi-wavelength lidar system

3.1 Technical specifications and optical layout

The implementation at the Jungfraujoch observatory of a multi-wavelength (Rayleigh–Mie-Raman) LIDAR system started at the end of 1999. By March 2000, the system took part in the aerosol measurement campaign (CLACE I [61]). The initial configuration and the technical specifications are described in detail in [27, 62]. In May-June 2002, the system configuration has been modified, passing from three separated off-axis emission beams to co-axial and on-axis emission. The telescope was also displaced from the second floor of the astronomic cupola (ambient conditions) to the Coudé room, where it was mounted in a more compact configuration and was closer to the laser source (see related pictures in annex A4). These modifications allow better overlap between the field of view of the telescope (FOV) at lower altitude (~100 - 250 m AGL)

than the previous configurations (750 - 1000 m AGL). This configuration is definitely more stable and compact, easier to align, but it is nevertheless prone to perturbation by meteorological conditions, such as flying snow, very low temperatures, and other specific constraints that occur at high altitudes. This new setup is schematically shown in Figure 10.

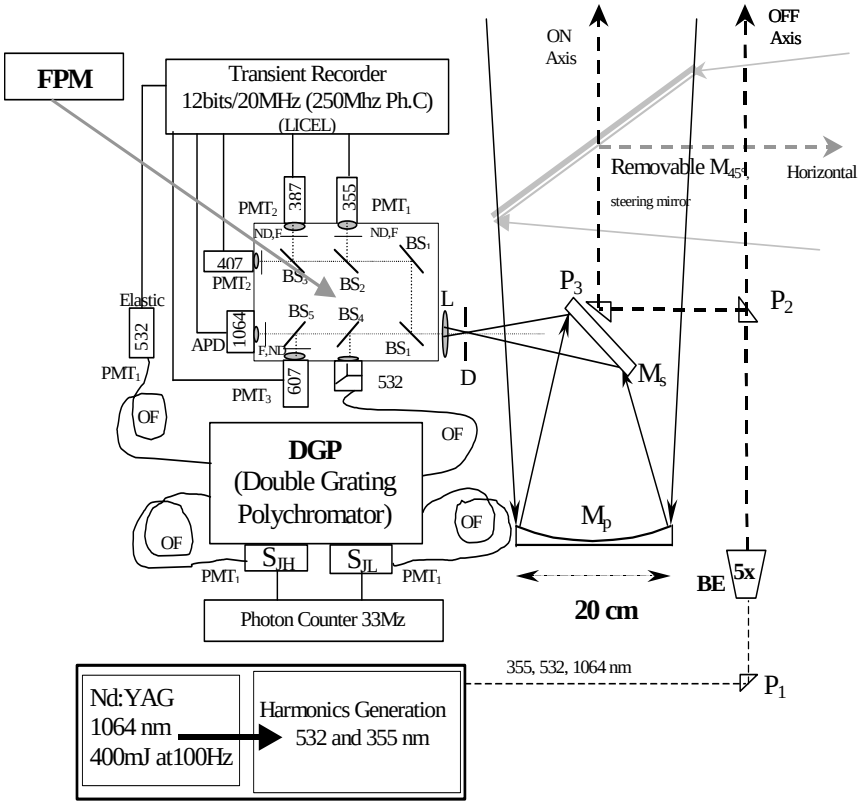

Figure 10 Optical layout of the JFJ LIDAR system (configuration of January 2004)

The lidar transmitter is a Nd:YAG laser (400 mJ at the fundamental 1064 nm and a variable repetition rate up to 100 Hz). Besides the laser radiation at 1064 nm, the 532 nm and the 355 nm are obtained as second and third harmonics of non-linear generation performed by BBO (β-BaB_2O_4 -Beta Barium Borate) crystals. More laser technical information may be consulted in annex A5. The beams' divergence is reduced at ~ 0.14 mrad by using a 5 times beam expander (BE). The coaxial beams are sent to the atmosphere via three guiding and

alignment prisms (P_i). These prisms allow for coarse (P_1 and P_3) and the fine alignment of the laser beam. The prism (P_2) is mounted on a piezoelectric two-axis controlled stage. The receiver part a Newtonian telescope (Vixen, R200SS) is used for the collection of the elastically backscattered light. The telescope uses a ϕ 20 cm parabolic primary mirror, and has an f/4 (0.8 m focal length) optical aperture ratio. The telescope is mounted upright and can be tilted $\pm$ 5^o around the zenith, which enables for coarse alignment of the receiver. Light collected by the Newtonian telescope is sent via a secondary mirror (Ms) to the polychromator filter module (PFM, see Figure 11).
There, the beam encounters first a diaphragm and then is collimated to ϕ 10 mm using a positive - convex lens (L1). This diaphragm, close to the focal point of the telescope, sets the field of view of the receiver, which can be varied from 0.2 to 3.8 mrad by using different diameter diaphragms (D). A set of dichroic beam-splitters (BS1-BS5) separates light by wavelength and directs it to the different channels: Raman scattering of nitrogen at 387 and 607nm, water vapor Raman scattering at 408 nm, and Mie-Rayleigh scattering at 355, 532 and 1064nm. The beam-splitters, optimized for the different wavelengths, operate at a 45^o angle of incidence and their coatings work for both parallel and perpendicular polarization. The light then passes through a combination of broadband and narrowband interference filters (F1-F6) and neutral density filters (ND). These combinations are employed to adapt the light intensity of the signals to the corresponding detectors' sensitivity and they have high out-of-band rejection ratios (10^{-6} -10^{-7}).
Till May 2002, on the 532 nm channel, a Wollaston prism (WP)[8] separates the parallel-polarized backscattered signal from the perpendicular polarized one with an extinction ratio of 10^{-5}. The angle of separation of the two outgoing beams is wavelength dependent: at 532nm this angle is about 12^o. A 2x beam compressor (L1+L2) adapts the incoming beam size to the prism aperture.
The Wollaston prism, the beam compressor and the two detecting PMTs are mounted on a holder that can be rotated precisely around the common optical axis of the elements.
This design allows precise alignment and easy calibration of the depolarization ratio by circular permutation of the "parallel (p)" and "perpendicular-cross (c)" corresponding light detectors.

In order to obtain pure rotational Raman spectra (PRRS) excited at 532 nm, a double grating polychromator (DGP) was optically coupled to the existent polychromator filter module FPM) system replacing the former depolarization

[8] In order to control precisely the polarization state of the radiation transmitted at 532 nm, an air-spaced Glan-Thompson prism was also temporarily inserted into the 532 nm optical path.

module at 532 nm (as shown in Figure 11). PRRS is used then for temperature profile retrieval and as well as a Raman nitrogen-oxygen based molecular atmosphere reference signal (as explained in detail in the devoted chapter V).

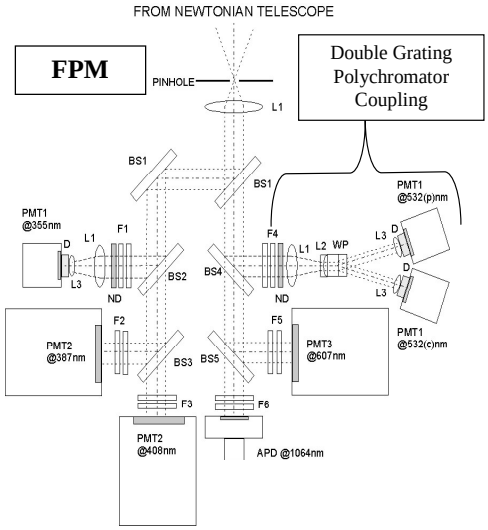

Thus optically separated, the light is finally detected using fast response, relatively high gain and quantum efficiency, low noise level detectors. Photosensors Hamamatsu modules (Type H678, technical specifications in annex A6) are employed for 355 and 532 nm, (PMT_1) and an avalanche photodiode (APD, see annex A8) for 1064 nm.

Figure 11 Layout of the filter polychromator module (FPM). Since May 2002 a double grating polychromator (DGP) was optically coupled and used for measurements instead of the originally used depolarization module at 532 nm.

The Raman signals corresponding to water vapor at 407 nm and to nitrogen at 387 nm were detected using Thorn-Emi (Type QA9829B, technical specifications in A7) photomultiplier tubes (PMT_2). The PMT_2, i.e. Thorn Emi PMT QA9829 series, has a higher gain than the Hamamatsu PMT and thus it is used on the Raman wavelengths at 387 and 408nm. The PMT_3 i.e. Thorn Emi PMT B9202 has a higher sensitivity at 607nm. The Hamamatsu PMT's holders are designed to focus a 10 mm parallel beam on the active area of the detector and this size is the key parameter for setting the position of the collimating lens. The other detectors have an effective cathode size of 45 mm and do not pose restriction on the beam size. The same is valid for the effective aperture of the 45^o beam-splitters whose value is 35 mm, and for the filters whose diameter is 25 mm. In order to avoid the effects of the non- uniform surface response of the Hamamatsu PMT's anodes, a combination of diffuser plate and lens has been employed [63].

Transient recorders are used to digitize the signals. The data acquisition system (Licel, Berlin), is devised for fast, repetitive signals, which are recorded simultaneously in analog and photon-counting modes. By using this combination of analog (A) and photon counting (P.C.) detection, the dynamic range of the signal is largely extended.

Signals below a frequency of 10 MHz pass through an anti-alias filter and are digitized by a 12 bit / 20 MHz analog to digital converter (ADC). Each signal is written to a fast memory, which is read out after each shot and co-added to 24 bit RAM (up to 4096 shots). Depending on the trigger input, signal is added to one of the two RAM, which allows for acquisitions of two channels, measured sequentially. At the same time the high frequency component of the signal (>10 MHz) is amplified. A 250 MHz discriminator detects single photon events above a selected threshold voltage (64 different discriminator levels). Two different settings of the preamplifier can be software-controlled. Signal is written to a fast memory and added to the 16 bit co-adding RAM after each acquisition cycle. Data files were typically recorded upon a 4000-shots (20-80 Hz repetition rate, 200-400 mJ at 1064 nm) average of up to 3000 bins (i.e. ~ 26 km ASL, 1 bin ~7.5 m).
Seven transient recorders are controlled simultaneously using a LabView software via a NI-DAQ (National Instruments) card, installed in a PC. The recorders are synchronously triggered as per the Q-switch of the laser.
For more information the annexes from A4 to A9 refer to the JFJ-LIDAR system specifications.

3.2 Lidar signals examples

The JFJ-LIDAR system, as described above, performs vertical and horizontal observations acquiring elastic signals at 355, 532 and 1064 nm and inelastic rotational-vibrational Raman signals at 387, 407 and 607 nm. Since May 2002, pure rotational signals at ~532 nm have been recorded as a result of the coupling of a double grating polychromator (DGP) to the existent filter polychromatic module (PFM). Figure 12 shows (a) the elastic signals in analog (A) and photon-counting (PC) modes along with one Raman signal at 387 nm. It is worth noting that reasonable SNR is obtained upon acquisition of 4000 shots (at 20Hz and 200 mJ) with a 7.5 m resolution, up to the lower stratosphere (~15-18 km ASL). The 1-file profile shows the backscatter returns from a thin cloud. The backscatters are almost wavelength independent. On the contrary, the backscatter is clearly different in the upper troposphere below the cloud due to the different, nearly molecular (Rayleigh) backscatter (i.e. $\sim\lambda^{-4}$ dependency). The differences at low altitude between analog (A) and photocounting (PC) modes are due to saturation effects in PC mode. To overcome this problem, a correction is required (a detector dead-time correction is proposed later in chapter IV). The Raman signal at 387 nm indicates the sensitivity of the system within the cloud, and thus the potentiality of Raman signals for detection of cirrus cloud extinction (see algorithms proposed in chapter III and V). Interesting to note the fact that no significant cross-talk effect is observed from the strong cloud elastic backscatter in the Raman channel at 387nm.

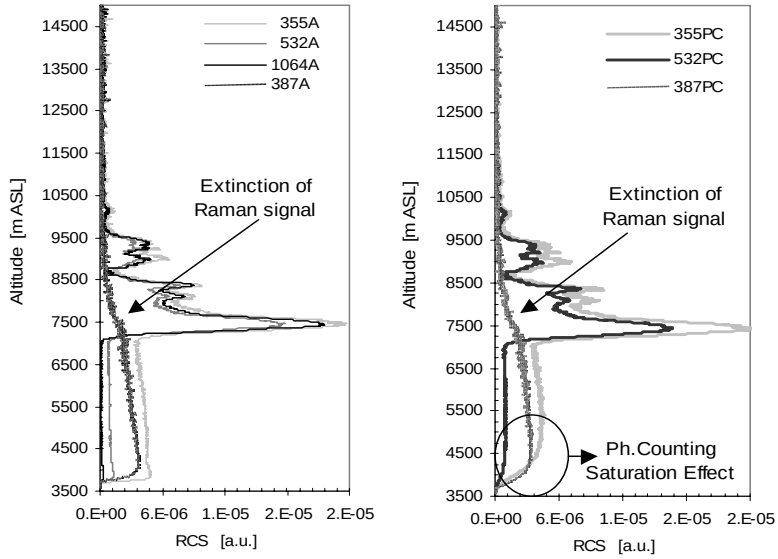

Figure 12 Example of analog (A) and photon-counting (PC) mode vertical LIDAR signals at 7.5 m resolution and averaged over 4000 shots (repeated at 20 Hz).

The 24-h time series of the range-corrected signal at 1064 nm (Figure 13) demonstrates the stability of the LIDAR system. Fog at low altitude and intrusions of air masses from the PBL may be seen as well as cirrus clouds at different altitudes.

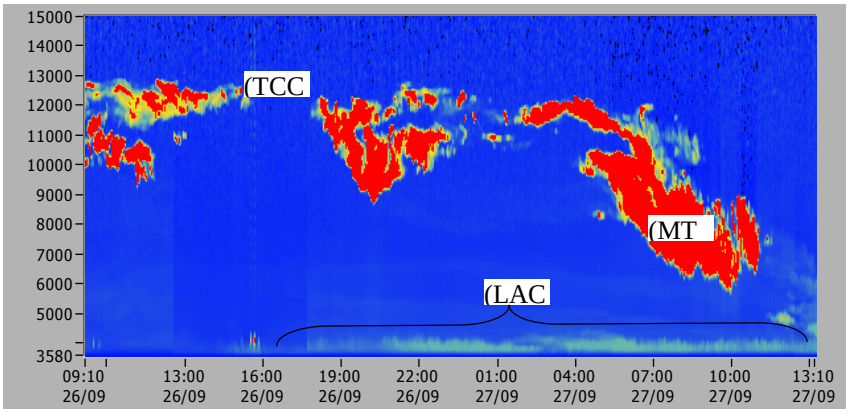

Figure 13 False color intensity graph time series of RCS at 1064 nm. Continuous measurements were performed during more than 24 h. Note the acronyms: TCC – tropopause cirrus clouds, MTC – middle troposphere cirrus, LAC – low altitudes (i.e. 3500 m) clouds. Note: increasing intensity (blue to red)

For performing not only vertical but also horizontal observations above the Aletsch glacier, a steering flat mirror allows one to direct the laser emission and detection at 90°. In this way, horizontal observations are performed. Example of elastic and Raman LIDAR signals at 355 and 532 nm obtained from horizontal observations are shown Figure 14.

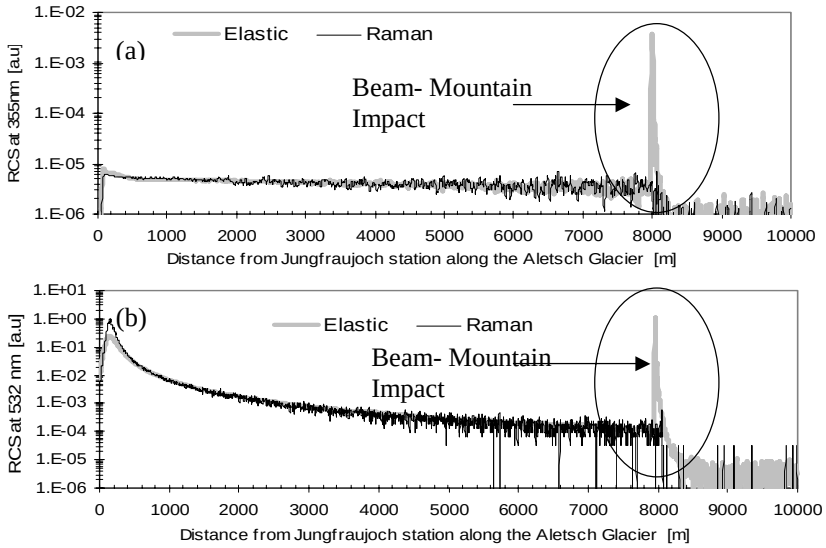

Figure 14 Example of horizontal elastic and Raman signals (a) 355 and (b) 532 nm.

The beam was oriented to a hard target, which was a mountain peak covered by snow at 8 km distance. The huge signal peak at 8000 m on the elastic returns is due to reflection from the snow-covered mountain. It must be noticed that the peak is not observed in the Raman channels, which demonstrates excellent rejection of the very strong elastic backscattered radiation and cross-talk free operation. The horizontal lidar observations value is related to the determination of the aerosol optical properties within the same atmospheric layer as the *in situ* sampling inlets. This will offer the possibility of inter-comparing and calibrating the aerosol measurements between ambient lidar determined optical properties and the *in situ* (dry or ambient) set of measurements (i.e. number concentration, optical properties, microphysics, etc). The estimation of the water vapor and temperature over the longest high alpine glacier in Europe may be of great scientific interest when correlated with glaciological observations.

3.3 System inter-comparisons

The JFJ-LIDAR system was inter-compared to other two LIDAR systems installed temporarily at the JFJ station. The first comparison was made on May 2001 with the one–wavelength (532 nm) LIDAR system of the Neuchatel Observatory within the frame of the EARLINET project [64]. A second inter-comparison (3) was made on October 2003 with a multi-wavelength elastic LIDAR of the Johns Hopkins University [65]. Two examples of the results of these campaigns are shown in Figure 15.

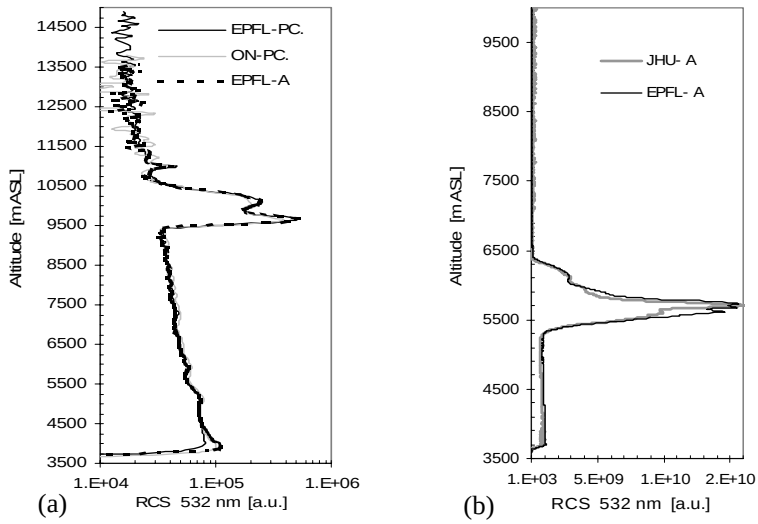

Figure 15 JFJ-LIDAR inter-comparisons: Range-corrected signals (RCS) at (a) 532 nm along with Neuchâtel Observatory LIDAR signal (May 2001), and at (b) 355 nm with JHU LIDAR system in October 2003.

The good agreement observed between the three systems indicates appropriate operation of JFJ-LIDAR, particularly in terms of the detection, signal-to-noise ratio, and achievable vertical range. The time period elapsed between the two comparisons indicates also the stability of the system in the long term (bearing in mind the changes performed between the two Inter-comparison campaigns). More examples extracted from these two inter-validation campaigns may be consulted in the annexes A10 and A11.

4. Conclusion

A multi-wavelength LIDAR system was successfully implemented at the Jungfraujoch observatory. The current configuration was designed to acquire elastic (355, 532 and 1064 nm) and inelastic (387, 407, ~532) backscatter signals from the upper troposphere (3.5 - 15 Km ASL). This system was operated on a regular basis (see data series inventory in annex A13) since March 2000. It also integrated the **E**uropean **A**erosols **R**esearch **Li**dar **N**etwork (EARLINET project [66]) during the entire time-project period May 2000 - January 2003 [67]).
The current configuration of the JFJ-LIDAR system will be modified in the near future in order to extend its capabilities for the detection of stratospheric signals, including a new application i.e. the measurement of stratospheric ozone. This development will be based on the use of the astronomic Cassegrain telescope (ϕ 0.76 m diameter, 11.4 m focal length) which will improve ~15 times the present system sensitivity. The implementation and the use of a more powerful (~ 3 times) Nd:YAG laser has been also considered as well as potential for remote control operation.

References

1. JFJ, *1998-2002 Jungfraujoch Foundation Annual Reports*. 2002.
2. Delbouille, L. and G. Roland, *High resolution solar and atmospheric spectroscopy from the Jungfraujoch high altitude station.* Optical Engineering, 1995. **34**: p. 2736-2739.
3. Zander, R., Mahieu, E. , C. Servais, G. Roland, P. Duchatelet, P. Demoulin, L. Delbouille, C.P. Rinsland, M. De Mazière, and R. Blomme. *Potential of the NDSC in International Foundation HFSJGActivity Report 2002: support of the Kyoto Protocol: Examples from the station Jungfraujoch*. in *The Third International Symposium on Non-CO2 Greenhouse Gases: Scientific Understanding, Control Options and Policy Aspects*. 2002. Maastricht-The Netherlands: J. Van Ham et al. Eds., Millpress-Rotterdam.
4. MeteoSwiss, *WebSite: Climate Research*. 2004.
5. Philipona, R., C. Wehrli, A. Heimo, and L. Vuilleumier. *Radiation Measurements and Climate Change in the Alps*. in *Workshop on 'Atmospheric Research at the Jungfraujoch and in the Alps*. 2002. Davos-Switzerland.
6. Ingold, T., C. Matzler, N. Kampfer, and A. Heimo, *Aerosol optical depth measurements by means of a Sun photometer network in Switzerland.* Journal of Geophysical Research-Atmospheres, 2001. **106**(D21): p. 27537-27554.
7. Ingold, T., B. Schmid, C. Matzler, P. Demoulin, and N. Kampfer, *Modeled and empirical approaches for retrieving columnar water vapor from solar transmittance measurements in the 0.72, 0.82, and 0.94 mu m absorption bands.* Journal of Geophysical Research-Atmospheres, 2000. **105**(D19): p. 24327-24343.
8. Schmid, B., J.J. Michalsky, D.W. Slater, J.C. Barnard, R.N. Halthore, J.C. Liljegren, B.N. Holben, T.F. Eck, J.M. Livingston, P.B. Russell, T. Ingold, and I. Slutsker, *Comparison of Columnar Water-Vapor Measurements from Solar Transmittance Methods.* Applied Optics, 2001. **40**: p. 1886-1896.

9. Blumthaler, M., M. Huber, and J. Schreder. *Spectral measurements of vertically and horizontally polarized UV sky distribution*. in *Remote Sensing of the AtmosphereOcean, Environment, and Space*. 2002. Hangzhou, China: SPIE.
10. Schaub, D., S. Reimann, K. Stemmler, A.K. Weiss, B. Buchmann, and P. Hofer. *Potential Source Regions of Trace Gases Observed at Jungfraujoch,*. in *3rd GAW-CH Conference*. 2002. Zurich-Switzerland: SAEFL Environmental Documentation.
11. NABEL, *Luftbelastung 2001:Schriftenreihe Umwelt*. 2001, Luft, Bundesamt für Umwelt Wald und Landschaft: Bern.
12. PSI-GAW, *In situ aerosols monitoring at Jungfraujoch station*. 2004, PSI-LAC.
13. Nessler, R., N. Bukowiecki, S. Henning, E. Weingartner, B. Calpini, and U. Baltensperger, *Simultaneous dry and ambient measurements of aerosol size distributions at the Jungfraujoch.* Tellus Series B-Chemical and Physical Meteorology, 2003. **55**(3): p. 808-819.
14. Baltensperger, U., *Analysis of aerosols.* Chimia, 1997. **51**(10): p. 686-689.
15. Weingartner, E., M. Gysel, and U. Baltensperger, *Hygroscopicity of aerosol particles at low temperatures. 1. New low-temperature H-TDMA instrument: Setup and first applications.* Environmental Science & Technology, 2002. **36**(1): p. 55-62.
16. Gerber, D., I. Balin, D. Feist, N. Kämpfer, V. Simeonov, B. Calpini, and H. van den Bergh, *Ground-based water vapour soundings by microwave radiometry and Raman lidar on Jungfraujoch (Swiss Alps).* Atmospheric Chemistry and Physics Discussions, 2003. **3**: p. 4833-4856.
17. Flückiger, E.O., R. Bütikofer, and M.R. Moser. *Cosmic Ray Measurements at Jungfraujoch and Gornergrat.* in *Workshop on 'Atmospheric Research at the Jungfraujoch and in the Alps*. 2002. Davos, Switzerland: Swiss Academy of Sciences.
18. Guerova, G., E. Brockmann, J. Quiby, F. Schubiger, and C. Matzler, *Validation of NWP mesoscale models with Swiss GPS Network AGNES.* Journal of Applied Meteorology, 2003. **42**(1): p. 141-150.
19. SwissTopo, *Website of Swiss Institute of Topopgraphy*. 2004.
20. Ginot, P., F. Stampfli, D. Stampfli, F. Schwikowski, and H.W. Gäggeler. *FELICS, a new ice core drilling system for high-altitude glaciers*. in *Ice Drilling Technology 2000*. 2000: Memoirs of National Institute of Polar Research.
21. Levin, I. and V. Hesshaimer, *Radiocarbon – a unique tracer of global carbon cycle dynamics.* Radiocarbon, 2000. **42**: p. 69-80.
22. AEROCAB, *Airborne European Regional Observations of the Carbon Balance*. 2004.
23. Sigrist, M., *Air Monitorinc by Spectroscopic Techniques*. Chemical Analysis. Vol. 127. 1994: John Willey&Sons, Inc.
24. Penndorf, R., *Tables of the refractive index for standard air and the Rayleigh scattering coefficient for the spectral region between 0.2 and 20.0 μm and their application to atmospheric optics.* Journal of the Optical Society of America, 1957. **47**: p. 176-182.
25. Bodhaine, B.A., *On Rayleigh Optical Depth Calculations.* American Meteorological Society, 1999. **16**: p. 1854-1861.
26. Lazzaraotto, B., *Ozone and Water Vapor Measurements by RAMAN lidar in the Planetary Boundary layer*, in *DGR*. 2001, EPFL.
27. Larcheveque, G., *Development of the Junfraujoch multi-wavelenght lidar system for continous observations of the aerosols optical properties in the free troposphere*, in *Environmental and Engineering Dpt.* 2002, EPFL: Lausanne.
28. Collis, R.T.H. and P.B. Russell, *Lidar Measurement of Particles and Gases by Elastic Backscattering and Differential Absorption*. Laser Monitoring of the Atmosphere, ed. E.D. Hinkley. 1976: Springer Verlag.

29. NOAA, NASA, and USAF, *U.S. standard atmosphere (76)*. 1976, U.S. government Printing Office: Washington / USA.
30. Hinkley, E.D., *Laser Monitoring of the Atmosphere*. Topics in Applied Physics, ed. E.D. Hinkley. Vol. 14. 1976: Springer-Verlag.
31. Mc Cartney, E.J., *Optics of the Atmosphere*. 1976: Wiley. 408.
32. Harrison, R.M., and van Grieken, R. E., *Atmospheric particles*. IUPAC series on analytical and physical chemistry of environmental systems, ed. J. Buffle, and van Leeuwen H. P. Vol. Volume 5. 1998, New-York: John Wiley & Sons. Ltd.
33. Angström, A., *On the atmospheric transmission of sun radiation and on dust in the atmosphere*. Geogr. Ann., 1929. **11**: p. 156-166.
34. Finlayson-Pitts, B.J. and J.N.J. Pitts, *Atmospheric Chemistry : Fundamentals and Experimental Techniques*. 1986: Wiley Interscience. 1098.
35. Moulin, C., F. Dulac, C.E. Lambert, and U. Dayan, *Control of atmospheric export of dust from North America by the North Atlantic Oscillation*. Nature, 1997. **387**: p. 691-694.
36. Seinfeld, J.H. and S.N. Pandis, *Atmospheric Chemistry and Physics*, ed. J.W.S. ed. 1998: Wiley Interscience. 1326.
37. Sassen, K., *The depolarization lidar technique for cloud research: a review and current assessment.* Bulletin of the American Meteorological Society, 1991. **72**(12): p. 1848-1866.
38. Biele, J., G. Beyerle, and G. Baumgarten, *Polarization lidar: Corrections of instrumental effects*. Optics Express, 2000. **7**(12): p. 427-435.
39. McNeil, W.R., and Carswell, A. I., *Lidar polarization studies of the troposphere*. Applied Optics, 1975. **14**(9): p. 2158-2168.
40. Murayama, T., H. Okamoto, N. Kaneyasu, H. Kamataki, and K. Miura, *Application of lidar depolarization measurement in the atmospheric boundary layer: Effects of dust and sea-salt particles*. Journal of Geophysical Research-Atmospheres, 1999. **104**(D24): p. 31781-31792.
41. Bockmann, C., *Hybrid regularization method for the ill-posed inversion of multiwavelength lidar data in the retrieval of aerosol size distributions.* Applied Optics, 2001. **40**(9): p. 1329-1342.
42. Mironova, I., C. Bockmann, and R. Nessler. *Microphysical Parameters from 3-Wavelength Raman Lidar*. in *ILRC*. 2002. Quebec: R&D Defence Library Services.
43. Yoshiyama, H., Ohi, A., and Ohta, K., *Derivation of the aerosol size distribution from a bistatic system of a multiwavelength laser with the singular value decomposition method*. Applied Optics, 1996. **35**(15): p. 2642-2648.
44. Rajeev, K., and Parameswaran, k., *Iterative method for the inversion of multiwavelength lidar signals to determine aerosol size distribution.* Applied Optics, 1998. **37**(21): p. 4690-4700.
45. Detlef, M., Wagner, F., Wandiger, U., Ansmann, A., Wendisch, M., Althausen, D., and Hoyningen-Huene, W., *Microphysical particle parameters from extinction and backscatter lidar data by inversion with regularization: experiment*. Applied Optics, 2000. **39**(12): p. 1879-1892.
46. Herzberg, G., *Molecular Spectra and Molecular, vol.3 : Electronic Spectra and Electronic Structure of Polyatomic Molecules*. 1966, New-York: Van Nostrand Reinhold Company. 745.
47. Placzek, G., *Rayleigh -streuung und Raman-effekt*, in *Handbuch der radiologie*, G. Marx, Editor. 1934. p. 205.

48. Inaba, H. and T. Kobayashi, *Laser-Raman Radar -Laser-Raman scattering methods for remote detection and analysis of atmospheric pollution-*. Opto-Electronics, 1972. **4**: p. 101-123.
49. Inaba, H., *Laser Monitoring of the Atmosphere*. Topics in Applied Physics: Detection of atoms and molecules by Raman scattering, ed. E.D. Hinkley. Vol. 14. 1976: Springer-Verlag. 153-232.
50. Measures, R.M., *Laser Remote Sensing. Fundamentals and Applications*, ed. J.W.a. Sons. 1992, New-York: Krieger. 510.
51. Browell, E., S. Ismail, and S.T. Shipley, *Ultraviolet DIAL measurements of O_3 profiles in regions of spatially inhomogeneous aerosols.* Applied Optics, 1985. **24**: p. 2827-2836.
52. Esposito, S.T. and C.R. Philbrick. *Raman/DIAL Technique for Ozone Measurements*. in *19 th ILRC*. 1998. USA.
53. Simeonov, V., B. Lazzarotto, G. Larchevêque, P. Quaglia, and B. Calpini, *UV Ozone DIAL based on a Raman Cell Filled with Two Raman Actives Gases.* SPIE Europto series "Environmental Sensing and Applications", 1999. **3821**: p. 54-61.
54. Simeonov, V., B. Calpini, I. Balin, P. Ristori, R. Jimenez, and H. van den Bergh. *UV ozone DIAL based on a N2 Raman converter, design and results during ESCOPMTE field campaign*. in *21st International Laser Radar Conference Quebec Canada*. 2002. Quebec Canada.
55. Simeonov, V., B. Lazzarotto, P. Quaglia, H. Van den Bergh, and B. Calpini. *Three Wavelength UV Ozone DIAL based on a Raman Cell Filled with Two Raman Active Gases*. in *Extended Abstract of the 20th ILRC*. 2000.
56. Jimenez, R., *Uv-Vis and M-IR spctroscopic techniques for air pollution measurements*, in *SSIE*. 2004, EPFL: Lausanne.
57. Platt, U., *Differential optical absorption spectroscopy (DOAS)*, in *Chem. Anal. Series*. 1994. p. 27 - 83.
58. Balin, I., R. Jimenez, v.d.B. H., and B. Calpini, *DOAS: Differential Optical Absorbtion Spectroscopy Techniquefor Air Pollution Measurements*. 1999.
59. Jimenez, R., A. Martilli, I. Balin, H. Van den Bergh, B. Calpini, B. Larsen, G. Favaro, and D. Kita, *Measurement of formaldehyde (HCHO) by DOAS : Intercomparison to DNPH measurements and interpretation from Eulerian model calculations.* Proceedings of A&WMA 93rd Annual Conference, Salt Lake City (UT), 2000: p. Paper # 829.
60. Whiteman, D.N., S.H. Melfi, and R.A. Ferrare, *Raman Lidar System for the Measurement of Water-Vapor and Aerosols in the Earths Atmosphere.* Applied Optics, 1992. **31**(16): p. 3068-3082.
61. Bukowiecki, N., S. Henning, A. Hoffer, E. weingartner, and U. Baltensperger. *Cloud and Aerosol Characterization Experiment in the free troposphere (CLACE) - a field experiment at the Jungfraujoch (3580 m asl)*. in *European Aerosol Conference*. 2000. Dublin: Aerosol Sci.
62. Larcheveque, G., I. Balin, R. Nessler, P. Quaglia, V. Simeonov, H. van den Bergh, and B. Calpini, *Development of a multiwavelength aerosol and water-vapor lidar at the Jungfraujoch Alpine Station (3580 m above sea level) in Switzerland.* Applied Optics, 2002. **41**(15): p. 2781-2790.
63. Simeonov, V., G. Larchevêque, P. Quaglia, H. Van den Bergh, and B. Calpini, *The influence of the photomultiplier spatial uniformity on lidar signals.* Applied Optics, 1999. **38**: p. 5186-5190.
64. Matthias, V., V. Freudenthaler, A. Amodeo, I. Balin, D. Balis, J. Bosenberg, A. Chaikovsky, G. Chourdakis, A. Comeron, F. de Tomasi, R. Eixmann, A. Hagard, L.

Komguem, S. Kreipl, R. Matthey, V. Rizi, J.A. Rodrigues, U. Wandinger, and X. Wang, *Aerosol lidar intercomparaison in the framework of EARLINET: Part I - instruments.* Applied Optics, 2004. **43**(4): p. 961-976.

65. Adam, M., M. Pahlow, V. Kovalev, J. Ondov, I. Balin, V. Simeonov, H. van den Bergh, and M. Parlange. *Determination of the Vertical Extinction Coefficient Profile in the Atmospheric Boundary Layer and the Free Troposphere.* in *EGS-AGU-EUG*. 2003. Nice France.
66. Bösenberg, J., and al., *EARLINET: A European Aerosol Research Lidar Network.* Advances in Laser Remote Sensing, ed. J. Pelon, Loth, C., Dabas, A. 2001, Palaiseau: Editions de l'Ecole polytechnique.
67. Bosenberg, J. and V. Matthias, *EARLINET:A European Aerosol Research Lidar Network to Establish an Aerosol Climatology (final repport).* 2003.

Chapter III

Upper troposphere aerosols-cirrus-contrails optical properties

The effects of aerosols on the Earth's radiative balance (direct, indirect via clouds or semi-direct) are still unknown both in terms of sign and magnitude. Global models' uncertainties due to the aerosols' effects are unacceptably high. In particular, the radiative forcing due to natural and aviation-induced (contrails) cirrus clouds is still poorly known.

As a contribution to this much-needed knowledge, this chapter deals with the optical properties of aerosols and cirrus clouds in the upper troposphere (UT) region based on a multi wavelength lidar measurement. These addressed optical properties refer to high-resolution vertical profiles of the backscatter (β_a) and extinction (α_a) coefficients and their integrated column extinction (AOD- aerosols optical depth). These retrievals may be estimated by using both elastic (Mie) lidar signals (355, 532 and 1064 nm) and inelastic (Raman) lidar signals (387 and 532 nm) in a combined methodology. A 2-year statistical analysis of the regular measurements within the EARLINET project is discussed based on the determination of UT aerosol optical properties using only the elastic (Mie) lidar signals. The comparisons with the co-located sun photometer measurements (PFR) show relatively good and realistic agreement in terms of AOD and Angstrom coefficients. The use of the Angstrom law on lidar and complementary sun-photometer retrievals made it possible to distinguish and to define different UT aerosol load degrees: aerosol-free reference, typical UT aerosols, and cirrus-contrails load.

Range corrected signals, Mie-Raman combined methods, and measures of the depolarization ratio at 532 nm allow a lidar-based classification of the UT cirrus clouds. A pure contrail case study that examines its geometrical, optical, and microphysical properties is also presented.

1. Introduction

1.1 Aerosols and cirrus clouds: climatic significance

Aerosols[1] are liquid or solid particles, $10^{-3} \rightarrow 10$ μm, suspended in the atmosphere. Particles larger than 2.5 μm (i.e. coarse mode) are easily removed by wet and dry deposition from the atmosphere. Particles between 0.1 to 2.5 μm (i.e. accumulation mode) form the largest amount of atmospheric aerosols. Particles smaller than 0.1 μm (i.e. Aitken nuclei mode) serve as condensation nuclei for forming larger particles and then they will finally migrate to the accumulation mode. These particles remain longer in the atmosphere, and they have various origins and types. One may divide the aerosols sources into anthropogenic (particles from industrial emissions and photochemical transformation in urban pollution plumes), and natural (stratospheric aerosols of sulphuric acid, mainly from volcanic eruptions, tropospheric marine aerosols from the oceans, mineral aerosols from desert or semi-desert areas, forest fires, pollens, etc). An important topic in the Global Change program [1] is the study of the biogeochemical cycle of tropospheric aerosols, and specifically the generation of aerosols from the surface, their uplift and transport as well as their interaction with other cycles [1, 2]. The aerosols have both a direct and indirect impact on climate. Their impact is direct through the diffusion and absorption of solar radiation, leading to cooling (e.g sulfuric) or warming effects (e.g carbonaceous). The indirect effect is related to their role in forming and interacting with clouds. Aerosols act as condensation nuclei and affect the microphysical properties of clouds, which in turn modulate the Earth's radiation budget (i.e. brighter clouds formed in this way would reflect more solar radiation) [3]. The aerosols decrease precipitation efficiency by increasing the number of droplets in warm clouds thereby increasing the clouds' lifetimes and enhancing the indirect radiative forcing associated with these changes in cloud properties [4]. There is also a semi - direct effect that is related to the aerosols capacity to absorb the solar radiation and produce local heating, which in turn will evaporate the surrounding clouds.

The aerosols have different physical and optical properties, depending on their chemical composition, size, and other intrinsic factors as their hygroscopic behavior. Condensation of water vapor on atmospheric aerosol particles significantly affects the size, shape, and chemical composition of these particles, and therefore modifies their optical properties and thus further affects the direct radiative forcing. As the distribution of aerosol concentrations is highly space - time dependent, with short atmospheric lifetimes (i.e. days to weeks) they cannot be considered responsible for a long-term offset to the warming such as in the case with the greenhouse gases (i.e. CO_2, NO_2, CH_4, CFC, etc).

[1] See diagram in annex A12

Cirrus/contrails are aggregations of particles of water or ice suspended in the air, formed when air containing water vapor is cooled below a critical temperature (i.e. dew point) and the moisture condenses into droplets on microscopic particles (condensation nuclei) in the atmosphere. The air is cooled either by expansion during the upward convection resulting from intense solar heating of the ground; by a cold wedge of air (cold front) near the ground causing a mass of warm air to be forced aloft; by orographic movements, and occasionally by a reduction of pressure aloft or by the mixing of warmer and cooler air currents (i.e. aircraft exhausts) [5]. Cloudiness (the proportion of the sky covered by any form of cloud), measured in tenths, is a key element in the estimation of radiative global forcing. One may observe high clouds (6-12 km, cirrus, cirrostratus and cirrocumulus); intermediate clouds (2-6 km, cumulus, altostratus and altocumulus); low clouds (< 2 km, stratus, nimbostratus, stratocumulus) and clouds with vertical development, (0.5–6 km, cumulonimbus) [6]. The effect of the upper troposphere clouds (i.e. natural cirrus or contrails) on chemistry and radiative forcing has recently become a focus of scientific interest. Cirrus clouds are increasing the Earth's *albedo* and at the same time trapping the infrared radiation that the Earth is emitting to space. The warming or cooling effects are both possible depending on clouds location, cover, composition and structure. The greenhouse effect is weak for low altitude clouds, so their *albedo* effect dominates and they have a net cooling effect on the Earth's climate. In contrast, cold high altitude cirrus clouds may either cool or warm the air. They have a strong greenhouse effect, which may outweigh their *albedo* effect [7]. Generally the cirrus greenhouse effect (warming) is expected to prevail over the *albedo* effect (cooling). In addition, the effect of the multiple scattering within a cloud is more important for the long wavelength waves (i.e. *albedo* 0.4-0.7) augmenting the warming effect in the lower atmosphere by as much as 2° [8]. Cirrus clouds may also play a role in heterogeneous chemistry in the upper troposphere, particularly in mid-latitude ozone depletion. The tropopause cirrus may also contribute to the adiabatic heating of the upper troposphere, modifying the temperature profile at the tropopause regions [9].

It is thought that cirrus clouds form naturally in the upper troposphere, when highly dilute sulfate aerosols cool and become supersaturated with respect to ice. These cloud particles freeze homogeneously when water vapor reaches ice super-saturations of around 150%. It has been shown (i.e. MOZAIC experiment, [10]) that the free upper troposphere contains regions which present a super-saturation state with respect to the ice. Thus it is important to analyze the relationships between the number, concentration, and type of aerosols as well as temperature and relative humidity conditions when examining the homogeneous or heterogeneous freezing (condensation) processes with respect to ice or water saturation pressure [11]. It has been suggested that cirrus clouds could also be formed from heterogeneous nucleation on insoluble solids (e.g sulfates). A

recent focus has thus been made on the formation of ice clouds on soot particles which are by-products of fossil fuel combustion at the Earth surface and of aircraft emissions throughout the atmosphere [12].
Contrails are aircraft trace plumes producing a cloudiness up to ~ 0.1-0.2% (1992). This is estimated to increase up to ~0.5-0.8% by the year 2050 [8]. Their formation and influence on the radiation budget are becoming an important scientific topic. Like natural cirrus, the contrails reflect short wave (0.2-5 μm) and they absorb long wave (5-50 μm) radiation having thus an overall positive effect (warming). The contrails' formation and persistence is due to the injection of the warm water vapor, soot, nitrogen oxides, sulfates, carbon dioxide, unburned hydrocarbons, metallic particles, etc in the supersaturated over ice (~ 125-150 %) upper troposphere regions. These emissions may enhance the ozone formation and the decrease in methane. The carbon dioxide emitted is ~ 2% of the total amount produced by anthropogenic activities. Large numbers (about 1017 particles/kg fuel) of small (radius 1 to 10 nm) volatile particles are formed in the exhaust plumes of cruising aircraft (8 -13 km ASL altitudes), as shown by in situ observations and model calculations [8, 13]. The global radiative forcing by persistent contrails was estimated to be some ~ 0.02 Wm^{-2} in 1992 increasing to ~ 0.1 Wm^{-2} in 2050 [14]. Their impact on increasing the daytime maxima and decreasing the nighttime minima of temperatures was observed during the 11 September aviation traffic break [15]. Extensive aircraft-induced cirrus clouds have been observed after the formation of persistent contrails. However, the mechanisms associated with increases in cirrus cover are not well understood and need further investigation.

1.2 Optical properties of aerosols and cirrus clouds: considerations

The extremely variable nature of physical and chemical properties and their distribution over time and space make the study of aerosols and cirrus clouds quite complex. In addition to laboratory measurements of their chemical and physical properties, climate models require "real atmosphere" measurements of aerosol size distribution and optical properties for their radiative budget (forcing) calculations cf. [7]. Global measurements are not available for many aerosol properties, so models must be used to interpolate and extrapolate the available data. Such models now include the types of aerosols that are most important for climate change, but there are large discrepancies between the different models concerning the estimation of sources and spatial distribution of different types of aerosols. Despite this complex but essential influence there is still a big uncertainty on the direct and indirect effects that aerosols have on radiative forcing, as concluded in the last IPCC report [16]. The models' uncertainty is due to: (a) extrapolation of experimentally determined source strengths to other regions and seasons, (b) secondary aerosols (precursors and atmospheric processes), (c) optical properties and (d) aerosol-cloud interaction. More

scientific investigations (e.g. field measurements) concerning chemical and physical properties of aerosols and their involved processes [17] are required to estimate and predict direct and indirect climate forcing.

The aerosols – light interaction can be quantified based on a set of measured or estimated parameters[2]: the extinction (α_a), the scattering (α_a^{scat}), the backscattering (β_a), the lidar ratio (LR, i.e. the extinction to backscatter ratio), the single-scattering *albedo* ($\omega_o = \alpha_a^{scat}/\alpha_a$, i.e. the scattering to extinction ratio), the absorption coefficient ($\alpha_{abs}(z) = \alpha_a - \alpha_a^{scat}$), the functional dependence of light-scattering on relative humidity (i.e. f(RH)), the complex refractive index (m), the asymmetry parameter (g), …([18] and chapter II, section 2.2 for more details and definitions). One of the most often-used parameters is the aerosols' optical depth or thickness (AOD or AOT), which is the extinction coefficient integrated on an atmosphere path cf. Eq. (1) generally scaled at the zenith direction.

$$AOD = \int_{Zo}^{Z} \alpha_a(z)dz \qquad \text{Eq. (1)}$$

The clouds' *albedo* depends on their AOD, the droplet effective radius (r_{eff}) and the geometrical thickness [3].

The wavelength dependence of these parameters is critical and is generally known as Ångstrom's [19] turbidity formula cf. Eq. (2) described already in the chapter II section 2.2.2.

$$\alpha_a = B\,\lambda^{-A} \qquad \text{Eq. (2)}$$

The measurement of the light depolarization degree (φ), see chapter II section 2.2.3 by aerosols/cirrus is giving a good estimation of the particles shape (spherical or non-spherical) and indirectly of their physical phase (water or ice content).

The above-defined aerosol parameters are measured via various complementary techniques at global (i.e. satellites) and local (i.e. ground based) scales. The ground based measurements can be realized *in situ* (e.g. nephelometer [20], aethalometer [21], epiphaniometer [22] on a atmospheric integrated path (e.g. sun photometer [23]), atmospheric profiling (i.e. lidar and radar techniques [24-26]). Generally the ground based observations are made within a network (e.g. AERONET [27], EARLINET [28]). At the global scale these observations are performed via various satellite observations such as AVHRR (Advanced Very High Resolution Radiometer) Ångström coefficient, TOMS (Total Ozone Mapping Spectrometer) aerosol index (AI) and MODIS (Moderate Resolution Imaging Spectroradiometer) AOT data, SAGE (Stratospheric Aerosol and Gas

[2] Indexes: a = aerosol, m = molecular, t = total, scat = scattering, abs = absorption

Experiment) and many (see a quasi-complete list of instrumented satellites for Earth and Atmosphere devoted observations on [29]). The backward trajectory calculations and global circulation model simulations complement the satellite observations. Based on measured optical properties, one may indirectly calculate the aerosols' size and number distribution based on the Mie theory and using regularization inversion method [30].
In the above-described context this chapter deals with the analysis of the upper troposphere aerosols and cirrus/contrails optical properties based on lidar measurements taken regularly with the JFJ-LIDAR.
In section 2, the two main lidar approaches (i.e. Mie and Raman) used to determine the backscatter-extinction coefficients are separately discussed. Section 3 is reserved for a three-part presentation and discussion of the results. The first part refers to the definition of the free troposphere as a pure molecular (Rayleigh) reference based on simulated and real lidar signals and a comparison with measurements taken by a sun-photometer instrument. The second part presents the Mie (elastic) method procedure, the EARLINET database statistical analysis, the comparison with the co-located sun-photometer (i.e. Precision Filter Radiometer - PFR [23]) of AOD measurements and the microphysics calculations corresponding to the median aerosol load situation estimated over two years (e.g. ~ 500 measurement series of ~30 min). The third part starts with a lidar-based presentation of typical observed cirrus clouds in the UT and then a methodology using the Raman (inelastic) combined with Mie (elastic) approaches together with the results obtained from depolarization studies is illustrated. Finally, optical and geometrical properties and the microphysics of a pure contrail are addressed. The chapter conclusion will be separately formulated in section 4.

2. LIDAR-based algorithms

The determination of aerosol and clouds optical properties using the interaction of the atmosphere with a laser beam is based on the detection of the atmospheric returns (i.e. backscatter light) and their further analysis. The emission (transmitter) of the laser beams and the range resolved detection (receiver) was realized with the Jungfraujoch multi-wavlength lidar system (JFJ-LIDAR), largely described in the chapter II section 3.1. The basic configuration and the technical specifications are described also in [31, 32]. The JFJ-LIDAR system was operated regularly since March 2000 and it took part at the **E**uropean **A**erosols **R**esearch **Li**dar **N**etwork (EARLINET [28]) between May 2000 and January 2003 [33]. Further analysis, taking into account the Rayleigh, Mie and Raman light-atmosphere processes, was based on the retrieval algorithms described below.

2.1 Mie and Rayleigh: elastic backscattering

The elastic backscatter signals (i.e.$\lambda_D = \lambda_L$) are due both to the molecular (i.e. Rayleigh scattering) and to aerosols/clouds (i.e. Mie scattering) backscatters. The backscatter light is proportional to the number density of diffusers (i.e.molecules and aerosols) and to the volume backscatter cross-sections of Rayleigh [34-36] and Mie processes [37, 38]. The lidar-detected signals S(z) at λ_L may be written cf. Eq. (3) as follows

$$RCS(\lambda_L, Z) = C_S(\lambda_L, Z)\beta_t(\lambda_L, Z)\exp\left[-2\int_0^Z \alpha_t(\lambda_L, z)dz\right] + b(\lambda_L, Z) \quad \text{Eq. (3)}$$

where λ_L is the laser emitted – detected wavelength (i.e. λ_L = 355, 532 and 1064 nm), C_S is a system function, β_t is the total backscatter coefficient, α_t is the total extinction coefficient and b is the background signal (electronic, solar-moon induced noise, light contamination sources, homogeneous or shaped offsets of the detector's base line, etc). The β_t [$m^{-1}sr^{-1}$] and α_t [m^{-1}] coefficients may be expressed cf. Eq. (4) as the sum of the aerosols (a) and molecular (m) contributions:

$$\begin{aligned}\beta_t(\lambda_L, Z) &= \beta_a(\lambda_L, Z) + \beta_m(\lambda_L, Z) + \beta_{tracegases}(\lambda_L, Z)\\ \alpha_t(\lambda_L, Z) &= \alpha_a(\lambda_L, Z) + \alpha_m(\lambda_L, Z) + \alpha_{abs}(\lambda_L, Z)\end{aligned} \quad \text{Eq. (4)}$$

The effect (i.e. $\beta_{tracegases}$ and α_{abs}) in Eq. (4) was neglected due to the very weak contribution of backscatter and absorption of trace gases at the lidar wavelengths. The molecular contribution β_m and α_m may be estimated taking into account the Rayleigh scattering theory for which many Rayleigh differential cross-section ($^{\pi}d\sigma/d\Omega$) formulations [34-36, 39, 40] are available. The volume molecular extinction coefficient may be written as

$$\alpha_m(\lambda_L, Z) = \frac{8\pi}{3}\beta_m(\lambda_L, Z) = \frac{8\pi}{3}n_{air}(Z)\frac{^{\pi}d\sigma(\lambda_L, Z)}{d\Omega} \quad \text{Eq. (5)}$$

where the factor $8\pi/3$ is the inverse of Rayleigh scattering phase function. For this work we consider for the molecular backscattering differential cross-section, the semi-empirical formula cf. Eq. (6) given by [41] as follows:

$$\frac{^{\pi}d\sigma}{d\Omega} = 5.45\times10^{-32}\left(\frac{550}{\lambda}\right)^{4.09} \quad \text{Eq. (6)}$$

with $d\sigma/d\Omega$ expressed in m^2sr^{-1} and the wavelength λ in nm. The calculation of air number density $n_{air}(Z)$ in [molec m^{-3}] is estimated based on the US Standard Atmosphere 1976 [42] based on pressure $P_{air}(Z)$ and $T_{air}(Z)$ profiles initialized at Jungfraujoch station (see example of calculation in annex A3).

The aerosol extinction (α_a), and backscatter (β_a) coefficients at the three wavelengths may be derived from Eq. (3) using different inversion techniques [43, 44]. In addition to the estimation of the molecular contribution for the inversion [43] of Eq. (3), two *a priori* assumptions are necessary to allow the retrieval of $\alpha_a(z)$ and $\beta_a(z)$ profiles: (i) the guess of the lidar ratio (LR) value (extinction/backscatter) and (ii) a known reference value at a given altitude (e.g. a region with a molecular value). The inversion technique in this work was based on the Fernald inversion [44] and uses the following derived formula [32]:

$$\beta_a(Z-dz)+\beta_m(Z-dz)= \frac{LR(Z-1)\cdot RCS(Z-dz)\exp\left[A(Z,Z-dz)\right]}{\frac{RCS(Z)}{\beta_a(Z)+\beta_m(Z)}+\left\{S_a(Z)\cdot RCS(Z)+S_a(Z-dz)RCS(Z-dz)\exp\left[A(Z,Z-dz)\right]\right\}dz} \qquad \text{Eq. (7)}$$

where RCS (Z) is the range corrected signal at the altitude Z, LR is the lidar ratio, dz is the spatial resolution and A(Z, Z-1) is defined as follows:

$$A(Z,Z-dz)=\left\{\left[LR_a(Z-dz)-LR_m\right]\times\beta_m(Z-dz)+\left[LR_a(Z)-LR_m\right]\times\beta_m(Z)\right\}\cdot dz \qquad \text{Eq. (8)}$$

where LR_m is the molecular extinction to backscatter ratio, β_m is the molecular backscatter coefficient. The lidar ratio value is guessed and kept constant and a backward [45] iteration is started from a molecular assumed value at high altitude. The main criterion for stopping the iteration procedure is reaching a minimum in the difference between the total extinction and the molecular profiles along a clearly identified molecular window. Conducting the inversion with a variable lidar ratio value is also possible [46].

This above-described algorithm was implemented [32] and inter-compared within the EARLINET lidar community [33, 47, 48]). The results of these inter-comparisons of the lidar inversion algorithms and software were published in [49]. The errors analysis may be found in [32] and is taking into account the statistical errors due to the signal detection and the systematic errors due to the estimation of the lidar ratio (LR), the molecular backscatter coefficient, the choice of the reference value, the effect of the multi-scattering and the averaging of data. In conclusion, this study shows two distinct cases: (i) clear sky situation where the total error varies from 3 % (at 3000m) to 8 % (at tropopause) with a main contribution due to the molecular reference (1–7 %) and to the signal detection (3-4 %), with the choice of the molecular reference and the lidar ratio

affect the error by less than 0.25 % and (ii) hazy day situation, in which the errors can reach up to ~15 %, most of them icoming from the signal detection (~80 %); however, the lidar ratio and the molecular estimations are not negligible.

2.2 Raman: inelastic backscattering

Raman backscatter signals/shifts (i.e. $\lambda_D = \lambda_R = \lambda_L \pm \Delta\lambda_R$) may also be used for determining the optical properties of the atmosphere. The Raman scattering results from the interaction between the exciting radiation and the electric dipole moment of the atmospheric nitrogen, oxygen and water vapor molecules. The de-excitation of the induced rotational and/or vibrational states (i.e. via the induced dipole moment due to the changes in the polarisability of the diffuser) by the incident electromagnetic wave produces shifted radiation both at larger (Stokes: $\lambda_R = \lambda_L + \Delta\lambda_R$) or at smaller (anti-Stokes: $\lambda_R = \lambda_L - \Delta\lambda_R$) wavelengths compared with the excitation one. The magnitude of the Raman shifts ($\Delta\lambda_R$) is specific to the excited molecule, and the amount of the detected light is proportional with the molecular atmospheric concentration (see details in chapter II, section 2.3). The Raman lidar equation [50] may be written cf. Eq. (9) below

$$RCS(\lambda_R, Z) = C_S(\lambda_R, Z) \cdot \beta_R(\lambda_{L,}\lambda_R, Z) \exp\left[-\int_0^Z (\alpha_t(\lambda_L, z) + \alpha_t(\lambda_R, z))dz\right] + b_{\lambda_R}(z) \qquad \text{Eq. (9)}$$

with the Raman backscatter coefficient

$$\beta_R(\lambda_{L,}\lambda_R, Z) = n_R(Z)\frac{^{\pi}d\sigma_R(\lambda_L, \lambda_R, Z)}{d\Omega} \qquad \text{Eq. (10)}$$

where R denotes the Raman channels, C_S is the system constant, n_R is the number density of Raman scattering molecule, $^{\pi}d\sigma/d\Omega$ is the differential Raman backscatter cross-section, α_t is the total extinction coefficient (molecular + aerosols + trace gases absorption) and b is the background signal (electronic or sky noise).

This Raman lidar equation helps solving the ill-posed elastic lidar equation. Therefore analysis of this signal alone permits the determination of the aerosol extinction profile $\alpha_a(\lambda_L, z)$ at the laser emitted wavelength [51-53]. The molecular part, $\alpha_m(\lambda_L, z)$ is again calculated cf. [54]. By assuming a wavelength dependence of the extinction coefficient (i.e. an Angstrom law, $\alpha_a \sim \lambda^{-A}$), the aerosols' extinction $\alpha_a(\lambda_L, Z)$ may be obtained. One of the most frequently used approaches is described in [55, 56] and gives this formula:

$$\alpha_a(\lambda_L,Z)=\frac{\frac{d}{dz}\left\{\ln\left[\frac{n_{air}(Z)}{z^2S(\lambda_R,Z)}\right]\right\}-\alpha_m(\lambda_L,Z)-\alpha_m(\lambda_R,Z)}{1+\left(\frac{\lambda_L}{\lambda_R}\right)^A} \qquad \text{Eq. (11)}$$

In this work a similar formulation is proposed as follows. After writing Eq. (9) for a pure molecular atmosphere and then forming the ratio of the two correspondent equations (aerosols load and pure molecular) one may extract the aerosol extinction as expressed in Eq. (12)

$$\alpha_a(\lambda_R,Z)=-\frac{1}{1+\left[\frac{\lambda_L}{\lambda_R}\right]^A}\frac{d}{dz}\left\{\ln\left[\frac{RCS_R(\lambda_R,Z)}{RCS_m(\lambda_R,Z)}\right]\right\} \qquad \text{Eq. (12)}$$

where the $RCS_R\ (\lambda_R, Z)$ and the $RCS_m\ (\lambda_R,Z)$ are the range corrected signals (i.e. RCS = S x Z^2) for Raman and molecular simulated signal. Simplification of Eq. (12) is immediate in the case of pure rotational Raman signals (i.e. $\lambda_R \sim \lambda_L$) as the Angstrom correction may be neglected and the extinction coefficient may be calculated as below:

$$\alpha_a(\lambda_R,Z)=-\frac{1}{2}\frac{d}{dz}\left\{\ln\left[\frac{RCS_R(\lambda_R,Z)}{RCS_m(\lambda_R,Z)}\right]\right\} \qquad \text{Eq. (13)}$$

However, the advantages of using the Raman signals may be combined with those of elastic lidar by introducing the Raman-estimated aerosol extinction coefficient in the elastic lidar equation and thus allowing a more realistic determination of the backscatter coefficient without using a constant-guessed value of the lidar ratio.

The above-described Raman based approaches are applied in this work, first based on the rotational-vibrational Raman backscatters returns detected from nitrogen at $\lambda_{N2} \sim 387$ nm (excited at $\lambda_L \sim 355$ nm), and since May 2002, based also on the pure Raman rotational backscatters at ~ 532 nm ([57], see chapter V). The depolarization at 532 nm, the Angstrom law fits and correspondent A and B coefficients and the determination of microphysics (as described in chapter II, sub-section 2.2) are also used here for a better characterization of the UT aerosols-cirrus-contrails.

3. Results and discussions

The JFJ-LIDAR, upper troposphere systematic measurements (see annex A 16) obtained for the elastic (355, 532 and 1064 nm), Raman (387 and ~532 nm) and depolarized (at 532 nm) were considered for this work. The proposed procedure for treating the corresponding lidar signals in order to obtain the backscatter and extinction coefficients are summarized schematically in the block diagram presented in the Figure 1.

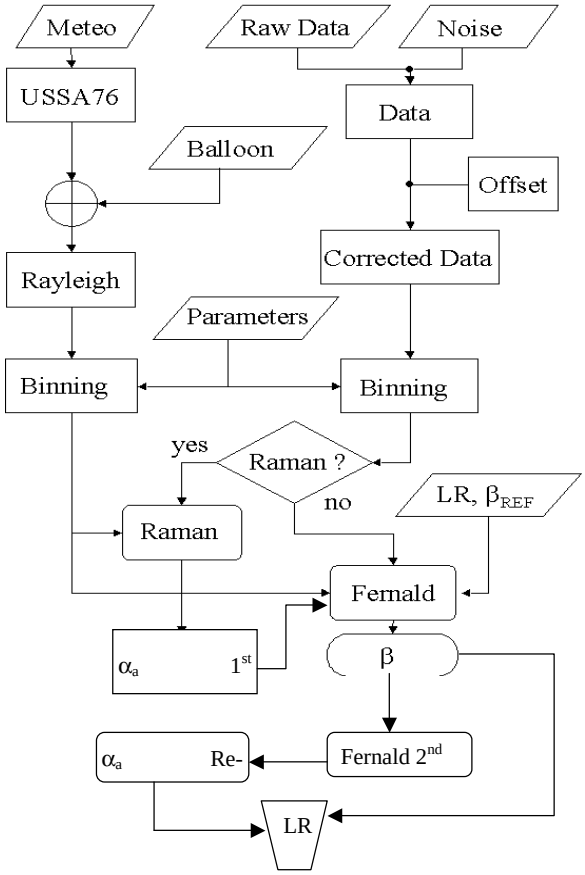

Figure 1 Block diagram representing the combined Raman-elastic approaches for retrieval of backscatter and extinction coefficients

The above-described protocol is taking into account both elastic and Raman acquired signals and it is integrating complementary local meteorological and regional radiosounding data[3]. Raman technique allows a preliminary estimation of the absolute value of aerosol's extinction coefficients. The obtained low-resolution (i.e. highly smoothed data) extinction profile is then introduced, instead of the a priori lidar ratio profile, in the Fernald inversion, in order to obtain the high-resolution backscatter coefficient. By reapplying the Fernald inversion using this newly determined high-resolution backscatter coefficient, the extinction coefficient can be retrieved at the same resolution as the elastic backscatter. Finally this allows a more precise determination of the lidar ratio, which can then be used as a more realistic approximation in case of similar considered atmospheric conditions.

3.1 Molecular upper troposphere

The backscatter coefficients based on Eq. (5) and Eq. (6) corrected for the Rayleigh extinction allow simulation of the Rayleigh (i.e. pure molecular atmosphere) correspondent lidar signals. These molecular simulated backscatter signals were compared both to Raman (387 and 532 nm) and elastic (1064 nm) signals for clear sky situations. Simulated pure molecular lidar shows very good agreement with real lidar detected signals (elastic or inelastic) in the aerosol-free upper troposphere situation for all relevant wavelengths as shown in the example presented in Figure 2 (a).
The extremely good correlation validates the proposed semi-empirical approach [54] to estimate the molecular upper troposphere above the Alps. In order to verify the degree of molecular purity of an apparently perfectly clear blue-sky day, measurements of the total optical depth (TOD) using a sun-photometer (i.e. RSL 10 channels Reagan, specifications in annex A20) were also considered. The related sun-photometer measurements are plotted in annex A21. In Figure 2 (b) only the TOD measured at midday on May 8, 2001 (e.g. an apparently clear sky day) is plotted together with the calculated molecular extinction coefficients.
Fitting a power law in $\sim\lambda^{-A}$ one may easily observe that despite the high visibility and the apparently clear sky the A exponent for the sun-photometer AOD is ~ 2.14, smaller than the simulated Rayleigh one ~ 4.09, suggesting the presence of a certain amount of small size particles in the upper troposphere.

[3] A quasi-complete set of MatLab, LabView and Delphi software routines were developed within the present work for implementing the proposed procedure as depicted in Figure 1. The main examples are illustrated in the annexes: A17 to A19.

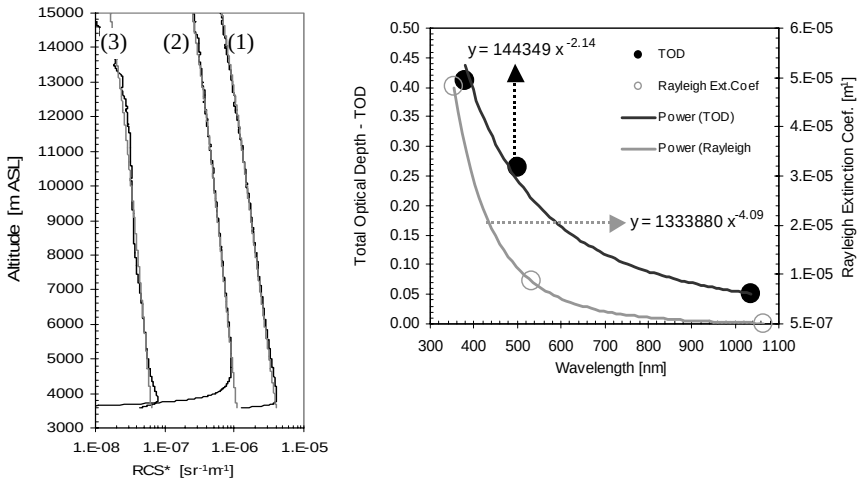

Figure 2 (a) Range corrected signals[4] (RCS*) for Rayleigh simulated signals and Raman (or elastic for 1064 nm) in (1) 387, (2) 532, and (3) 1064 nm; (b) Rayleigh calculated extinction and TOD measured power law representations.*

3.2 Upper troposphere aerosols

Regular observations[5] taken since May 2000 were used to determine the backscatter and extinction coefficients based on the elastic signals and using a validated algorithm within EARLINET ([44, 49]). The main limitation of this data treatment algorithm is the use of *a priori* lidar ratio values. A case example of the elastic inversion at 532 nm is illustrated in Figure 3 for an upper troposphere loaded with aerosol layers and cirrus clouds. Similar inversions were also regularly performed for 355 nm and 1064 nm.

[4] RCS* in [$m^{-1}sr^{-1}$] - are the range corrected signals scaled (calibrated, normalized) using an appropriate molecular value

[5] See the inventory of the data series represented in the annex A13;

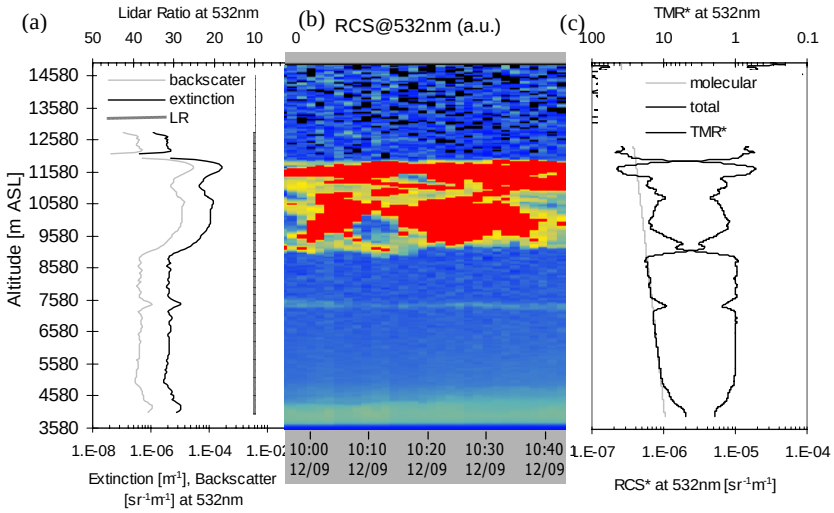

Figure 3 (a) Backscatter-extinction coefficients obtained using Fernald inversion algorithm with a LR = 10; (b) RCS at 532 nm graph intensity time series and (c) Simulated Rayleigh and Elastic at 532 nm range corrected (molecularly scaled at 6000 m ASL) signals (RCS) together with the total to molecular ratio[6] (TMR*).*

In Figure 4 are presented the histogram plots of the aerosols optical depth (AOD or AOT) and the averaged extinction * (the weighted AOD*, averaged over the measurement vertical range) calculated from the extinction coefficient profiles at 355A, 532A and 1064A nm. The index A indicates the fact that only the analog signals were considered

[6] The TMR* is the total (elastic) to molecular signal ratio after being scaled to an appropriate molecular value.

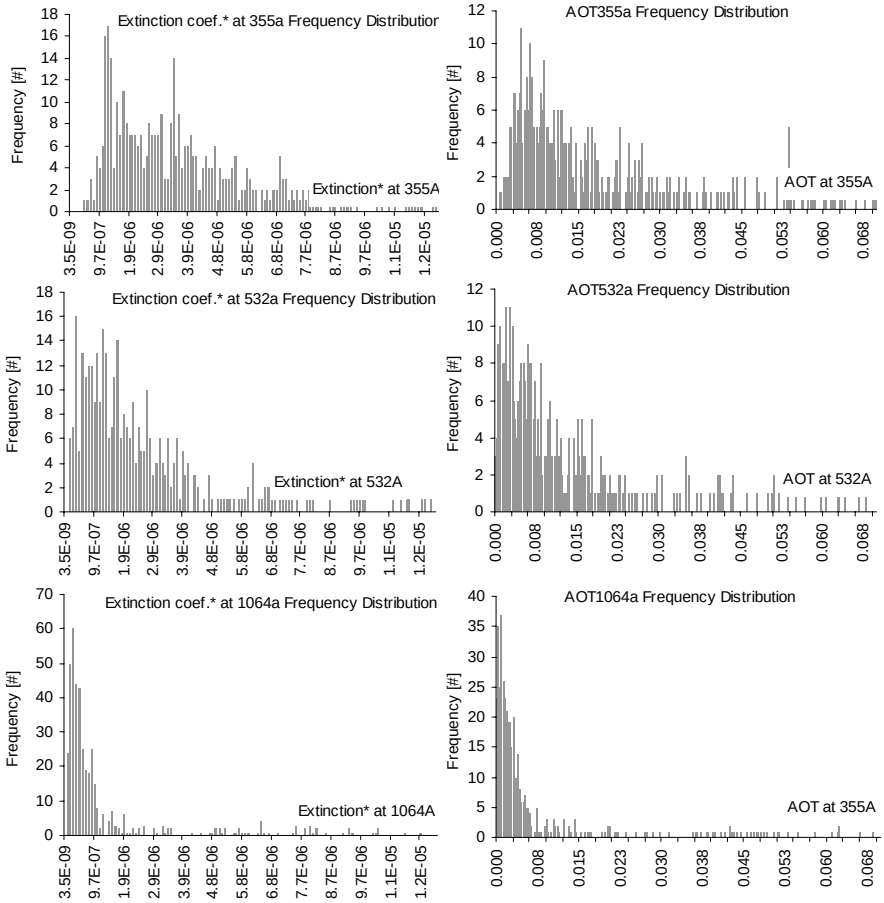

Figure 4 Frequency distribution of the AOD and the range averaged extinction coefficient for ~500 x 30 min data series / wavelength, taken from May 2000 to May 2002 for 355, 532 and 1064 nm. Only the results from the inversion corresponding to analog (A) acquisition mode were considered.

Statistics involving the above used aerosols lidar-based optical parameters are given in the in Table 1. One notices that the minimum valid altitude is around 500 m above the station and can reach up to 10 000 m. In order to avoid the bias due to the presence of clouds or possible artifacts in the data treatment one proposes to consider the median value more representative than the average one.

The AOD median of the upper troposphere aerosols is ~ 0.016 at 355 nm, ~ 0.011 for 532 nm and ~ 0.004 for 1064 nm.

Aerosol Parameter	AOD [total range]				Ext* [Ext. Avg over Range]				Ranges* [m]			
Statistics	avg	min	max	med	avg	min	max	med	avg	min	max	med
355A	0.083	0.001	1.724	0.018	1.E-05	5.E-07	4.E-04	4.E-06	4949	474	9000	4860
355Ph.C	0.093	0.001	1.978	0.028	1.E-06	5.E-08	4.E-05	4.E-07	5712	472	9540	5910
532A	0.081	0.0001	1.654	0.011	1.E-05	2.E-07	4.E-04	2.E-06	4906	472	8550	5160
532Ph.C	0.091	0.0004	4.810	0.016	1.E-05	1.E-07	1.E-03	2.E-06	6250	900	10620	6300
1064A	0.124	0.0001	10.86	0.004	2.E-05	3.E-08	2.E-03	8.E-07	5603	1350	9300	5850

Table 1 Statistics of the lidar extinction and AOD from May 2000 to May 2002.

Both total column and averaged extinction decrease with the wavelength. These results seem realistic when compared with the AOD values obtained from the co-located Precision Filter Radiometer (PFR, [23, 58]). The PFR measures the AOD corresponding to the total atmospheric column projected at zenith, at 368, 412, 450, 500, 610, 675, 778, 862 and 1024 nm. The AOD measured by PFR was recalculated at the lidar wavelengths (355, 532 and 1064 nm) using a wavelength dependency law, determined from the PFR data taken during the same period as the lidar measurements. This law, considered for median values, is:

$$AOD_{PFR} \sim 23.4\ \lambda^{-1.176} \qquad \text{Eq. (14)}$$

The Angstrom exponent of ~ 1.176 indicates the presence of an aerosol fraction characterised by relatively small size particles in the upper troposphere. The AOD time series are shown in Figure 5 for both instruments, at lidar wavelengths. They are in quite good agreement in terms of the median values.

The power law fitting of the AODs determined from both lidar and PFR instruments is shown in Figure 6. For this representation only median values have been considered. The AOD median from lidar measurements is constantly lower (e.g. negative offset) than the PFR correspondent AOD median values. This is understandable, as the PFR are measuring the total atmospheric column while the lidar is mostly integrating only up to the tropopause. Nevertheless, the wavelength dependence is quite similar and the power law exponents are comparable (1.36 for lidar and 1.18 for PFR). In Figure 6 the Angstrom ? law fit for the median values of the range averaged extinction coefficients is also plotted. The corresponding Angstrom coefficients are: A ~ 1.48 and B ~ 0.025, indicating small size particles with relatively high concentration.

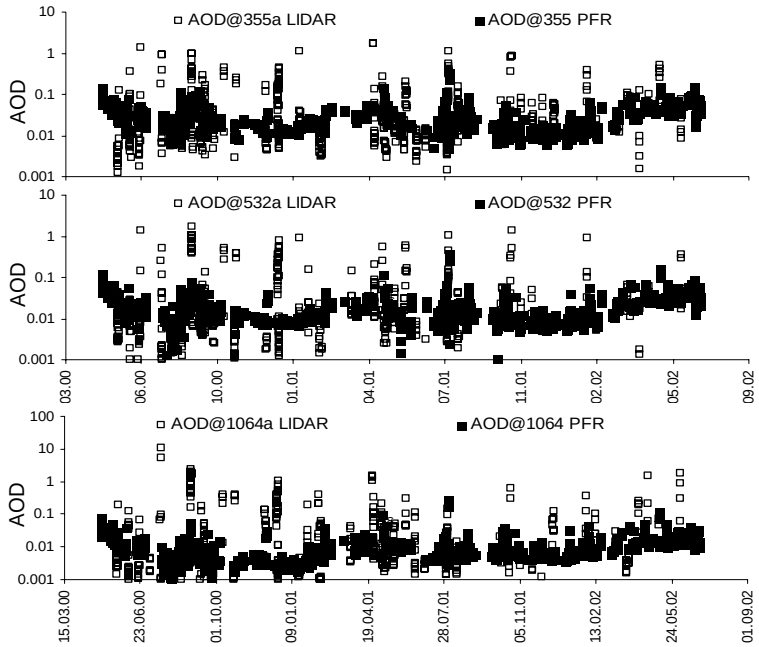

Figure 5 AOD time plot from LIDAR and PFR during the EARLINET project at lidar wavelengths.

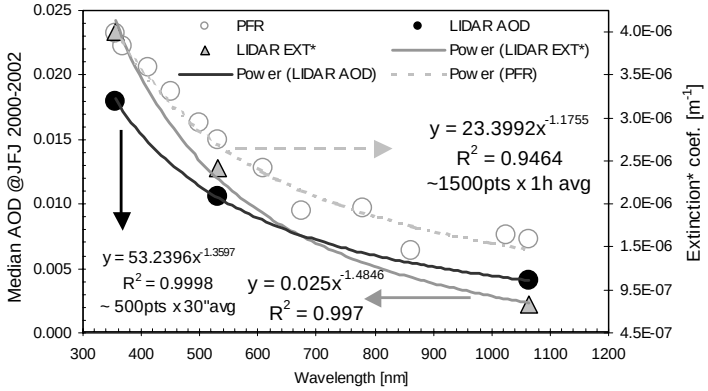

Figure 6 Power law fits of AOD (LIDAR and PFR) and of the range averaged extinction (LIDAR) considered for the median values from measurements taken from May 2000 to May 2002.*

Based on the backscatter and extinction coefficients median values at 355, 532 and 1064 nm, the microphysics correspondent to a representative UT aerosol load ?? were preliminary calculated using the regularization method described in chapter II (section 2.2.4). The results of the simulations are illustrated in Figure 7 for a maximum aerosol radius set at 2 μm.

The median effective radius was estimated at r_{eff} ~ 0.173 μm, the total number density n_t at 68 particles cm^{-3}, the total surface concentration s_t ~ 6.4 $\mu m^2 cm^{-3}$ and the total volume concentration v_t ~ 0.37 $\mu m^3 cm^{-3}$. The median complex refractive index m ~ 1.5474+ 0.0005i indicates very few absorption of the UT aerosols. The *single scattering albedo* ω_0 ~ 0.99 confirm the almost insignificant light absorption aerosol by the UT representative aerosols.

Regarding the size distribution (see Figure 7) one may notice in term of number density a maximum located around 0.05-0.1 μm, which reveals the presence of Aitken (nuclei condensation) mode. In term of surface concentrations one note a bi-modal asymmetric distribution with a first bigger peak at ~ 0.1-0.2 μm and a smaller one at 0.5-0.6 μm (i.e. accumulation mode).

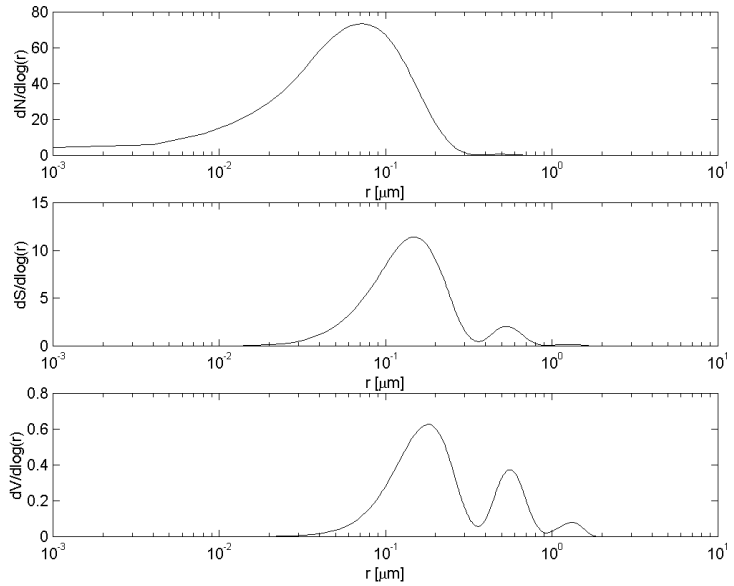

Figure 7 Number, surface and volume size distributions calculated -based on median values determined by elastic-lidar inversion algorithm over 500 x 30 min measurement series.

Finally the volume size distribution is revealing a tri-modal distribution for which, in addition to the two peaks observed in case of surface size distribution, a third small peak is noticed around ~1.5 μm, which can be assimilated to the presence of relatively larger size particles (e.g. coarse mode) in the UT regions.
For the above analysis, the median values could be considered statistically representative for both instruments; however, one should keep in mind that the results of this comparison depend on the use of *a priori* lidar ratio values for the elastic signal inversions.
Despite this uncertainty associated with the lidar ratio assumptions, the above analysis remains realistic and valuable for the following achievements:

- Lidar sensitivity to the UT aerosols mode;
- Realistic agreement between the lidar and PFR measurements;
- Estimation of upper troposphere aerosols' optical properties;
- Appropriate choice for the molecular atmospheric model;
- Lidar stability and potentiality for long-term monitoring;
- Use of the microphysics regularization algorithms based on lidar data.

In the next section the attention will move to the optical and microphysics properties of the cirrus clouds, which are one of the most significant atmospheric load at the UT altitudes in term of radiative budget but still poorly quantified.

3.3 Cirrus clouds

The lidar-based methodology is using a Mie –Raman combined approach for determining the cirrus backscatter-extinction coefficients and the lidar ratio. The depolarization measurements are also used to identify the particles' shape asymmetry. Then the lidar retrievals were used as solution for hybrid - regularization methods for the estimation of number-surface-volume size distributions, of the complex refractive index and of the *single scattering albedo* [30, 59]. The cirrus clouds study based on lidar in this work were separated as follows:
Lidar-based UT cirrus typology: The JFJ-LIDAR, has a unique ability to measure the upper troposphere cirrus clouds without being limited by low altitude phenomena such as PBL aerosols, occurrence of thick low stratus clouds or valley fog and haze.
Figure 8 represents the intensity graph of RCS at 532 nm (parallel polarization correspondent signal in relative units) for various observation periods selected to represent the most typical observed cirrus in the upper troposphere over a one-year period (May 2000 → May 2001). A lidar-based cirrus typology may be defined based on the simple analysis of RCS signals, which already give precise information concerning the geometric characteristics including depth, top-bottom-mid cloud heights, and horizontal extent (if a complementary information about UT wind is available).

One may classify the observed UT clouds formations (see lidar RCS in Figure 8) as follows:

- *low altitude* "clouds" (LAC) located in the first 500m above the station, are generally due to one or more of the following: air mass intrusions from the PBL in summer time, orographic air mass movements, flying snow crystals coming from surrounding mountains, or the glacier, or the foehn induced clouds and haze, fog, …
- *middle-troposphere* cirrus (MTC) between 4500-7500 m are a family of cirrus having various geometrical depths from thin contrails[7] (100 -750 m) to thick cirrus (~2000 m) which may caused by the PBL → Free Troposphere air mass exchanges, from long range transport, a vertical dynamics or aviation traffic.
- *tropopause cirrus clouds* (TCC) are often observed and easily identified as they have their top always trapped at the bottom of the tropopause. Their geometrical thickness may vary from very thin (~100 m, almost lenticular) to very thick (~ 4000 m) and they may have different consistencies from very dense and compact to expanded ones containing large air pockets.

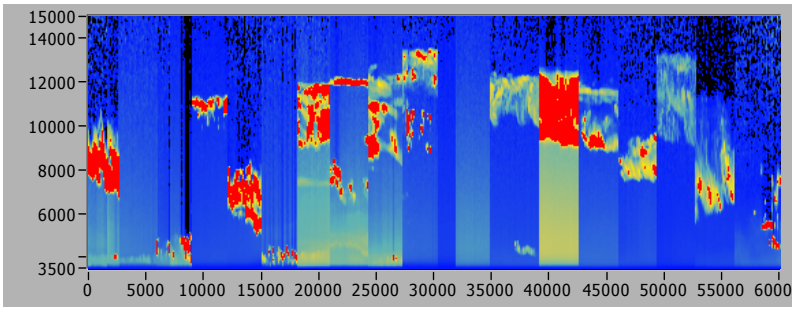

Figure 8 Range corrected signals (RCS) at 532 nm (parallel polarization) from 6000 selected files from May 2000 to May 2001 representing the typical observed cirrus[8]

Raman-Mie combined techniques for cirrus cloud studies: One of the main limitations of the elastic-lidar inversion technique is the use of *a priori* lidar ratio (LR) value. In order to overcome this assumption the Raman signals may be used for the estimation of the absolute value of the extinction profile. The extinction absolute values can be determined from JFJ-LIDAR measurements at 387 nm using the vibrational-rotational Raman, cf. Eq. (12), and at 532 nm using the pure rotational Raman, cf. Eq. (13). The extinction values at 355 as well as at

[7] Contrails is the common term used to design the specific cirrus clouds formed as a result of the injection into the atmosphere of aerosols-gases mixed by the aircrafts exhausts.
[8] A black and white camera was also design to work simultaneously with the lidar data acquisition and was set up to take sequences of zenith sky pictures (see examples in annex 16).

1064 nm may be obtained by extrapolation using the extinction wavelength dependency (e.g. $\alpha \sim \lambda^{-1.35}$, as statistically determined from lidar measurements for the upper troposphere typical aerosols). In the case of cirrus clouds, the assumption of the wavelength independency of the backscatter coefficient is commonly accepted. The extinction coefficients $\alpha_a(Z)$ determined from Raman signals and extrapolated, as explained above, at the corresponding elastic wavelengths, are then introduced in the elastic Fernald inversion algorithm.

Thus the backscatter coefficients $\beta_a(Z)$ may be retrieved without using a lidar ratio assumption. On the contrary, at the same time, this procedure allows the direct determination of the lidar ratio (LR). These lidar ratio values can be used when the Raman signals are not available for similar cloud or aerosol layers. In Figure 9, two examples of the application of the above-described procedure both at 355 nm (a) and 532 nm (b) are shown. In addition to the absolute calculation of these optical properties, the lidar ratio is obtained. The lidar ratio ranges from ~10 to 20 sr in the regions occupied by cirrus clouds.

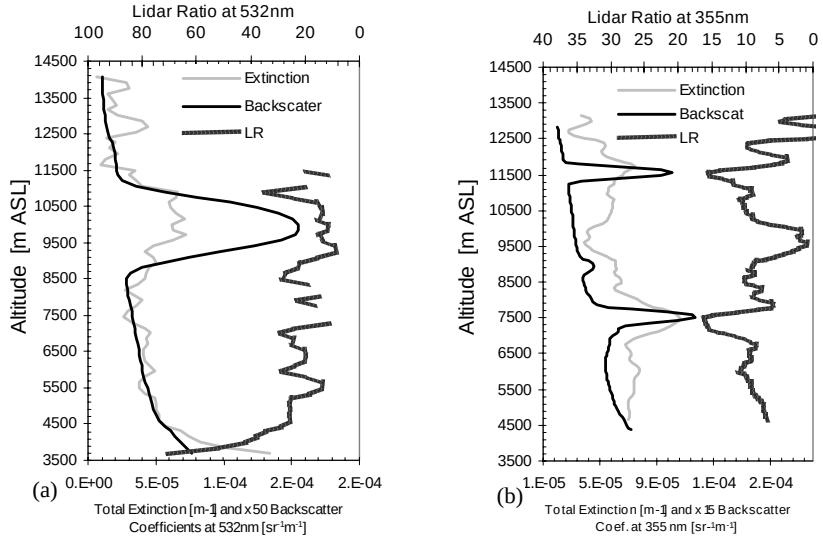

Figure 9 The Raman based backscatter and extinction coefficients retrieval on two different atmospheric situations: (a) at 532 nm in situation with many MTC and (b) at 355 nm in a situation with a thick TCC and a LAC due to PBL air masses intrusions at the station altitude.

Despite the advantage offered by the absolute calculation of the extinction, the Raman retrieval is subject to many error sources such as: (i) statistical error due to signal detection, (ii) systematic errors due to the estimation of the temperature and pressure profiles on which the calculation of the molecular backscatter reference is based, (iii) accuracy of the Angstrom's exponent, (iv) multiple-scattering effects and (v) high smoothing of the Raman raw signals. From a

consistent errors analysis expressed in [60] one may conclude that the Raman errors are a complex issue that can reach significant values. The errors due to the detection may reach up to 10% at the tropopause altitudes. The variation of Angstrom exponent (0.5 to 1) induces ~2 - % error. The temperature profile influence has to be particularly accounted for when strong gradients and inversions are noticed. It is possible for the error associated with multiple scattering effects in clouds to vary from less than 10 and up to 50 %. Finally the data averaging may contribute from 10 (at the base) to 30% (at the top) of thick cirrus clouds while 10% is reached at the top of thin cirrus.
Depolarization studies: The information obtained from the analysis of the depolarization measurements at 532 nm allows the determination of the diffusers' shape asymmetry, which may be related to their aggregation state. The cloud content particles may range from liquid water quasi-spherical droplets (no depolarization) to complex irregular ice crystals exhibiting 30-40% depolarization ratio.

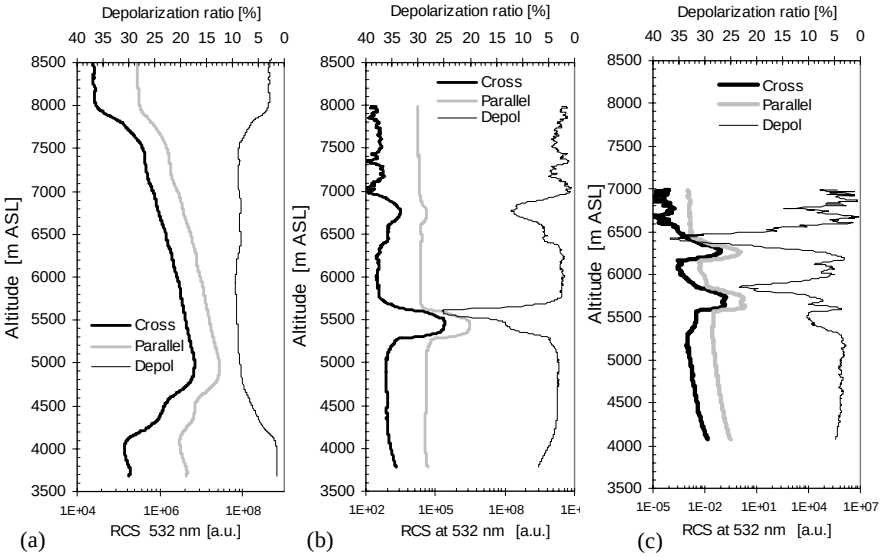

Figure 10 Depolarization at 532 nm case studies: (a) no depolarizing LAC < 4000 m and a huge mixed liquid water - ice crystals MTC (~10%); (b) no depolarizing LAC < 4250 m and two different relatively thin MTC (25% respectively ~12%) and (c) high depolarization ice crystal content MTC (~ 38%).

The depolarization ratio is obtained by taking the ratio of the two signals, 532c and 532p, corresponding respectively to the perpendicular and parallel polarization state radiations[9]. In order to take into account the differential

[9] See the front panel of the devoted to depolarization calculations LabView routine in annex A17

detection but also the depolarization due to the system itself, a calibration constant was calculated based on measurements taken in an almost pure molecular atmospheric situations [61, 62] when the depolarization is expected to be very low (i.e. 1-2 %). In Figure 10, three selected examples of depolarization by upper tropospheric clouds are presented. Figure 10 shows LACs < 4500m which are mostly liquid water content clouds that exhibit very low depolarization ratio (< 10%) as may be seen in all a, b, and c panels. Various mixed water-ice phases MTCs depolarize up to 10-20%. Ice content clouds (MTC or TCC) exhibit up to 35-40 % depolarization values (Figure 10). As a general observation, for the thin cirrus presented in Figure 10, the depolarization ratio increases from the bottom and reaches the maximum at the top of the cloud and a phenomenon that is likely due to multiple scattering.
Particular "cirrus" on the UT sky are the aviation-induced plumes, named contrails and the next section is proposing to characterize a typical fresh contrail based on lidar measurements.

3.4 Contrail: case study

The contrail (C) studied below was observed during its 10 minutes passage ~ above JFJ station on the morning (~10:00h LTC) of September 15, 2000. Figure 11 the RCS of the contrail (C) is plotted at 355, 532 and 1064 nm.

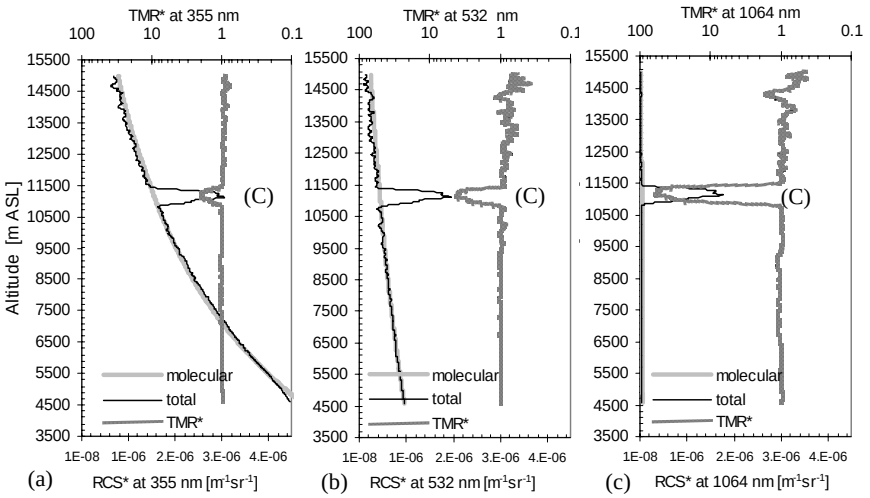

Figure 11 Contrail: total RCS, molecular and Total to Molecular Ratio (TMR*) at (a) 355, (b) 532 and (c) 1064 nm. Note: the total was molecularly scaled at 7500 m.*

The contrail geometrical depth is estimated at ~ 700 m. The absolute Mie- to-Molecular ratios are: 1.8 (at 355 nm), 3.8 (at 532 nm) and 54.8 (at 1064 nm), with values calculated at the maximum of the peak situated at the bottom of the tropopause at 11285 m ASL. This value increases from UV to NIR, being 14 times enhanced at 1064 nm compared at 355 nm. The depolarization (Figure 12) is relatively low, exhibiting ~ 7 % at the top of the contrail at 11540 m ASL.

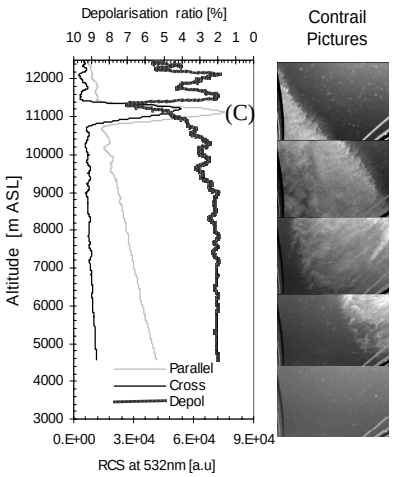

The low depolarization value may suggest that the initial micron-sized contrail particles are growing very slowly or not at all into the large ice crystals typical of cirrus. [63].

Figure 12 Parallel and cross (perpendicular) RCS at 532 nm, depolarization ratio (in %) together with simultaneous sky pictures taken each 3 minutes during the 10-min lidar detected passage.

Due to the interfering of the solar light on the Raman channels in daytime, the corresponding Raman signals were too noisy to be used in determining the contrail backscatter and extinction coefficients.

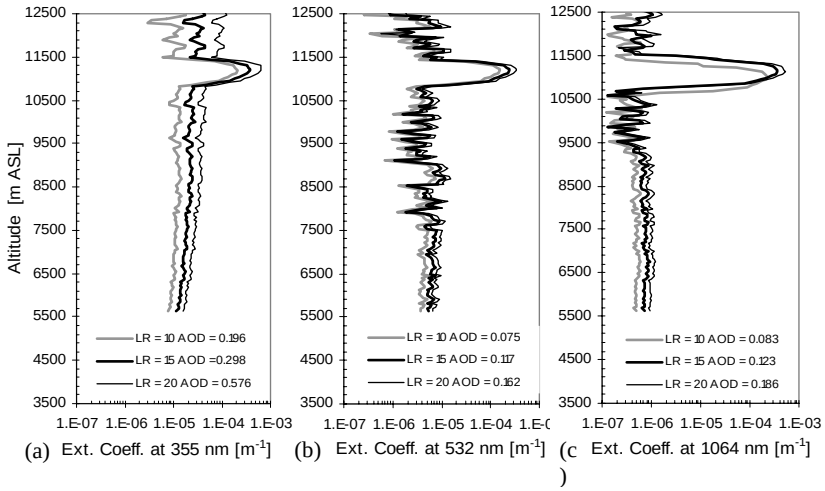

Figure 13 Contrail extinction coefficient obtained using Fernald inversion for three lidar ratio values: 10, 15 and 20 at (a) 355, (b) 532 and (c) 1064 nm.

The elastic (Mie) signals were inverted using the Fernald formula cf. Eq. (7) and Eq. (8) at 355, 532 and 1064 nm. For each wavelength case, three-lidar ratio values for cirrus clouds (i.e 10, 15 and 30 sr), were used. These three values were chosen symmetrically about an indicative value of ~15 sr – which is a typical value proposed in the literature [64]. For a more precise selection of the lidar ratio, a zero wavelength dependency of the contrail backscattering was considered (see Figure 14 a, b).

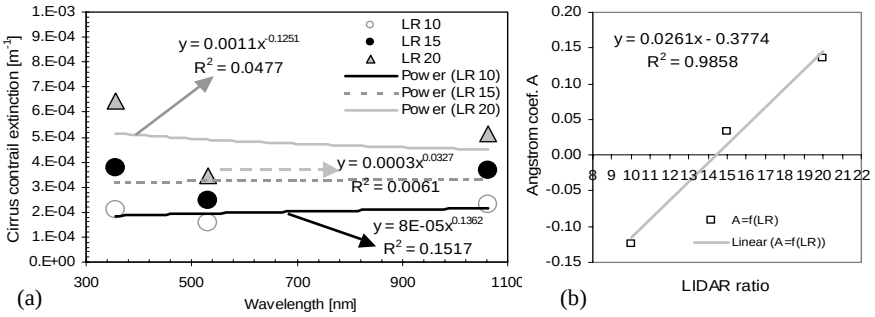

Figure 14 (a) The power-law fittings of the contrail peak extinction and (b) the interpolation of a more precise contrail lidar ratio

Power law fitting of the peak contrail extinctions, determined as shown in Figure 14 a, led to three different Angstrom exponents (A), for the three different lidar ratios. The corresponding lidar ratio to A→ 0 (i.e. no wavelength dependence) is ~14.5 and it was obtained as shown in Figure 14 (b). The subsequent $AOD_{contrail}$ value is ~ 0.12 for the UV-VIS-NIR regions and the maximum peak extinction reaches ~2.5 x 10^{-4}.

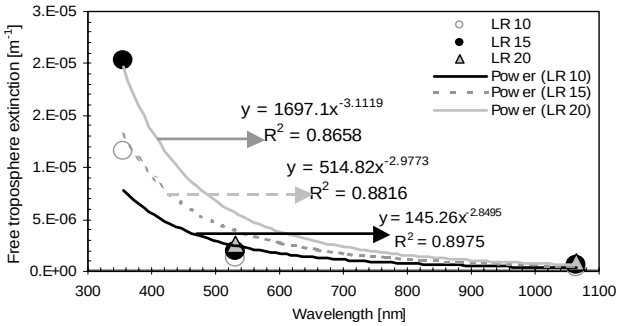

Figure15 The Ångström law fittings of the almost pure molecular extinction determined from elastic signals at lidar ratios i.e. 10, 15 and 20 sr. Note: the lidar ratio considered here are probably underestimated, a more realistic lidar ratio may be ~40-50 sr for the UT aerosols situations.

The extinction values at ~7500 m ASL, an altitude which may be considered as corresponding to a free troposphere zone, were also fitted with a power-law as shown Figure15. The wavelength dependency in this region is clearly evident. The Angstrom exponents obtained are relatively high (A ~ 3). This value indicates the presence of very small particles (e.g accumulation or Aitken modes) in the free atmosphere. The realistic wavelength dependency of the lidar extinction at 7500m ASL demonstrates the JFJ-LIDAR lidar sensitivity in recording backscattered light from such small particles

The lidar backscatter and extinction coefficients at the elastic wavelengths are also used as reference values (solutions) for retrieving some microphysical properties based on regularization inversion methods (see section 2.2.4). For this analysis simulations were run considering, in the first approximation, quasi-spherical particle shapes. These preliminary results estimate the microphysical properties of the contrail and those corresponding to the quasi-free upper troposphere at 7500 m ASL. An example of results obtained from such a simulation is shown in Figure 16, for both contrail and free troposphere. The radius (r) range, considered for iterations, was limited at 10 μm for the contrail case and at 1 μm for the free atmosphere case.

The results of these preliminary and approximate microphysics calculations are for the two considered cases as follows:

Contrail:
r_{eff} ~ 2.22 μm, n_t ~ 89 # cm^{-3}, s_t ~ 560 $\mu m^2 cm^{-3}$, v_t~ 415, $\mu m^3 cm^{-3}$,
m ~ 1.4597+ 0.0000i, ω_o ~ 1 (uv-vis-nir);

Quasi-free troposphere:
r_{eff} ~ 0.29 μm, n_t ~ 41 # cm^{-3}, s_t ~ 11 $\mu m^2 cm^{-3}$, v_t~ 1 $\mu m^3 cm^{-3}$,
m ~ 1.5439+ 0.0053i, ω_o ~ 0.960 (uv), 0.969 (vis); 0.968 (nir).

Comparatively analyzed, the two cases in term of microphysics calculation outputs are realistically represented demonstrating that the initial approximation of quasi-spherical particles made was acceptable.

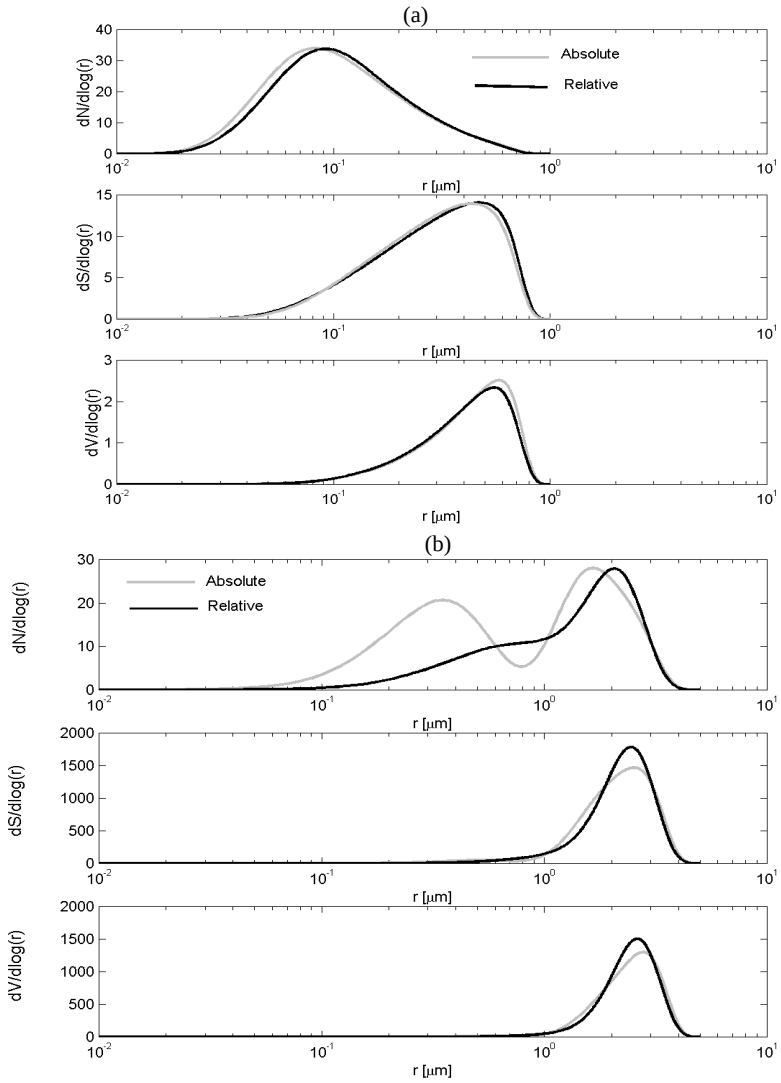

Figure 16 Number, surface and volume size distributions calculated for (a) upper troposphere at 7500 m ASL. and (b) peak contrail at 11250 m The two curves are related to the criteria used (absolute or relative minimal values between lidar retrievals and those simulated) for stopping the iteration processes.

Resuming our analysis, one may affirm that the analyzed cirrus cloud seems to be a fresh one containing a high amount (Figure 16 a) of relatively small ice crystals (~ 1-2 μm). The depolarization ratio was found relatively low (~7 %) probably indicating a combination of water and growing ice particles. The approximation of quasi-spherical particles may thus be acceptable. The cirrus calculations show also (e.g. see number concentration Figure 16 a) a fraction of small size particles. Despite the realistic values obtained, it is important to bear in mind that these results used an algorithm based on the assumption of spherical particles. In addition, the complex effect of the multiple scattering within the cloud (e.g negligible if FOV < 0.2 mrad) is not considered here. This pure cirrus with an $AOD_{contrail} \sim 0.12$ and a lidar ratio $LR_{contrail} \sim 14.5$ may be classified as optically thin exhibiting an average extinction coefficient, $\alpha_{contrail} \sim 2 \times 10^{-4}\ m^{-1}$.

4. Conclusion

This chapter reports the state of the art of the Jungfraujoch lidar capacity to determine the optical properties of upper troposphere in different situations (i.e. free troposphere, typical aerosols and cirrus/contrails). A statistical analysis of two years of measurements based on the inversion of elastic – lidar signals is presented. The comparisons between the lidar determined AOD and the co-located measurements from a PFR instrument show a good and realistic agreement. The microphysics calculation based on the extinction and backscatter median values at 355, 532 and 1064 nm over a statistically representative set of 500x 30min data series reveals a tri-modal realistic size distribution as well as realistic values for the complex refractive index and single scattering albedo coefficient of the UT aerosols. The use of the elastic (Mie) and inelastic (Raman) techniques for retrieving the upper troposphere optical properties were separately described and a methodology to combine them for absolute determination of the extinction and backscatter coefficients was proposed. A lidar-based characterization of the cirrus clouds is presented together with examples of the application of Mie-Raman combined techniques for determination of the cirrus optical properties. Examples of depolarization by various types of cirrus are shown. The analysis proposed for studying a typical upper troposphere contrail allowed determining its optical and microphysical properties.

The efforts to monitor the clouds and contrails at the Jungfraujoch station [65-67] may be continued in the future based on a statistical analysis of the upper troposphere mid-latitude cirrus cloud. Such statistics on cirrus were already reported [68] based only on a reduced set of existent observations (70 data series). The use of the JFJ-LIDAR cirrus database that contains systematic measurements since 2000 (see all available data series 2000 → 2003 in annex A13) could be statistically more relevant.

The results of such a statistical analysis may be valuable for global models and climatologic studies.

References

1. IPCC, *Climate change 1994*. 1995, Cambridge: Press Syndicate of the University of Cambridge.
2. Ramanathan, V., P.J. Crutzen, J.T. Kiehl, and D. Rosenfeld, *Aerosols, Climate, and the Hydrological Cycle.* Science, 2001. **294**: p. 2119-2124.
3. Twomey, S., *The influence of pollution on the short-wave albedo of clouds.* Journal of the Atmospheric Sciences, 1977. **34**: p. 1149-1152.
4. Ramanathan, V., Crutzen, P.J., Kiehl, J.T., Rosenfeld, D., *Aerosols, Climate, and the Hydrological Cycle.* Science, 2001. **294**: p. 2119-2124.
5. Schumann, U., *Contrail cirrus*. Cirrus, ed. D.K.L.e. al. 2000: Oxford Univ. Press.
6. Day, S.e., *Dictionnaire Encyclopédique de l'Ecologie et des Sciences de l'Environnement*, ed. F. Ramade. 1993: Ediscience international. 421.
7. Houghton, J.T., Y. Ding, D.J. Griggs, M. Noguer, P.J. van der Linden, and D. Xiaosu, *Climate Change 2001: The Scientific Basis: Contribution of Working Group I to the Third Assessment Report of the Intergovernmental Panel on Climate Change (IPCC)*. 2001, Cambridge University Press, UK. p. 944.
8. Penner, J.E., J.E. Lister, D.J. Griggs, D.J. Dokken, and M. McFarland, eds. *Aviation and the Global Atmosphere: Intergovernmental Panel on Climate Change (IPCC)*. 1999, Cambridge University Press. 373.
9. Ramaswamy, V. and V. Ramanathan, *Solar absorption by cirrus clouds and the maintenance of the tropical upper troposphere thermal structure.* Journal of the Atmospheric Sciences, 1989. **46**(14): p. 2293-2310.
10. Gierens, K.M., U. Schumann, M. Helten, H. Smit, and A. Marenco, *A distribution law for relative humidity in the upper troposphere and lower stratosphere derved from three yers MOZAIC experiment.* Ann. Geophys., 1999. **17**(1218-1226).
11. DeMott, P.J., D.J. Cziczo, A.J. Prenni, D.M. Murphy, S.M. Kreidenweis, D.S. Thomson Borys, and D.C. Rogers, *Measurements of the concentration and composition of nuclei for cirrus formation.* PNAS-Geophysics, 2003. **100**(25): p. 14655-14660.
12. Alcala-Jornod, C., H.v.d. Bergh, and M.J. Rossi, *Can Soot Particles Emitted by Airplane Exhaust contribute to the Formation of Aviation Contrails and Cirrus Clouds?* Geophysical Research Letters, 2002,. **29**: p. 1820.
13. Kärcher, B., Busen, R. , A. Petzold, F.P. Schröder, U. Schumann, and E.J. Jensen, *Physicochemistry of aircraft-generated liquid aerosols, soot, and ice particles. Comparison with observations and sensitivity studies.* Journal of Geophysical Research-Atmospheres, 1998. **103**: p. 17129–17148.
14. Minnis, P., U. Schumann, D.R. Doelling, K.M. Gierens, and D.W. Fahey, *Global distribution of contrail radiative forcing.* Geophysical Research Letters, 1999. **26**(13): p. 1853-1856.
15. Travis, D., M. Carleton, and R. Lauritsen, *Contrails reduce daily temperature range.* Nature, 2002. **418**: p. 601.
16. IPCC, *Climate Change 2001: The Scientific Basis*. 2001: Cambridge University Press.
17. Finlayson-Pitts, B.J. and J.N.J. Pitts, *Atmospheric Chemistry : Fundamentals and Experimental Techniques*. 1986: Wiley Interscience. 1098.
18. Charlson, R.J., and Heintzenberg, J. (Eds.), *Aerosol forcing of climate*. Dahlem Workshop Reports, ed. R.J. Charlson, and Heintzenberg, J. Vol. Environmental Sciences Research Report 17. 1995, New-York: John Wiley & Sons, Ltd.
19. Angström, A., *On the atmospheric transmission of sun radiation and on dust in the atmosphere*. Geogr. Ann., 1929. **11**: p. 156-166.

20. Doherty, S.J., T.L. Anderson, and R.J. Charlson, *Measurement of the lidar ratio for atmospheric aerosols with a 180 degrees backscatter nephelometer*. Applied Optics, 1999. **38**(9): p. 1823-1832.
21. Lavanchy, V.M.H., H.W. Gaggeler, S. Nyeki, and U. Baltensperger, *Elemental carbon (EC) and black carbon (BC) measurements with a thermal method and an aethalometer at the high-alpine research station Jungfraujoch*. Atmospheric Environment, 1999. **33**(17): p. 2759-2769.
22. Gaggeler, H.W., U. Baltensperger, D.T. Jost, M. Emmenegger, and W. Nageli, *Applications of the Epiphaniometer to Environmental Aerosol Studies*. Journal of Aerosol Science, 1989. **20**(8): p. 1225-1228.
23. Ingold, T., C. Matzler, N. Kampfer, and A. Heimo, *Aerosol optical depth measurements by means of a Sun photometer network in Switzerland*. Journal of Geophysical Research-Atmospheres, 2001. **106**(D21): p. 27537-27554.
24. Wang, Z. and K. Sassen, *Cirrus cloud microphysical property retrieval using lidar and radar measurements. Part II: Midlatitude cirrus microphysical and radiative properties*. Journal of the Atmospheric Sciences, 2002. **59**(14): p. 2291-2302.
25. Donovan, D.P. and A.C.A.P. van Lammeren, *Cloud effective particle size and water content profile retrievals using combined lidar and radar observations - 1. Theory and examples*. Journal of Geophysical Research-Atmospheres, 2001. **106**(D21): p. 27425-27448.
26. Ansmann, A., F. Wagner, D. Muller, D. Althausen, A. Herber, W. von Hoyningen-Huene, and U. Wandinger, *European pollution outbreaks during ACE 2: Optical particle properties inferred from multiwavelength lidar and star-Sun photometry*. Journal of Geophysical Research-Atmospheres, 2002. **107**(D15): p. art. no.-4259.
27. Holben, B.N., T.F. Eck, I. Slutsker, D. Tanre, J.P. Buis, A. Setzer, E. Vermote, J.A. Reagan, Y.J. Kaufman, T. Nakajima, F. Lavenu, I. Jankowiak, and A. Smirnov, *AERONET - A federated instrument network and data archive for aerosol characterization*. Remote Sensing of Environment, 1998. **66**(1): p. 1-16.
28. Bösenberg, J., and al., *EARLINET: A European Aerosol Research Lidar Network*. Advances in Laser Remote Sensing, ed. J. Pelon, Loth, C., Dabas, A. 2001, Palaiseau: Editions de l'Ecole polytechnique.
29. NASA., G.S.F.C., *http://eospso.gsfc.nasa.gov/ftp_docs/measurements.pdf*. 2004, EOS: Earth Oberving System.
30. Bockmann, C., *Hybrid regularization method for the ill-posed inversion of multiwavelength lidar data in the retrieval of aerosol size distributions*. Applied Optics, 2001. **40**(9): p. 1329-1342.
31. Larcheveque, G., I. Balin, R. Nessler, P. Quaglia, V. Simeonov, H. van den Bergh, and B. Calpini, *Development of a multiwavelength aerosol and water-vapor lidar at the Jungfraujoch Alpine Station (3580 m above sea level) in Switzerland*. Applied Optics, 2002. **41**(15): p. 2781-2790.
32. Larcheveque, G., *Development of the Junfraujoch multi-wavelenght lidar system for continous observations of the aerosols optical properties in the free troposphere*, in *Environmental and Engineering Dpt.* 2002, EPFL: Lausanne.
33. Bosenberg, J. and V. Matthias, *EARLINET:A European Aerosol Research Lidar Network to Establish an Aerosol Climatology (final repport)*. 2003.
34. Bates, D.R., *Rayleigh scattering by air*. Planetary Space Science, 1984. **32**: p. 785-790.
35. Bodhaine, B.A., *On Rayleigh Optical Depth Calculations*. American Meteorological Society, 1999. **16**: p. 1854-1861.
36. Young, A.T., *On the Rayleigh-scattering optical depth of the atmosphere*. Journal of Applied Meteorology, 1981. **20**: p. 328-330.

37. Seinfeld, J.H. and S.N. Pandis, *Atmospheric Chemistry and Physics*, ed. J.W.S. ed. 1998: Wiley Interscience. 1326.
38. Hinkley, E.D., *Laser Monitoring of the Atmosphere*. Topics in Applied Physics, ed. E.D. Hinkley. Vol. 14. 1976: Springer-Verlag.
39. Bucholtz, A., *Rayleigh-scattering calculations for the terrestrial atmosphere.* Applied Optics, 1995. **34**: p. 2765-2773.
40. Placzek, G., *Rayleigh -streuung und Raman-effekt*, in *Handbuch der radiologie*, G. Marx, Editor. 1934. p. 205.
41. Collis, R.T.H. and P.B. Russell, *Lidar Measurement of Particles and Gases by Elastic Backscattering and Differential Absorption*. Laser Monitoring of the Atmosphere, ed. E.D. Hinkley. 1976: Springer Verlag.
42. NOAA, NASA, and USAF, *U.S. standard atmosphere (76)*. 1976, U.S. government Printing Office: Washington / USA.
43. Klett, J.D., *Stable analytical inversion solution for processing lidar returns.* Applied Optics, 1981. **20**: p. 211-220.
44. Fernald, F.G., *Analysis of atmospheric lidar observations: some comments.* Applied Optics, 1984. **23**: p. 652-653.
45. Sasano, Y., Browell, E., V., and Ismail S., *Error caused by using a constant extinction/backscattering ratio in the lidar solution.* Applied Optics, 1985. **24**(22): p. 3929-3932.
46. Klett, J.D., *Lidar inversion with variable backscatter/extinction ratios.* Applied Optics, 1985. **24**(11): p. 1638-1643.
47. Böckmann, C., and al., *Algorithm intercomparison of the backscatter lidar*. in EARLINET: Quality Assurance Report. internal note, 2001: p. 8-18.
48. Matthias, V., Böckmann, C., Freudenthaler, V., Pappalardo, G., and Bösenberg, J., *EARLINET: Quality Assurance Report*, in *internal note*. 2001.
49. Bockmann, C., U. Wandinger, A. Ansmann, J. Bosenberg, V. Amiridis, A. Boselli, A. Delaval, F. Tomasi de, A. Hagard, I.V. Grigorov, M. Frioud, H. Horvath, M. Iarlori, L. Komguem, S. Kreipl, G. Larcheveque, V. Matthias, A. Papayannis, G. Papalardo, V. Matthias, F. Rocadenbosch, J.A. Rodrigues, J. Schneider, V. Shcherbakov, and M. Wiegner, *Aerosol lidar intercomparison in the framework of EARLINET: Part II - Aerosol backscatter algorithms.* Applied Optics, 2004. **43**(4): p. 977-989.
50. Measures, R.M., *Laser Remote Sensing. Fundamentals and Applications*, ed. J.W.a. Sons. 1992, New-York: Krieger. 510.
51. Leonard, D.A., *Observation of Raman Scattering from the Atmosphere using a Pulsed Nitrogen Ultraviolet Laser.* Nature, 1967. **216**: p. 142-143.
52. Cooney, J., *Measurements of the Raman component of Laser Atmospheric backscatter*. Applied Physics Letters, 1968. **12**(2): p. 40-42.
53. Inaba, H. and T. Kobayashi, *Laser-Raman Radar for Chemical Analysis of Polluted Air*. Nature, 1969. **224**: p. 170-172.
54. Russell, P.B., Swissler, T. J., and McCormick, M. P., *Methodoloy for error analysis and simulation of lidar aerosol measurements.* Applied Optics, 1979. **18**(22): p. 3783-3797.
55. Ansmann, A., M. Riebesell, and C. Weitkamp, *Measurement of Atmospheric Aerosol Extinction Profiles with a Raman Lidar.* Optics Letters, 1990. **15**(13): p. 746-748.
56. Ansmann, A., M. Riebesell, U. Wandinger, C. Weitkamp, E. Voss, W. Lahmann, and W. Michaelis, *Combined Raman Elastic-Backscatter Lidar for Vertical Profiling of Moisture, Aerosol Extinction, Backscatter, and Lidar Ratio.* Applied Physics B-Photophysics and Laser Chemistry, 1992. **55**(1): p. 18-28.

57. Ansmann, A., Y. Arshinov, S. Bobrovnikov, I. Mattis, I. Serikov, and U. Wandinger. *Double-grating monochromator for a pure rotational Raman lidar*. in *Fifth International Symposium on Atmospheric and Ocean Optics*. 1998: Proc. SPIE.
58. Schmid, B., Spyak, P. R. , S.F. Biggar, C. Wehrli, J. Sekler, T. Ingold, C. Matzler, and N. Kampfer, *Evaluation of the applicability of solar and lamp radiometric calibrations of a precison Sun photometer operating between 300 and 1025 nm.* Applied Optics, 1998. **37**(3923-3941).
59. Mironova, I., C. Bockmann, and R. Nessler. *Microphysical Parameters from 3-Wavelength Raman Lidar*. in *ILRC*. 2002. Quebec: R&D Defence Library Services.
60. Pappalardo, G., and al., *Algorithm intercomparison of the Raman lidar*. in EARLINET: Quality Assurance Report. internal note, 2001: p. 18-25.
61. Sassen, K., *The depolarization lidar technique for cloud research: a review and current assessment.* Bulletin of the American Meteorological Society, 1991. **72**(12): p. 1848-1866.
62. Biele, J., G. Beyerle, and G. Baumgarten, *Polarization lidar: Corrections of instrumental effects.* Optics Express, 2000. **7**(12): p. 427-435.
63. Del Guasta, M. and K. Niranjan, *Observation of low-depolarization contrails at Florence (Italy) using a 532-1064 nm polarization LIDAR.* Geophysical Research Letters, 2001. **28**(21): p. 4067-4070.
64. Deepak, A., and Gerber, H. E. (Eds), *Report on the experts meeting on aerosols and their climatic effects*. 1983, WMO: Williamsburg, VA.
65. Balin, I., G. Larchvêque, R. Nessler, P. Quaglia, V. Simeonov, H. van den Bergh, and B. Calpini. *Monitoring of water vapor, aerosols and clouds/contrails in the free troposphere by lidar from Jungfraujoch station (3580 m ASL).* in *21st International Laser Radar Conference*. 2002. Quebec Canada.
66. Balin, I., G. Larchevêque, R. Nessler, H. van den Bergh, and B. Calpini. *Aerosols and water vapor by lidar from the Jungfraujoch research station*. in *NDSC meeting (Network for Detecting of Stratospheric Changes)*. 2001. Arcachon - France.
67. Larchevêque, G., Balin I., Quaglia P., Nessler R., Simeonov V., H. van den Bergh and Calpini B. *Optical properties of aerosols-clouds-contrails and water vapor mixing ratio by lidar from Jungfraujoch Research Station (3580 m ASL)*. in *EGS (European Geophysical Assembly)*. 2002. Nice-France.
68. Reichardt, J., *Optical and geometrical properties of northern midlatitude cirrus clouds observed with a UV Raman lidar*. Physics and Chemistry of the Earth Part B-Hydrology Oceans and Atmosphere, 1999. **24**(3): p. 255-260.

Chapter IV

Water vapor retrieval based on the Raman lidar technique

Atmospheric water vapor is the most important greenhouse gas and is the agent of the hydrological cycle. Atmospheric water vapor is highly variable, and its quantification is still complex and is inducing huge uncertainties into the global climate models calculation and weather predictions. New measurement techniques are currently being developed with the goal of reducing the lack of global distributed measurement networks.
This chapter addresses the implementation of the water vapor Raman lidar technique at the Jungfraujoch observatory. The ratio of the rotational-vibrational Raman wavelength shifted radiation -- water vapor at 407 nm and nitrogen at 387 nm-- excited at 355 nm, radiation emitted by a Nd:YAG laser, is proportional to the water vapor mixing ratio. The Raman lidar setup and the procedure for the retrieval of the water vapor mixing ratio, including a discussion of the corrections and errors, are presented in detail. Using the *in situ* value, one point external calibration, specific humidity was estimated in the upper troposphere above the Swiss Alps. Typical nighttime water vapor mixing ratio vertical profiles obtained up to 8-10 Km ASL with 1-2h integration and 75-150 m vertical resolution are shown. The integrated water vapor Raman profiles from regular measurements performed in 2000-2003 are compared with similar measurements obtained from a Sun photometer and a co-located GPS receiver. The closest regional radiosoundings are also considered for comparison.

1. Introduction

1.1 Water vapor significance for Earth's climate

Due to its unique physical and chemical properties, water is crucial for the Earth system both on the local-short time scale (weather) and in long-term (global climate) related processes. Water is a universal solvent and is the main transport vector of matter and energy from the microscale of molecules and individual cells to the planetary scale. In the range of the pressure and temperature values encountered on the Earth's surface and in its atmosphere, a water molecule can change phase easily between solid, liquid and gas, releasing or absorbing heat in the process (latent heat). Water vapor is the primary heat exchanger on the planet Earth. Because of its high latent heat value, and large thermal inertia, water also acts as a climatic thermostat [1]. Water circulation at the global scale (the hydrological cycle [2]) is solar powered and is connected with the rotation of the Earth. The global redistribution of precipitation occurs via atmospheric water vapor transport, synoptic-scale wind formations (jet stream), the southern oscillation (El Niño and La Niña) phenomena, and many others. Water participates in all its three phase states in a multitude of chemical reactions in the atmosphere. Water vapor is involved in the formation of the ice content polar stratospheric clouds (reservoirs of halogenated molecules involved in the spring polar ozone depletion). Acid rain (H_2CO_3, HNO_3, H_2SO_4, etc) is formed by reactions of CO_2, NO_2 or SO_2 in their aqueous phase. Water vapor is also the main source of the OH radical, an important atmospheric oxidant that is obtained from a homogeneous gas phase reaction of the water vapor molecule with the single-D excited state oxygen O^{1D} resulting from ozone photo-dissociation. Compared to other atmospheric trace greenhouse gases such as carbon dioxide (CO_2), methane (CH_4), nitrous oxide (N_2O), or chlorofluorocarbons (CFCs), water vapor is the most efficient greenhouse gas because of its global concentration and its spectral properties (i.e transparent to incoming short-wave radiation from the Sun and opaque to long-wave radiation leaving the Earth). Indeed the electronic absorption spectrum of water vapor is located in the far UV (< 186 nm) while its vibrational-rotational spectrum contains three main bands centered at $\nu_1 \sim 3657$ cm^{-1} (λ_1~2.73 μm), $\nu_2 \sim 1595$ (λ_2~6.3 μm), and $\nu_3 \sim 3756$ cm^{-1} (λ_1~2.66 μm), with overtones, combinations and hot bands in the infrared and visible parts of the spectrum. The most intensive and broad H_2O vibration-rotation band is ν_2 centered at 6.3 μm that completely absorbs solar radiation between 5.5 and 7.5 μm. The overlap of the ν_1, ν_3 and the overtone of ν_2 (3.14 μm) also absorb completely the radiation from 2.6 to 3.3 μm. Other vibration-rotation bands are centred close to 1.87,

1.38, 1.10, 0.94, 0.81 and 0.72 μm and even some weaker bands are present in the visible part of the spectrum. The large dipole moment of H_2O and its isotopes are responsible for an intensive rotational spectrum that occupies a very broad region, extending from 8μm to wavelengths of several cm [3]. The contribution of water vapor to the total greenhouse effect is estimated from 50-60% [4] up to ~95% [5] and is still a controversial subject. The positive feedback between atmospheric temperature and water vapor is of crucial importance. To a first approximation, a 1°C increase in atmospheric temperature will cause a 6% increase in water vapor concentration, leading to further warming and thus initiating a positive feedback [6]. This direct effect combined with the indirect effect (through cloud formation) of the water vapor on the Earth budget radiation is still poorly quantified [7] and scientific consensus is only qualitative at this point. The uncertainties stem from a lack of information on the high space-time variability of water vapor, which is difficult to measure due to the complex natural processes involved. Water vapor averages about one per cent by volume in the atmosphere and its distribution in time and space is highly variable: it comprises about 4 percent of the atmosphere by volume near the surface, but only 3-6 ppmv (parts per million by volume) above 10 to 12 km. Nearly 50% of the total atmospheric water is trapped in the planetary boundary layer (PBL, from 0 to 1-3 km) while less than 6 % of the water is above 5 km, and only 1 % above 12 km. The annual average precipitation over the globe is about 1 meter, while the water-vapor column density (precipitable water) averages about 5 cm in the tropical regions and less than 1 mm at the poles. The average lifetime of the water vapor molecule in the atmosphere is about 9 days [4]. At any given location in the atmosphere, the water vapor content can vary markedly in a relatively short time span, owing to the passage of cold or warm fronts, precipitation, etc. Because of the critical role that water vapor plays in most atmospheric processes, accurate water vapor profiles are needed in atmospheric modeling applications. Water vapor profiles are also needed for basic meteorology applications (i.e. the identification and study of frontal boundaries, dry lines,...), boundary layer studies (such as cloud formation/dissipation), development of climatological records, and for radiative transfer calculations.

1.2 Water vapor measurements

However, measurements of water vapor through the troposphere have proven to be difficult to obtain with good accuracy. A wide variety of observational technologies have been developed to address this. Inexpensive *in situ* sensors (ground, towers) provide reasonably accurate water vapor measurements, but do not provide information on the water vapor content of the atmosphere at higher altitudes. *In situ* sensors have also been installed on commercial and research aircraft to measure water vapor. Measurements from commercial aircraft are a

promising but yet unproven technique[8]; however, data would only be available when and where scheduled flights occur – a significant limitation. Research aircraft can provide high-quality measurements at any location but the cost is high for dedicated aircraft flights. Another well established approach that provides a detailed vertical profile is radiosounding. In this technique, sondes are carried in the atmosphere by meteorological balloons and equipped with appropriate humidity sensors. However, the temporal and global coverage resolution is typically fairly coarse (launches every 12 h at specific meteorological stations). Moreover, radiosondes are expensive because their implementation is labor-intensive. Satellites can provide excellent global coverage of water vapor distribution, but the horizontal and vertical resolution is very coarse. Water vapor measurement sensors have evolved from goldbeater skin, hairs, lithium chloride, carbon hygristor, and thin film capacitors to the more recent frost point hygrometers (chilled mirror). Different types of Lyman - α hygrometers have been developed based on the photo dissociation of H_2O at λ < 137 nm and the detection of the fluorescence (λ~305-325 nm) of the excited OH radical. Open path measurements have also been made with tunable diode laser spectroscopy (TDLS) technique, which is based on the laser absorption in the near and mid infrared water vapor rotation-vibration spectrum. Microwave instruments using the H_2O emission lines at 22.2 GHz or even 183 GHz are used mainly for the estimation of the stratosphere – mesosphere humidity. The inversion techniques for retrieving vertical profiles are still in development, and the results have very poor vertical resolution. The FTIR spectrophotometers and the precision filter radiometers (PFR) are used to estimate the integrated total column water vapor based on various IR absorption bands and on VIS (719, 817 and 946 nm) atmospheric absorption. Based on the delays induced by the atmospheric water vapor on the paths between the antennas of the receiver and the satellites of the GPS network, the total column may be estimated. More specific details of the technical specifications, advantages and limitations of all these techniques operating in upper troposphere - lower stratosphere regions (UTLS) are reviewed in [9].

The continuous profiling of the water vapor dynamics with high spatial and temporal resolution is possible with the use of the lidar techniques -- both differential absorption (DIAL, [10]) or rotational-vibrational Raman techniques [11, 12].

1.3 Upper troposphere water vapor specificity

Despite the small amount of water vapor in the free troposphere (above 2-3 km), recent studies [13-15] have shown that the middle and upper troposphere (600 - 200 hPa) water vapor content contributes as ~27-35% of the absolute greenhouse forcing due to the strong absorption in 100-600 cm^{-1} spectral region which is within the spectral band of Earth surface infrared re-emission. Another

study [16] shows that the contribution of water vapor in layers of equal mass to the climate sensitivity varies by about a factor of two with the height. The largest contribution comes from layers between 450 and 750 hPa, and the smallest, from layers above 230 hPa. The water vapor positive feedback is of crucial importance but poorly understood. The positive feedback of water vapor on the global mean surface temperature is also altitude sensitive. For example, the response of water vapor to the doubling of CO_2 concentrations is 2.6 times greater above 750 hPa than below 750 hPa in terms of its effects on the Earth surface temperature. High resolution and more accurate upper troposphere and low stratosphere water vapor measurements are also needed for investigations into tropopause phenomena, vertical troposphere-stratosphere exchanges, nucleation processes, cirrus/contrail cloud formation, and lower stratosphere water vapor increasing concentrations (e.g. already observed increasing partially related to the CH_4 oxidation). In addition, these data are necessary for initializing the Numerical Weather Prediction (NWP) and Global Climate and Circulation models.
In this context, this chapter presents the implementation of the Raman lidar technique at the Jungfraujoch observatory (3600 m ASL, 46.55 °N, 7.98 °E) for profiling the upper troposphere water vapor above the Swiss Alps. In section 2, after a brief comparative presentation of the DIAL and Raman techniques, the principle of the water vapor retrieval by Raman lidar is detailed and the Raman lidar layout is described. Section 3 addresses the water vapor retrieval algorithm, and describes the first water vapor profile obtained above the Alps using Raman lidar technique. Errors and corrections, as well as *in situ* calibration, and typical upper troposphere profiles are presented. Finally different comparisons with co-located PFR and GPS techniques and with the closest space-time radiosounding (i.e. Payerne) are discussed. The conclusions and recommendations for the perspectives are given in section 4.

2. Method

2.1 DIAL and RAMAN lidar techniques

As already mentioned, high spatial-resolution monitoring of atmospheric water vapor is possible using the DIAL or the Raman lidar techniques.

The DIAL technique, first demonstrated in 1966 [10], exploits the differential absorption of water wapor in the VIS and NIR using two lidar emitted wavelengths: one on the peak of the absorption (λ_{ON}) and other in the wing of the absorption line (λ_{OFF}). The average absolute water vapor molecular number density $n_{H2O}(z)$ between z and $z + \Delta z$ is retrieved as given in Eq. (1):

$$n_{H_2O}(Z) = \frac{1}{2\Delta\sigma\,\Delta z} \ln \frac{S_{on}(Z) S_{off}(Z+\Delta z)}{S_{on}(Z+\Delta z) S_{off}(Z)} \pm \delta N_{H_2O}(Z) \qquad \text{Eq. (1)}$$

where *S* are the lidar backscatter signals and $\Delta\sigma = \sigma_{on} - \sigma_{off}$ is the differential absorption cross-section. The DIAL technique is self-calibrated, providing absolute water vapor concentration in both daytime and nighttime. In addition, the OFF signal can be simultaneously considered for aerosol investigations. In spite of these advantages the water vapor DIAL technique requires specific laser sources emitting at various and precise $\lambda_{ON,}$ (tunable lasers), having relatively narrow (~ 10^{-4} nm) bandwidths, and precise, stable and well-known line shapes. In addition, the knowledge and accuracy of the absorption cross-section values is a systematic challenge due to their variation within a normal range of atmospheric temperature and pressure. In Eq. (1) the correction term δN_{H2O} (Z) is due to the interference (differential extinction) from various atmospheric gases and aerosols; and thus for a precise calculation, the atmospheric composition (aerosols and gases) has to be relatively well known. Several DIAL systems, ground based or airborne, using the water vapor absorption bands at 724, 815, 830 and 940 nm were developed [17-21] and they provide troposphere and stratosphere water vapor profiles. Due to the high absorption of the on-line in the lower troposphere, the ground based DIAL is less frequently used than the airborne or space nadir systems.

The Raman technique is based on the Raman effect. When a substance is subjected to an incident exciting wavelength, it exhibits the Raman effect; it reemits secondary light at wavelengths that are shifted from the incident radiation. The magnitude of the shift is unique to the scattering molecule, while the intensity of the Raman band is proportional to the molecular number density. The water vapor Raman lidar technique uses the ratio of rotational-vibrational Raman scattering intensities from water vapor and nitrogen molecules [11, 12], which is a direct measurement of the atmospheric water vapor mixing ratio. The water vapor profile may be retrieved as expressed below:

$$q_{H_2O}(Z) = C(Z)\ \Gamma(Z) \frac{S_{H_2O}(Z) - b_{H_2O}(Z)}{S_{N_2}(Z) - b_{N_2}(Z)} \qquad \text{Eq. (2)}$$

where *q* is the water vapor mixing ratio in [g/Kg dry air] or in [ppmv], *S* is the detected Raman lidar backscatter signal corresponding to nitrogen and water vapor, b is the background (noise) signal, Γ is the correction factor related to the differential atmospheric absorption on the return paths and C is the calibration function (see section 2.2).
This technique is relatively free of systematic errors (aerosol effects), it can be operated from the ground (the radiation is not absorbed by the water vapor

itself) and it can use relatively simple, robust and inexpensive laser sources. Its main limitation is the relatively small backscatter Raman cross- sections ($^{\pi}\sigma_R$), that result in weak Raman signals compared with the elastic backscatters or the electronic noise induced in daytime by solar radiation. The use of the Raman lidar in daytime is theoretically possible in the solar blind region (< 300 nm) [22]. For this a third wavelength is necessary for the determination of the O_3 absorption correction and also the absorption of many other gases has to be taken into account, as for example SO_2 and NO_2. For example, the 4th harmonic at 266.1 nm of Nd: YAG laser was used to excite the O_2 (277.5), N_2 (283.6) and H_2O (294.6) Raman shifts and then used for O_3 and H_2O retrievals into the PBL [22]. Another possibility for performing daytime measurements is to tune appropriately the exciting laser lines such that the water vapor and nitrogen Raman shifts fall on the Fraunhofer solar spectral bands, thus reducing the solar-induced signal noise. To this end, an excimer laser was used to pump a dye laser to produce appropriate wavelengths i.e. H_2O (344.4 nm using p-terphenyl) and for N_2 (360.4 nm using DMQ) in order to fall in the Fraunhofer band at 393.5 nm [23]. The high complexity of the required laser equipment is the main inconvenience of this method.

Several Raman lidar systems were developed in different spectral regions and configurations [24-37]. Various simulation studies were conducted in order to find the most appropriate technique [38-40].

As already mentioned, powerful laser sources, large telescopes, high performance optical filtering, and long integration times are required for the application of the Raman technique. In addition, external calibration methods [41] or precise calculations [42] are needed for determining the calibration function C (Z).

2.2 Water vapor mixing ratio from atmospheric Raman backscatter

The rotational - vibrational Q branch Raman shift are: $\Delta\nu_{H2O} \sim 3652$ cm^{-1} for the water vapor molecule and $\Delta\nu_{N2} \sim 2331$ cm^{-1} (~ 32 nm) for the nitrogen molecule [43]. In the present case, using the third harmonic at λ_L~354.7 nm from an Nd: YAG laser, the Raman backscatter returns cf. Eq. (3) are detected at $\lambda_{H2O} \sim$ 386.68 nm ($\Delta\lambda_R \sim 58$ nm) and $\lambda_{N2} \sim 407.51$ nm ($\Delta\lambda_R \sim 32$ nm).

$$\lambda_R = \frac{\lambda_L}{1-\lambda_L \cdot \Delta\nu_R} \qquad \text{Eq. (3)}$$

The Raman backscatter signals $S_{\lambda_R}(z)$ are described generically by:

$$S(\lambda_R, z) = \frac{K_S(\lambda_R, Z)}{Z^2} n_R(Z) \frac{^{\pi}d\sigma(\lambda_L, \lambda_R, Z)}{d\Omega} \exp\left[-\int_0^Z \left(\alpha_{\lambda_L}(z) + \alpha_{\lambda_R}(z)\right) dz\right] + b_{\lambda_R}(Z) \qquad \text{Eq. (4)}$$

where *R* denotes the Raman channel (λ_R = 407.51 or 386.68 nm), $K_S(\lambda_R, Z)$ is a system function that is dependent on the optical transmission and detector efficiency, and is proportional to the power and duration of the laser pulse, the overlap function and the area of the collector mirror of the telescope, n_R is the number density of Raman active molecule, $^{\pi}d\sigma/d\Omega$ is the differential Raman backscatter cross-section, α is the extinction coefficient and *b* is the background signal (electronic and sky noise).

One important issue for the application of the Raman lidar technique is the value of the water vapor differential Raman backscattering cross section. One of the first estimated values (by Derr and Little, not referenced) is ~ 1.86 x 10^{-29} cm^2sr^{-1} with a Raman stimulation radiation at 337.1 nm. The best estimation is given by Penney and Lapp [44] and is ~ 6 x 10^{-30} cm^2sr^{-1} which is 2.5 times weaker than the nitrogen differential Raman cross-section and ~ 10^3 times weaker than the Rayleigh differential cross section. The water vapor differential cross-section was also calculated in [45].

The water vapor mixing ratio q_{H2O} (specific humidity) is the mass of the water vapor divided by the mass of the dry air in a given volume:

$$q_{H_2O}(Z) = \frac{n_{H_2O}(Z) \cdot M_{H_2O}}{n_{dry\cdot air}(Z) \cdot M_{dry\cdot air}} \qquad \text{Eq. (5)}$$

where *M* is the molecular weight and *n* the number density. When n_{air} and n_{H2O} are extracted from Eq. (4) written for N_2 and H_2O Raman channels, and then introduced in Eq. (5), one arrives at the expression of $q_{H2O:}$

$$q_{H_2O}(Z) = C(Z)\Gamma(Z)\frac{S_{H_2O}(Z) - b_{H_2O}(Z)}{S_{N_2}(Z) - b_{N_2}(Z)} \qquad \text{Eq. (6)}$$

where
$$C(Z) = \frac{K_{N_2}\dfrac{^{\pi}d\sigma_{\lambda_L,\lambda_{N_2}}(Z)}{d\Omega} M_{N_2} n_{N_2}}{K_{H_2O}\dfrac{^{\pi}d\sigma_{\lambda_L,\lambda_{H_2O}}(Z)}{d\Omega} M_{H_2O} n_{air}} \qquad \text{Eq. (7)}$$

C(Z) can be determined using an external calibration method (radiosonde, *in situ* value, etc) or by calculation in the case when the parameters involved in Eq. (7) may be determined. The correction term Γ(z) is the differential extinction on the return path of the two Raman backscattering radiations and can be expressed as:

$$\Gamma(Z) = \exp\left[\int_0^z \alpha\,(\lambda_{H_2O}, z) - \alpha(\lambda_{N_2}, z)dz\right] = \Gamma_a(Z)\cdot\Gamma_m(Z)\cdot\Gamma_{abs}(Z) \qquad \text{Eq. (8)}$$

where α is the total extinction coefficient at wavelength λ and is the sum of the contributions of aerosol (Mie, α_a) and molecular (Rayleigh, α_m) light scattering as well as of gas absorption (α_{abs}),

$$\alpha(\lambda, Z) = \alpha_a(\lambda, Z) + \alpha_m(\lambda, Z) + \alpha_{abs}(\lambda, Z) \qquad \text{Eq. (9)}$$

The background noise *b* has to be extracted from the signals and is generally composed of the sky-solar induced signal superposed on the electronic noise of the detector itself. For the water vapor channel the b_{H2O} value determines the water vapor detection limit.

2.3 Raman lidar setup at Jungfraujoch station

The water vapor Raman lidar technique has been implemented in the JFJ-LIDAR system [46] since August 1st, 2000. The system layout of the water vapor Raman lidar is schematically presented in Figure 1.

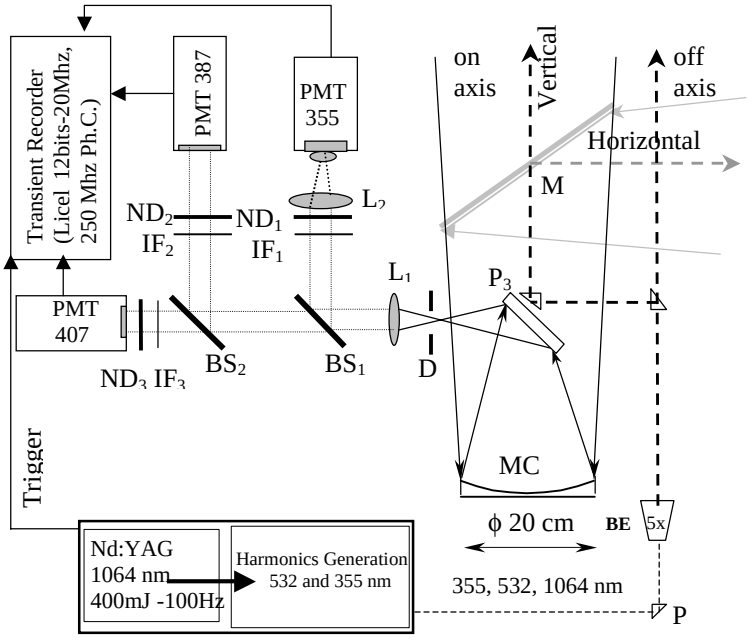

Figure 1 Simplified part of the water vapor Raman lidar layout: L lens, IF interference filters, ND neutral densities, D diaphragm M steering removable flat mirror disposed at 45°, MS telescope secondary mirror, MC collector mirror, PMT 387 and 407 (Thorn Emi photomultiplier tubes), PMT 355 (Hamamatsu photosensor module), BS different λ dichroic beam splitters, BE beam expander, P alignment and guidance prisms.

Related technical specifications are summarized in Table 1.

Transmitter

Laser, wavelength, rep.rate	Nd:YAG, 354.8 nm, 1-100 Hz rep rate
Energy/pulse at 355 nm	30-70mJ
Beam Expander	5X, fused silica, antireflection coatings
Beam Diameter, Divergence	ϕ ~ 5.5 mm, 0.14 mrad
Pulse duration	~ 3 ns

Receiver

Telescope	Newtonian: ϕ 0.2 m/ 0.8 focal length, FOV: 0.2 - 3.8mrad
Detection Optics	
Beam Splitters	ϕ 2", 45° incident angle, Barr Associates Inc BS1: R = 97% at 355 nm, T = 70% at 387 nm T = 85% at 407 nm BS2: T = 97% at 408 nm, R = 99% at 387 nm (a BS is acting before BS1 and BS2 , with R = 95%
Interferential Filters	ϕ 1", 0° incident angle, Barr Associates Inc IF1: CW= 354.7nm, BW=1.4nm, T_{max}~56%, T_{out} ~ 10^{-4} IF2: CW= 386.7nm, BW=3.0nm, T_{max} ~78%, T_{out}~10^{-5} CW= 386.7nm, BW=0.5nm, T_{max} ~65%, T_{out}~10^{-5} IF3: CW= 407.2 nm, BW=0.46nm, T_{max} ~50%, T_{out}~10^{-6} CW= 407.2 nm, BW=3.8nm, T_{max} ~70%, T_{out}~10^{-5}
Neutral Densities	T~ 0.1 to 90% add generally on 355, 387 for desaturation of the Ph. Counting signals from low altitudes
Detectors	PMT355 = Hamamatsu photosensor module, H6780-06 (8mm eff. 185-650nm, gain~105, 43 μA/nW, dark current 0.2-10nA PMT407 = Thorn EMI, QA9829 series PMT 387 = 45mm eff.area, 320-650 nm, dark current 0.4nAgain ~7.10^6
Digitizer/channel	3 LICEL transient recorders in Analog (20Mhz-12 bit) and Photon Counting (< 250Mhz) modes

Table 1 Technical specifications of the water vapor Raman lidar layout.

The third harmonic at 354.7 nm is used to excite nitrogen (386.68 nm) and water vapor (407.51 nm) Raman backscatter returns. The typical laser emission was ~30 - 70 mJ/pulse at 354.7 nm, with 20 – 50 Hz repetition rate. The separation by wavelength of the atmospheric returns is assured via a polychromator based on various dichroic beam splitters (BSi) that selectively reflect the wavelength of interest. Narrow bandpass interferential filters (IF) (bandwidths ~0.5 nm for H_2O and ~ 1nm for N_2) were used for the spectral selection of the nitrogen (386.68 ± 1nm) and the water-vapor Q branches (407.51 ± 0.3 nm) [35]. They also assure the suppression of the sky background and block the elastic backscatter returns. The filters are combined with various neutral density filters

(ND). Taking into account the cross-section values, the typical expected water vapor concentrations in the UT regions (and the optical rejection rates of the BS ($\sim 10^{-4}$) and of the IF ($\sim 10^{-5}$ for one filter, 10^{-10} for two superposed filters), one may easily reach up to $\sim 10^{-12}$ total rejection of the radiation at 355 nm corresponding to the injection into 408 nm in the water vapor Raman channel. This value is enough to completely reject the Rayleigh scattering and elastic backscatters from cirrus clouds at 355nm. The main limitation is the electronic noise of the 407 nm channel itself in photon-counting mode. The data acquisition is performed using LICEL transient recorders working at 20Mz/12 bit in analog (A) mode and 250 MHz maximum count rate for the photon-counting (P.C) mode. Typically an acquisition file contains 4000 shots averaged for each wavelength in A and P.C modes of 3000 bins (1 bin = 7.5 m resolution).
In addition, the acquisition of the pure rotational Raman at 532 nm since May 2002 allows the retrieval of the temperature profile T (z) above Jungfraujoch station (see chapter V). Simultaneous measurements of temperature and water vapor profiles are thus performed. These profiles may be combined to retrieve the relative humidity, which allows identification of inversions and super-saturation over water/ice throughout the upper troposphere. Horizontal observations above the Aletsch glacier using a steering mirror (M) disposed as shown in Figure 1 may also be performed (see an example in chapter V)

3. Results and discussions

3.1 Retrieval algorithm

In order to obtain the water vapor mixing ratio and other related parameters, the signals recorded at 407 and 387 in photon-counting mode as well as the local meteorological measurements are used. The signal processing procedure is schematically summarized in the block diagram presented in Figure 2.
Due to the low water vapor concentrations in the upper troposphere and to the relatively very weak water vapor Raman cross-section, the water vapor signal was detected only in the photon counting mode at 407 nm. The molecular reference is the nitrogen photon-counting signal at 387 nm, which is used after being corrected for the saturation effect (dead time-DT-correction).
Then the two signals are time-space averaged and background corrected. The background value (the time-space average of last 500-1000 bins) for the water vapor is used for the calculation of the signal-to-noise ratio and for the estimation of the detection limit.

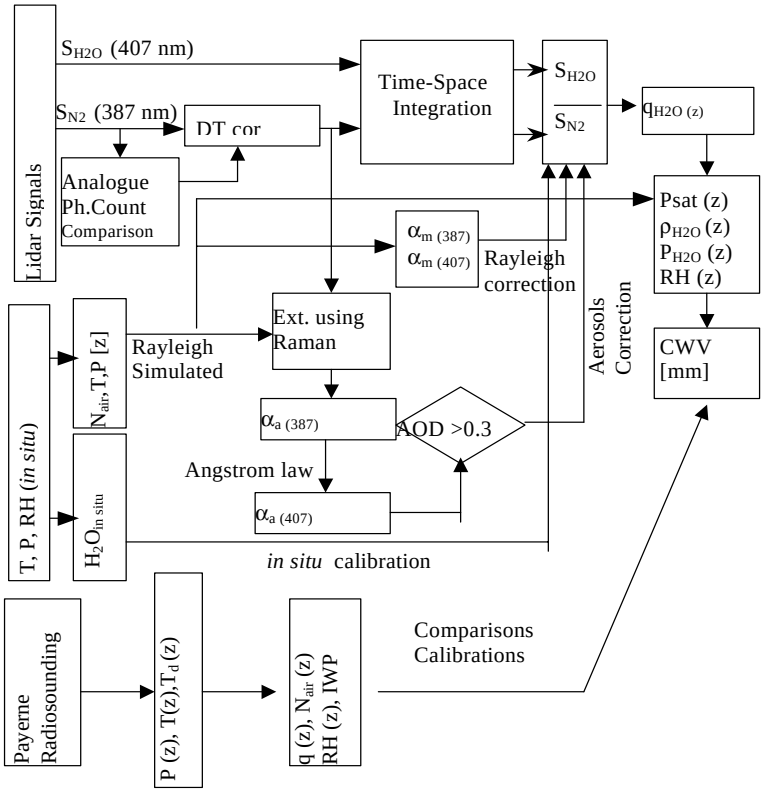

Figure 2 Block diagram of Raman lidar signals processing for water vapor mixing ratio retrieval and its related parameters.

The ratio of the 407 and 387 signals is proportional to the water vapor ratio as shown in Eq. (2). After the application of the differential extinction (Γ) correction, the calibration function C is retrieved based on *in situ* external calibration. The *in situ* water vapor mixing ratio is used to approximate the first value of the Raman lidar water vapor profile, which may be situated between 75 up to 300 m above the station. The *in situ* water vapor mixing ratio q_{H2O} [g/kg] value is calculated as shown in Eq. (10).

$$q_{H_2O} = \frac{6.22\ P_{sat}\ RH}{P_{air} - 0.01\ P_{sat}\ RH} \qquad \text{Eq. (10)}$$

where q is in [g H2O /Kg dry air], the pressure P in [hPa] and the relative humidity RH in [%]. The calculation of the saturation vapor pressure (P_{sat}) was

based on the Magnus formula [47] which is used in meteorology for temperatures between –50 to 50 °C and cf. Eq. (11).

$$P_{sat} = 6.1086 \ \exp\left(\frac{17.856\ T}{245.52 + T}\right) \qquad \text{Eq. (11)}$$

where T is in [°C] and P in [hPa]. The air temperature (T_{air}), air pressure (P_{air}) and relative humidity (RH) are continuously measured at the Jungfraujoch meteorological station (i.e. Meteolabor hygrometer VTP6 (±0.15°K, 0.1% RH). These *in situ* values are also used for initializing the US 1976 atmospheric model of pressure P(z), temperature T(z) and air number concentration $N_{air}(z)$ [48]. The temperature profile T(z) is used for the estimation of the saturation pressure P_{sat} (z) with the same Magnus formula used in Eq. (11). Then the relative humidity RH (z), and the water vapor partial pressure (P_{H2O}) may also be determined from Eq. (10) and the q_{H2O} (z) profile calibrated in g/Kg. Finally, the water vapor density ρ_{H2O} [g m^{-3}] profile is obtained and integrated for the estimation of the integrated water vapor (IWV) column in mm or in kg m^{-2}.
The calculations of different errors, corrections and comparisons (e.g. with Payerne radiosounding) complete the above-described procedure. For the operations schematically presented Figure 2, a corresponding LabView complete software package was developed (see annexes A23, A24 and A25).
Related constants, equations, transformations, definitions, and formulas are listed in the annex A22.

3.2 Corrections and Errors Discussion

3.2.1 Photon counting de-saturation

Although the number of photon counts in the water vapor channel at 407 nm, is largely under the maximum counting rate of the LICEL transient recorder, this is not the case for the nitrogen channel at 387 nm. Thus at low altitude a clear underestimation of the nitrogen signal (saturated) is observed, which will result in an overestimation of the ratio of the two signals and finally will induce an underestimation of the water vapor mixing ratio profile after calibration.
As the saturation of the nitrogen photon-counting signal occurs at low altitudes, it is sensitive to the calibration with the in situ value, and therefore the de-saturation correction (dead time-DT-correction) is mandatory (see its critical effect in the Figure 3).

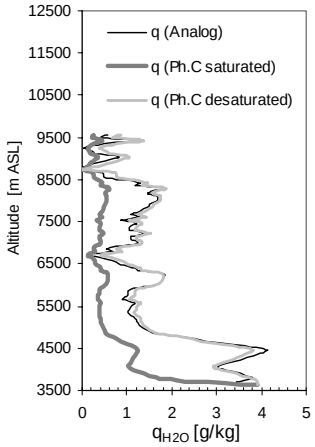

Based on the principle of the photon-counting detection and the Poisson statistics (see annex A14) one may correct the signal following Eq. (12).

$$S_{desat}^{387} = S_{sat}^{387} \frac{1}{1 - \frac{S_{sat}^{387}}{f_{sat}}} \qquad \text{Eq. (12)}$$

where the S_{desat} is the true (corrected) photon-counting rate, the S_{sat} is the recorded photon-counting rate and the f_{sat} is the maximum of LICEL counting rate, all expressed in [MHz].
The value of the f_{sat} was precisely determined from the comparison of photon counting with analogue signals at 387 for each data series.

Figure 3 The photon counting saturation effect on the water vapor mixing ratio retrieval.

3.2.2 Aerosols differential extinction

As expressed in section 2.2, Eq. (8) and Eq. (9), the differential extinction at 387 and 407 nm may be estimated as a product of aerosol- molecular scattering and gas absorption.
The aerosol correction (Γ_a) may be neglected in many cases in the free troposphere. The calculations were based on the Angstrom [49] power law wavelength dependence of the extinction $\alpha \sim \lambda^{-A}$. The Angstrom exponent A ~ 1.18 is found from the median value of sun-photometer observations between 1999 and 2003 [50]. The 407 and 387 nm differential extinction correction due to aerosols is Γ_a ~1 – 2 % for the situation when the 387 and 408 nm shifts pass through aerosol layers having an AOD = 0.25-0.30. In the upper troposphere, the median AODs are 0.024-0.022 in this UV range, which is one order of magnitude lower [50]. In the case of thick clouds and even for particular Saharan dust cases, the Angstrom coefficient tends to zero ($A \rightarrow 0$) and practically no wavelength dependence is expected, which makes the differential transmission correction unnecessary (i.e. $\Gamma_a \sim 1$). Particular attention has to be paid to aerosol layers such as PBL intrusions or low altitude thick clouds. As a general rule, the AOD (Aerosol Optical Depth) is calculated only for altitudes where $SNR_{H2O}>1$ and it is based on the Raman shift at 387 nm and a molecular simulated signal [51]. For $AOD_{387} < 0.3$, the aerosol correction is neglected. If the $AOD_{387} > 0.3$ and if a wavelength dependence is noticed, an aerosol correction is suitable. For this, the Raman signal at 387 nm and a molecular

(Rayleigh) simulated signal [51] is used cf. Eq. (13) for retrieving the absolute extinction coefficient at 387 nm.

$$\alpha_a^{387}(Z) \sim -\frac{1}{2}\frac{d}{dz}\left[\ln\frac{RCS_{387}(Z)}{RCS_m(Z)}\right] \qquad \text{Eq. (13)}$$

Then the extinction coefficient at 408 nm is obtained by extrapolation using the Angstrom law [49] with a realistic experimentally determined value e.g. A ~1.188 as determined from complementary experiments or considerations.
In Figure 4 the aerosols differential correction necessity is illustrated in two distinguished cases.
Figure 4 (a) shows the good agreement between the simulated Rayleigh (molecular) signal and the Raman at 387 nm in an almost aerosol-free situation.
Figure 4 (b) presents an example of the extinction calculation at 387 nm in the case of a low altitude (4000-5500 m ASL) aerosol layer with a higher (~8500 m ASL) cirrus cloud occurrence

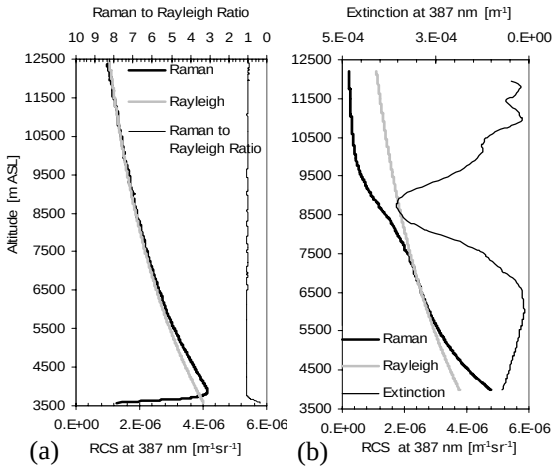

Figure 4 (a) Raman and Rayleigh (simulated) range corrected signals (RCS) at 387 nm in an aerosol- and cloud-free troposphere situation; (b) Raman and Rayleigh (simulated) range corrected signals (RCS) and the extinction coefficient at 387 nm in presence of low aerosol layer (< 5500 m) and a cirrus cloud at ~ 8500 m.

3.2.3 Molecular differential extinction

Based on n_{air} (Z) calculated from [48] and the Rayleigh cross-section formula from [51], the simulated molecular backscatter signals at 387 and 407 nm are obtained and used for the calculation of Γ_m.
For the free troposphere, as shown in Figure 5, this is a systematic correction and it reaches ~3% at the tropopause altitudes.

Finally $\Gamma_{abs} \sim 0$ because the molecular differential absorption (α_{abs}) by ozone and other trace gases can in first approximation be neglected at the 387 and 408 nm [24, 32, 34].

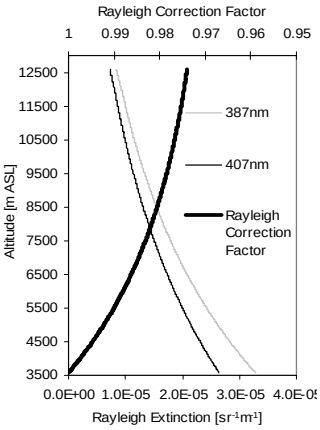

The contamination from the Raman liquid water signal can also be considered negligible for such narrow spectral filtering. The filtering is, however, large enough to avoid the temperature dependence of the signals due to the integration of the Q branch spectral band [52].

Figure 5 Rayleigh (molecular) simulated extinction at 387 and 407 nm as well as the differential Rayleigh correction factor. Note: the atmospheric pressure and temperature at Jungfraujoch station (~3500 m) were considered 0° C and 650 hPa.

3.2.4 SNR, detection limit, statistical and calibration errors

The signal to noise ratio is estimated as the ratio between the water vapor detected signal at 407 nm and b_{H2O} which is the average of the last 500-1000 bins (~ last 3-7.5 km) from the end of the signal. The detection limit is estimated as the water vapor equivalent mixing ratio due to the noise (b_{H2O}) and it is ~ 10^{-2}g/kg. As for one single water vapor profile many data files have to be averaged (i.e. min. 30 min at 50 Hz 300mJ@1064nm), the statistical error can be estimated as 1σ standard deviation. For the time average at a given altitude, the Poisson statistics (see annex A14) is used ($\sigma^2 \sim N_{photon\text{-}counts}$) for the variance of the signal and if added to the background variance, the relative statistical error in time becomes:

$$\left.\frac{\delta q_{H_2O}}{q_{H_2O}}(z)\right|_{time} = \sqrt{\frac{1}{S_{H_2O}(z)}\left[1+2\frac{\widehat{b_{H_2O}}}{S_{H_2O}(z)}\right]} \qquad \text{Eq. (14)}$$

The final statistical error is calculated as the root square of the sum of previously obtained time variances, cf. Eq. (14), corresponding to the number of bins considered in the spatial gliding-averaging window (i.e. reported resolution). The statistics of the nitrogen signal may be neglected as it reaches only ~ 0.2 % at the tropopause.

At the present time, the major uncertainty remains the approximated external calibration using the *in situ* value. In spite of the availability of this one point *in situ* calibration, future calibrations using radiosoundings performed regularly at

the station itself will give a more precise value of the calibration constant. The horizontal measurements can be also used for calibration purposes.

3.3 Water vapor Raman lidar example profile: August 2nd, 2000

The first measurement results at the Jungfraujoch station were already reported on 02 August 2000 [53]. This first water vapor profile and its related parameters such as nitrogen and water vapor signals, the signal to noise ratio - SNR, 1σ standard deviation, relative statistical error, water vapor partial and saturation pressure and the relative humidity are presented in Figure 6 (a,b,c). The SNR-signal to noise ratio- was considered as the ratio between the signal to the average of the last 500 # channels of the acquisition (i.e. noise)

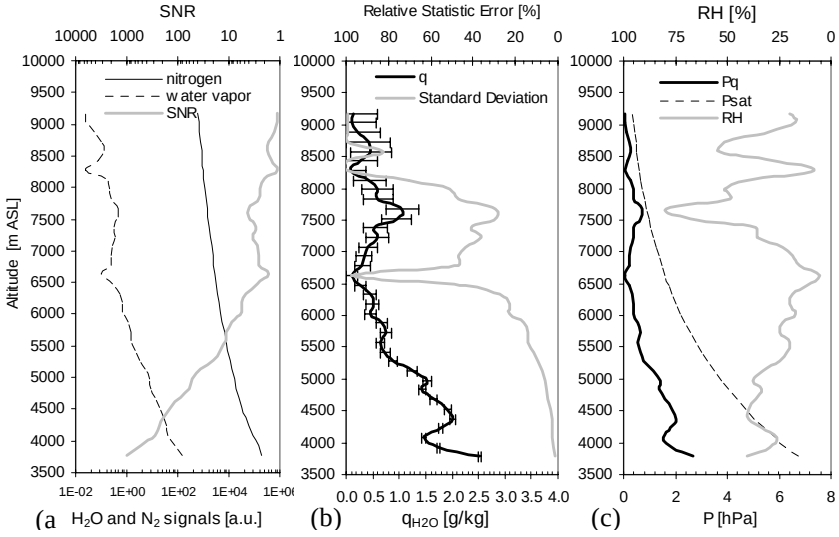

Figure 6 (a) Water vapor, nitrogen signals and the signal to noise ratio (SNR, (b) water vapor mixing ratio profile (q_{H2O}) and the statistic errors, (c) water vapor partial pressure (P_q), the saturation pressure ((P_{sat}) and the relative humidity (RH).

Note that this first Raman lidar water vapor profile (resolution 150 m with a gliding average window of 300 m) was obtained at Jungfraujoch on 02.08.2000 (0:00-1:10 LT), with the laser emission set at 400 mJ (1064 nm) and a repetition rate of 20 Hz (~84000 averaged shots). The calibration altitude was considered at 3780 m with the *in situ* water vapor 2.5 g/kg (T~ 1.3°C, P ~ 669 hPa and RH ~ 40%). The integrated profile (IWV) between 3600 and 9000 m ASL gives ~ 3.1 ± 0.5 mm of precipitable water column (PWV).

3.4 Typical profiles and integrated columns

Since August 2000 many regular data series have been taken and treated in conformity with the above-discussed operations (illustrated in Figure 2). In Figure 7 are selected some typical profiles observed above the Alps.

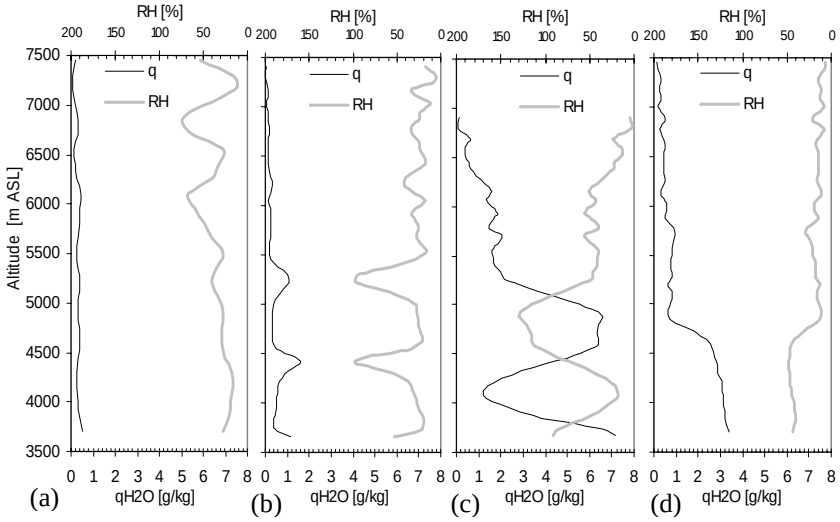

Figure 7 Upper troposphere typical Raman lidar profiles (a) dry (occurrence December-February), (b) cirrus clouds presence, (c) wet (occurrence July-August) and (d) PBL residual layer (August 2003).

Figure 7 (a) presents the situation of a very dry water vapor content (IPW < 0.5 mm) which occurs often in winter (December to January) while in Figure 7 (b) one may distinguish water vapor layers often attributed to the presence of cirrus clouds.
A relatively wet (IPW~ 3-5 mm) upper troposphere occurring mostly in summer (July to August) corresponds to the profile shown in Figure 7 (c) and Figure 7 (d) illustrates the nighttime residual layer consequent to a daytime high PBL convection as was the case in August 2003 heat wave period.
In Figure 8, the time series of the integrated water vapor column are presented together with the estimated 1σ standard deviation.

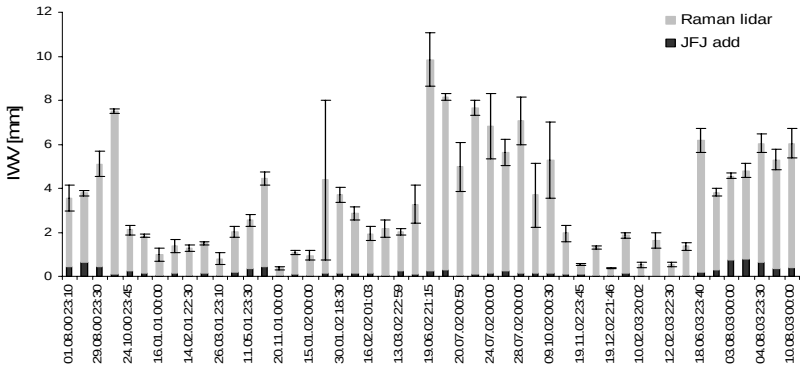

Figure 8 Integrated water vapor columns (IWV) calculated from Raman lidar profiles and the estimated contribution (JFJ add) of the non-measured first layer above the Jungfraujoch station.

The water vapor content of the first atmospheric layer above the station (non measured effectively by the lidar) is added to the total column (JFJ add in Figure 8). Seasonal variation with minima in February and maxima in August can be observed. The driest measured upper troposphere nighttime air was ~ 0.28 mm and the wettest was ~10 mm, with the median value at 2.7 mm. Within the time step used in the data series (30 min to 2 h) the 1σ standard deviation varied from very low (stable) ~1% to very high ~78% variability in the atmospheric water vapor content, with a median value of 16%.

3.5 Raman lidar and co-located water vapor measurements at Jungfraujoch

Water vapor measurements are performed at Jungfraujoch observatory by other complementary techniques as follows.

Microwave Radiometer (MR): A microwave radiometer measures the stratospheric water vapor content based on the 183 GHz water microwave emission. Tropospheric water vapor is considered more as a perturbation (limitation), and thus it is not measured by the microwave radiometer. In combination with MR technique, the Raman lidar is used to complete a profile covering the upper troposphere and the stratosphere regions and it can also be used to verify the inversion methods used by microwave technique for the retrieval of low resolution stratospheric profile [54] .

Precision Filter Radiometer (PFR): A sun tracker photometer derives the daytime total column water vapor taking into account the water vapor absorption at 718, 816 and 946 nm [55, 56].

Fourier Transform Infrared Spectroscopy (FTIR): Integrated daytime column measurements are performed using various infrared ro-vibrational absorption bands recorded by the high resolution, FTIR Spectrometer [57].

Geophysical Positioning System (GPS): The technique is based on the estimation of microwaves (1.2-1.5 GHz) propagation delay between the satellite (transmitter) and antenna (receiver) due to the atmospheric refractivity [58]. The ionospheric (dispersive part of the atmosphere) induced path delay is cancelled by the use of combination of dual emission frequencies. The tropospheric (non-dispersive atmospheric part) delay can be decomposed on a dry part (i.e. zenith hydrostatic delay (ZHD) due to the induced dipole moment) and a wet part (i.e. zenith wet delay (ZWD) due to the permanent dipole of the water vapor). The data recorded by a GPS antenna (Swiss Topography Institute) at the station is used to derive the wet zenith atmospheric delay (ZWD), which is proportional to the water vapor column (IWV). The ZWD is generally obtained as the difference between the zenith total delay and the dry hydrostatic contribution (ZHD) [59] (see also details of the GPS principle of the retrieval in annex A26).
The GPS is the single co-located technique that takes nighttime measurements simultaneously with the Raman lidar. For comparison, the GPS data were first corrected for a bias (offset) probably due to the modeling of the GPS antenna. This offset was calculated by taking as reference the daytime PFR hourly-integrated column data based on the water vapor absorption at 946 nm. The GPS and PFR daytime data scatter plot was built for a statistically significant number of points (~ 20.000 points) covering many seasons (2000-2002 period) and is expressed in Eq. (15).

$$IWV_{GPS}[mm] = 1.040\ IWV_{PFR}[mm] - 1.342mm \qquad \text{Eq. (15)}$$

Application of the above regression model led to homoscedastic residuals with a fairly low variance $1\sigma_{residuals}$ ~ 0.9 mm, a relatively good correlation coefficient r^2 ~ 0.8 and a regression line slope close to unity at 1.040. These considerations allow further comparison of the Raman lidar upper troposphere integrated column with the GPS nighttime co-located measurements. Thus in Figure 9 the PFR (daytime), GPS (day and nighttime) and the Raman lidar (nighttime) IWP data are represented.

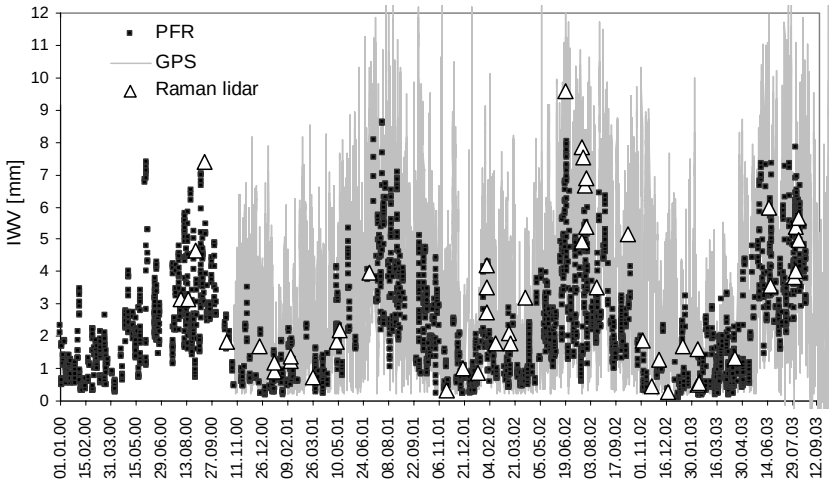

Figure 9 Water vapor integrated column (IWV) estimation from precision filter radiometer (PFR), geographical positioning system (GPS) and Raman lidar collocated instruments at Jungfraujoch observatory. The GPS data were calibrated in daytime with the PFR data.

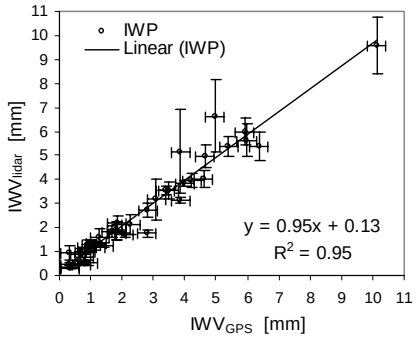

Figure 10 Water vapor integrated column (IWV) scatter plot between the Raman lidar and the GPS collocated instruments at Jungfraujoch observatory. The 1σ statistical variation is represented for the lidar data while the GPS variation is related to the calculation constants variation and not to natural water vapor fluctuations.

A fairly good agreement between the GPS and Raman lidar data (slope ~ 0.95, r^2~0.95, ~0.1 mm bias, 50 points) is noticed. Figure 10 indicates that the approximate calibration method of the Raman lidar allows a realistic estimation of the water vapor above the Alps. Furthermore, it proves also that a well-calibrated Raman lidar system can be used for GPS correction [60] by independently determining the wet zenith delay (WZD).

3.6 Jungfraujoch Raman lidar and the regional radiosounding

In order to check the vertical profiles obtained by Raman lidar, the single available possibility was to compare these profiles with the closest

radiosoundings. The closest space-time sondes are launched generally at midday and midnight from the meteorological station in Payerne (490 m, at ~ 80 Km North-West from Jungfraujoch). A typical radiosonde i.e. SRS400 is equipped with a Copper-Constantan thermocouple for measuring the temperature, a carbon-cellulose hygristor for the humidity and three times a week with an ozone detection unit based on ECC method [61]. In Figure 11 water vapor mixing ratio from radiosonde and Raman lidar are compared in two summer and wintertime cases. Figure 11 (a) refers to a dry upper troposphere case in the winter (February) when the sonde was equipped with a frost point - chilled mirror hygrometer (i.e. Snow-White, SW35/N from Meteolabor AG). Figure 11 (b) refers to a wet summer situation (August) when the sonde was equipped with a standard carbon-cellulose thin film hygristor (i.e. from VIZ/Sippican) [62]. In both cases there is relatively good agreement for large altitude ranges in the homogeneous upper troposphere above the Swiss plateau.
Some differences between the two profiles are evident at low altitudes, but these are expected and mainly due to the different geographical locations, local orographic effects, atmospheric variability, etc.

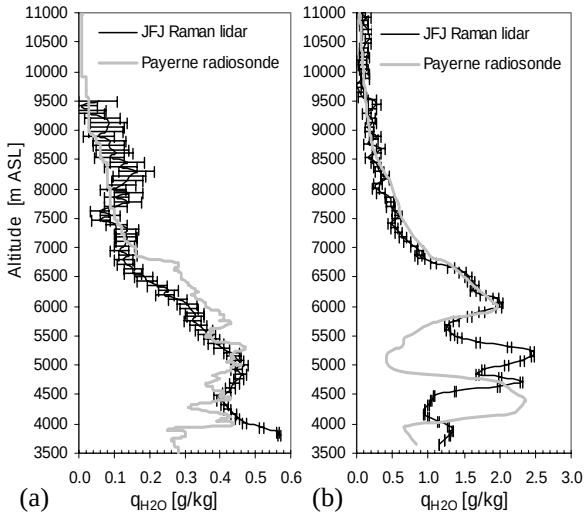

Figure 11 Raman lidar and the closest space-time (Payerne) radiosounding water vapor profiles: (a) Snow-white sonde equipped with a chilled hygristror detector launched at ~ 20:00 LT and Raman averaged profile from 20:00 to 22:00 LT on 14.02.2001; (b) standard meteorological sonde equipped with carbon – cellulose hygristor launched at 1:00 LT and the Raman averaged profile from 1:00 to 2:00 LT on 23.07.2002.

In Figure 12 the Raman lidar integrated columns (3500 to 8 -10.000 m ASL) together with upper troposphere total integrated columns above Payerne are plotted.

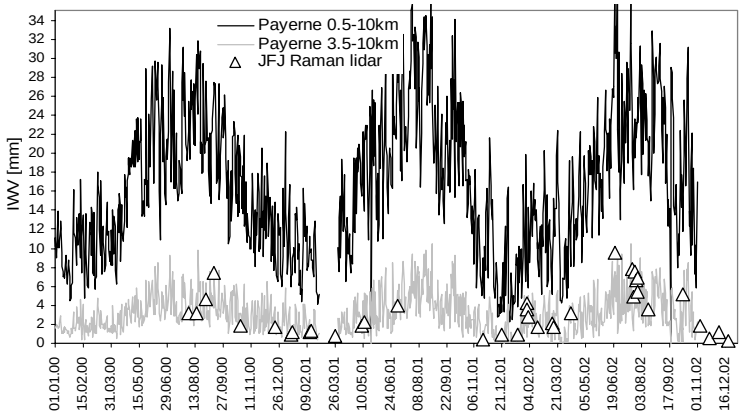

Figure 12 Comparison of the integrated water vapor columns (IWV) from Raman lidar at JFJ profiles with the closest space-time radiosounding from Payerne- Switzerland.

A relatively realistic and good agreement between Raman lidar and Payerne upper troposphere sounding as well the upper troposphere seasonal variation is evident.

4. Conclusion

This work reviews the implementation of a Raman lidar technique at the JFJ station for the measurement of the water vapor mixing ratio. The ratio of the rotational - vibrational Raman shifts at ~ 407 nm (water vapor) and at ~387 nm (nitrogen), is used to derive the upper troposphere water vapor mixing ratio as a direct measurement. The Raman lidar setup specifications are described together with the water vapor retrieval procedure (profile calculation, corrections, errors, and calibration). After application of the necessary corrections, the absolute values of this profile are obtained by assimilating the first point (~ 75-300 m above the station) of the Raman profile with the *in situ* value determined from simultaneous meteorological measurements. The present configuration (i.e. 30-70 mJ/355 nm laser pulse, 20-50 Hz repetition rate, 20 cm Newtonian telescope, ThornEmi PMT detectors) allows high resolution (75-150 m) profiling of the water vapor in the upper troposphere (< 8-10 km) within 1-2 h integration time. The present detection limit is ~10^{-2} g/kg (~15 ppmv). Regular measurements have been taken since August 2000, and selected typical profiles are presented. Different comparisons with co-located techniques such as PFR and GPS at Jungfraujoch or with the closest radiosoundings show realistic agreement. At

present, the Raman lidar setup is the only technique that is able to profile at high resolution the nighttime water vapor above JFJ station. A more precise calibration method based for example on *in situ* launches of radiosondes equipped with new frost point hygrometers is necessary. The stability of the calibration constant may then be verified based on the horizontal measurements, which might be a simple and inexpensive solution.

The sensitivity of the method is expected to increase (~15-20 times $\Leftrightarrow$ 1 ppmv) by coupling the existing astronomic Cassegrain telescope (ϕ 76 cm) with a 3X more powerful laser source. The use of the Hamamatsu photosensor modules instead of the ThornEmi PMT detectors may improve the detection efficiency and particularly its stability at local electromagnetic influences. These further developments will allow retrieval of the stratospheric water vapor profiles, and make it possible to investigate the increase in lower stratosphere water vapor and troposphere-stratosphere exchanges.

An important future challenge is to address the difficulty of obtaining daytime water vapor measurements.

References

1. Eagleson, P.S., *The role of water in climate.* Proceedings of the American philosophical society, 2000. **144**(1).
2. Chahine, M.T., *The hydrological cycle and its influence on climate.* Nature, 1992(359): p. 373.
3. Zuev, V.E., *Laser Monitoring of the Atmosphere*. Topics in Applied Physics, ed. E.D. Hinkley. Vol. 14. 1976: Springer-Verlag. 29-69.
4. Starr, D.O., and Melfi, S. H. (Eds.), *The role of water vapor in climate: a strategic research plan for the proposed GEWEX, water vapor project (GVaP)*. 1991: NASA Conf. Publ.
5. Broecker, W., *Lecture presnted AGU1996 - Baltimore US.* 1996, Lamont-Doherty Earth Observatory, Columbia University.
6. Jones, R.L. and J.F.B. Mitchell, *Climate Change - Is Water-Vapor Understood.* Nature, 1991. **353**(6341): p. 210-210.
7. Houghton, J.T., Y. Ding, D.J. Griggs, M. Noguer, P.J. van der Linden, and D. Xiaosu, *Climate Change 2001: The Scientific Basis: Contribution of Working Group I to the Third Assessment Report of the Intergovernmental Panel on Climate Change (IPCC)*. 2001, Cambridge University Press, UK. p. 944.
8. Gierens, K.M., U. Schumann, M. Helten, H. Smit, and A. Marenco, *A distribution law for relative humidity in the upper troposphere and lower stratosphere derved from three yers MOZAIC experiment.* Ann. Geophys., 1999. **17**(1218-1226).
9. Kley, D., J.M. Russell, and C. Phillips, *SPARC Assesement of upper tropospheric and stratospheric water vapor*. 2000, WMO/ICSU/IOC: World Climate Research Progamm. p. 11-91.
10. Schotland, R.M. *Some observations of the vertical profile of water vapor by means of a ground based optical radar*. in *4th Symposium on Remote Sensing of Environment.* 1966. U. Michigan, Ann Arbor.
11. Melfi, S.H., J.D. Lawrence, and M.P. McCormick, *Observation of Raman Scattering by Water Vapor in the Atmosphere.* Applied Physics Letters, 1969. **15**(9): p. 295-297.

12. Cooney, J., *Remote measurement of atmospheric water vapor profiles using Raman component of laser backscatter*. Journal of Applied Meteorology, 1970(9): p. 182-184.
13. Shine, K.P. and A. Sinha, *Sensitivity of the Earths Climate to Height-Dependent Changes in the Water-Vapor Mixing-Ratio*. Nature, 1991. **354**(6352): p. 382-384.
14. Clough, S.A., M.J. Iacono, and J.L. Moncet, *Line by line calculations of atmospheric fluxes and cooling rates: applications to water vapor*. Journal of Geophysical Research-Atmospheres, 1992(97): p. 15761-15785.
15. Sinha, A. and J.E. Harries, *Water vapor and greenhouse traping: the role of far infrared absorbtion*. Geophysical Research Letters, 1995(22): p. 2147-2150.
16. Schneider, E.K., B.P. Kirtman, and R.S. Lindzen, *Tropospheric water vapor and climate sensitivity*. Journal of the Atmospheric Sciences, 1999(56): p. 1649-1658.
17. Browell, E., T.D. Wilkerson, and T.J. McIlrath, *Water vapor differential absorption lidar development and evaluation*. Applied Optics, 1979.
18. Bosenberg, J., *Ground-based differential absorption lidar for water vapor and temperature profiling: methodology*. Applied Optics, 1998. **37**(18): p. 3845-3860.
19. Ehret, G., C. Kiemle, W. Renger, and G. Simmet, *Airborne Remote-Sensing of Tropospheric Water-Vapor with a near-Infrared Differential Absorption Lidar System*. Applied Optics, 1993. **32**(24): p. 4534-4551.
20. Wulfmeyer, V. and J. Bosenberg, *Ground-based differential absorption lidar for water-vapor profiling: assessment of accuracy, resolution, and meteorological applications*. Applied Optics, 1998. **37**(18): p. 3825-3844.
21. Higdon, N.S., E.V. Browell, P. Ponsardin, B.E. Grossmann, C.F. Butler, T.H. Chyba, M.N. Mayo, R.J. Allen, A.W. Heuser, W.B. Grant, S. Ismail, S.D. Mayor, and A.F. Carter, *Airborne Differential Absorption Lidar System for Measurements of Atmospheric Water-Vapor and Aerosols*. Applied Optics, 1994. **33**(27): p. 6422-6438.
22. Lazzarotto, B., M. Frioud, G. Larcheveque, V. Mitev, P. Quaglia, V. Simeonov, A. Thompson, H. van den Bergh, and B. Calpini, *Ozone and water-vapor measurements by Raman lidar in the planetary boundary layer: error sources and field measurements*. Applied Optics, 2001. **40**(18): p. 2985-2997.
23. Stead, R., *Development of a Prototype Raman Lidar for Daytime Measurements of Water Vapour Mixing Ratio*, in *LPAS*. 2003, EPFL: Lausanne.
24. Ansmann, A., M. Riebesell, U. Wandinger, C. Weitkamp, E. Voss, W. Lahmann, and W. Michaelis, *Combined Raman Elastic-Backscatter Lidar for Vertical Profiling of Moisture, Aerosol Extinction, Backscatter, and Lidar Ratio*. Applied Physics B-Photophysics and Laser Chemistry, 1992. **55**(1): p. 18-28.
25. Behrendt, A., T. Nakamura, M. Onishi, R. Baumgart, and T. Tsuda, *Combined Raman lidar for the measurement of atmospheric temperature, water vapor, particle extinction coefficient, and particle backscatter coefficient*. Applied Optics, 2002. **41**(36): p. 7657-7666.
26. Cooney, J., K. Petri, and A. Salik, *Measurements of High-Resolution Atmospheric Water-Vapor Profiles by Use of a Solar Blind Raman Lidar*. Applied Optics, 1985. **24**(1): p. 104-108.
27. de Tomasi, F., G. Torsello, and M.R. Perrone, *Water-vapor mixing-ratio measurements in the solar-blind region*. Optics Letters, 2000. **25**(10): p. 686-688.
28. Eichinger, W.E., D.I. Cooper, F.L. Archuletta, D. Hof, D.B. Holtkamp, R.R. Karl, C.R. Quick, and J. Tiee, *Development of a Scanning, Solar-Blind, Water Raman Lidar*. Applied Optics, 1994. **33**(18): p. 3923-3932.
29. Ferrare, R., S.H. Melfi, D. Whiteman, K. Evans, G. Schwemmer, Y.J. Kaufman, and R.G. Ellingson. *Raman Lidar and Sun Photometer Measurements of Aerosols and Water Vapor*. in *18th ILRC*. 1996. Berlin.

30. Goldsmith, J.E.M. and S.E. Bisson. *Daytime Raman lidar for vertical profiling of atmospheric water vapour*. in *17th ILRC*. 1994. Sendai / Japan.
31. Lahmann, W., I. Eck, J. Glauer, and S. Köhler. *Solar-Blind Raman Lidar Measurements of Tropospheric Water Vapor Profiles*. in *poster*.
32. Sherlock, V., A. Garnier, A. Hauchecorne, and P. Keckhut, *Implementation and validation of a Raman lidar measurement of middle and upper tropospheric water vapor.* Applied Optics, 1999. **38**(27): p. 5838-5850.
33. Vaughan, G., D.P. Wareing, L. Thomas, and V. Mitev, *Humidity measurements in the free troposphere.* Quarterly Journal of the Royal Meteorological Society, 1988(114): p. 1471-1484.
34. Whiteman, D.N., S.H. Melfi, and R.A. Ferrare, *Raman Lidar System for the Measurement of Water-Vapor and Aerosols in the Earths Atmosphere.* Applied Optics, 1992. **31**(16): p. 3068-3082.
35. Melfi, S.H. and D. Whiteman, *Observation of Lower-Atmospheric Moisture Structure and Its Evolution Using a Raman Lidar*. Bulletin of the American Meteorological Society, 1985. **66**(10): p. 1288-1292.
36. Mattis, I., A. Ansmann, D. Althausen, V. Jaenisch, U. Wandinger, D. Muller, Y.F. Arshinov, S.M. Bobrovnikov, and I.B. Serikov, *Relative-humidity profiling in the troposphere with a Raman lidar.* Applied Optics, 2002. **41**(30): p. 6451-6462.
37. Renaut, D., J.C. Pourny, and R. Capitini, *Daytime Raman-lidar measurements of water vapor.* Optics Letters, 1980. **5**(6): p. 233-235.
38. Grant, W.B., *Differential Absorption and Raman Lidar for Water-Vapor Profile Measurements - a Review.* Optical Engineering, 1991. **30**(1): p. 40-48.
39. Goldsmith, J.E.M. and R. Ferrare. *Performance Modeling of Daytime Raman Lidar Systems for Profiling Atmospheric Water Vapor*. in *16th ILRC*. 1992. Cambridge / UK.
40. Marenco, F. and B. P.T, *Diffrent possibilities for water vapor measurements by lidar in daytime at ENEA's obervatory in Lampedusa, Italy: a simulation.* Journal of Optics A: Pure and Applied Optics, 2002(4): p. 408-418.
41. Ferrare, R.A., S.H. Melfi, D.N. Whiteman, K.D. Evans, F.J. Schmidlin, and D.O. Starr, *A Comparison of Water-Vapor Measurements Made by Raman Lidar and Radiosondes.* Journal of Atmospheric and Oceanic Technology, 1995. **12**(6): p. 1177-1195.
42. Sherlock, V., A. Hauchecorne, and J. Lenoble, *Methodology for the independent calibration of Raman backscatter water-vapor lidar systems.* Applied Optics, 1999. **38**(27): p. 5816-5837.
43. Hinkley, E.D., *Laser Monitoring of the Atmosphere*. Topics in Applied Physics, ed. E.D. Hinkley. Vol. 14. 1976: Springer-Verlag.
44. Penney, C. and M. Lapp, *Raman scatering cross-section for water vapor.* Journal of the Optical Society of America, 1976(66): p. 422-425.
45. Avila, G., J.M. Fernandez, B. Maté, G. Tejeda, and S. Montero, *Ro-vibrational Raman cross-sections in the OH stretching region.* Journal of Molecular Spectroscopy, 1999(196): p. 77-92.
46. Larcheveque, G., I. Balin, R. Nessler, P. Quaglia, V. Simeonov, H. van den Bergh, and B. Calpini, *Development of a multiwavelength aerosol and water-vapor lidar at the Jungfraujoch Alpine Station (3580 m above sea level) in Switzerland.* Applied Optics, 2002. **41**(15): p. 2781-2790.
47. Magnus, G., *Versuche über die Spannkräfte des Wasser-dampfs.* Ann. Phys. Chem, 1844. **61**: p. 225-247.

48. NOAA, NASA, and USAF, *U.S. standard atmosphere (76)*. 1976, U.S. government Printing Office: Washington / USA.
49. Angström, A., *On the atmospheric transmission of sun radiation and on dust in the atmosphere*. Geogr. Ann., 1929. **11**: p. 156-166.
50. Ingold, T., C. Matzler, N. Kampfer, and A. Heimo, *Aerosol optical depth measurements by means of a Sun photometer network in Switzerland.* Journal of Geophysical Research-Atmospheres, 2001. **106**(D21): p. 27537-27554.
51. Collis, R.T.H. and P.B. Russell, *Lidar Measurement of Particles and Gases by Elastic Backscattering and Differential Absorption*. Laser Monitoring of the Atmosphere, ed. E.D. Hinkley. 1976: Springer Verlag.
52. Turner, D.D. and D. Whiteman, *Remote Raman Spectroscopy. Profiling Water Vapor and Aerosols in the Troposphere Using Raman Lidars*, in *Handbook of Vibrational Spectroscopy*, J.M.C.a.P.R.G. (Editors), Editor. 2002, John Wiley & Sons Ltd, Chichester.
53. Balin, I., G. Larchevêque, P. Quaglia, V. Simeonov, H. van den Bergh, and B. Calpini, *Water vapor profile by Raman lidar in the free troposphere from the Jungfraujoch Alpine Station*, in *Advances in global change research*, M.e. Beniston, Climatic Changes: Implications for the Hydrological Cycle and Water Management, Editor. 2002, Kluwer Academic Publisher: Dordrecht and Boston,. p. 123-138.
54. Gerber, D., I. Balin, D. Feist, N. Kämpfer, V. Simeonov, B. Calpini, and H. van den Bergh, *Ground-based water vapour soundings by microwave radiometry and Raman lidar on Jungfraujoch (Swiss Alps).* Atmospheric Chemistry and Physics Discussions, 2003. **3**: p. 4833-4856.
55. Schmid, B., J.J. Michalsky, D.W. Slater, J.C. Barnard, R.N. Halthore, J.C. Liljegren, B.N. Holben, T.F. Eck, J.M. Livingston, P.B. Russell, T. Ingold, and I. Slutsker, *Comparison of Columnar Water-Vapor Measurements from Solar Transmittance Methods.* Applied Optics, 2001. **40**: p. 1886-1896.
56. Ingold, T., B. Schmid, C. Matzler, P. Demoulin, and N. Kampfer, *Modeled and empirical approaches for retrieving columnar water vapor from solar transmittance measurements in the 0.72, 0.82, and 0.94 mu m absorption bands.* Journal of Geophysical Research-Atmospheres, 2000. **105**(D19): p. 24327-24343.
57. Demoulin, P., B. Schmid, G. Roland, and C. Servais. *Vertical column abundance and profile retrievals of water vapor above the Jungfraujoch*. in *Atmospheric Spectroscopy Applications, ASA96*. 1996. Reims.
58. Bevis, M., S. Businger, T.A. Herring, C. Rocken, R.A. Anthes, and R.H. Ware, *Gps Meteorology - Remote-Sensing of Atmospheric Water-Vapor Using the Global Positioning System.* Journal of Geophysical Research-Atmospheres, 1992. **97**(D14): p. 15787-15801.
59. Guerova, G., E. Brockmann, J. Quiby, F. Schubiger, and C. Matzler, *Validation of NWP mesoscale models with Swiss GPS Network AGNES.* Journal of Applied Meteorology, 2003. **42**(1): p. 141-150.
60. Tarniewicz, J., O. Bock, J. Pelon, and C. Thom, *Raman lidar for external GPS path delay calibration devoted to high accuracy height determination.* Physics and Chemistry of the Earth, 2002. **27**(4-5): p. 329-333.
61. Richner, H. and S. Hunerbein, *Grundlagen aerologischer Messungen speziell mittels der Schweizer Sonde SRS 400*. 1999, SMA MeteoSchweiz.
62. Jeannet, P., P. Ruppert, B. Hoegger, and G. Levrat. *Atmosph¨ arische Wasserdampfprofile mit-mittels Taupunktspiegel–Hygrometer*. in *DACH–MT 2001*. 2001. Wien.

Chapter V

Temperature and other atmospheric retrievals based on pure rotational Raman lidar technique

The retrieval of the UTLS temperature profile based on the use of pure rotational Raman spectra (PRRS) of atmospheric nitrogen and oxygen is the main subject of this chapter. The implementation[1] of a double grating polychromator (DGP) on the existent JFJ-LIDAR enables from May 2002 the recording of pure rotational Raman lidar nitrogen and oxygen atmospheric returns around 532 nm. The DGP module allows the spectral separation (1st chamber) and appropriate optical combination (2nd chamber) of two narrow spectral bands from each Stokes and anti-Stokes branches, excited at 532 nm. Thus beside the elastic at 532 nm, two other lidar signals are acquired corresponding to pure rotational radiation at low (i.e. S_{JL} (Z)) and at high quantum numbers (i.e. S_{JH} (Z)).

The sum of S_{JL} (Z) and S_{JH} (Z) is demonstrated to be temperature independent and may be used as a molecular reference. Furthermore it is used for calculation of the true absolute value of the elastic to molecular ratio and to determine the lidar overlap or system function. In the presence of aerosols or clouds, this signal together with a Rayleigh reference allows direct calculation of backscatter, extinction and lidar ratio values.

From the ratio of S_{JL} (Z) and S_{JH} (Z) signals, nighttime temperature profiles are retrieved. The temperature profiles together with the water vapor mixing ratio profiles, derived using the vibrational Raman signals of water vapor at 407 nm and nitrogen at 387 nm, allow the estimation of atmospheric relative humidity.

These atmospheric retrievals are illustrated in this chapter based on an appropriate set of lidar observations in different atmospheric conditions.

[1] With the essential collaboration of Institute for Atmospheric Optics, SB-RAS, Tomsk-Russia (Dr. Y. Arshinov, Dr. S. Brobovnikov and Dr. I. Serikov)

1. Introduction

Simultaneous measurements of atmospheric temperature profiles together with water vapor and aerosol optical properties (i.e. backscatter and extinction coefficients) are required for the retrieval and interpretation of atmospheric relative humidity, planetary boundary layer (PBL) height and dynamics. Vertical temperature and humidity profiles are usually obtained by systematic, worldwide radiosonde measurements. However, the standard radiosondes are not equipped with instruments for aerosol measurements. More, the temporal resolution of the observations is rather low, typically two radiosonde launches a day, with only single data readout per height bin. As a result, the measured profiles are often not representative. Therefore, some important weather phenomena such as the development of a convective boundary layer and the transition between cold and warm fronts cannot be resolved.

Alternative remote sensing techniques like lidar can be extremely useful for supplying temperature, humidity, and aerosol data with high temporal and spatial resolution. The two lidar techniques used for temperature profiling are the Rayleigh and the pure rotational Raman methods. The Rayleigh approach [1] employs the proportionality of the lidar return signal due to molecular backscatter to the atmospheric density. This method requires data on the density and pressure at a relatively high altitude (30-40 km) as a starting point for the retrieval and assumes hydrostatic equilibrium through the entire atmospheric column below this point. In addition, it does not work within the atmospheric layers having aerosol load [2]. Consequently, it can be used mainly in free of aerosols stratospheric regions [3]. The Rayleigh method applicability can be extended to lower altitudes by employing a vibrational Raman signal from atmospheric nitrogen to compensate for the aerosol influence [4].

Cooney [5] was the first to propose the use of temperature dependence of the pure-rotational Raman spectra (PRRS) of atmospheric N_2 and O_2 molecules for temperature profiling. The temperature is deduced by measuring the intensity ratio of two portions with reverse temperature dependence from the S or/and O bands of the air PRRS [6, 7] excited by a laser radiation. Because of the low cross section of the spontaneous Raman scattering the resulting PRRS lidar returns from the atmosphere are normally about six orders of magnitude weaker than the return signal due to elastic light scattering closely spaced in the spectrum. To prevent the contamination of the pure rotational Raman-lidar returns with spurious light from the elastic scattering one has to use devices with the out-of-band rejections higher than 10^8 for spectral isolation of the PRRS portions. ?? For this reason narrowband interference filters usually isolate PRRS signals or diffraction grating based instruments are used. The interference filters are easy to use, have a relatively high transmission and out-of-band rejection up

to 10^{-9}. However, their bandwidth and central wavelength position are sensitive to temperature variations and have long-term drifts [8]. To achieve the necessary rejection ratio, the grating instruments have to be used either in combination with atomic resonance absorption filters or as double-grating devices [9]. The advantages of the grating based instruments are their proven long-term stability and the possibility to sum portions from the O and S branches with the same temperature dependence enhancing the signal to noise ratio (SNR) [9]. Further improvement of the technique for daytime operation (aimed at the signal-to-background enhancement) is achieved by employing an additional Fabry-Perot interferometer (FPI) with free spectral range equal to the spectral spacing between the nitrogen PRRS lines [10]. The FPI cuts out the unwanted daylight background from the spectral gaps between the PRRS lines without reducing the optical transmission of the rotational lines themselves.

The aerosol extinction profile is usually measured by elastic backscatter lidars. In order to retrieve the extinction coefficient by inverting the elastic-lidar equation in the most frequently used Fernald or Klett approaches, the aerosol extinction–to-backscatter ratio and the extinction at a reference altitude have to be assumed [11, 12]. Using the elastic and vibrational Raman signals, the retrieval of the aerosol extinction coefficient is possible [13] with the single assumption made on the wavelength dependence of the aerosol extinction [14].

Because of the spectral closeness of the PRRS and the Cabannes line, the aerosol extinction can be obtained from the PRRS signal without any assumption about the aerosol and atmosphere optical properties (see Figure 1).

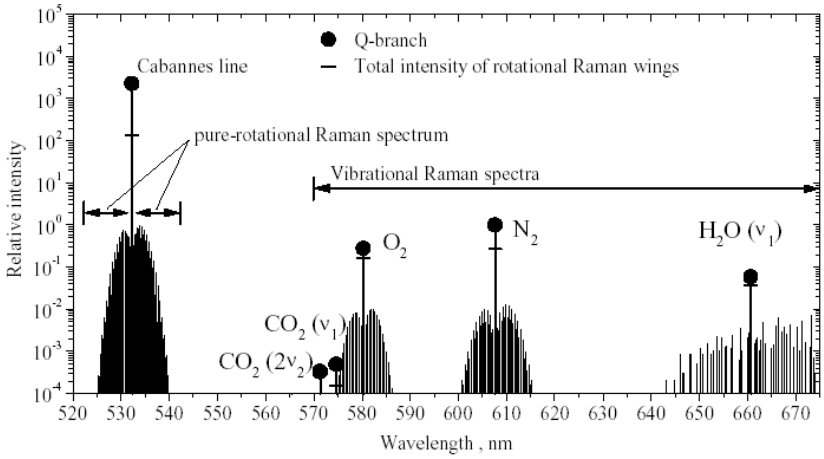

Figure 1 Overview of lidar-backscattered signals at 532 nm. Note: the PRRS is ~two order of magnitude higher then the ro-vibrational of nitrogen and oxygen (from [15]).

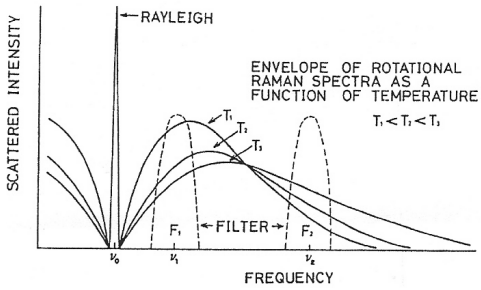

The temperature dependence (Figure 2), of the PRRS, which is the main obstacle for aerosol measurements, can be solved considering that the sum of the integrals of the O and S or of parts of them is temperature invariant. On the contrary, the use of their ratio will give a signal with an enhanced sensitivity to the temperature variations.

Figure 2 PRRS dependency with the temperature (from [16])

It is known that the intensity of the spectral envelope of either O- or S- branch of a PRRS is expressed by Eq. (1)

$$I_{J',J''} = A \cdot c_J \cdot w_J \cdot \exp\left[-\frac{Bhc \cdot J(J+1)}{KT}\right] \qquad \text{Eq. (1)}$$

where A is a normalizing parameter to establish the absolute value (A ~1/T), C_J is the relative line strength, w_J is the nuclear spin weight, B is the molecular rotational constant and J is the rotational quantum number designating a mean value for the upper (J') and lower (J'') quantum states. The frequency separation of the exciting and scattering lines is 4B (J''+3/2), with B ~1.83 cm^{-1} for the N_2 molecule. The rotational lines are discrete and separated by some tenths of nm. The record and the use afterwards of the lidar signals correspondent to PRRS excited at 532 nm are presented here after as follows.

In the next section (2) are described in the 1st part (2.1.) the implementation of the DGP module on the JFJ-LIDAR system and in the 2nd part (2.2.) the PRRS-based algorithms for the temperature, aerosol extinction, backscatter coefficients, and other related retrievals such as relative humidity, cirrus lidar ratio, lidar system overlap function, etc. These above-mentioned retrievals are illustrated in section 3 on different atmospheric conditions.

2. PRRS: implementation and retrievals algorithms

2.1 Implementation of the DGP on the JFJ-LIDAR

The double grating polychromator (DGP) was implemented in May 2002 on the existing JFJ-LIDAR [17] at the Jungfraujoch station. The system described on

[17] was also modified in May 2002 passing from an OFF axis configuration (separated three beams emission) to an ON/OFF axis configuration (coaxial emission). A schematic overview of the new layout and the positioning of the DGP were already shown in chapter II - section 3.1 in Figures 9 and 10. The former depolarization module at 532 nm was removed and instead, the DGP was optically coupled to the existent Filter Polychromator Module (FPM) of the JFJ-LIDAR system as shown in the Figure 3.

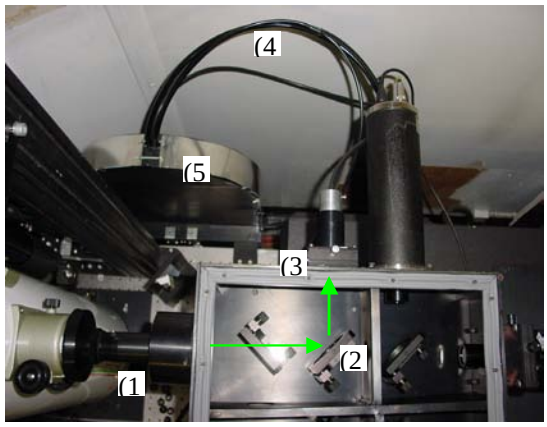

(1) Telescope optical coupling → Filter Polychromator Module (FPM)

(2) Dichroic beam splitter

(3) Optical fiber (OF) adjustable (x, y, z) head

(4) Optical fibers coupling: FPM→ DGP→PMTs

(5) DGP protection cover

(6

Figure 3 Optical coupling of the DGP module with the existent FPM

The initial spectral separation of the optical signals is carried out by a modified version of the Filter Polychromator Module (FPM) described in Chapter II (Section 3.1 and Figure 11) as well as in [17].
The backscattered radiation around 532 nm is focused on the head of an optical fiber (OF) mounted in an adjustable (x,y,z) support. The radiation is thus injected trough the optical fiber on the first chamber of the double grating polychromator (DGP). The DGP module used here is a slightly modified version of the largely described version in [18].
A picture of the DGP opened is presented in Figure 4 (a) while in Figure 4 (b) the correspondent simplified optical layout is illustrated.
The input of the DGP is connected to the 532 nm output of the filter-polycromator via a 600 μm silica fiber. The fiber serves also as a scrambler and an entrance slit for the first part of the DGP, and the fiber diameter defines the overlap function of the lidar temperature channel.

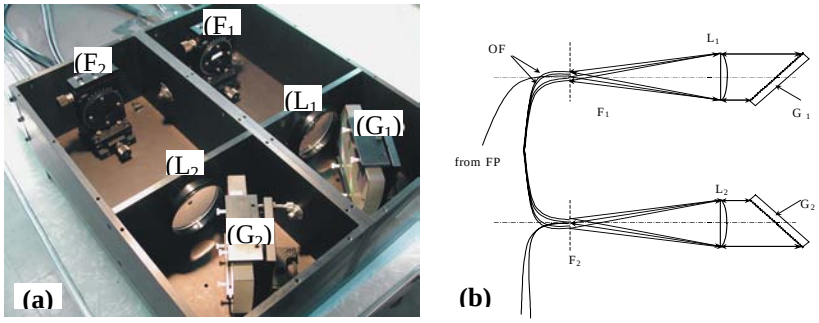

Figure 4 DGP (a) picture view and (b) simplified optical layout. Note: L lenses, G refractive diffraction gratings and F focal points/slits.

The DGP consists of two identical, Litrow configuration polychromators, based on 600 gr/mm gratings (G) operated in the 5th order. Achromatic doublet lenses (L) perform collimation and imaging in the polychromators. The inverse linear dispersion of each of the two parts is ~1.0 nm/mm. Four 600 μm core diameter fused silica fibers connect the two parts of the DGP operated in a dispersion subtraction mode. As a result, the radiation of the pairs symmetric to the 532 nm line is optically summed at the exit fibers of the second polychromator leading to the signal enhancement.

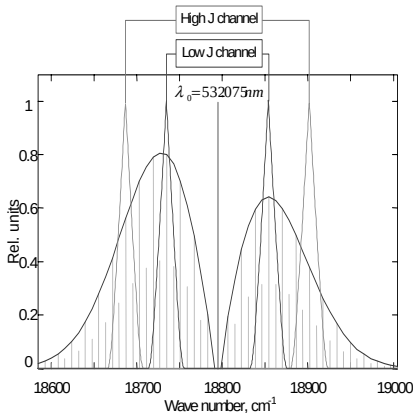

Figure 5 Illustration of the four PRRS portions

The double grating polychromator (DGP) configuration is needed to achieve suppression level of the elastically scattered light higher than 10^{-8}. DGP selects four portions from the Stokes and anti-Stokes branches of the PRRS centered on the excitation wavelength at 532 nm (as shown in Figure 5). This radiation, composed of the nitrogen and oxygen rotational lines (0.05 cm^{-1} width, 8 cm^{-1} inter-lines separation), is proportional to the pure molecular atmosphere, without aerosols backscattered light.

The output optical fibers have a core diameter of 1300 μm and deliver the signal to the detecting PMTs. The elastic signal at 532 nm is taken from the first stage

of the DGP by a 600 μm fiber. Detailed information about the DGP design can be found in [18] and annex A27.
Modified Hamamatsu photosensor modules in photon-counting mode, model H-7421-40, detect the pure rotational Raman signals. The original TTL forming stage in the electronic block of this module was eliminated because it caused reduction in the counting rate.
A separate multi-channel scaler MS 8/10 developed at IOA[2] acquires the PRRS signals. A computer (PC) via LabView based software controls the transient digitizers. A second computer controls the multi-channel scaler under Delphi 6 based custom software.

2.2 Algorithms of the atmospheric retrievals

2.2.1 Temperature profiling

The PRRS lidar method exploits the reverse or inverse temperature dependence of the low- and high-quantum number transitions intensities of the pure rotational Raman spectra. The temperature is derived from the ratio of lidar signals $S_{JH}(z)$ and $S_{JL}(z)$, [5] corresponding to portions of the pure rotational Raman spectra with high and respectively low rotational quantum numbers using the following relationship [9]

$$T(Z) = \frac{A}{\ln \frac{S_{JL}(Z)}{S_{JH}(Z)} - B} \qquad \text{Eq. (2)}$$

where A and B are calibration constants which may be both calculated or experimentally determined. To enhance the signal levels, the Stokes and anti-Stokes bands with equal rotational quantum numbers (same temperature dependence) are optically summed as will be explained in the system description (2.2). The 1σ statistical errors formula (δT_{stat}) is given by

$$\delta T_{stat}(Z) = \frac{\mathrm{A}}{\left[\ln \frac{S_{JL}(Z)}{S_{JL}(Z)} - \mathrm{B}\right]^2} \sqrt{\left(\frac{\delta S_{JL}(Z)}{S_{JL}(Z)}\right)^2 + \left(\frac{\delta S_{JH}(Z)}{S_{JH}(Z)}\right)^2} \qquad \text{Eq. (3)}$$

In addition to the statistical error (δT_{stat}), the calibration error (δT_{AB}) due to the determination and the variability of A and B is estimated as

[2] Institute of Applied Optics , Tomsk-Russia

$$\delta T_{AB}(Z) = \frac{1}{\left[\ln\frac{S_{JL}(Z)}{S_{JH}(Z)} - \mathrm{B}\right]} \sqrt{(\Delta \mathrm{A})^2 + \frac{\mathrm{A}^2}{\left[\ln\frac{S_{JL}(Z)}{S_{JH}(Z)} - \mathrm{B}\right]^2} (\Delta \mathrm{B})^2} \qquad \text{Eq. (4)}$$

In this work, the calibration constants were estimated by non-linear fitting with the closest space-time radiosonde temperature profile (Payerne, ~ 80 km NW)[3]. For comparison, the A and B constants were also calculated from the temperature profile given by US Standard Atmosphere 1976 model [19].

2.2.2 Pure rotational Raman signal: a molecular reference

The surface envelope of the rotational lines (Stokes or anti-Stokes) is invariant with respect to the temperature changes and thus the sum of the portions with high (J_H) and respectively low (J_L) rotational quantum numbers may compensate the temperature dependence. The sum of selected pure-rotational Raman spectra portions with low and high J

$$S_R(Z) = S_{JL}(Z) + S_{JH}(Z) \qquad \text{Eq. (5)}$$

that have almost equal but opposite temperature dependence is practically temperature independent. This sum is proportional to the molecular number density and may be used as a pure molecular reference. The ratio between the elastic at 532nm (E_{532nm}) to S_R signals is thus proportional to the total to molecular backscatter ratio, which is a simple parameter quantifying the aerosols atmospheric load for the altitudes with complete overlap[4]. Normalizing this ratio to the unity in regions of pure molecular evidence, the proportionality constant can be derived and finally, the true value of the total to the molecular backscatter can thus be retrieved. For the incomplete overlap altitudes, the ratio between the $PRRS_{532}$ in free troposphere conditions and a simulated molecular (Rayleigh) signal offers a very good estimation of the overlap function. As generally used in this work, the simulated molecular lidar signals, are based on the molecular backscattering (β_m) and extinction (α_m) coefficients given below [20]:

$$\beta_m(z) = 5.45 \times 10^{-32} \cdot n_{air}(Z) \cdot \left(\frac{550}{\lambda}\right)^{4.09} \qquad \text{Eq. (6)}$$

$$\alpha_m(Z) = \frac{8\pi}{3} \beta_m(Z) \qquad \text{Eq. (7)}$$

with β_m expressed in $m^{-1}sr^{-1}$, α_m in m^{-1} and λ in nm.

[3] All radiosondes used here were launched at the midnight 01:00 LT from Payerne meteorological station
[4] The overlap is related to the degree of spatial coverage between the field of view of the telescope and the laser beam

The air number density (n_{air}) is estimated based on the US Standard Atmosphere 1976 model [19] initialised with the measured temperature (T) and pressure (P) at the Jungfraujoch station (see annex A3).

2.2.3 Backscatter - Extinction Coefficients and Lidar Ratio

To measure the aerosol extinction by the PRRS method we use the sum S_R,

$$S_R(Z) = S_{JL}(Z) + S_{JH}(Z) = Const \frac{1}{Z^2} \beta_R(Z) \exp\left[-2 \int_{Z_0}^{Z} [\alpha_m(z) + \alpha_a(z)] \cdot dz \right] \qquad \text{Eq. (8)}$$

where β_R is the average value for the Raman backscattering, α_a and α_m are correspondingly the aerosol and molecular extinction coefficients. It can easily be shown by direct calculations that S_R is practically temperature independent for suitably selected $S_{JL}(z)$, and $S_{JH}(z)$. The aerosol extinction is then derived as

$$\alpha_a(Z) = -\frac{1}{2} \frac{d}{dz} \left[\ln \frac{RCS_R(Z)}{RCS_m(Z)} \right] \qquad \text{Eq. (9)}$$

where RCS_m is a simulated range corrected molecular signal. The RCS_m was calculated following [20] and using air number density profiles based on the US Standard Atmosphere model [19] initialized with the actual temperature and pressure values at the lidar site. In Eq. 9, the extinction wavelength dependence was neglected because of the small separation between the excitation and scattered wavelengths.

The total extinction $\alpha(z)$ is then obtained as the sum of the particle $\alpha_a(z)$ and calculated molecular extinction $\alpha_m(z)$ profiles. Finally, the total backscatter coefficient $\beta(z)$ is retrieved from the extinction profile and the elastic signal measured at the excitation wavelength $S_E(z)$:

$$\beta(Z) = K_s Z^2 S_E(Z) \exp\left[2 \int_{Z0}^{Z} \alpha(z) dz \right] \text{ Eq. (10)}$$

The system constant K_s is found by normalizing the backscatter profile to a pure molecular signal at a reference altitude defined with the help of the sum S_R signal. The scattering (total to molecular backscatter) ratio is retrieved from the S_E/S_R ratio for altitudes with complete overlap. The proportionality constant between the scattering ratio and the S_E/S_R ratio is derived from measurements taken in aerosol free conditions.

All above – described algorithms were implemented in Lab View routines (see the example of temperature retrieval shown in annex A28).

3. Results and Discussions

3.1 PRRS as molecular reference

The pure rotational Raman transitions are specific to the N_2 and O_2 molecules and independent of aerosols interference and thus the corresponding lidar signals may be used as molecular reference (see Figure 6, left panel). To compensate the temperature dependence the sum (S_R) is considered. Un example of calculation of total to molecular ratio is given (Figure 6, right panel).

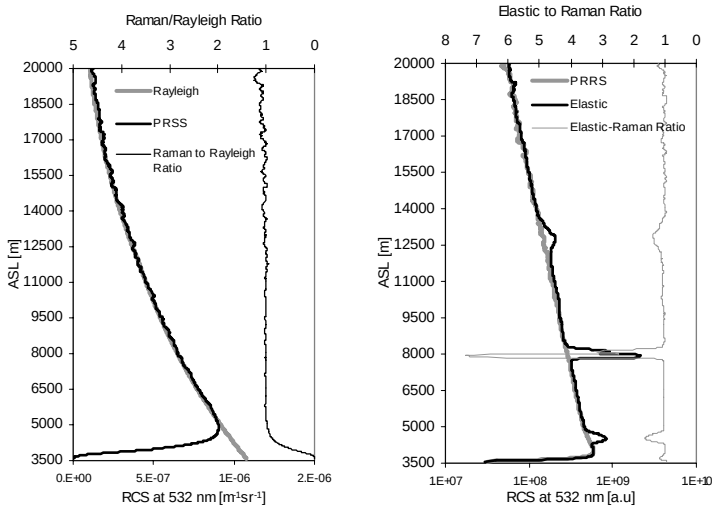

Figure 6 The PRRS and the calculated [20] Rayleigh range corrected backscatter profiles in a clear sky atmosphere situation (left panel) and their ratio (right panel) in an aerosol-cirrus-clouds load.

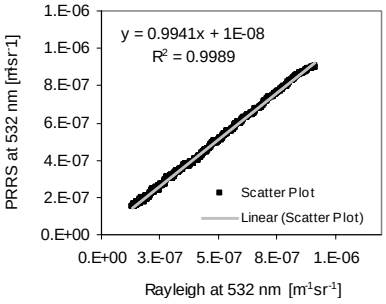

Figure 7 Scatter plot between Rayleigh and PRRS at 532 nm (only complete overlap points were considered)

An excellent correlation (see Figure 7) is noticed when compare the PRRS (S_R) with the simulated lidar Rayleigh signal based on US1976 atmospheric model and the semi-empirical backscatter cross-section proposed by [20]. This confirm: (i) the possibility to use the sum of PRRS signals as molecular reference and (ii) the accuracy of both US 1976 model and backscatter cross-section used [20]

PRRS signal ($S_{R)}$ may be successfully used for the determination of the system function K_S (Z). Particular advantage is the determination of the system function in regions with incomplete overlap (Figure 8). Thus lower altitudes signals can be retrieved. These determinations are preferable to be done from measurements taken in free of aerosol regions.

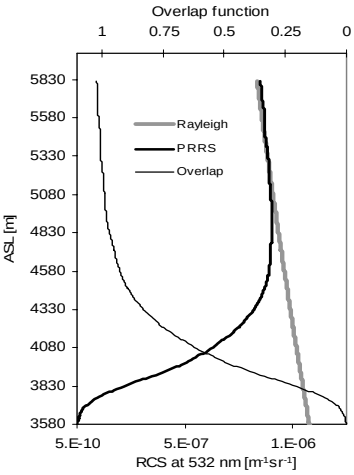

Figure 8 The scatter plot between Rayleigh and PRRS at 532 nm for the complete overlap (left panel) and the Rayleigh and PRRS togheter with the overlap function O(z) estimation (right panel)

3.2 Backscatter - extinction – lidar ratio[5]

Following the algorithms described in Chapter III - Section 2.2 total backscatter and total extinction coefficients, and the lidar ratio were obtained. They are shown together with the temperature profile in Figure 9. Related examples are illustrated in Figure 11 b and in Figure 12 a.

3.3 Temperature profiling

The first step towards regular operation of the temperature channel was to determine the calibration constants A and B in Eq. (2). They were initially obtained by non-linear fitting of the lidar to a model temperature profiles. The model profile was calculated according to the US standard atmosphere model [19] and initialized with pressure and temperature corresponding to the values measured *in situ* at the lidar altitude (3580 m). To verify the applicability of the atmospheric model, a simulated pure molecular (Rayleigh) lidar profile S_m, calculated from the model-derived density, was compared to a S_R profile. The lidar profile was taken on the night of 27th July, 2002 in the middle of a four-day

[5] This approach is completely described in Chapter III, Section 2.

period of high-pressure conditions and negligible aerosol load. The simulated and the lidar profiles were fitted at an altitude of 7500 m. The result of this comparison is presented in Figure 9a. The almost perfect agreement between the two profiles shows: (i) that the atmospheric model describes adequately the air density i.e. the temperature and pressure profiles above Jungfraujoch, and (ii) that the sum of PRRS signals (S_R) depends on the temperature only trough the air density. The calibration constants retrieved by using the model temperature are correspondingly: A = 310.8 K and B = 0.67. We derived the A and B values for the same lidar measurements by fitting a lidar to a radiosonde temperature profile, assuming horizontal homogeneity of the atmosphere. Since the measurements were taken in the middle of a period of stable, high atmospheric pressure conditions, such an assumption seems to be reasonable. The radiosonde was launched during the lidar measurement from Payerne, situated at approximately 80 km West of Jungfraujoch.

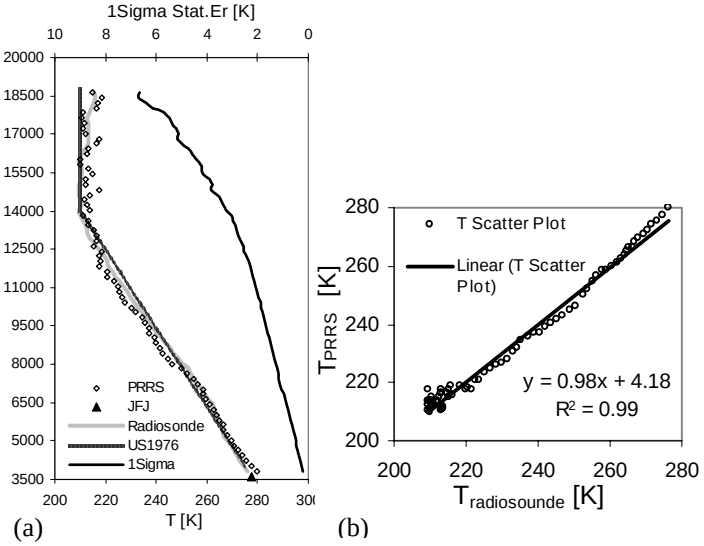

Figure 9 (a) PRRS, radiosonde and US1976 model temperature profiles together with the lidar statistical error estimation, and (b) Scatter plot between radiosonde and PRRS temperature profiles

The A and B values derived from radiosonde comparison are correspondingly 307.1 K and 0.66. The model, radiosonde, and lidar temperature profiles for 27 July are presented in Fig. 6b. All the three profiles show clearly the tropopause height at ~14000 m. The lidar and radiosonde data show very good agreement for the lower part of the profile as seen from the scattered plot presented in Figure 9c. The most serious disagreement is observed in the tropopause region

where both instruments and especially the lidar have lower accuracy. The statistical error of the lidar is lower than 0.5 K for altitudes bellow 9500 m, 1.5 K at the top of the troposphere, reaching values of 4.5 K at the highest point of the profile. To estimate the reliability of the calibration method, we studied also the variance of the calibration constants, derived from a comparison between the lidar and the radiosonde temperature profiles. Only profiles with temperature deviation of less than ± 2° at 3580 m with respect to the temperature measured at the lidar site and drifted in the direction of Jungfraujoch were used for this calibration. The average values of A and B derived by fitting to eight radiosonde profiles, taken in July 2002 (four profiles) and August 2003 (four profiles), are correspondingly A = 301.8 (min. 298.4 max. 307.1) and B = 0.65 (min. 0.62 max. 0.67). The calibration constant values derived by fitting to a radiosonde profile show relatively low variance and their values do not differ by more than 4% for A and 8% for B, from the values determined by the use of the atmospheric model for calibration. The differences appear mostly because the retrieval of A and B is based on comparison of data obtained with different radiosondes and using different time and space averaging of the lidar data profiles. Furthermore, the radiosondes and the lidar, with rare exceptions, sample different air masses. Differences of 1 % for A and B lead to temperature errors of correspondingly ~ 1% and 0.5%.

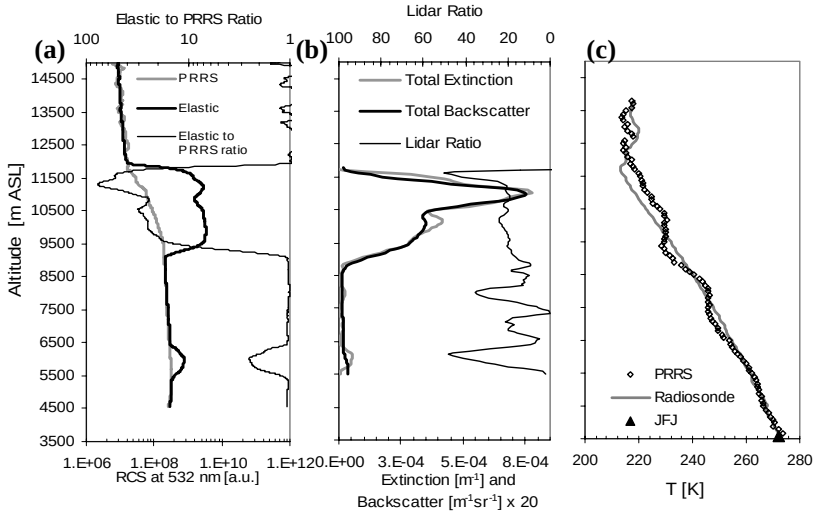

Figure 10 a) Range corrected sum PRRS (S_R), elastic (S_E) and the S_E/S_R ratio b) lidar ratio, and backscatter and extinction coefficients c) lidar and radiosonde temperature profiles. The profiles were taken on 13.05.2001 between 23:00-23:30 LT

Therefore, to achieve a better calibration method more, accurate measurements are needed. Since the A and B values depend mostly on the relative position of the PRRS portions used for temperature retrieval, i.e. on the parameters of the DGP, an absolute calibration of the lidar is possible. Such a calibration can be performed by observing the Raman scattering from the air at different temperatures in laboratory conditions using only the DGP and the operational photodetectors from the lidar receiver. Therefore, we plan to make an absolute calibration in the near future.
We performed some tests of the PRRS channel in order to verify the rejection level at the Cabannes wavelength in the PRRS channels. The initial test measurements were taken under weather conditions with thick and optically dense clouds producing high backscatter.
The simultaneously measured range corrected 532 nm elastic and PRRS sum signals, presented in Figure 10a, clearly demonstrate, that there is no enhancement in the PRRS sum signal within the cloud i.e., there is no cross talk even for total-to-molecular backscatter ratio values exceeding 70. This ratio, shown in the same figure, was obtained by normalizing the elastic-PRRS sum signals ratio to the pure molecular scattering in the aerosol free region around 5000 m. The, derived by the PRRS method, nighttime profiles of the aerosol extinction and backscatter at 532 nm are presented Figure 10b. They exhibit maximum extinction of up to 8.10^{-4} m^{-1} and strong backscatter of up to $0.4.10^{-4}$ $m^{-1}sr^{-1}$ in the cloud at 11 000 m ASL. The temperature profile, retrieved from the same measurement shown Figure 10c, also follows the general behavior of the radiosonde profile but reveals the local features. For example, two inversions, one below, and the other near the cloud base are well pronounced. The second inversion is well linked to the cloud stratification and corresponds to the cloud region with lower backscatter and extinction i.e. lower particle concentration.

3.4 Aerosol - water vapor - temperature: horizontal sounding

In the subsequent tests, scattering from a topographic target was used. The lidar was pointed at a steep, snow-covered mountain at approx. 8 km distance. The PRRS sum signal (S_R) shows no increase at 8 km, whilst the corresponding 532 nm elastic signal at the same distance has signature of saturation and even overshot (see Figure 11b).

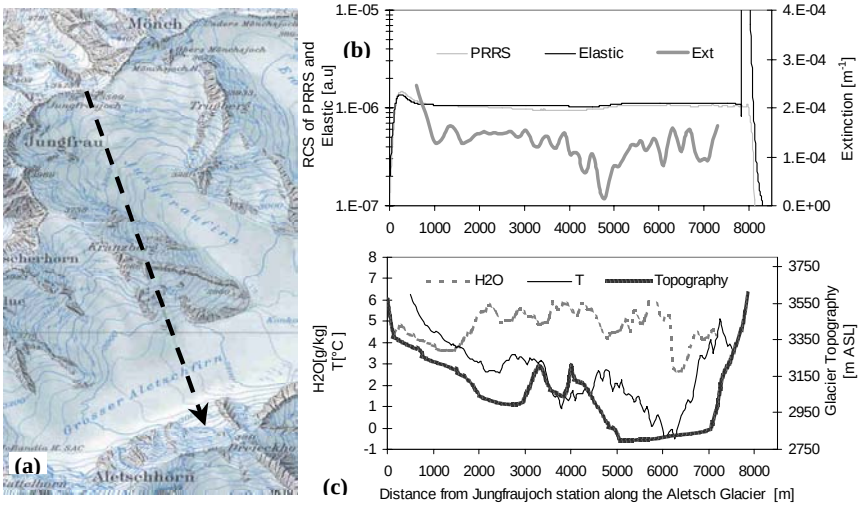

Figure 11 a) Laser beam trajectory during the horizontal observations along an ~8-km-long path above the Aletsch glacier, b) Range corrected sum PRSS and elastic signals together with the PRRS derived total extinction coefficient, c) water vapor mixing ratio and temperature horizontal lidar profiles and the topography of the glacier below the laser beam path from a 1:100 000 map (Swiss Topographic Institute). The measurements were taken on 27.07.2002 between 2:00 and 4:30 h.

During the test period, initial measurements of the aerosol extinction, water vapor and temperature along a horizontal optical path above Aletsch glacier have been carried out. The data will be used for a comparative study of the aerosol optical properties derived from the lidar and *in situ* measurements. The measurements presented here were taken at night, under stable weather conditions with the lidar pointing in Southern direction. A map of the region with the lidar optical path marked with a dashed line is shown in Figure 11a. Temperature and water vapor mixing ratio profiles are also presented in Figure 11c, together with a cross-section of the topography below the lidar optical path. The extinction of the order of 10^{-4} m^{-1} and the water vapor mixing ratio values between 2.5 to 6.5 g/kg are relatively high and indicate hazy conditions. The temperature varies from +5° at the station to almost 0°C above the deepest valley. Both, the water vapor mixing ratio and the temperature (Figure 11c) may suggest possible influence of the glacier topography. Note the general decrease of the temperature and the water vapor content above the valleys and the increase near to the mountain relief. The example demonstrates the potential of the method to measure simultaneously atmospheric extinction, temperature, and water vapor over the glacier. More systematic observations may bring useful

data for the estimation of the atmospheric dynamics over complex terrain, particularly over covered by glaciers mountains surfaces [21].

3.5 Aerosol- water vapor - temperature: vertical sounding

Regular measurements of extinction, backscatter, lidar ratio, water vapor mixing ratio, relative humidity, and temperature have been taken with the lidar since June 2002. The vertical profiles measured on 24 July 2002 are presented in Figure 12 as an example.

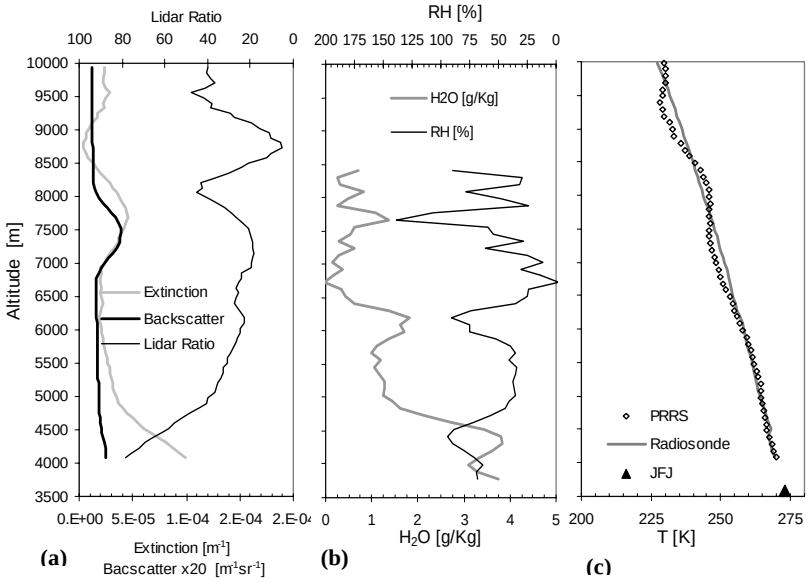

Figure 12 a) Extinction, backscatter and lidar ratio derived using PRRS - based method, b) Water vapor mixing ratio and relative humidity, c) lidar and radiosonde temperature profiles. The measurements were taken on 24.07.2002 between 1:00 and 2:00 h LT

In the water vapor and aerosol profiles several atmospheric layers can be seen, some of which are noticeable also in the temperature profile. The cirrus cloud between 7 and 8 km is well defined, with relative humidity exceeding 100 % and a lidar ratio of up to 45. The temperature profile follows the general wet lapse rate of ~ 6.7 K/km recorded by the radiosonde and reveals some local characteristics such as the temperature inversion in the upper part of the cirrus cloud. The lower part of the atmosphere (up to ~ 4700 m) is characterized by high specific humidity of up to 3 g/kg (RH above 70 %). The high humidity is

probably the reason for the high extinction observed up to this altitude. Despite the high relative humidity of above 70% measured at 6000 m there is no formation of water aerosol, as seen from the extinction and backscatter profiles.

4. Conclusion

This chapter reported the implementation of the PRRS method for measurement of temperature, aerosol extinction and backscatter coefficients on the existing Jungfraujoch multiwavelength elastic-Raman lidar. The portions of the PRRS are isolated with a double-grating polychromator. This technique shows better immunity against contamination of the PRRS signals with elastically scattered light compared to interference filter based polychromators. The high level of suppression of the elastic light in the PRRS channels is demonstrated by measurements in a dense cloud with scattering ratio higher than 70 and by scattering from a solid target. A method based on comparison with an experimentally verified atmospheric model was used for calibration of the temperature channel. Inter-comparison calibration measurements with a radiosonde show good agreement. The use of the PRRS for direct calculation of the total to molecular ratio, of the backscatter, the extinction coefficients, and of the lidar ratio is presented. The PRRS temperature profile is also used in combination with the water vapor mixing ratio for estimation of the relative humidity. Nighttime temperature profiles, measured by the PRRS technique were obtained up to the lower stratosphere (18-20 km), with 30 min – 1 h time average.

References

1. Hauchecorne, A. and M.L. Chanin, *Density and temperature profiles obtained by lidar between 35 and 70 km.* Geophysical Research Letters, 1980.
2. Gross, M.R., T.J. McGee, R.A. Ferrare, U.N. Singh, and P. Kimvilakani, *Temperature measurements made with a combined Rayleigh-Mie and Raman lidar.* Applied Optics, 1997. **36**(24): p. 5987-5995.
3. Nedeljkovic, D., A. Hauchecorne, and M.L. Chanin, *Rotational Raman Lidar to Measure the Atmospheric-Temperature from the Ground to 30 Km.* Ieee Transactions on Geoscience and Remote Sensing, 1993. **31**(1): p. 90-101.
4. Keckhut, P., M.L. Chanin, and A. Hauchecorne, *Stratosphere Temperature-Measurement Using Raman Lidar.* Applied Optics, 1990. **29**(34): p. 5182-5186.
5. Cooney, J., *Measurement of atmospheric temperature profile by raman backscatter.* Journal of Applied Meteorology, 1972. **11**: p. 108-112.
6. Cohen, A., J. Cooney, and N. Kenneth, *Atmospheric temperature profiles from lidar measurements of rotational Raman and elastic scatering.* Applied Optics, 1976. **15**(11): p. 2896-2901.
7. Cooney, J.A., *Atmospheric-Temperature Measurement Using a Pure Rotational Raman Lidar - Comment.* Applied Optics, 1984. **23**(5): p. 653-654.

8. Behrendt, A. and J. Reichardt, *Atmospheric temperature profiling in the presence of clouds with a pure rotational Raman lidar by use of an interference- filter-based polychromator*. Applied Optics, 2000. **39**(9): p. 1372-1378.
9. Arshinov, Y.F., S.M. Bobrovnikov, V.E. Zuev, and V.M. Mitev, *Atmospheric-Temperature Measurements Using a Pure Rotational Raman Lidar*. Applied Optics, 1983. **22**(19): p. 2984-2990.
10. Arshinov, Y. and S. Brobovnikov, *Use of a Fabry-Perot interferometer to isolate pure rotational Raman spectra of diatomic molecules.* Applied Optics, 1999. **38**(21).
11. Klett, J.D., *Stable analytical inversion solution for processing lidar returns.* Applied Optics, 1981. **20**: p. 211-220.
12. Fernald, F.G., *Analysis of atmospheric lidar observations: some comments.* Applied Optics, 1984. **23**: p. 652-653.
13. Ansmann, A., M. Riebesell, and C. Weitkamp, *Measurement of Atmospheric Aerosol Extinction Profiles with a Raman Lidar.* Optics Letters, 1990. **15**(13): p. 746-748.
14. Angström, A., *On the atmospheric transmission of sun radiation and on dust in the atmosphere*. Geogr. Ann., 1929. **11**: p. 156-166.
15. Behrendt, A., T. Nakamura, M. Onishi, R. Baumgart, and T. Tsuda, *Combined Raman lidar for the measurement of atmospheric temperature, water vapor, particle extinction coefficient, and particle backscatter coefficient.* Applied Optics, 2002. **41**(36): p. 7657-7666.
16. Hinkley, E.D., *Laser Monitoring of the Atmosphere*. Topics in Applied Physics, ed. E.D. Hinkley. Vol. 14. 1976: Springer-Verlag.
17. Larcheveque, G., I. Balin, R. Nessler, P. Quaglia, V. Simeonov, H. van den Bergh, and B. Calpini, *Development of a multiwavelength aerosol and water-vapor lidar at the Jungfraujoch Alpine Station (3580 m above sea level) in Switzerland.* Applied Optics, 2002. **41**(15): p. 2781-2790.
18. Ansmann, A., Y. Arshinov, S. Bobrovnikov, I. Mattis, I. Serikov, and U. Wandinger. *Double-grating monochromator for a pure rotational Raman lidar*. in *Fifth International Symposium on Atmospheric and Ocean Optics*. 1998: Proc. SPIE.
19. NOAA, NASA, and USAF, *U.S. standard atmosphere (76).* 1976, U.S. government Printing Office: Washington / USA.
20. Collis, R.T.H. and P.B. Russell, *Lidar Measurement of Particles and Gases by Elastic Backscattering and Differential Absorption*. Laser Monitoring of the Atmosphere, ed. E.D. Hinkley. 1976: Springer Verlag.
21. Barry, R.G., *Mountain Weather and Climate*. Routledge Physical Environment. 1992: London and New York: Routledge.

Chapter VI

Optical properties of Saharan dust

Both the sign and magnitude of the direct-indirect mineral dust effects on the global radiative balance are poorly understood and various observations are used to reduce this lack of information. Within this general research effort, this chapter presents results concerning the optical properties of long-range transported mineral dust during the Saharan dust outbreaks (SDO), which are often noticed over the Western Europe. This work focuses on the August 2, 2001 SDO event in which a dust plume was observed above the Swiss Alps in the upper troposphere. Co-located *in situ*, lidar, sun photometer, nephelometer and aethalometer measurements at the JFJ station were taken on August 1 and 2, 2001 in three different sub-periods: (a) no dust occurrence (b) dust plume and (c) cloud-dust mixture. The measurements are comparatively analyzed. Lidar range corrected signals (RCS), elastic to molecular backscatter ratio, backscatter (β_a) and extinction (α_a) coefficients at 355, 532 and 1064 nm as well as the depolarization ratio at 532 nm are discussed. Simultaneous aerosol *in situ* measurements and aerosol optical depth (AOD) from a sun photometer precision filter radiometer are presented. The aerosol Angstrom coefficients determined from *in situ* measurements, sun-photometer instrument and lidar observations are used to link and compare these co – located observations. The dust microphysical properties, initially calculated in a spherical approximation of the shape of the dust particles, are also presented as a preliminary result.

1. Introduction

Soil dust is one of the major contributors to global atmospheric aerosol loading and optical thickness, especially in sub-tropical and tropical regions. Estimates of its global source strength range from 1,000 to 5,000 Mt yr^{-1} with very high spatial and temporal variability. Compared with the global continental mineral aerosols estimated emission in 2000 all other categories of aerosols (black carbon, organic matter, fossil fuel, aviation, industrial dust, biogenic, forest fires, etc) have been estimated ten times lower. With an estimated loading of about 3340 (Tg yr^{-1}), sea salt seems to be the main contributor to global aerosol load. In the northern hemisphere, dust and sea salt loading has been estimated to 1800 Tg yr^{-1} and 1400 Tg yr^{-1}, respectively, while contributions from all other aerosol categories reach only ~ 300 Tg yr^{-1}. The Saharan dust aerosol optical depth (AOD) is quantified up to 0.35-0.45 compared with 0.15-0.25 for sea salt or with 0.20-0.25 for the all other categories over continental Europe [1, 2].

Dust source regions are deserts, dry lakebeds, and semi-arid desert fringes, but also areas where vegetation has been reduced or soil surfaces have been disturbed by human activities. The desert regions of the Northern Hemisphere are considered major sources compared with minor contributions from the Southern Hemisphere. In addition to the desert sources, about 50 % of the mineral dust loading is attributed to anthropogenically disturbed soil [3]. Mineral dust may be redistributed across large regions of the Earth via the synoptic weather systems. Satellite images show mineral dust transported from the Sahara to the southeastern United States [4]. Evidence for long-range transport of mineral dust has even been observed in Antarctica, where snowflakes have been demonstrated to contain mineral dust originating from long-range transport [5].

In spite of the important amount and global scale transport and distribution, both the magnitude and sign of mineral dust on the direct net radiative forcing remain unclear. The complexity in estimating dust radiative forcing is mainly due to the non-uniform distribution of sources and sinks. In addition, the residence time of mineral dust in the atmosphere is highly variable ranging from seconds to years (for dust injected into the UTLS by volcanoes). The global models are beginning to address the complications of emission, sedimentation and wet removal with many simplified parameterizations [6]. Nevertheless the models have difficulty accounting for the mineral surface chemistry, interactions with other aerosols or cloud processing [7]. Mineral dust from the Saharan desert absorbs much less solar radiation than previously thought.

The desert dust absorption of incident sunlight of the solar spectrum varies from 1-5 % to 10-15 %. The estimation of how much sunlight is absorbed and reflected by desert dust vary widely - some show a net warming effect on the atmosphere while others a net cooling- that both climate warming and cooling

scenarios were associated with mineral dust effects in the recent report by the Intergovernmental Panel on Climate Change [1].

Satellite observations (e.g. a dust storm over Senegal along the western African coast) show clear differences in the brightness of solar radiation reflected by the land surface and the heavy dust clouds indicating that nearly all the sunlight, from the VIS and NIR part of the solar spectrum, incident on the dust cloud, was reflected back into space [8]. Very little is absorbed by the iron-rich dust particles, and this absorption mainly occurs in the UV. Concerning the indirect effects, dust may affect clouds in two ways. The dust inhibits precipitation by increasing the number density of small particles, which are much less likely to collide, resulting in an increased lifetime of low altitude clouds. The clouds with a dust supply have greater reflection of solar radiation, thereby trapping more infrared radiation, which produces stronger cloud-top cooling and cloud-base heating. Conversely, by interacting with high-altitude clouds (i.e. cirrus) the dust may induce precipitation. Indeed, the dust acts as aggregation nuclei for growing ice crystals and causes the water droplets to freeze at higher temperatures than expected. This induces the precipitation of the coarse ice crystals, which then collide with water droplets and transform into rainfall. The response of the climate system to cloudiness is differential; a decrease in low altitude clouds leading to a cooling effect and an increase in high altitude clouds leading to a warming effect. This is a present general consensus [9, 10].

In addition to the laboratory measured chemical and physical properties of aerosols the climate models require ambient atmospheric measurements of aerosol optical properties for a better parameterization of the interaction between solar radiation and dust. This interaction can be quantified based on measurements of different aerosol-related parameters[1] such as: extinction (α_a), absorption (α_a^{abs}), total scattering (α_a^{scat}), backscattering (β_a), the extinction/backscatter ratio (i.e. lidar ratio LR), the single scattering *albedo* (ω_o), and the depolarization ratio (φ)[2]). The degree of depolarization (φ) of light, backscattered by dust, gives information on the particle shape (spherical or non spherical), and it can be related to hydration state (humid or dry) or to atmospheric lifetime (aged or fresh) [11, 12]. The functional dependence of light-scattering on relative humidity (f[RH]), the complex refractive index (n) and the asymmetry parameter (g) are also important [13].

The aerosol optical depth e.g. AOD cf. Eq. (1) is the most commonly used integrated value to characterise the aerosol load into the atmosphere,

$$AOD = \int_{Zo}^{Z} \alpha_a(z)dz \qquad \text{Eq. (1)}$$

[1] The index **a** refers to aerosols, **m** to molecules (molecular) and **d** to the situations with pure mineral dust

[2] Ratio of parallel to perpendicular polarization of atmospheric backscattered light, excited by a linear polarized laser beam, as already defined in chapter II and used in chapter III.

where ΔZ = Z - Zo is the optical path (generally scaled to the zenith direction) and the aerosol total extinction.

$$\alpha_a = \alpha_a^{scat} + \alpha_a^{abs} \qquad \text{Eq. (2)}$$

The wavelength dependence of the extinction coefficient exhibits a power law dependence known as the Angstrom [14] turbidity formula:

$$\alpha_a = B_{ext}\, \lambda^{-A_{ext}} \qquad \text{Eq. (3)}$$

where A_{ext} and B_{ext} are the Angstrom coefficients in agreement with Mie theory [15]. As the Angstrom coefficients already give a first indication of the aerosol size (i.e. A_{ext}) and the number concentration (i.e. B_{ext}), they may be used to distinguish and characterize different aerosol load situations (- as already used in chapter II and III). A similar power law of the wavelength dependence can be assumed for the total scatter (α_a^{scat}), backscatter (β_a), absorption (α_a^{abs}) and the single scattering *albedo* (ω_0) as described from Eq. (4) to Eq. (10) with different meaning of the parameters A and B.

$$\alpha_a^{scat} = B_{scat}\, \lambda^{-A_{scat}} \qquad \text{Eq. (4)}$$

$$\beta_a = B_{backscat}\, \lambda^{-A_{backscat}} \qquad \text{Eq. (5)}$$

$$\alpha_a^{abs} = B_{abs}\, \lambda^{-A_{abs}} \qquad \text{Eq. (6)}$$

The single scattering *albedo* ω_0 (the scattering component of the extinction),

$$\omega_0 = \frac{\alpha_a^{scat}}{\alpha_a} \qquad \text{Eq. (7)}$$

can also be written as power law function of wavelength as

$$\omega_0 = B_{ssa}\, \lambda^{-A_{ssa}} \qquad \text{Eq. (8)}$$

where

$$B_{ssa} = \frac{B_{scat}}{B_{ext}} \qquad \text{Eq. (9)}$$

$$A_{ssa} = A_{scat} - A_{ext} \qquad \text{Eq. (10)}$$

The parameter A_{ssa} is called the exponent of the single scattering *albedo* [16] and it is usually positive. This is because the scattering coefficient (α_a^{scat}) usually decreases more rapidly with increasing wavelength than the absorption

coefficient (α_a^{abs}). This smaller wavelength dependency of the absorption will induce a smaller A_{ext} value than A_{scat} that results in a positive A_{ssa}. For coarse particles, scattering becomes dominated by a geometrical optics regime, so that a wavelength independence of the scattering coefficient is predicted (i.e. $A_{scat} \rightarrow 0$). Since A_{abs} becomes greater for desert dust [17] , A_{ssa} in consequence becomes negative. As a result, negative values of the exponent of single scattering albedo (A_{ssa}) are a reliable indicator of coarse mineral particles. The A_{ssa} was demonstrated to be negative in presence of mineral dust and thus an excellent tracer for a series of SDO events [17] .

A general effort is made to estimate the above-defined aerosol parameters via many complementary techniques both at global (i.e. satellites) and local (i.e. ground-based) scales. In recent years many observations show regular Saharan dust outbreaks (SDO)[3] occurring over Europe, and the model predictions generally map well the day – by - day dust plume trajectories [18]. During the 2000-2003 period, the dust outbreaks observed by the EARLINET [19] network show an average of 5 - 10 events for northern Europe and up to 40 events in Southern Europe [20]. Different studies are attempting to combine continental lidar vertical profiles with other related observations [21], [22], [23] for determining more dust related parameters as accurately as possible. One relatively recent analysis of the microphysics and optical properties of dust transported over the Atlantic was reported based on lidar ship-borne measurements [24].

In this context the present chapter presents the characterization of the optical properties of a mineral dust plume transported over the Swiss Alps. This upper-troposphere dust plume was detected on August 2, 2001 from 04:00 LT[4] to the late afternoon by many co-located observational systems at the JFJ station (3580 m)[5]. These systems (i.e. lidar, sun-photometer and *in situ* nephelometer – aethalometer) are briefly described in section 2. In section 3, the evidence for Saharan dust in the upper troposphere on August 2, 2001 is demonstrated while the results of backward trajectory calculations are presented in section 4. The analysis of this observational data set is presented in Section 5 while section 6 contains the conclusions.

2. Measurement techniques

2.1 Multi-wavelength lidar

The JFJ-LIDAR system configuration at the moment of the SDO observation has already been described in [25] and [26]. The transmitter was based on a Nd:YAG laser (400 mJ at the fundamental 1064 nm and a variable repetition

[3] SDO is the acronym from Saharan Dust Outbreak (Occurrence)
[4] All times are JFJ local time (LT; LT = UTC + 1)
[5] All altitudes are in meters (m) above see level (ASL)

rate up to 100 Hz) emitting at 355, 532 and 1064 nm. The three beams were emitted separately and were independently aligned. The measurement series used here were taken with the system operating at 200 mJ (at1064 nm) and 50 Hz. The 20 cm diameter telescope, in Newtonian configuration, was placed together with the polychromator filter, detectors and the acquisition system in the cupola dome (see chapter II, Figure 2). The minimum altitude, due to the incomplete overlap between the telescope field-of-view and the laser beams, was at least 500 m above the lidar station (i.e. ~4000 m ASL). The depolarization measurements at 532 nm were taken based on the depolarization module (described in the chapter II, section 3.1). The raw lidar signals were acquired using the Licel transient recorders (same as described in chapter II, section 3.1) as averaged of 4000 shots with a vertical resolution of 7.5 m. The lidar returns were background subtracted and space-time averaged using constant or variable window gliding filtering techniques. In this analysis, the lidar range corrected signals (RCS) cf. Eq. (11) are used to estimate the total to molecular backscatter ratio.

$$RCS(Z) = S(Z)Z^2 = K_S(Z)\cdot[\beta_m(Z)+\beta_d(Z)]\cdot\exp\left(-2\int_{Z0}^{Z}[\alpha_m(z)+\alpha_d(z)]\cdot dz\right) \quad \text{Eq. (11)}$$

The intensity of RCS signals is obviously proportional to the aerosols' backscattering, weighted by the atmospheric extinction. The dust extinction (α_d), and backscatter (β_d) coefficients, at the three wavelengths, were derived from the elastic lidar signals using the Fernald-based inversion algorithm as described in chapter III section 2.1. Unfortunately, this inversion is based on an *a priori* value of the lidar ratio (LR = α_d/β_d). A reference value is also needed for initializing the iteration. This value was the molecular simulated value at an aerosol-free altitude (i.e. β_t ($Z_{ref,}$ λ) ~ β_m (Z_{ref} , λ) and β_d ($Z_{ref,}$ λ)~0). These assumptions reduce the number of unknowns in Eq. 11 (K_s, α_a and β_a) to only one (e.g. β_a) and thus the equation can be inverted as was already explained in chapters II and III.

The molecular backscattering (β_m) and the extinction (α_m) are calculated based on Eq. (12) and Eq. (13) from [27].

$$\beta_m(Z) = 5.45E\text{-}32\cdot n_{air}(Z)\left[\frac{550}{\lambda}\right]^{4.09} \quad \text{Eq. (12)} \qquad \alpha_m(Z) = \frac{8\pi}{3}\beta_m(Z) \quad \text{Eq. (13)}$$

where βm is expressed in m^{-1} sr^{-1} and λ in nm. In these equations, the air number density n_{air} (Z) was estimated based on the US Standard Atmosphere 1976 [28], initialized at the station altitude

The mineral dust extinction coefficient $\alpha_a(Z)$ determined from lidar at three wavelengths (355, 532 and 1064 nm) are then used for the retrieval of the Angstrom coefficients vertical profile by using the values at two wavelengths cf. Eq. (14).

$$A_{ext}(Z) = -\frac{\ln\left[\frac{\alpha_a(\lambda_1,Z)}{\alpha_a(\lambda_2,Z)}\right]}{\ln\left[\frac{\lambda_1}{\lambda_2}\right]}, \qquad B_{ext}(Z) = \alpha_{ext}(Z)\lambda^{A_{ext}} \qquad \text{Eq. (14)}$$

The A and B profiles indicate the size and number density within the dust plume.

The depolarization ratio φ (z) was determined as the ratio of perpendicular to parallel backscatter returns at 532nm:

$$\varphi_{532nm}(Z) = C_{532nm}(Z) \cdot \frac{S_c(Z)}{S_p(Z)} \qquad \text{Eq. (15)}$$

where C_{532nm} is the calibration function taking into account the whole system depolarization effects and the differential detection of both channels at 532 nm [29] and is determined from measurements in clear atmosphere.

2.2 *In situ* nephelometer and aethalometer

Continuous measurements of a number of aerosol parameters have been performed since 1995 at JFJ by the Laboratory of Atmospheric Chemistry from PSI as part of the Global Atmospheric Watch (GAW) project, [30]. The air at the JFJ station is sampled through a heated inlet (25°C, 10% RH) designed to evaporate all cloud droplets at a very early stage. Then the air flows through a nephelometer and an aethalometer [31]. The total scattering (α_a^{scat}) and the backscattering ($\beta_a^{nephelo}$) coefficients are simultaneously measured at three wavelengths (λ= 450, 550, and 700 nm) by an integrating nephelometer (IN, TSI 3563). Data are collected with a 5 min resolution. Simultaneously, the absorption coefficient (α_a^{abs}) was calculated at seven wavelengths (λ = 370, 470, 520, 590, 660, 880 and 950 nm) based on aethalometer (AE-31, Magee Scientific) measurements [32] at 10 min resolution. In this analysis, hourly means are used for both scattering and absorption coefficients. A power law wavelength dependency was fitted to the scattering coefficients, measured at the three-nephelometer wavelengths. This allows a determination of the scattering exponent A_{scat}. Based on $A_{scat,}$ the scattering coefficients are inter-extrapolated to the corresponding aethalometer 7-wavelengths. The extinction coefficients at 7-

wavelengths are calculated as the sum of the absorption (α_a^{abs}) and the scattering (α_a^{scat}). A wavelength dependency as a power law was fitted to the single scattering *albedo* in order to obtain the single scattering *albedo* exponent (A_{ssa}). All parameters defined from Eq. (3) to Eq. (10) were obtained in this way. However, these *in situ* measurements as performed at room temperature 25 ± 4°C and 10% RH are representative of dried aerosols, and not for ambient outdoor aerosols.

2.3 Sun photometer

A sun photometer (SPM)- precision filter radiometer (PFR) instrument is installed on a sun-tracker unit, at the JFJ. This SPM-PFR is an automated system and it belongs to MeteoSwiss Institute. The UV_VIS_NIR radiation detection is based on a set of Precision Filter Radiometers (PFR; developed by PMOD/WRC-Davos and built by CSEM-Neuchâtel). Each channel is equipped with a Si-diode interference filter (bandwidth ~ 5 nm, 0.1% uncertainty on the central wavelength). The field-of-view of the detector, defined by two apertures, is 2.8° with a slope angle of 0.7°. The filters and the detectors are assembled into a temperature-stabilized enclosure. SPM-PFR calibrations are based on the Langley plot technique and are performed regularly during clear weather conditions in a stable atmosphere. A more detailed technical description of the SPM-PFR can be found in [33, 34]. The solar radiation is detected at a complete set of twelve wavelengths recommended by the WMO (368 to 1024 nm) and serve to determine the atmospheric aerosol, ozone and water vapor total contents [35].
One-hour averaged AOD measurements at 368, 412, 450, 500, 610, 675, 778, 862 and 1024 nm are considered for this analysis. The AOD detection limit is ~ 4.10^{-3} with a (standard deviation) 1σ of ~10^{-4} at central wavelengths. The AOD retrievals are corrected for Rayleigh molecular contribution and for the possible absorption of gas traces molecules such as NO_2, SO_2, and O_3. The AOD follows an empirical Angstrom relation as shown in Eq. (16)

$$AOD(\lambda) = B\left(\frac{\lambda}{\lambda_0}\right)^{-A} \qquad \text{Eq. (16)}$$

with λ_0 = 500 nm. The coefficient, A (size related) and B (related to turbidity at λ_0) are found from the linear regression between ln(λ) and ln(AOD) or by direct fitting with a power law [35]. The exponent A from in Eq. (16) is considered similar to A_{ext}.

3. Upper troposphere Saharan dust evidence

The SDO occurring over Europe on August 2nd, 2001 was observed between 06:00 and 18:00 by all above-mentioned (2.1, 2.2, 2.3) observational techniques

from the JFJ station (3580m). The period of this study also includes the preceding day, August 1st, 2001, considered as reference for a dust-free situation.

3.1 Local meteorological context

Local meteorological conditions during the two selected days August 1st-2nd, 2001 are plotted for T, RH and Wind (direction/speed) in Figure 1.

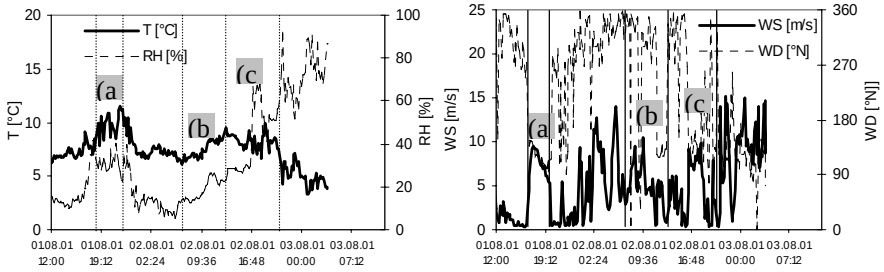

Figure 1 Local meteorological parameters on August 1st to 2nd, 2001: temperature (T) and relative humidity (RH) (left panel) and wind direction and speed (right panel).

On the morning of 1st August 2001, a typical free troposphere situation with low wind (i.e. 2-3 ms^{-1} blowing from N-W), dry air (10-20 % relative humidity), and summer temperatures (~ 5-6 °C) occurred. In the afternoon (16:30), the wind changed direction to S/SE, increased in speed to ~10 ms^{-1} and brought warmer (~10 °C) and more humid air masses (35 - 40%). After sunset (21-22:00), the wind direction changed again to N-W increasing in intensity from 1-2 m s^{-1} at midnight to 15 m s^{-1} in the morning of August 2, 2001. The relative humidity also gradually increased from 10 % in the morning to 30 % in the late afternoon (16:00). The temperature was some ~7-8°C. After 16:00, the wind direction changed to S/SE bringing air masses initially containing small thin clouds, whose thickness progressively increased. Temperature and pressure decreased and rainfall was noticed around 19:00. A hazy sky was observed all morning and afternoon on August 3, 2001. Three different types of meteorological situations are labeled (a), (b) and (c) in Figure 1.

These situations correspond to: (a) August 1, 2001 (13:00-20:00) - a typical summer afternoon with uplifted air masses (from the glacier, from the PBL, and from surrounding valleys) to the JFJ station; (b) August 2, 2001 (06:00-12:30) - unusual hazy atmosphere (i.e. Saharan dust) and (c) August 2, 2001 (13:00-18:00) - mixture of cirrus clouds, moisture, fog and haze.

3.2 Saharan dust patterns on lidar signals

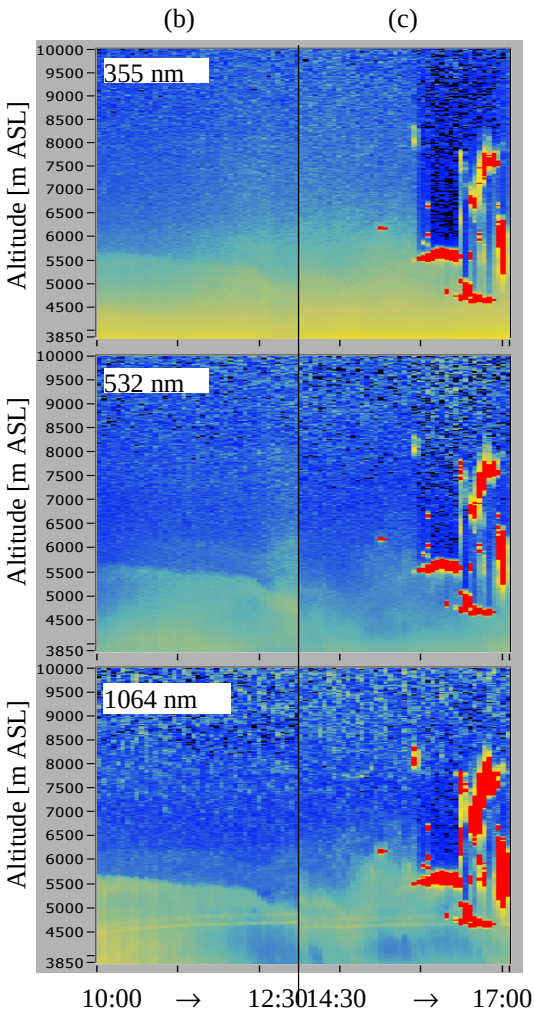

The dust was clearly detected by lidar on the morning and afternoon of August 2, 2001. This is noticed on the lidar RCS signals represented in Figure 1 for 355, 532 and 1064 nm in the morning (10:00 to 12:30, situation (b)) and in the afternoon (14:30 to 17:00, situation (c)). The intensity of RCS is proportional to the aerosols' load. The "blue" corresponds to the upper troposphere background (no aerosol load). The "yellow" to "red" colour scales corresponds to aerosol and cloud load. A homogeneous layer up to 5500-6000 m was lidar-detected during the morning of August 2. Later, in the afternoon (~16:00), it mixed with humid air masses, various cirrus clouds and haze from the valleys. The lidar observations were stopped at ~ 17:00 due to the occurrence of very deep fog, clouds and rainfall latter in the evening.

Figure 2 RCS (a.u.) lidar signal represented as a 2D intensity graph at 355 nm, 532nm and 1064 nm. The X-axis represents the time while the Y-axis is the altitudes in m ASL. The Saharan dust is detected at all three wavelengths. Note (b) is corresponding to the morning 10:00 to 12:30 and (c) to the afternoon 15:45 to 17:00 lidar measurement series. The intensity color bar is increasing from low (blue) to high (red) values.

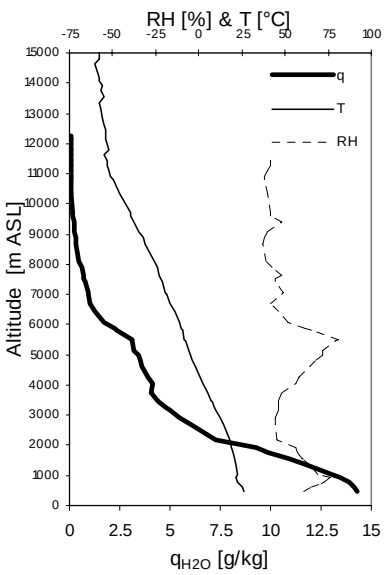

In Figure 3 are plotted the temperature (T), water vapor mixing ratio (q) and relative humidity (RH) profiles obtained from the radiosonde launched at Payerne on August 2, 2001, at 13:00. The q and RH profiles exhibit gradients within an atmospheric layer between ~ 3500 and 5500-6000 m. In the assumption of a homogeneous dust plume above the Swiss plateau and the Alps (~100 km area), this layer may correspond to the dust layer observed by lidar at JFJ station at the same altitude ranges.

Figure 3 Water vapor mixing ratio (q), temperature (T) and relative humidity (RH) (radiosonde 13:00 LT on August 2nd, 2001 at Payerne at 80 km, NW of the JFJ). Data were obtained from Payerne Aerological Station (MeteoSwiss).

3.3 *In situ* Angstrom coefficients and single scattering *albedo*

The *in situ* Angstrom coefficients (A_{ext} and B_{ext}) and the exponent of single scattering *albedo* A_{ssa} determined as described in 2.2, from nephelometer and aehalometer measurements are plotted in Figure 4 for August 1 and 2, 2001.

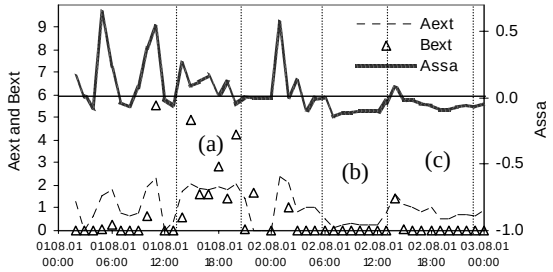

Figure 4 Angstrom coefficients (A_{ext} and B_{ext}) and the exponent of the single scattering albedo *A_{ssa} from* in situ *measurements on 01-02.08.2001. Note the negative values of A_{ssa} during periods (b) and (c). These data were obtained from LAC-PSI laboratory and MeteoSwiss [30].*

The parameter A_{ssa} is positive during period (a) and negative on the (b) and (c) periods. The negative value of A_{ssa} indicates the presence of mineral dust [17]. The wavelength dependency of the extinction is very slight (see the power law fits in Figure 5) during the dust period (b). The value of the Angstrom exponent (A_{ext} ~ 0.26) corresponds to large particle sizes. The A_{ext} value corresponding to the dust-free upper troposphere reference period (a) is ~ 1.85 and those for the

mixture dust-clouds in the afternoon, period (c) is ~ 1. These values correspond to smaller size particles.

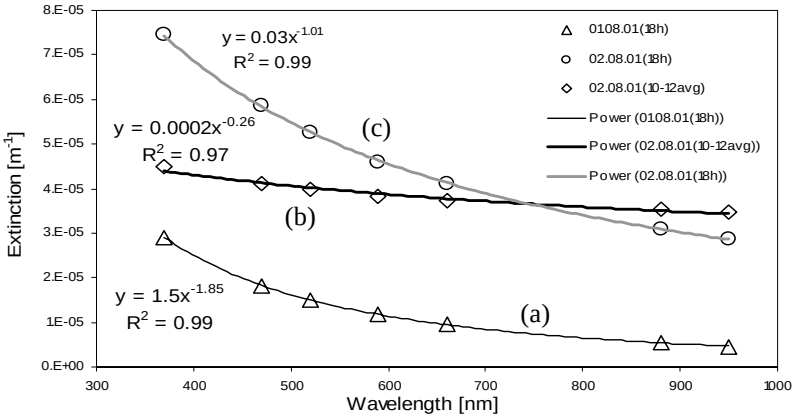

Figure 5 Extinction wavelength dependence for in situ *measurements and the Angstrom power law fits for the periods (a), (b) and (c). Note that for period (b) the Saharan dust extinction was averaged for the lidar measurement correspondent period, between 10:00 and 12:30. These data were obtained from LAC-PSI laboratory and MeteoSwiss [30].*

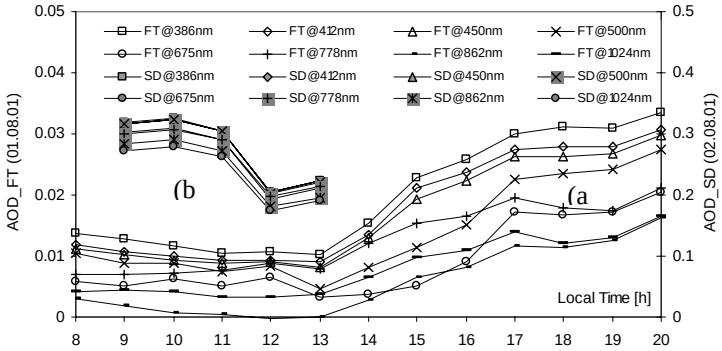

Figure 6 The AOD on 01 and 02.08.2001 from the sun photometer observations at JFJ. Note the AOD of the Saharan dust (SD) is 30 times higher than during free troposphere conditions and 10 times higher than the afternoon PBL air masses intrusions from the valleys. AOD was not available for period (c). Data were obtained from MeteoSwiss.

The Angstrom coefficient B_{ext} ~ 0.002 in the dust period (b) shows very low aerosols number density when compared with ~ 0.03 for period (c) or with ~ 1.5

for the dust-free reference period (a), values which correspond to higher aerosol number density.
The case (a) corresponds to the typical upper troposphere air masses (relatively high amount of small particles) while in the case (b) these values are typical for a pure Saharan dust (small amount of large particles). In the case (c) the situation is more complex due to the mixture of dust, cirrus clouds, haze, and water vapor.

3.4 Sun photometer: AOD and Angstrom coefficients

AODs obtained from the SPM-PFR observations (as described in section 2.3) are shown in Figure 6. The AODs values during the morning of August 2 (dust period b, gray filled symbols) are about 30 - 40 times higher than those of the previous morning (i.e. quasi-free troposphere). They are also 10 times higher when compared with the period of reference (a) for all considered wavelengths (Figure 6). During the dust period (b) the AODs ranges from 0.18 to 0.33. The AOD at 500 nm at 10:00 was ~ 0.32 while the previous morning, in a quasi-dust-free troposphere, this was no larger than ~0.008. Relative to this quasi-aerosol-free tropospheric situation, the attenuation of the total incoming solar radiation due to the dust extinction was ~ 45 - 80 Wm^{-2}.
The average dust extinction (α_{dust} ~ $1x10^{-4}$ m^{-1}) for the incoming radiation at ~550 nm corresponds to an AOD_{550nm} of ~ 0.25 for a ~ 2500 m thick homogeneous dust layer. The approximate value of the meteorological visibility[6] (V_M, cf. [36]) within the homogeneous dust layer may be estimated at ~ 40 km. The calculations of the meteorological visibility V_M for a free troposphere, corresponding to a molecular extinction α_m ~ $1x10^{-5}$ m^{-1} at 550 nm is ~ 400 km.
During the dust period (b) the AOD wavelength dependency was found to be extremely low with a corresponding Angstrom exponent A_{ext} = 0.15 (note the power law fits in Figure 7). This value is smaller (i.e. large size particles) compared with ~ 1.6 (i.e. small size particle -- see Figure 7, curve 01.08.01 at 10:00) or with ~1 for the dust-free reference period (a) (Figure 7, curve 01.08.01 at 18:00).
The A ~ 0.15 from the sun photometer ambient measurements (lower than A_{ext} ~ 0.26 from *in situ* measurements) proves that the ambient particles are larger in size that those measured *in situ*. One may expect that the *in situ* particles are smaller as they are expected to diminish in size by removal of their water content, as they have to pass from ambient air conditions to 10% RH and 25 °C conditions.

[6] $V_{M@550nm}[m] = \frac{3.912}{\alpha_{550nm}[m^{-1}]}$, corresponding to maximum sensitivity of human eye assuming the threshold of contrast sensitivity at 0.02.

This indirectly suggests a possible humidity uptake by the mineral dust from Sahara, which may have a hygroscopic fraction.

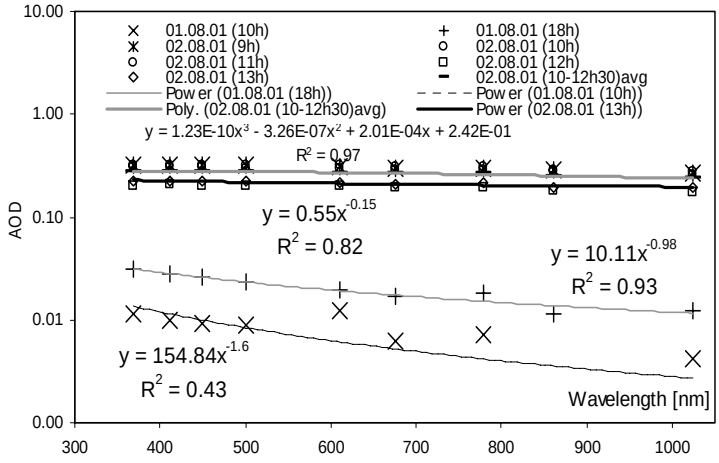

Figure 7 Aerosol optical depth (AOD) during the SDO

The Saharan origin of this above described layer has been demonstrated by the backward calculated trajectories presented in the next section.

4. Backward trajectory analysis

4.1 Calculation procedure

Backward trajectories have often been used to analyze Saharan dust outbreaks [37, 38]. For this study, analyzed wind fields with a temporal separation of six hours were used to calculate three-dimensional kinematic backward trajectories with the software package «Lagranto». The calculations presented here were made at the Air Pollution/Environmental Technology Department from EMPA (Swiss Federal Laboratories for Materials Testing and Research) [39]. The wind fields were provided by the European Center for Medium-Range Weather Forecasts (ECMWF) model with a resolution of 1° × 1°. The trajectories are resolved in 60-minute time steps and their length has been limited to 7 days backward in time. In order to account for transport at different levels but also for inaccuracies, the arrival points have been varied both horizontally and vertically. In the horizontal plane, the accurate location of the JFJ (7.98 ° E, 46.55 ° N) was supplemented by 4 arrival points being displaced by ± 0.5 ° in latitude and ± 0.5 ° in longitude, respectively. In the vertical plane, the levels between 800 hPa and

400 hPa were covered in 25 hPa steps. Although 85 trajectories were calculated, only trajectories indicating paths of air masses potentially contributing to the measured Saharan dust episode are shown in the Figure 8. In order to filter the multitude of possible trajectories, only trajectories located at least one time step within a 20-hPa deep layer over the African continent were taken into account.

4.2 The 2nd August 2001 SDO case

Two main trajectory paths seem to be responsible for the Saharan dust arriving at the JFJ. One path starts over the Mediterranean Sea and propagates during several days southward and then westward over Libya, Tunisia and Algeria. A relatively low-pressure gradient was situated over Northern Africa during this time. The air mass movement was mainly influenced by a weak high-pressure system over the Mediterranean near the Tunisian coast, which resulted in the clockwise trajectory movement during July 26 - 29. The calculated 7-day backward trajectories (Figure 8) show the origin and the movement of air masses during the investigated period.

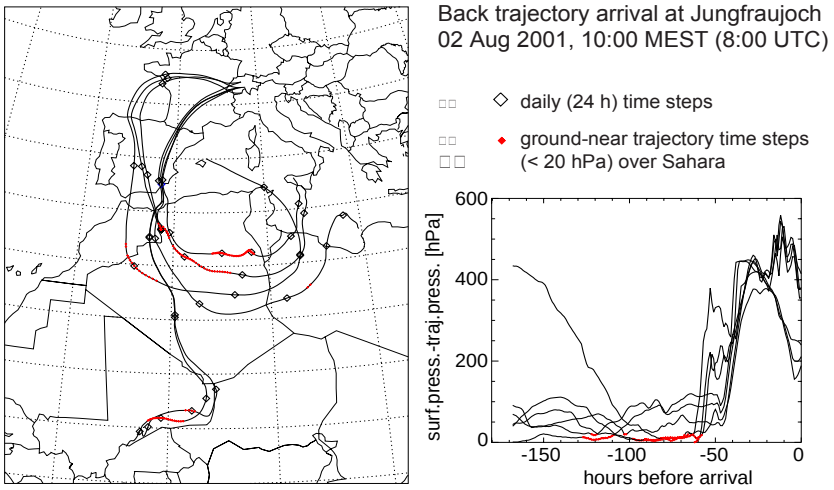

Figure 8. 7-day backward-trajectories arriving at the JFJ on 2nd of August. Note: Represented trajectories are located at least one time step within a 20-hPa deep layer over the African continent.

The other main path indicates trajectories originating further towards the south, over Mali. The trajectory model results show that Saharan dust arriving at the JFJ can originate from an extended region covering Libya, Algeria and Morocco (trajectory path 1) but also from Mali (trajectory path 2). The trajectories originating above Mali indicate a further northward movement of the air masses

before meeting the other trajectories over Algeria and then starting over the Mediterranean Sea. Above Algeria and Morocco, all the trajectories are then suddenly lifted on 31st of July. This can often be seen during Saharan dust events in Switzerland when (cold) fronts propagate from the west and lift the air masses containing Saharan dust [17]. In our case, however, no frontal activity was found during this period over northwestern Africa and southern Europe, where a flat pressure distribution predominated. Another explanation could therefore be the cut-off low that had been developing since July 27th over Western Europe and moving southward during the following days (Figure 9, left).

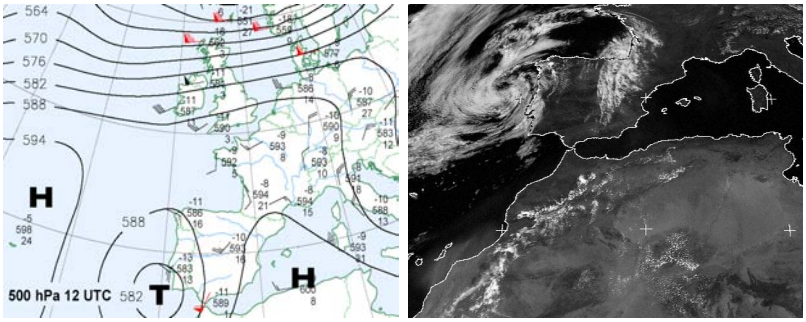

Figure 9 Weather chart (500 hPa) from MeteoSwiss for 30th of August with the cut-off low south-west of the Iberian Peninsula (left) and Meteosat image from 1st of August, at 15:30 LT. Note the cut-off low west of Portugal and the convective activities over the Saharan desert. A dust plume can be seen located between the coast of Africa and the Canary Islands.

This low pressure surely explains the last part of the trajectory movement where the air masses travel in the middle troposphere at altitudes of about 4000 to 6000 m. Once the air masses reached these altitudes in the free troposphere, they were accelerated between the cut-off low situated west of Portugal and a high-pressure system over the Mediterranean Sea. More influenced by the latter, the air turned eastward, subsided again and finally reached JFJ.

The remaining question is how the air masses were lifted from surface levels to the middle troposphere. The clouds in the Meteosat image from 1st of August indicate convection over the north-western part of the Saharan desert, (Figure 9, right). It even seems that strong dust storms were active during this time, with a dust plume over the Canary Islands. Figure 10 shows the aerosol index from TOMS indicating the extended region with convection and dust storms and therefore the potential for Saharan dust upload into the middle troposphere.

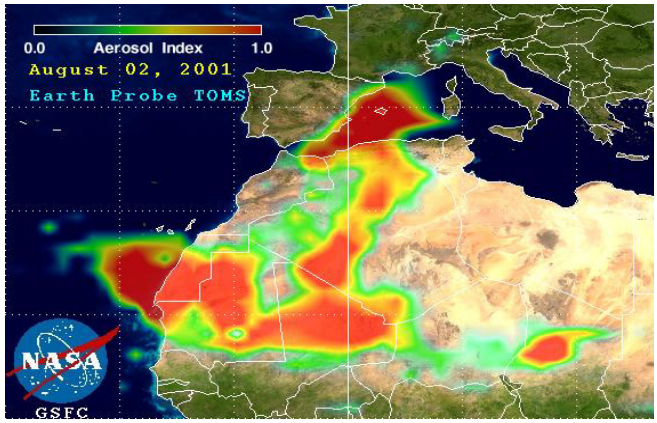

Figure 10 TOMS aerosol index showing the strong dust storm activity over the Saharan desert during the investigated period. The TOMS index is linked to the measurement of differential reflectivity at two UV wavelengths and is proportional to the AOD and to the UV absorption of the aerosols.

The convection over the Saharan desert can be a reason for the uplift of the air masses to the middle troposphere. This uplift is probably stronger over the north-western part of Africa (over north-western Algeria and Morocco) as the cut-off low may additionally contribute to the uplift of the air masses. Trajectory analyses have their limitations concerning the reproduction of complex surface air mass flows. Therefore, a crude approach was used that defined the location of potential sources to be regions in our grid where trajectories travel within a ground distance of 20 hPa. The potential source regions of the Saharan dust are situated in Libya, Algeria, Morocco and Mali.
Finally, the trajectories arrive 2.5 to 5 days later from the potential source regions above Switzerland at a (model) ground distance between 180 and 425 hPa. This range is enlarged because of the fact that not all four arrival points (being horizontally displaced by 0.5°) lie in the same grid as the JFJ having therefore a model ground being situated at another height level. Nevertheless, taking into account the fact that in the 1°× 1° ECMWF model, the JFJ is situated at a height of 877 hPa (8:00 LT), and the adjacent grids are about 930 hPa, we can estimate the air masses to arrive above Switzerland at altitudes between 3000 and 6000 m.

5. Results and Discussions

5.1 *In situ* measurements

The hourly mean of total scatter and backscatter obtained from nephelometer data are presented in Figure 11 for August 1st and 2nd, 2001.

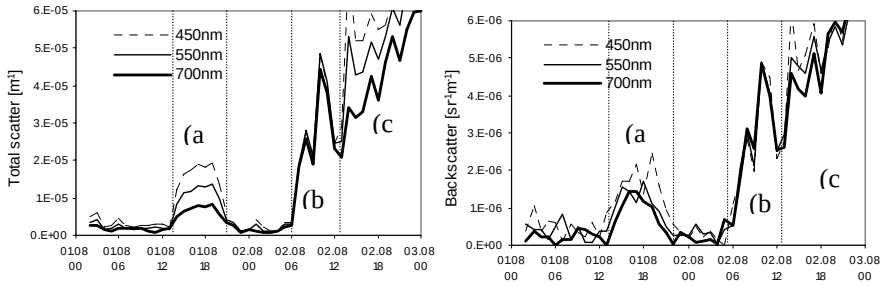

Figure 11 The scattering coefficients (α_a^{scat}) in the left panel and the backscattering coefficients (β_a^{nephel}) in the right panel during August 1st and 2nd, 2001 at the three wavelengths of the nephelometer. Note: β_a^{nephel} is measured under ~ 7-170° while β_a determined from lidar observations is concerning only the unidirectional backscatter light at ~180 °.

In situ backscattering (β^{nephel}) values represent ~ 10% of the total scatter. In the case of Saharan dust (b), the wavelength dependency is very weak. This is not the case for the dust-free reference period (a) and for cloud-haze and dust mixture period (c). The dust total scattering is 4-5 times higher than in the reference case (a) and obviously lower than the scatter measured in the clouds-dust-haze mixture, period (c). The 7-wavelengths inter-extrapolated extinction values are plotted in Figure 12 together with the absorption coefficients.

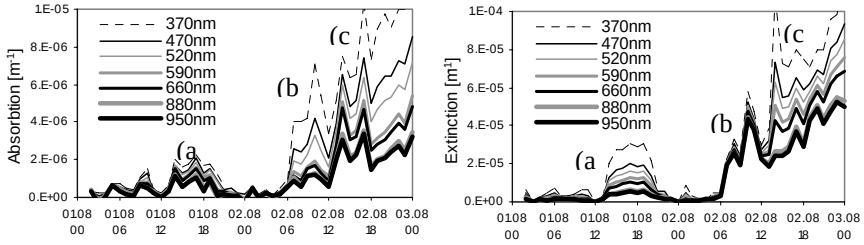

Figure 12 The aethalometer absorption coefficients (α_a^{abs}) in the left panel and the calculated corresponding extinction coefficients (α_a^{ext}) in the right panel at different wavelengths during August 1st and 2nd, 2001.

The dust extinction (~ 5 x 10^{-5} m^{-1}) exhibited almost no wavelength dependency. The slight wavelength dependency is due to the Saharan dust absorption, which remains wavelength dependent. The absorption represents ~ 10% of the total extinction in UV and less than 3-5 % in VIS and NIR.

5.2 Total to molecular backscatter ratio: a lidar-based estimation

The total to molecular backscatter ratio, TMR (Z), is a relative indicator of the aerosols-clouds load compared to a clean molecular atmosphere. Ideally, the best solution is to use the Raman signals as molecular reference. When only the elastic signals are available the ratio (i.e. noted ERR*) of the elastic (E) and a molecular Rayleigh (R) is a good estimator of the TMR. The molecular RCS signal was simulated based on [40] and the molecular reference was set at 9500m ASL.
The ERR* is proposed to be compared at 355 (UV), 532 (VIS) and 1064 (IR) nm for the three situations (a, b, c). The lidar corresponding data series are summarized in Table 1 below.

Start Time	Stop Time	T [C]	RH [%]	P [mb]	ID
01.08.01 16:00	01.08.01 20:00	9	29	670	(a)
02.08.01 10:00	02.08.01 12:30	8	34	669	(b)
02.08.01 14:30	02.08.01 17:00	8	52	668	(c)

Table 1 Lidar selected time series data corresponding to three distinct meteorological situations (a) = free troposphere with influence of valley air masses, (b) = pure Saharan dust (layer 3500-6000m) and (c) = Saharan dust mixed with free troposphere clouds

The simulated Rayleigh [27] and the elastic signals are presented together with the EMR* for periods (a), (b) and (c) at 355, 532 and 1064 nm in Figure 13.

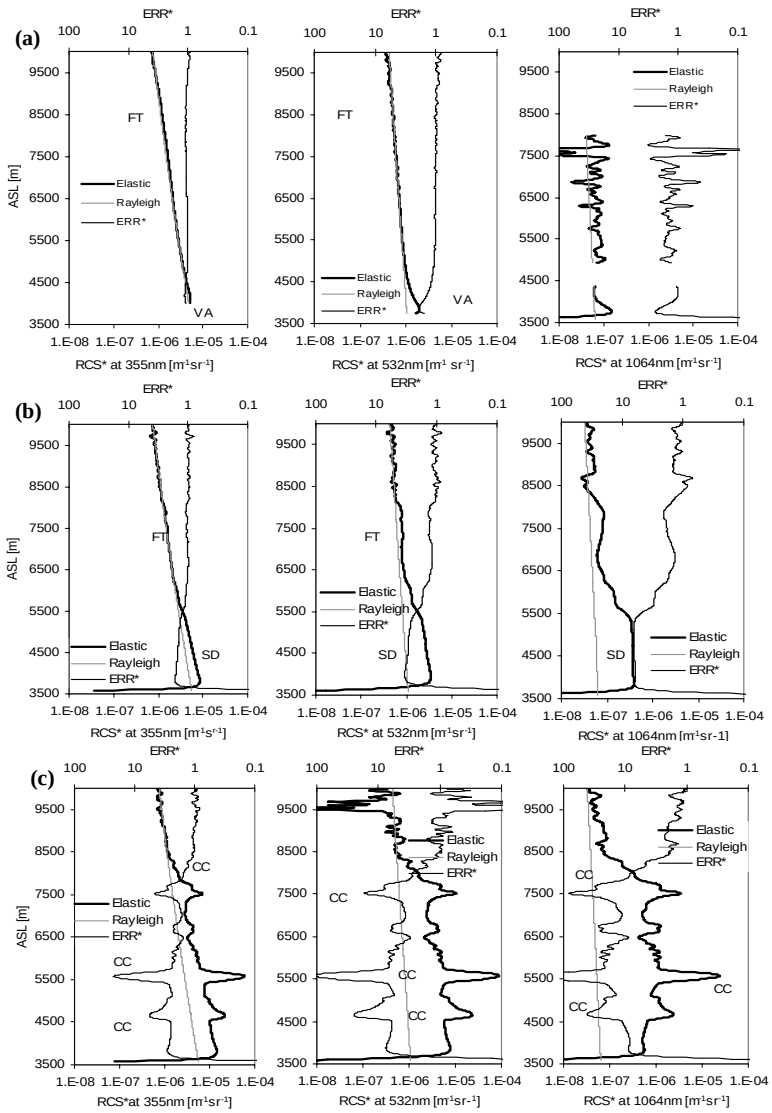

Figure 13 Range corrected signals normalized to the molecular calculated backscatter (RCS) at 9500 m ASL, simulated Rayleigh signals, and elastic to Rayleigh ratio (ERR*) at 355, 532 and 1064 nm during periods (a), (b) and (c). Notes: CC cirrus clouds, VA valley aerosols, SD Saharan dust and FT regions.*

In Table 2, ERR* related parameters are extracted at 4050 m, the lowest valid altitude of the lidar measurements and thus the closest to the in *situ* sampling inlet.

4050m	355 nm			532 nm			1064 nm		
	M	E	EMR*	M	E	EMR*	M	E	EMR*
a	4.74E-6	5.27E-6	1.11	1.01E-6	1.63E-6	1.61	0.061E-6	6.88E-8	1.13
b	**4.74E-6**	**7.50E-6**	**1.58**	**1.01E-6**	**3.39E-6**	**3.34**	**0.061E-6**	**3.75E-7**	**6.15**
c	4.74E-6	1.23E-5	2.58	1.01E-6	6.93E-6	6.84	0.061E-6	5.13E-7	8.42

Table 2 Comparative molecular (M), Elastic (E) and the elastic to molecular (Rayleigh) ratio (EMR or ERR*) during meteorological periods (a), (b) and (c), at 355, 532 and 1064 nm at 4050 m (overlap =1)*

One observes the increase of total to molecular ratio (ERR*) for the Saharan dust from 1.6 (355 nm) to 3.2 (532nm) and to 6.2 (1064nm). In the afternoon (period c), these values are considerably enhanced (see Table 2) which is obviously due to the clouds' contribution.

5.3 Depolarization ratio at 532 nm

Due to their "non-spherical" shape the mineral aerosols are expected to depolarize the laser light. The ratio of the RCS corresponding to perpendicular and parallel polarization states in the backscatter signal at 532 nm was used to estimate the atmospheric depolarization. The calibration constant was determined based on measurements taken in the quasi-free atmospheric situation (morning of August 1, 2001) following the procedure proposed in [29]. In Figure 14, the cross/perpendicular (Depol) and the corrected ratios (Depol_cor) are shown for periods (a), (b) and (c) at 532 nm. The dust (b) exhibits a depolarization of about 10 ~ 12 % (with a maximum at ~ 5000 m) while the fairly clean atmosphere depolarization is about 2-3 % (period a) reaching up to 30 % within the cirrus clouds at ~5700 m during period (c). These depolarization values are comparable with those retrieved for a dust plume over the Atlantic Ocean in a recent work [24] corresponding to 8-day aged Saharan dust with 50-70 % relative humidity. Slightly higher values (15-17 %) were reported for the same 02.08.2001 SDO event based on lidar measurements above Leipzig, Germany [23].
In the case (c), of the clouds-dust-fog mixture, both increasing (positive effect ~ 5580 m) and decreasing (negative effect at ~ 4700 m) in dust depolarization by clouds were noticed. A gradual increase in depolarization within the ice cloud from the bottom (19%) to the top (30 %) is observed. The typical dry dust depolarization is ~ 45 % for hydrophobic dust.

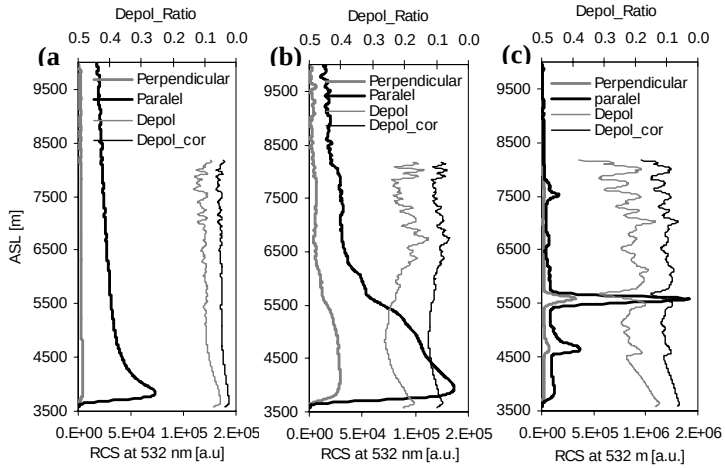

Figure 14 Depolarization ratio (φ) at 532 nm during periods (a), (b) and (c). Dust depolarization is ~10- 12% compared with the unperturbed free troposphere 2-3% or within ice-cold cirrus cloud ~30.

Recent observations [23] suggest that the Saharan dust may get a soluble fraction and in humid conditions (~ 50 % RH) they may condense partially and pass to the liquid phase. This may explain the relatively low ~10-15% depolarization ratio specific to water vapor content particles.

In the next section vertically resolved extinction and the backscatter coefficients will be presented.

5.4 Backscatter - extinction coefficients and lidar ratio

Based on the inversion of elastic lidar signals, dust backscatter (β_d) and extinction (α_d) coefficients were calculated during the dust period (b) for different lidar ratios (LR) ranging from 5 to 100. The data concerned were averaged on whole (b) dust period (between 10:00 and 12:30). The molecular reference was considered at 9500 m for 355a and 532 nm and at 7500 m ASL for 1064 nm. The decrease of the backscatter with an increase in the wavelength is observed. The backscatter sensitivity to lidar ratio, within the dust plume, decreases with wavelength as may be seen in Figure 15. The extinction profile is quite distinct with a clear enhancement at the top of the layer (~5500 m). The extinction at 355 nm exhibits an interesting behavior at low altitudes (~3500 m). In the hypothesis that the radiosounding is representative for the Saharan dust layer, the extinction by lidar and the RH from the balloon are positively correlated. For the 1064 nm channel, the inversion was not possible at higher altitudes due to the strong attenuation of the signal within the dust.

Misalignment could also be responsible for this limitation as it was quite difficult to align the IR beam within the plume dust. Thus backscatter and extinction at 1064 nm have to be taken into account with criticism.
In addition the enhancement of the extinction above 6000 m may be artifacts due to the use of the same constant lidar ratio simultaneously for the dust and the clear sky above.

5.5 Dust AOD: sun photometer and lidar

In order to find an appropriate lidar ratio for the mineral dust the lidar elastic signals were inverted at many lidar ratios to obtain the backscatter and elastic coefficients and after extinction profile integration the AODs from lidar were compared with AOD given by sun photometer instrument.

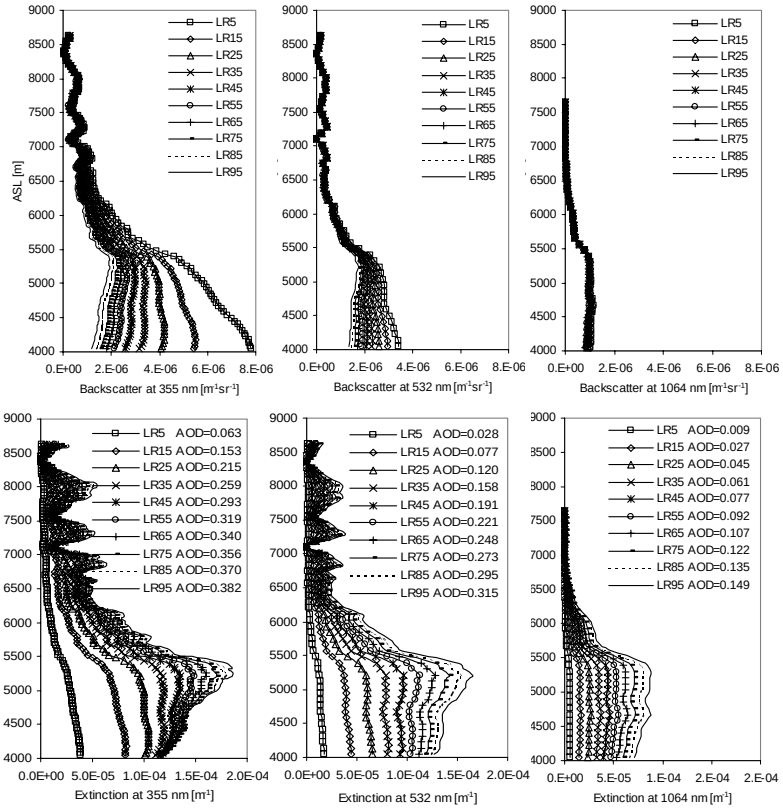

Figure 15 Backscatter (a) and extinction coefficients (b) for the Saharan dust calculated by inverting the 355, 532 and 1064 nm elastic lidar signals at different lidar ratios (5 -100).

An approximate comparison of the AOD of the total atmosphere given by SPM-PFR and by lidar (4000 to 9000 m) is considered. Fundamentally, for non-spherical particles, the forward (sun photometer) scatter function is larger than the backward (lidar) scatter function. Lidar and SPM-PFR AODs are considered comparable in first approximation, on the dust period (b) for two reasons: (i) the optical path of the sun photometer is close to the zenith and (ii) the main contribution to the AOD is due to the fairly homogeneous dust layer.

A realistic lidar ratio (LR) is estimated as the one for which the AOD_{lidar} approaches the $AOD_{SPM\text{-}PFR}$. This approximate estimation of LR is preferable to the use of *a priori* values. First $AOD_{SPM\text{-}PFR}$ (λ) was estimated at the lidar wavelengths from the Angstrom law fits (Figure 7). Then AOD^{7}_{cor} was calculated by adding the equivalent AOD between 3600 and 4100, corresponding to a homogeneous dust layer above the station. This layer contribution is not measured by lidar but integrated by SPM-PFR. The AOD_{lidar}, corresponding to the "clear sky" above 7000 m, was extracted from the AOD_{lidar} in order to avoid the potential artifacts due to an inversion with an inappropriate lidar ratio.

AOD_{lidar} variation with the lidar ratio corresponding separately to dust and clear sky contributions as well as to the corrected AOD_{cor}, at the three-lidar wavelengths, is presented in Figure 16 for the dust period (b).

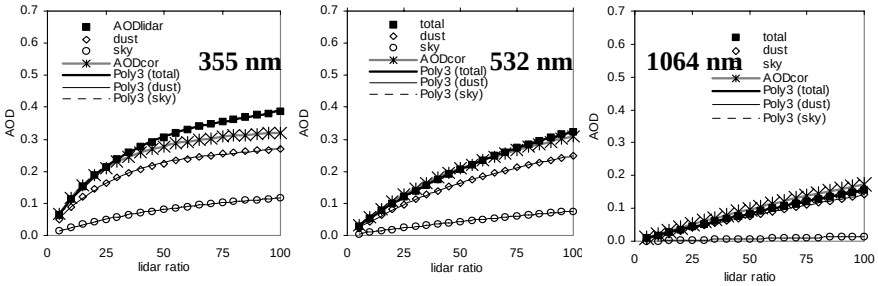

Figure 16 The AOD obtained from the integration of lidar extinction profiles variation with the lidar ratio for 355, 532 and 1064 nm from left to right.

Lidar ratios ~ 40 sr at 355 nm, ~65 sr for 532 nm and ~ 150 sr (probably overestimated) for 1064 nm correspond to (0.26 for 355 nm, 0.25 for 532 nm and 0.23 for 1064 nm) sun-photometer AODs. These relatively high lidar ratios are explained by the enhancement of the extinction values due to the increasing in scattering proper to non-spherical shape particles. In addition the internal absorption (i.e. particularly in UV~10%) or the multiple-scattering processes also contribute to enhance the total extinction [21, 23].

[7] $AOD^{cor}_{lidar} = AOD_{lidar} + (4050 - 3580) \times \alpha_a(4050) - AOD_{sky}$,lidar corrected AOD

5.6 Dust extinction coefficients: *in situ* and lidar

The *in situ* aerosol scattering coefficients corrected for the relative humidity uptake and for truncation errors and the absorption (not corrected by humidity) were summed in order to retrieve the ambient extinction coefficients [41]. The extinctions at the lidar wavelengths were determined based on the power law fit (see Figure 5). These extinction values are: 0.52 x 10^{-4} m^{-1} for 355 nm, 0.47 x 10^{-4} m^{-1} for 532 nm and ~ 0.41 x 10^{-4} m^{-1} for 1064 nm. The extinction at 4050 m, obtained from the lidar, using the lidar radios (deduced in previous section) for the dust period (b) are: 1.15 x 10^{-4} for 355 nm (at LR = 40 sr), 1.16 x 10^{-4} m^{-1} at 532 (at LR = 65 sr) nm and 0.975 x 10^{-5} m^{-1} (at LR =150 sr). The *in situ* values represent only 40-45% of the lidar values. Neglecting the retrieval and statistical errors due to time-space comparison, the major difference may come from the fact that the humidity at 4050 m may be much higher than that measure in *situ*. Differences of ~30 % (at 532 nm) between ambient lidar and in situ measurements due to the dust hygroscopic effect were already reported for mineral dust [23].

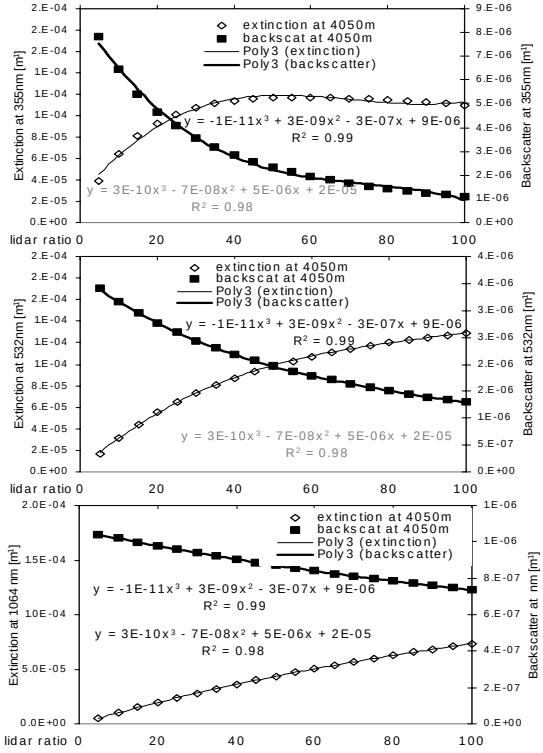

Instead of the expected ambient effect at 8°C, ~20-25% RH, it is probably more accurate to use the one corresponding to 3°C, ~55-60% from radiosounding (on the hypothesis of an homogeneous dust plume over Swiss plateau and the Alps). The increasing humidity within the Saharan dust layer was already observed [24].

Figure 17 Sensitivity of the extinction and backscatter coefficients to the lidar ratio at 4050m within the dust plume at 355, 532 and 1064 nm. In general, 3rd degree polynomials are suitable fits.

5.7 Lidar profile of the Angstrom coefficients

A_{ext} and B_{ext} coefficients were calculated based on Eq. (14) from the lidar extinction profiles at 355 (LR of 40 sr) and 532 (LR of 65 sr) and plotted as shown in Figure 18. In these Angstrom profiles, different layers can be identified: (i) the dust bottom (DB), (ii) the dust core (DC), the dust top (DT) and the upper free of dust troposphere (FT). The DB layer, between 4000 to 4250 m, seems to be composed of an accumulation of coarse particles (A~0.05) in relatively high number concentration (B ~ 8 x 10^{-5}) decreasing in both size and concentration with altitude. The CD layer, between 4250 m and 4800 m, has both smaller concentrations and smaller particles. The DT between 4800 to 5500 m ASL appears to be a peak of a large number of particles with no wavelength dependency (A $\rightarrow$ 0) which might be a combination of fewer large particles of dust situated at the top of the dust plume and sub-visible cirrus clouds formed at the top of the plume due to higher RH and smaller nuclei concentrations. The peak in number concentration is around 5200 m and the radiosounding measured at around this altitude a relative humidity about 70-80%. Above this layer, specific FT values (smaller particles and very low concentrations) may be noticed. The example in Figure 18 shows the potential of a simple high-resolution remote-sensing investigation of a dust plume based on lidar-determined Angstrom coefficients. Uncertainties have to be taken into account related to the approximate retrieval of lidar ratios from the sun photometer and lidar AOD comparisons, the hypothesis of a homogeneous dust layer, and non-consideration of possible multiple backscattering within the dust.

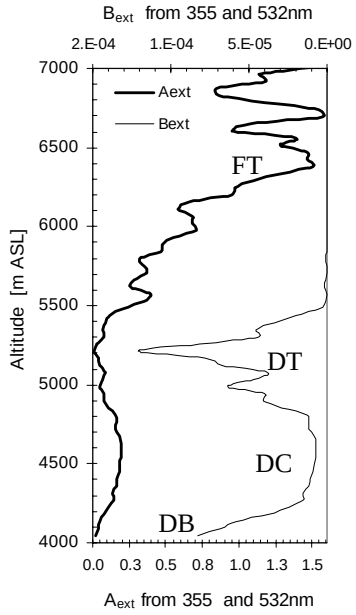

Figure 18 A potential vertical distribution of the Angstrom extinction coefficients determined from lidar measurements at 355 and 532 nm during the SDO, period (b). Note the non-homogeneous vertical structure with regard to the dust size and number concentrations.

These reasons, but also the statistical error sources which may reach 10-20% [25], may explain the differences between the lidar ratios and other similar studies [21, 24]. More precise determinations of the lidar ratio (or the extinction)

from the Raman signals are therefore desirable. For this study the induced noise on Raman channels by the midday strong sunlight does not allow their use.

5.8 Preliminary microphysics calculations

Preliminary calculation of the Saharan dust mycrophysical properties (i.e. number-surface-volume size distribution, single scattering albedo, refractive index) was done based on the hybrid regularization method [42, 43]. The results are presented in Figure 19 and show clearly the presence of a two-mode distribution (i.e. accumulation ~ 0.1 - 0.4 μm and coarse > 1 μm). Although the real part of the refractive index ~1.53 is in good agreement, the imaginary part ~0.02 and the single scattering albedo ~ 0.7 seem to be overestimated compared with the values reported in a reference work [44]. These differences could be partially explained by the fact that the inversion algorithms were run using a hypothesis of spherical particles.

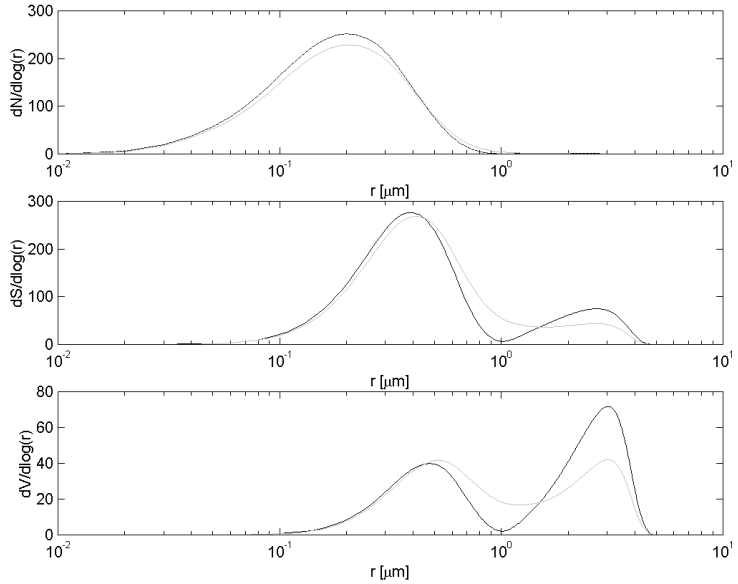

Figure 19 Preliminary results concerning the size and volume distribution for two chosen maximum values for the effective radius (i.e. 5 and 10 μm). Note: The evidence of a small number concentration of large size particles is clearly shown.

6. Conclusions

A dust mineral plume during August 2, 2001 was detected in the upper-troposphere above the Alps (up to ~ 5500- 6000m) based on lidar observations from JFJ. Backward trajectory calculations indicated the Saharan origin and estimated the traveling time of 2.5 to 5 days. Different potential source regions were found to be in Libya, Algeria, Morocco and even Mali. Three lidar data series are compared during different periods: (a) dust-free reference (16:00-20:00 on August 1, 2001), (b) dust (10:00-12:30 on August 2, 2001) and (c) a dust/cloud mixed phase (14:30-17h). Total to molecular ratios (estimated at 4050 m) at 355, 532 and 1064 nm were 1.6 (355), 3.4 (532) and 6.2 (1064), respectively. Dust depolarization ratio at 532 nm of ~ 10-12% proves a relatively wet and partially hydrophilic dust. The *in situ* dust measurements show negative Angstrom exponent of the single scattering *albedo* and high extinction in UV_VIS_NIR (in average up to ~ 5 x 10^{-5} m^{-1}), which is 10 times higher than those of the dust-free reference.
The slight wavelength dependence is mainly due to the absorption contribution (~10% in UV and less than 5% in NIR). The Angstrom coefficients, for *in situ* measurements, indicate low concentrations (B_{dry} = 2 x 10^{-4}) and large particle sizes (A_{dry} = 0.26). Sun photometer AOD measurements range from 0.2 to 0.3 at 500 nm, which are at least 10 times higher than the maximum annual free troposphere value (i.e. 0.03). Lidar backscatter-extinction coefficients show high (7.45 x 10^{-8} $m^{-1}sr^{-1}$ at 355 nm), middle (2.35 x $10^{-8}m^{-1}$ sr^{-1} at 532 nm) and low (0.32 x $10^{-8}m^{-1}sr^{-1}$ at 1064 nm) non-linear sensitivity with the lidar ratio. From comparison of lidar and sun-photometer AODs, the estimation of dust lidar ratios was made (~ 40 sr at 355 nm, ~65 sr at 532 nm and 150 sr at 1064). The huge lidar ratio at 1064 nm may be unrealistic and due to errors in the inversion (e.g. over estimation of the molecular reference). Ambient lidar estimated extinction values at 4050m are about 40-45 % higher than those from *in situ* corrected data. A potential vertical structure related to size-number density, based on the Angstrom coefficients, is discussed. Finally the preliminary calculations of dust microphysics, under the hypothesis of spherical shape of the particles, estimated an effective radius ~1.4μm, an average complex refractive index of 1.5298 + 0.0316i and the *single scattering albedo* of ~ 0.72 for the UV, 0.78 for the VIS and 0.82 for NIR.
More precise and absolute inversion lidar techniques (i.e. based on Raman signals) and better external calibration techniques (i.e. airborne or radio-sounding aerosols devices, or *in situ* ambient measurements) are still needed to confirm these results and to complement them. Possible further applications of this study would consider the influence of the Saharan dust deposition in decreasing the alpine glacier *albedo*, which may contribute to increase the glacier's melting rate.

References

1. IPCC, *Climate Change 2001: The Scientific Basis*. 2001: Cambridge University Press.
2. IPCC, *Climate change 1994*. 1995, Cambridge: Press Syndicate of the University of Cambridge.
3. Tegen, I., A.A. Lacis., and I. Fung, *The influence of mineral aerosols from disturbed soils onthe global radiation budget.* Nature, 1996. **380**: p. 419-422.
4. Toon, O.B., *African dust in Florida clouds.* Nature, 2003. **424**: p. 623-624.
5. Moreno, A., I. Cacho, M. Canals, M.A. Prins, M.F. Sanchez-Goni, J.O. Grimalt, and G.J. Weltje, *Saharan dust transport and high-latitude glacial climatic variability: The Alboran Sea record.* Quaternary Research, 2002. **58**(3): p. 318-328.
6. Marticorena, B. and G. Bergametti, *Two-year simulations of seasonal and interannual changes of the Saharan dust emissions.* Geophysical Research Letters, 1996. **23**(15): p. 1921-1924.
7. Sokolik, I.N., *Nuts and bolts of radiative forcing by mineral dust.* IGAC Newsletter, 1999.
8. Tanre, D., Y.J. Kaufman, B.N. Holben, B. Chatenet, A. Karnieli, F. Lavenu, L. Blarel, O. Dubovik, L.A. Remer, and A. Smirnov, *Climatology of dust aerosol size distribution and optical properties derived from remotely sensed data in the solar spectrum.* Journal of Geophysical Research-Atmospheres, 2001. **106**(D16): p. 18205-18217.
9. Penner, J.E., J.E. Lister, D.J. Griggs, D.J. Dokken, and M. McFarland, eds. *Aviation and the Global Atmosphere: Intergovernmental Panel on Climate Change (IPCC).* 1999, Cambridge University Press. 373.
10. Houghton, J.T., Y. Ding, D.J. Griggs, M. Noguer, P.J. van der Linden, and D. Xiaosu, *Climate Change 2001: The Scientific Basis: Contribution of Working Group I to the Third Assessment Report of the Intergovernmental Panel on Climate Change (IPCC).* 2001, Cambridge University Press, UK. p. 944.
11. Murayama, T., H. Okamoto, N. Kaneyasu, H. Kamataki, and K. Miura, *Application of lidar depolarization measurement in the atmospheric boundary layer: Effects of dust and sea-salt particles.* Journal of Geophysical Research-Atmospheres, 1999. **104**(D24): p. 31781-31792.
12. McNeil, W.R., and Carswell, A. I., *Lidar polarization studies of the troposphere.* Applied Optics, 1975. **14**(9): p. 2158-2168.
13. Charlson, R.J., and Heintzenberg, J. (Eds.), *Aerosol forcing of climate.* Dahlem Workshop Reports, ed. R.J. Charlson, and Heintzenberg, J. Vol. Environmental Sciences Research Report 17. 1995, New-York: John Wiley & Sons, Ltd.
14. Angström, A., *On the atmospheric transmission of sun radiation and on dust in the atmosphere.* Geogr. Ann., 1929. **11**: p. 156-166.
15. Finlayson-Pitts, B.J. and J.N.J. Pitts, *Atmospheric Chemistry : Fundamentals and Experimental Techniques*. 1986: Wiley Interscience. 1098.
16. Seinfeld, J.H. and S.N. Pandis, *Atmospheric Chemistry and Physics*, ed. J.W.S. ed. 1998: Wiley Interscience. 1326.
17. Collaud Coen, M., E. Weingartner, D. Schaub, C. Hueglin, C. Corrigan, M. Schwikowski, and U. Baltensperger, *Saharan Dust Events at the Jungfraujoch: Detection by wavelength dependence of the single scattering albedo and analysis of the events during the years 2001 and 2002.* Atmospheric Chemistry and Physics Discussions, 2003.

18. Nickovic, S.G.K., A. Papadopoulos, and O. Kakaliagou, *A model for prediction of desert dust cycle in the atmosphere*. Journal of Geophysical Research-Atmospheres, 2001:. **106**: p. 18113-18130.
19. Bösenberg, J., and al., *EARLINET: A European Aerosol Research Lidar Network*. Advances in Laser Remote Sensing, ed. J. Pelon, Loth, C., Dabas, A. 2001, Palaiseau: Editions de l'Ecole polytechnique.
20. Papayannis, A. and a. et, *Continental-scale vertical profile measurements of free tropospheric Saharan dust particles performed by a coordinated ground-based European Aerosol Research Lidar Network (EARLINET project).* To be submitted to Atmospheric Physics and Chemistry (October 2003), to be submitted.
21. Mattis, I., A. Ansmann, D. Muller, U. Wandinger, and D. Althausen, *Dual-wavelength Raman lidar observations of the extinction-to-backscatter ratio of Saharan dust*. Geophysical Research Letters, 2002. **29**(9): p. art. no.-1306.
22. Muller, D., I. Mattis, U. Wandinger, A. Ansmann, D. Althausen, O. Dubovik, S. Eckhardt, and A. Stohl, *Saharan dust over a central European EARLINET-AERONET site: Combined observations with Raman lidar and Sun photometer*. Journal of Geophysical Research-Atmospheres, 2003. **108**(D12): p. art. no.-4345.
23. Gobbi, G.P., F. Barnaba, v.R. Dingenen, J.P. Putaud, M. Mircea, and M.C. Facchini, *Lidar and in situ observations of continental and Saharan aersol: closure analysis of particles optical and physical properties*. Atmospheric Chemistry and Physics Discussions, 2003. **3**: p. 445-477.
24. Immler, F. and O. Schrems, *Vertical profiles, optical and microphysical properties of Saharan dust layers determined by a ship-borne lidar*. Atmospheric Chemistry and Physics Discussions, 2003. **3**: p. 2707-2737.
25. Larcheveque, G., I. Balin, R. Nessler, P. Quaglia, V. Simeonov, H. van den Bergh, and B. Calpini, *Development of a multiwavelength aerosol and water-vapor lidar at the Jungfraujoch Alpine Station (3580 m above sea level) in Switzerland.* Applied Optics, 2002. **41**(15): p. 2781-2790.
26. Larcheveque, G., *Development of the Junfraujoch multi-wavelenght lidar system for continous observations of the aerosols optical properties in the free troposphere*, in *Environmental and Engineering Dpt.* 2002, EPFL: Lausanne.
27. Collis, R.T.H. and P.B. Russell, *Lidar Measurement of Particles and Gases by Elastic Backscattering and Differential Absorption*. Laser Monitoring of the Atmosphere, ed. E.D. Hinkley. 1976: Springer Verlag.
28. NOAA, NASA, and USAF, *U.S. standard atmosphere (76)*. 1976, U.S. government Printing Office: Washington / USA.
29. Biele, J., G. Beyerle, and G. Baumgarten, *Polarization lidar: Corrections of instrumental effects*. Optics Express, 2000. **7**(12): p. 427-435.
30. PSI-GAW, *In situ aerosols monitoring at Jungfraujoch station*. 2004, PSI-LAC.
31. Weingartner, E., Nyeki, S., and Baltensperger, U., *Seasonal and diurnal variation of aerosol size distributions (10<D<750nm) at a high-alpine site (Jungfraujoch 3580m asl).* Journal of Geophysical Research-Atmospheres, 1999. **104**(21): p. 26809-26820.
32. Weingartner, E., H. Saathof, M. Schnaiter, N. Streit, B. Bitnar, and U. Baltensperger, *Absorption of light by soot particles: Determination of the absorption coefficient by means of Aethalometers*. Journal of Aerosol Science, 2003: p. in press.
33. Schmid, B., Spyak, P. R. , S.F. Biggar, C. Wehrli, J. Sekler, T. Ingold, C. Matzler, and N. Kampfer, *Evaluation of the applicability of solar and lamp radiometric calibrations of a precison Sun photometer operating between 300 and 1025 nm.* Applied Optics, 1998. **37**(3923-3941).

34. Schmid, B. and C. Wehrli, *Comparison of Sun photometer calibration by Langley technique and standard lamp.* Applied Optics, 1995. **34**: p. 4500-4512.
35. Ingold, T., C. Matzler, N. Kampfer, and A. Heimo, *Aerosol optical depth measurements by means of a Sun photometer network in Switzerland.* Journal of Geophysical Research-Atmospheres, 2001. **106**(D21): p. 27537-27554.
36. Hinkley, E.D., *Laser Monitoring of the Atmosphere*. Topics in Applied Physics, ed. E.D. Hinkley. Vol. 14. 1976: Springer-Verlag.
37. Schwikowski, M., P. Seibert, U. Baltensperger, and H.W. Gaggeler, *A Study of an Outstanding Saharan Dust Event at the High-Alpine Site Jungfraujoch, Switzerland.* Atmospheric Environment, 1995. **29**(15): p. 1829-1842.
38. Chiapello, I., G. Bergametti, B. Chatenet, P. Bousquet, F. Dulac, and E. Santos Soares, *Origins of African dust transported over the northeastern tropical Atlantic.* Journal of Geophysical Research-Atmospheres, 1997. **102**: p. 13701-13709.
39. Wernli, H. and H.C. Davies, *A Lagrangian-based analysis of extratropical cyclones. 1. The method and some applications.* Journal of the Royal Meteorological Society, 1997. **123(538)**: p. 467-489.
40. Russell, P.B., Swissler, T. J., and McCormick, M. P., *Methodoloy for error analysis and simulation of lidar aerosol measurements.* Applied Optics, 1979. **18**(22): p. 3783-3797.
41. Nessler, R., N. Bukowiecki, S. Henning, E. Weingartner, B. Calpini, and U. Baltensperger, *Simultaneous dry and ambient measurements of aerosol size distributions at the Jungfraujoch.* Tellus Series B-Chemical and Physical Meteorology, 2003. **55**(3): p. 808-819.
42. Bockmann, C., *Hybrid regularization method for the ill-posed inversion of multiwavelength lidar data in the retrieval of aerosol size distributions.* Applied Optics, 2001. **40**(9): p. 1329-1342.
43. Mironova, I., C. Bockmann, and R. Nessler. *Microphysical Parameters from 3-Wavelength Raman Lidar*. in *ILRC*. 2002. Quebec: R&D Defence Library Services.
44. Dubovik, O., B. Holben, F.E. Eck, A. Smirnov, Y.J. Kaufman, M.D. King, D. Tanre, and I. Slutsker, *Variability of absorbtion and optical properties of key aerosol types observed worldwide locations.* Journal of the Atmospheric Sciences, 2002. **59**: p. 590.

Chapter VII

High PBL convection related observations

The Planetary Boundary Layer (PBL) has a complex temporal and spatial evolution that depends on topography and meteorological conditions. PBL generally develops below high alpine areas covered by glaciers. A particular event was observed at the beginning of August 2003 when the PBL developed at high elevations, well over the peaks of the Swiss Alps. This chapter reports lidar and ultrasonic anemometer[1] measurements along with complementary regional radiosoundings, meteorological, hydrological or in situ aerosol observations related to this extreme meteorological event. Aerosols backscattering measurements, water vapor mixing ratio, wind field and temperature observations are presented during the August heat-wave period. These observations reveal an unusually high elevation of the PBL height (~ 5000 m) at daytime, followed by a persistent and relatively warm (~ 6° C) and wet (40-70 % RH) nighttime residual layer (RL) above the Swiss Alps. This strong convection was a continental scale phenomenon and it was observed under a persistent (i.e. 1 to 15 August 2003) anticyclonic regime over Western Europe, assimilated with a strong heatwave.

[1] In collaboration with the Johns Hopkins University (Team of Prof. M. Parlange)

1. Introduction

The planetary boundary layer (PBL) is the lowest layer of the atmosphere directly influenced by processes at the Earth surface. Important meteorological processes, such as evaporation, rainfall, snowfall, and low cloud formation are taken place in the PBL. The transport and transformation of pollutants, and chemical (i.e. photochemical ozone formation) processes occur also within the PBL [1]. The PBL average daytime height and its growth rate are highly variable and dependent on geographical location, time of the day, daily weather conditions and season. In many cases the PBL top is not well defined [2].
The layer above the PBL up to the tropopause is the free troposphere (FT). Intense mixing between the FT and PBL occurs during the diurnal rise and fall of the boundary layer. The interface between the PBL and the FT is defined by a strong, net temperature inversion. The altitude of this inversion increases from the ocean/sea border (lowest PBL height) up to 3 - 4 km over continental complex topography. Radiative heating and frictional forces at the Earth surface produce a well-mixed layer (ML) within the PBL. A residual layer (RL) may form in nighttime at high altitudes as a consequence of the fast decrease of the ML. Thus the ML during nighttime becomes a stable boundary layer (SBL) whose height doesn't exceed some hundred meters.
The physical and chemical properties of the PBL are determined by: thermal diurnal cycle, convective turbulent updrafts, moisture convection (clouds), orographic transport (i.e. valley-mountains thermal and hill slope winds), strong nocturnal low altitude inversions, nocturnal jets and even tropopause folding.
The PBL-FT dynamics are of major importance for the air pollution studies. The RL is a "reservoir" layer, which may contain ozone, ozone precursors, aerosols, and small clouds that will thermodynamically join the ML the next day. Thus, the RL contributes at the progressive increase in time of pollutant concentrations (e.g. ozone) in a stable anticyclone regime. This process stops when the regime changes (i.e. precipitations, fronts, changes in cloud cover, fog). Strong updrafts may break the inversion between the free troposphere and the PBL. When the inversion breaks, ozone and its precursors, stored in the RL during the night, mix into the PBL air [3]. Orographic forcing can also break through the PBL-FT inversion increasing the mountain ozone concentration in summer or bringing FT air into the valleys and decreasing the ozone concentration in winter [4]. In this sense the simultaneous consideration of the PBL evolution with the air pollutant measurements and model calculations is necessary to estimate the photochemical potential of a given region [5].
These complex effects of the planetary boundary layer dynamics and PBL - FT interaction are still difficult to reproduce in photochemical regional models, particularly over mountains regions. Typically the PBL mixing rate can affect the reaction rates due to the extension or confinement of the reaction space

scale. Many air pollutants models still assume that the PBL height is a constant value while for other models, significant differences (200 m at night, and 500 m during the day) between observed and modeled PBL heights are found [6]. Therefore more PBL - FT measurements over complex terrain are required. They are related to: (a) the definition of the representative chemical and physical PBL "tracers", (b) the choice of appropriate measurements techniques, and (c) the realization of experiments in various locations and meteorological situations.
The most common PBL tracers are the strong negative gradients of the water vapor mixing ratio (q_{H2O}) and the inversion in the virtual potential temperature (θv)[2] profiles [2]. The aerosol load and occasionally the presence of clouds at the PBL top may also be used as physical tracers.
This chapter concerns observations related to the tracking of the PBL air mass intrusions into the upper troposphere regions. In this aim, lidar ultrasonic anemometers, radiosoundings, glacier discharge, and aerosol *in situ* measurements have been considered. The experimental data sources considered for the analysis are presented in section 2.
In section 3, lidar and ultrasonic anemometers results are presented and discussed taking into account the local and regional meteorological context, the regional radiosonding, the discharge at the outlet of the Aletsch glacier catchment and in situ aerosols measurements. A brief conclusion will summarize this study in section 4.

2. Experimental data

JFJ-LIDAR vertical and horizontal observations were taken simultaneously with measurements of temperature and the three-components of the wind velocity vector from ultrasonic anemometers[3] on the glacier surface between April to August 2003. The relative positioning of the two instruments is schematically shown in Figure 1.

This experiment may be placed within the frame of mountain weather, climate, high alpine glaciers sensitivity and free troposphere dynamics- related topics [7]. High elevation "incursions" from the PBL can be quantified by measuring the atmospheric aerosols, water vapor and turbulence [8, 9].

---

[2] $\theta_v(Z) = T_v\left(\frac{P_0}{P(z)}\right)^k ; T_v(Z) = T(Z)[1+0.61q(Z)]; k = R_d\left[1-0.23q(z)/C_{pd}\right]$ where T is the air temperature, T_v is the virtual temperature, R_d is the gas constant and C_{pd} is the specific heat for dry air, q is the specific humidity, P the air pressure, P_0 the standard pressure.

[3] Realized in collaboration with Prof. M. Parlange team from Johns Hopkins University

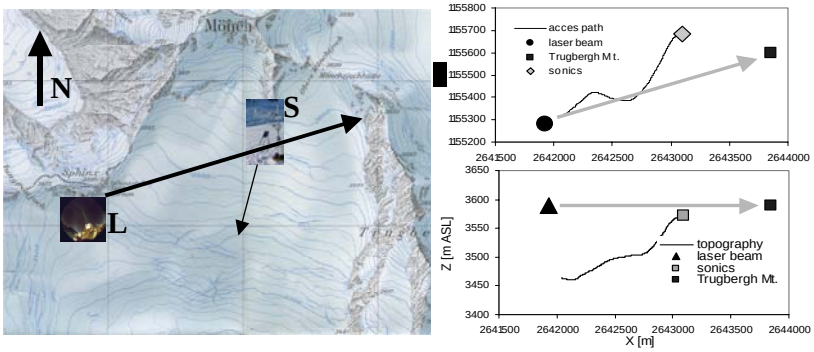

Figure 1 Relative locations of lidar (L) and sonics (S) instruments. The X and Y are the Swiss coordinates units. Note that North direction N, sonics orientations and the laser beam direction are represented by arrows). The lidar beam path is about 2000 m lengths and is passing at the same altitude, 200-300 m to the right of the ultrasonic anemometers.

The JFJ station is situated above the PBL excepting few days in summer time. The combination lidar-sonics measurements offers two important information: (i) lidar → PBL height and its spatial-temporal evolution together with the water vapor content and aerosols optical properties, (ii) ultrasonic anemometers → turbulence parameters at glacier surface with high temporal resolution (necessary for Eddy calculations).

2.1 Lidar setup

The lidar measurements were performed with the JFJ-LIDAR on the configuration presented in the chapter II - section 3.1. The system was operating in ON axis configuration with laser energies 300-350 mJ and 50-80 Hz repetition rates. The overlap was reached at 200-250 m distance from the station. The horizontal measurements were obtained using steering mirror assuring both horizontal emission and detection.
Aerosols backscattering at 532 nm and the water vapor mixing ratio are the main lidar measurements used here. The range corrected signal (RCS)[4] is used for tracking the atmospheric aerosol load. The night time water vapor mixing ratio (q_{H2O}) was derived as explained in chapter IV and [10].

[4] $RCS(z) = S(z) \times z^2$; S(z) is the lidar detected signal due to the light backscattered from the altitude z

2.2 Ultrasonic anemometers

Four sonic anemometers were installed on the Aletsch glacier as presented in Figure 1 in order to obtain high spatial and temporal resolution measurements of the three orthogonal component wind velocity vector (U, V, W) and of the sound speed (C) from which the temperature may be retrieved/found[5]. The principle of these measurements is based on the fact that the velocity of an acoustic pulse in air can be either augmented or impeded by the velocity of the air itself. Measuring the transit time of two opposite acoustic pulses between the emission and reception antennas, the wind speed along the line of sight of two antennas is determined. A precise description of the principles of the sonic anemometer can be found in [11]. In this experiment we used CSAT3 3-D sonic anemometers from Campbell Scientific Inc.'s model CSAT3 3-D (10 cm path, pulsed acoustic mode, output maximum rate of 60 Hz) that can measure winds < 30 m/s and have an error of < 0.04 m/s for the horizontal wind components and < 0.02 m/s for the vertical speed.
The anemometers array was oriented vertically with a 0.5 m vertical separation between each anemometer. The lowest sonic was located 0.6 m above the snow. A solar panel setup assured the autonomy of the system. The reference direction (Sonic arms) was oriented to South - South West. The temperature (T) and wind field (U, V and W) were *in situ* internally calibrated and directly recorded on an acquisition card. Data were stored with a 10 min average time step and at 20 Hz time resolutions. Only the 10 min data at 2.50 m above the glacier surface are considered here. The ultrasonic anemometers technical specifications may be consulted in Annex A32.

2.3 Complementary measurements

2.3.1 Regional radiosoundings

Water vapor mixing ratio, virtual potential temperature and ozone profiles have been obtained from radiosonde data. A typical radiosonde (SRS400 [12]) is launched generally at midday and midnight from Payerne station (490 m, at ~ 80 km North-West from Jungfraujoch). A typical sonde is equipped with Copper-Constantan thermocouple for measuring the temperature, a carbon-cellulose hygristor for the humidity and, three times a week, with a unit ozone detection based on electrochemical concentration cells (ECCs) method. The data used in this analysis were obtained from Payerne - SwissMeteo station. Additional radiosonding data from Lyon, Stuttgart and Milano were considered.

[5] $C = \sqrt{\gamma RT / M}$, with γ the adiabatic constant, R the gas universal constant and M air molecular weight

2.3.2 Meteorology

The meteorological station, at Jungfraujoch, provided a complete set of meteorological parameters: temperature, pressure, wind, solar radiation, and humidity.
The synoptic consideration was taken into account via synoptic maps and satellites images obtained from SwissMeteo (Payerne)

2.3.3 Glacier catchment discharge

The glacier related discharge was obtained at Blatten bei Naters, from a hydrometric gage on Massa River, situated at the outlet of the Aletsch glacier catchment, a hydrological station belonging to Swiss Federal Office for Water and Geology.

2.3.4 *In situ* aerosol measurements

Number density, scattering and absorption coefficients of the *in situ* (at 10 %RH, 25°C) aerosol properties (as described in chapter VI section 3.3) have been obtained. Data used are from the Laboratory of Atmospheric Chemistry (Paul Scherer Institute-Villigen-CH).

3. Results and Discussions

Between 17 April 2003 and 11 August 2003, series of lidar and sonic measurements were obtained. Three different situations of PBL height have been investigated: (a) lower, (b) medium and (c) higher, relative to the altitude of the Jungfraujoch station (3580 m). Accordingly lidar data series were considered (Table 1).

#	Start Time	Stop Time	T [C]	RH [%]	P [mb]	ID
1	17.04.03 23:03	17.04.03 0:20	-5.6	23	661	**B1**
2	18.04.03 11:30	18.04.03113 :30	-8.8	23	653	**A1**
3	04.08.03 12:20	04.08.02 18:00	8.9	70	674	**A2**
4	05.08.03 01:00	05.08.02 02:00	6.6	86	674	**B2**
5	09.08.03 12:30	09.08.02 15:30	6.3	70	671	**A3**
6	10.08.03 01:00	10.08.02 02:00	6.2	39	671	**B3**

Table 1 LIDAR selected data series and the corresponding averages of temperature, the relative humidity and pressure at the station. The identification (ID) notations are: A = day and B = night time, 1 = PBL < 3600m, 2 = PBL ~ 3600-4000m and 3 = PBL > 4000m

The reference data (1) from 17-18.04.2003 are typical for a free troposphere situation at 3600 m while the series (2) 1 - 5.08.03, and (3) 6 - 11.08.03 were selected during a persistent anticyclonic regime period.

3.1 Meteorological context

During the experiment period many anticyclonic regimes occurred but the most intense with unusual meteorological values was observed from 1 to 15.08.2003. In this period a stationary meteorological regime (Azores anticyclone) persisted over Western Europe. This high-pressure regime conducted to the interruption of the normal currents over Europe between 1 and 12 August 2003 Figure 2, a and b).
An historical heatwave was noticed at the continental scale in this period.

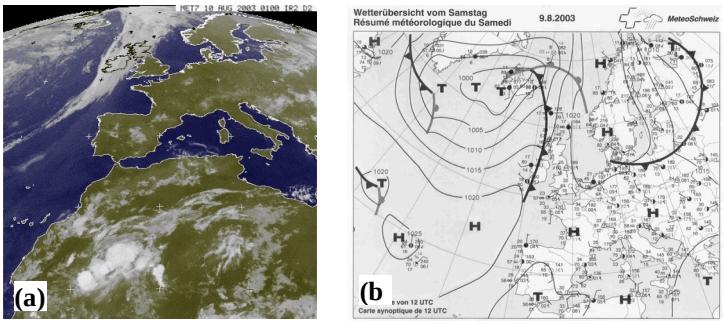

Figure 2 Representative day-by-day "frozen" picture for the first decade of the August 2003 from the METEOSAT Infrared channel on 10.08.2003 at 01:00 (a) and a synoptic map (from MeteoSwiss) showing the extension of the Azores anticyclone over Western Europe (b).

The local meteorology recorded at the Jungfraujoch observatory (Figure 3) shows unusually high pressure, temperature, moisture and weak winds field. Higher pressure (+10 mbar) and higher temperatures (+ 4 °C) were noticed compared to those observed during the hottest anticyclone regime in July 2003 (665 mbar, 3°C). The average wind speed was low (2.5 m/s) with peaks of 5-6 m/s blowing mainly from the North direction. Before sunset and sunrise the wind direction was generally turned to South with an average speed of 1-2 m/s (Figure 3, b). High solar short-wave incoming radiation (1050 W/m^2) occurred during the whole period. The first sub-period was clearly wetter, (i.e. 70 -100% RH) than the second (i.e. 30-50% RH) while the air average temperature was the same (6-7 °C) for both sub-periods (Figure 3, c).

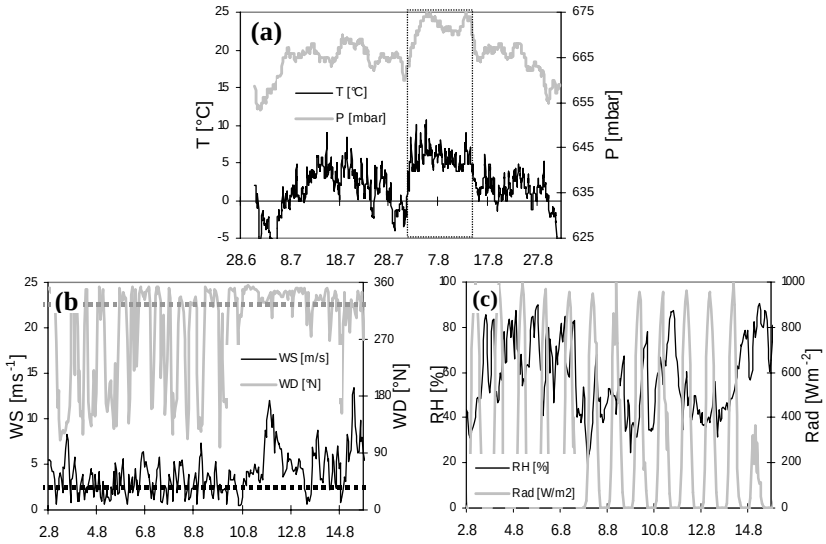

Figure 3 Meteorological parameters at the Jungfraujoch station. Temperature (T) and Pressure (P) are shown for July and August (a). Wind speed (WS), wind direction (WD) in (b) relative humidity (RH) and incoming total solar radiation (Rad) in (c) are plotted only from 02 to 15.08.2003, corresponding to the rectangle from (a).

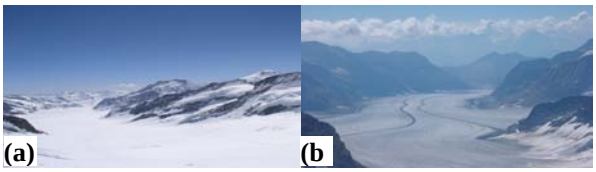

Figure 4 The Aletsch glacier: autumn-winter spring typical view (a) and in August 2003 (b). Note the huge difference in snow cover and melting processes as well as the possible PBL top indicated by the cirrus altitude.

The daily temperature amplitude of 7°C in the first half of the period decreased to only a 2-3 °C in the second half. There was not precipitation during the study period. In Figure 4 two pictures representing the glacier in winter-spring-autumn time and during August 2003 heat wave are shown comparatively.

3.2 Aerosols tracing of PBL and RL

As the lidar corrected signals (RCS) are direct proportional to the atmospheric attenuated aerosols backscatter light, the representation of the RCS in a 2D intensity graph (Figure 5) at 532 nm allows us to appreciate the vertical distribution and the time evolution of the aerosols layers. The reference situations AB1 are aerosols, clouds-free. The situations A2 and B2 show several well-identified (yellow colors on the blue background) aerosols layers. Their height increased during the day (A2) reaching 4000 m at midday and 4300 - 4400 m in the late afternoon (18:00 LT).

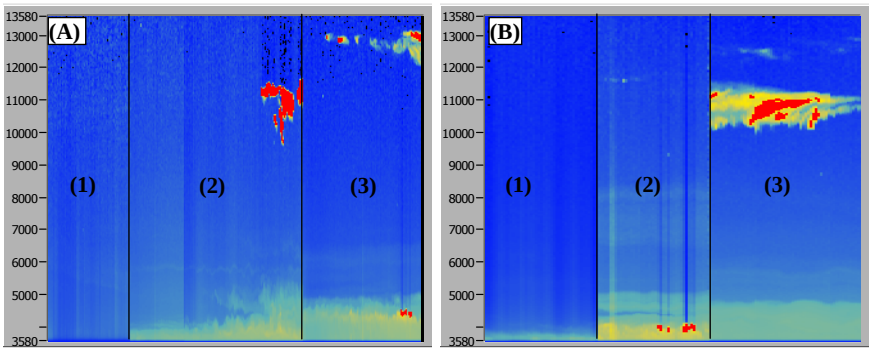

Figure 5 LIDAR range corrected signals intensity (RCS) at 532 nm tracing the aerosols above Jungfraujoch observatory during day (A) and night (B) time in three distinctive meteorological situations: (1) PBL < 3600 m, (2) PBL ~ 3600-4000 m, and (3) PBL > 4000 m. The color scale varies from blue (lowest RCS intensities for a free troposphere sky) passing through yellow (RCS medium intensities due to the aerosols layers) to read (high intensities of the RCS due to the cirrus cloud backscattered light).

A layer persists during the night (B2) at high altitude (~ 4000 m). In the B2 case, a secondary higher layer was noticed. Even more complex layer structures have been identified in nighttime during this heatwave period. In the cases A3 and B3, the altitude of the daytime layer increases at 4500 - 4750 m (A3). A residual layer is persisting over the night at ~ 4700 - 5000 m (B3). The corresponding RCS time averaged profiles are presented in Figure 6 for the above-cited series.
The profiles present net gradients (“steps”) at lower altitudes above the station on situations AB23, which is not the case for AB1 situations.
This net gradient is occasionally marked by the presence of small clouds at the top (e.g. B2 and A3) enhancing the backscatter signal.

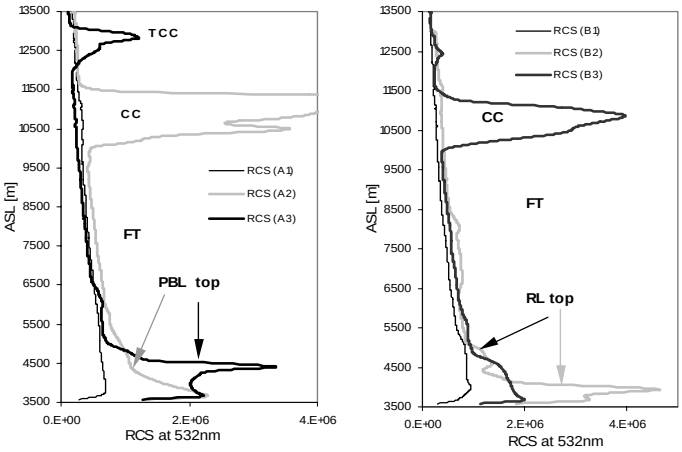

Figure 6 LIDAR Range correcting signals (molecular scaled) profiles at 532nm corresponding to day (A) and night (B) in the three different meteorological situations: (1) PBL < 3600 m, (2) PBL ~3600-4000 m and (3) PBL >4000 m. The PBL top in the daytime cases (A) and the RL top in the nighttime (B) are indicated by arrows. The occurrence of cirrus clouds (CC) or tropopause cirrus clouds (TCC) in the free troposphere (FT) can be seen.

In the AB3 cases, the layer is clearly higher than the Alps (the highest near peak being Jungfrau at 4200 m). These aerosol layers could be associated to the PBL top during the daytime and with the RL top in the nighttime. Already high aerosol layers (4000 m ASL) in the Alps were previously reported by lidar aerosol measurements [13] and the homogeneous elevation of the PBL at the Jungfraujoch station was shown up to 4200 m in the late afternoon by lidar aircraft embarqued observations [14].
In this case, the PBL elevation seems to be clearly higher followed by the persistence in the night of a high altitude RL.
Next section considers the water vapor mixing ratio measured by lidar Raman in nighttime.

3.3 Water vapor tracing of the RL

The nighttime water vapor mixing ratio vertical (B123v) vertical profiles (Figure 7) show a clear correlation with the RCS signals (B123).

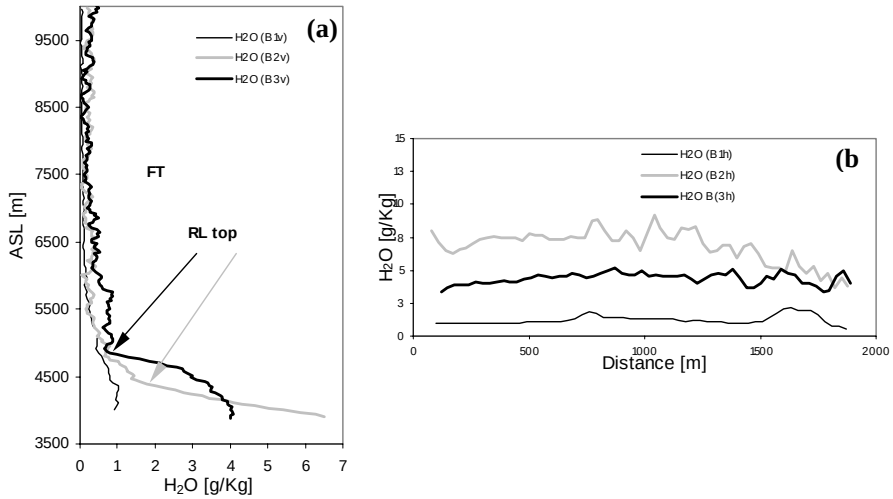

Figure 7 Nighttime (B) vertical (v) and horizontal (h) water vapor estimation using the Raman vibrational lidar technique above the Aletsch glacier for the three selected situations.

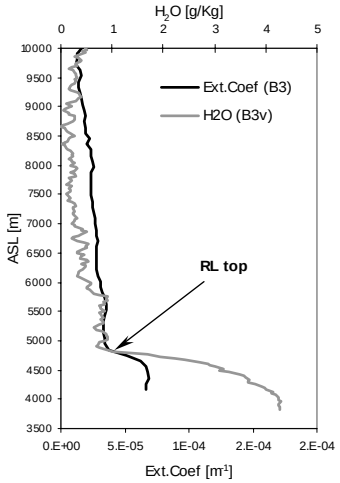

The Bv1 situation can be considered as a free troposphere reference with a quite low i.e. typical spring-autumn water vapor content (e.g. ~1 g/Kg). For the other two cases (B23v) the gradients steps on aerosols backscatters (RCS) are strongly correlated with the water vapor mixing ratio gradients. The RCS (B2) is greater than RCS (B3) due to the significant difference in the moisture level, 86% RH average compared to 39% respectively (for almost the same average temperature 6 °C).

Figure 8 LIDAR extinction coefficient at 532 nm and water vapor mixing ratio on 10.08.2003 (1:00-02:00) both showing the same top of a nighttime residual layer

The water vapor vertically integrated columns (from 3600 m to the tropopause) for the two August sub-periods (B23) are relatively high (4 - 5 mm) with high variability 25 - 35 % when compared with the free troposphere case (B1): about 1 mm with less than 10% variability. In addition, the correspondent horizontal profiles (B123h) above the Aletsch glacier show low mixing ratio (~ 1 - 2 g/kg) for the free troposphere case (B1v) and higher mixing ratio (4 - 8 g/kg) for the residual layer cases (B23h).
In the free troposphere case (B1v), the two peaks of the water vapor are probably due to the transfer of a wet air mass through the Jungfraujoch pass.
In the first period of August (B2v), the water vapor content was higher (~ 8 g/kg) and well correlated with the meteorological data. The water vapor profile and the aerosol extinction profile (Figure 8) are in perfect agreement concerning the altitude of the residual layer top. Within this residual layer, the observed values for the extinction coefficient (i.e. ~ 5 E-5 m^{-1}), at 532 nm, assuming a lidar ratio (LR) of 40, and for the water vapor (i.e. 4 -5 g/kg) are rather typical for the PBL air masses than for the free troposphere (e.g. less than 1E-5 and 2 - 3 g/kg for the same period of the year).

3.4 Turbulence patterns on the Aletsch glacier

Complementary simultaneous information regarding the turbulence above the glacier is derived from the sonic anemometers measurements of the wind vector (U, V, W) and temperature (T).

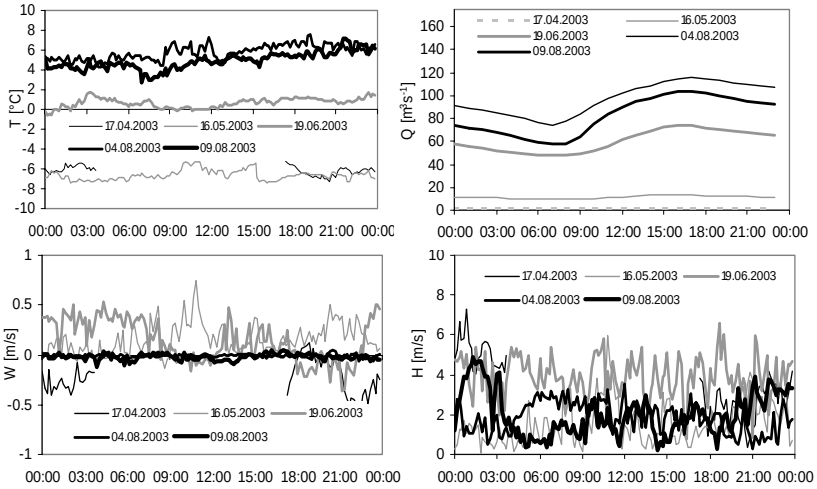

Figure 9 Temperature (T), glacier discharge (Q), vertical wind (W) and horizontal wind (H) on different selected days from April to August 2003. The T, W and H were extracted from anemometer measurements at ~2.5 m above the Aletsch glacier surface while the discharge (Q) is from the outlet of the glacier catchement.

Low temporal resolution turbulent quantities are obtained from 10 min data during 24 h with the aim to compare different days. In Figure 9, the temperature (T), the vertical wind (W) and the horizontal wind (H) on different days are shown together with the discharge (Q) at the outlet of the glacier. The daily average air temperature was about -6° C on April-May and about +6 °C in August 2003.

Correspondently, one notices the clearly evident correlation with the glacier melting when compare the discharge values (Q) of 1 - 15 m^3s^{-1} for negative air temperatures with maximums of 100-120 m^3s^{-1} corresponding to average air temperatures of 4 - 6 °C measured during 01 to15 August 2003. Compared with 0°C discharge, one estimate some ~7 - 8 m^3s^{-1} melting increasing for each 1 °C measured on the glacier surface. During the summer study period, minimum discharges were measured in the morning time at 7 ÷ 8:00 and they were unusually high (70 - 80 m^3s^{-1}), with values comparable with daytime maximums from other summer time periods. The very weak (1-2 m/s) horizontal wind velocities over the glacier are noticed during the 1-15 August 2003 period compared with 5-6 m/s recorded on a typical venting day such as 19.06.03. The absolute value of the vertical wind is extremely weak, about 0.01 m/s compared with 0.4 m/s for a well venting day such as 19.06.03.

These measurements at 2.5 m above the glacier surface confirm the relatively high temperatures in daytime 7 - 8 °C (maximum) and still 3 - 4 °C in the nighttime (minimum) on low wind conditions (no venting) at the glacier surface for the same lidar measurements periods. Wind speed, air temperature (average and standard deviation), mean kinetic energy (MKE), turbulent kinetic energy (TKE) and the correlation coefficient (R_{WT}) of the covariance between temperature (T) and vertical wind (W) are calculated as in [2] and presented in Table 2.

	MKE $[m^2/s^2]$	TKE $[m^2/s^2]$	H_{avg} [m/s]	σ_H [m/s]	W_{avg} [m/s]	σ_W [m/s]	T_{avg} [°C]	σ_T [°C]	R_{WT}
17.04.03	**3.04**	**4.38**	**3.51**	**0.45**	**0.24**	**0.15**	**-6.16**	**0.45**	**-0.37**
16.05.03	0.84	1.01	1.56	0.51	0.17	0.14	-6.63	0.51	0.56
19.06.03	2.96	5.34	3.92	0.49	0.14	0.15	0.66	0.49	0.01
04.08.03	**1.23**	**0.82**	**1.87**	**0.74**	**0.01**	**0.01**	**5.77**	**0.74**	**-0.02**
09.08.03	**1.11**	**1.53**	**2.00**	**0.87**	**0.03**	**0.02**	**4.91**	**0.87**	**-0.11**

Table 2 Wind, temperature and some turbulence parameters for selected days (for 10 min average time data). The bold selections are corresponding to the (1), (2) and (3) selected lidar measurements in the three PBL cases.

The decrease in the TKE and MKE when the atmosphere changes regimes from typical FT to PBL indicates that there is a decrease in turbulent intensity, while a decrease in the value of the correlation coefficient between the vertical component of velocity and temperature indicates that the boundary layer above the glacier is moving toward a change in stability. As this correlation approaches zero, the nature of the interaction between the atmosphere and the glacier

surface changes and thus stable atmospheric stratification becomes less dominant. Low TKE and MKE, very low W without correlation with T corresponds to this August period characterized by low turbulence, high temperatures and moisture above the Aletsch glacier. The whole set of Sonics anemometers measurements of at 10 min rate are shown in detail in annex A32.

3.5 Radiosoundings

In order to support the above observations, several radiosoundings from Payerne (meteorological station at 80 km NW of the observatory), Milano, Lyon and Stuttgart at noon (13:00 LT) and midnight (01:00 LT) were considered. The Payerne radiosounding is presented in (1), (2) and (3) cases. The other regional radiosoundings are compared only for the case (3) in order to investigate the possible regional meteorological patterns of the PBL and RL. The virtual potential temperature (θv) and the water vapor content (q_{H2O}) radiosonde profiles are plotted in Figure 10 for all AB123 situations considered.

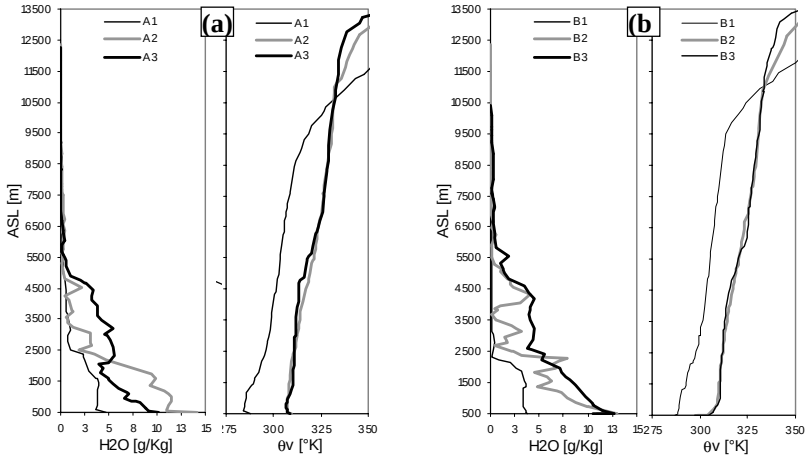

Figure 10 Water vapor and virtual potential temperature from the Payerne at 80 Km NW on the Swiss plateau on day (a) and night (b) of the three selected cases.

The tropopause level (~13000 m) on August 2003 (AB23) was some ~2000 m higher when compared with April (AB1). PBL top at midday is ~ 4500 - 4750 m, which is in good agreement with the determination based on lidar aerosols backscatter (curve RCS A3, Figure 6). Nighttime stable nocturnal boundary layer (SBL) below 1000 m and a very high residual layer (RL) up to 4800 m can be observed. The RL altitude is at the same height as determined by the lidar water vapor and extinction profiles (see Figure 5 and Figure 6). The PBL

development (see Figure 11, picture taken at 10:00 LT) over the Swiss plateau was homogeneous.

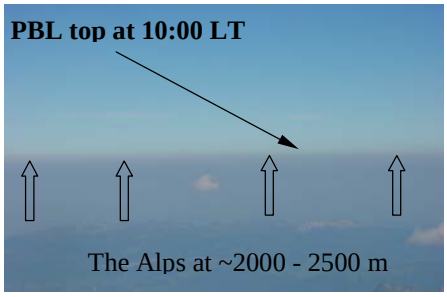

Figure 11 The homogenous PBL development in the morning (view over Swiss plateau from Jungfraujoch observatory at 10:00 LT).

In order to check the regional character of this development, in addition to Payerne, the Lyon, Milano and Stuttgart radiosoundings were considered (see Figure 12).

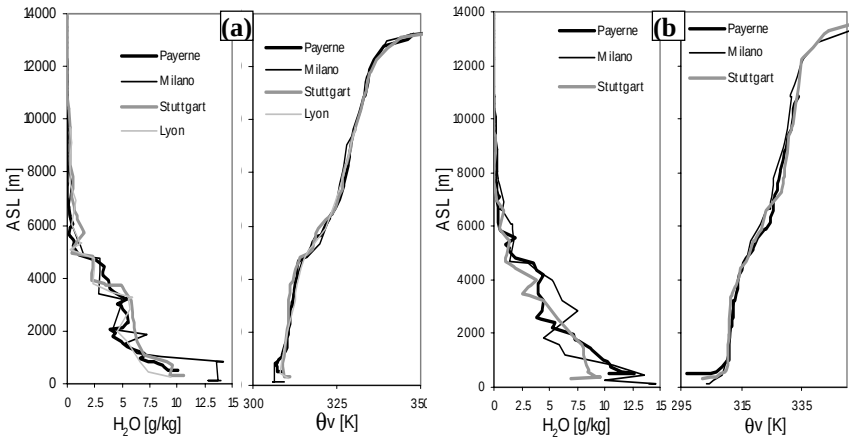

Figure 12 Water vapor and virtual potential temperature on 09.08.2003 at midday (a) and on 10.08.03 at midnight (b)

The same 4750 m top of the PBL and the persistence at 4500-4800 m of the same high temperature and moisture RL have been observed demonstrating the large regional behavior of both PBL and RL. One of the consequences of this intense 10-day anticyclonic weather is also the enhancement of the photochemical summer time smog.

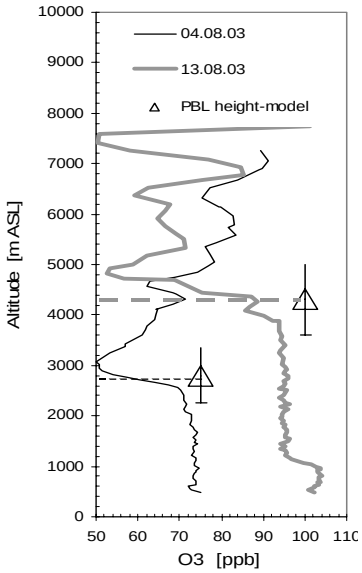

In Figure 13 are presented, in the same period as the lidar observations, ozone profiles from different radiosondes launched at Payerne at midday. One may note the homogeneous ozone layer of 70 ppb up to 3000 m (August, 4) and of 95-100 ppb up to 5000 m (August, 13) proving very high altitude mixing layers of the same height order as the PBL height deduced from lidar observations.
The model estimation of the PBL height was based on the consideration of the Turbulent Kinetic Energy (TKE) as PBL tracer and the calculations over the Swiss plateau were performed with the Methphomod [15] model using the k-ε parameterisation during 2-13 august 2003. The 1-sigma standard deviation is also plotted.

Figure 13 Midday various ozone vertical profiles from Payerne sounding, close in time to situations A123. Note the particular homogeneous vertical very high development of the ozone plume on 13.08.03 up to the same lidar-observed PBL altitudes. Methphomod model estimations of the PBL are also represented by triangles and 1 Sigma standard deviation.

3.6 In situ aerosols measurements

The progressive increase in scattering from April to August during the year 2003 may also be noticed on the in situ aerosol measurements at the Jungfraujoch station [16] as can be seen inFigure 14

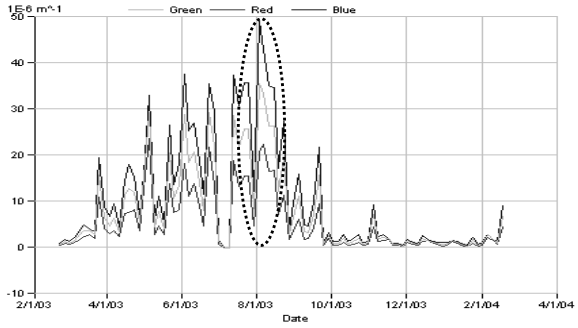

Figure 14 Scattering coefficients at 450 (blue), 550 (green) and 700 (red) nm during 2003 (data were obtained from http://gaw.web.psi.ch/

The high aerosols scattering coefficient value (~ up to 0.86 E-4 m^{-1} at 550 nm) is typical rather for PBL than for the free troposphere (~ 0.02 m^{-1} the median 2003 value at 550 nm). What is also particular in this case is the duration of the event ~10 days long and the persistence of the RL in the nighttime. A preliminary estimation, based on Angtrom coefficients, shows the presence of slightly bigger particles compared with the average and median size over 2003 year but up to 50 times bigger concentrations.

3.7 Aletsch glacier discharge

In Figure 15, the preliminary data obtained from the Swiss Federal Office for Water and Geology for the glacier discharge suggest possible correlation between the aerosols presence at JFJ station and the measured discharges. Principal component analysis (PCA) might allow the estimation of the aerosol impact on the glacier melting. All these aspects merit to be further analyzed.

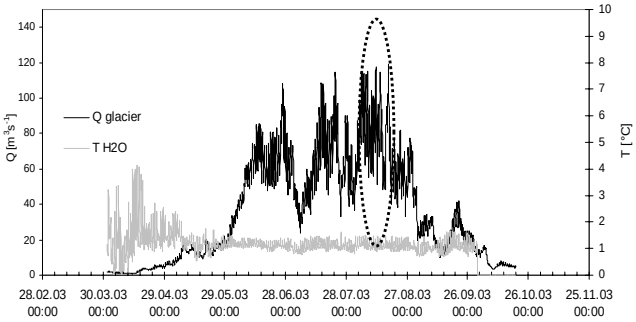

Figure 15 Aletsch glacier discharge measured at the outlet of the glacier catchment, at Blatten bei Naters (preliminary data)

Considerations are on going on the PCA method applied to the above-described topic in order to evidence and separate the possible indirect effect of the PBL aerosol on the accelerating melting rate of the high alpine glaciers.

4. Conclusion

Unusually high PBL convection (5000 m), during August2003 heatwave period, was evidenced from lidar, ultrasonic anemometers, radiosoundings, *in situ* aerosol, and glacier discharge measurements.
Nighttime RL, moist (~ 5 g/kg) and warm (~ 6 °C), persisting at ~ 4500-5000 was detected. The persistence, above the Alps, of a warm-humid RL may partially explain the unusual high melting rate of glaciers and permafrost rocks. For better estimation of this effect, the annual glacier mass balance has to be computed, which is an indicator of short-tem effects on glacier melting.

Simultaneous high photochemical pollution episodes occurred at continental scale.
The regional behavior is due to the persistence of the 10day Açores anticyclone over Western Europe.
Though the 2003 summer in Europe may be classified as an extreme event (i.e. intense heat-wave), we still cannot consider it as a direct consequence of the global warming. More extended, both past analysis and future observations will bring the complete answer.
Related analysis to this extreme event based mainly on temperature considerations (statistics, model calculations, etc) were recently expressed in [17, 18].
Further analysis related to the impact of the PBL high convection on the glaciers melting and to the quantification of the water vapor feedback, might be done based on different observations during this extreme event.

References

1. Brutsaert, W., *Evaporation into the Atmosphere:theory,history and applications*. Environmental Fluid Mechanics. 1982, Boston, London,Dordrecht: Kluwer Academic Publishers.
2. Stull, R.B., *An introduction to boundary layer meteorology*. Atmospheric Sciences Library. 1988, Dordrecht, Boston, London: Kluwer Academic Publishers.
3. Couach, O., I. Balin, R. Jiménez, P. Ristori, F. Kirchner, S. Perego, V. Simeonov, B. Calpini, and H. Van den Bergh, *An investigation of ozone and planetary boundary layer dynamics over the complex topography of Grenoble combining measurements and modeling.* Atmospheric Chemistry and Physics, 2003(3): p. 549-562.
4. Webe, R. and A.S.H. Prevot, *Climatology of ozone transport from the free troposphere into the boundary layer south of the Alps during North Foehn.* Journal of Geophysical Research, 2002. **107**(D3).
5. Couach, O., I. Balin, R. Jimenez, P. Ristori, S. Perego, F. Kirchner, V. Simeonov, B. Calpini, and H. van den Bergh, *An investigation of ozone and planetary boundary layer dynamics over the complex topography of Grenoble combining measurements and modeling.* Atmospheric Chemistry and Physics, 2003. **3**: p. 549-562.
6. Berman, S., J.-Y. Ku, and e. al., *Spatial and Temporal Variation in the Mixing Depth over the Northeastern United States during the Summer of 1995.* Journal of Applied Meteorlology, 1999. **38**: p. 1661-1673.
7. Barry, R.G., *Mountain Weather and Climate.* Routledge Physical Environment. 1992, London and New York: Routledge.
8. Baltensperger, U., Gäggeler, H. W., Jost, D. T., Lugauer, M., Schwikowski, M., Weingartner, E.,and Seibert, P., *Aerosol climatology at high-alpine site Jungfraujoch, Switzerland.* Journal of Geophysical Research-Atmospheres, 1997. **D102**: p. 19707-19715.
9. Nyeki, S., M. Kalberer, I. Colbeck, S. De Wekker, M. Furger, H.W. Gaggeler, M. Kossmann, M. Lugauer, D. Steyn, E. Weingartner, M. Wirth, and U. Baltensperger, *Convective boundary layer evolution to 4 km asl over high-alpine terrain: Airborne lidar observations in the Alps.* Geophysical Research Letters, 2000. **27**(5): p. 689-692.

10. Balin, I., G. Larchevêque, P. Quaglia, V. Simeonov, H. van den Bergh, and B. Calpini, *Water vapor profile by Raman lidar in the free troposphere from the Jungfraujoch Alpine Station*, in *Advances in global change research*, M.e. Beniston, Climatic Changes: Implications for the Hydrological Cycle and Water Management, Editor. 2002, Kluwer Academic Publisher: Dordrecht and Boston,. p. 123-138.
11. Wyngaard, J.C., *Cup, propeller, vane and sonic anemometers in turbulence reserach.* Abstracts of Papers of the American Chemical Society, 1981(Annual Reviews Fluid mechanics): p. 399-423.
12. Richner, H. and S. Hunerbein, *Grundlagen aerologischer Messungen speziell mittels der Schweizer Sonde SRS 400*. 1999, SMA MeteoSchweiz.
13. Frioud, M., V. Mitev, R. Matthey, C. Häberli, H. Richner, R. Werner, and S. Vogt, *Elevated aerosol stratification above the Rhine Valley under strong anticyclonic conditions.* Atmospheric Environment, 2003. **37**(13): p. 1785-1797.
14. Nyeki, S., K. Eleftheriadis, U. Baltensperger, I. Colbeck, M. Fiebig, A. Fix, C. Kiemle, M. Lazaridis, and A. Petzold, *Airborne lidar and in-situ aerosol observations of an elevated layer, leeward of the European Alps and Apennines.* Geophysical Research Letters, 2002. **29**(17): p. art. no.-1852.
15. Perego, S., *A numerical mesoscale model for simulation of the regional photosmog in complex terrain: model description and application during POLLUMET 1993 (Switzerland).* Meteorological Atmospheric Physics, 1999. **70**: p. 43-49.
16. PSI-GAW, *In situ aerosols monitoring at Jungfraujoch station*. 2004, PSI-LAC.
17. Schär, C., P.L. Vidale, D. Lüthi, C. Frei, C. Häberli, M.A. Liniger, and C. Appenzeller, *The role of incraesing temperature varaibility in European summer heatwaves.* Nature, 2004. **427**: p. 332-336.
18. Beniston, M., *The 2003 heat wave in Europe: A shape of things to come? An analysis based on Swiss climatological data and model simulations.* Geophysical Research Letters, 2004. **31**(L02202).

Chapter VIII

Conclusions

The main achievement of the presented work is the implementation of an operational multi-wavelength LIDAR system at the Jungfraujoch observatory (i.e. JFJ-LIDAR) and the analysis of the upper troposphere (UT) lidar-based measurements. These high spatial-temporal resolution measurements concern aerosol optical properties (i.e. backscatter and extinction coefficients), water vapor mixing ratio and air temperature profiles.
The JFJ-LIDAR design was based on LPAS-EPFL laboratory developments and implemented at JFJ at the beginning of 2000. The main specificity of this system is its multi-wavelength operation. The transmitter of the JFJ-LIDAR is based on a Nd: YAG laser emitting at 355, 532 and 1064 nm and operating with variable repetition rate up to 100 Hz and energies up to 400 mJ at 1064 nm. The JFJ-LIDAR receiver part is based on a Newtonian 20 cm diameter collector telescope and a polychromator filter module. The receiver was designed to record not only the UT elastic (i.e. Rayleigh - molecular and Mie - aerosols) backscattered radiation (i.e. 355, 532 and 1064 nm) but also the Raman rotational-vibrational backscattering from nitrogen (i.e. 387 and 607 nm), from the water vapor (i.e. 407 nm) and the pure rotational Raman of atmospheric nitrogen and oxygen excited at 532 nm. The backscatter at 532 nm was also separately detected for parallel and perpendicular polarization states relative to the linearly polarization state of the laser emitted light. The corresponding lidar signals are stored both in analog and photon-counting modes (i.e. on 14 simultaneous acquisition channels-- signals) via transient recorders (i.e. LICEL type) within typically 4000 shots and 20 Mhz (i.e. corresponding to 7.5 m vertical resolution) acquisition sampling rate.
Various system's configurations were tested and validated by inter – comparisons with the other two lidar systems installed temporarily at JFJ (i.e. lidar systems belonging to Neuchatel Observatory and the Johns Hopkins University).
The main achieved performances of the last configuration of JFJ-LIDAR are:

- Extremely good stability in operation (i.e. several days continuous operation);
- Acceptable signal to noise ratio up to the lower stratosphere (~ 15-18 km ASL/single acquisition file of 4000 shots, 50Hz/300mJ at 1064 nm) for the elastic backscatters using a 20 cm Newtonian telescope;
- Nighttime Raman signals acquisition was demonstrated up to the tropopause;

- Demonstration of long - term operation capacity; regular measurements since 2004

- Based on the inversion of the lidar elastic signals, the UT aerosols backscatter and extinction coefficients were regularly determined. A statistical analysis of data series taken from May 2000 to May 2002 shows good and realistic agreement, in terms of aerosol optical depth (AOD) when compared with observations made by the co-located sun-photometer instrument. A combined method based on elastic (Mie) – inelastic (Raman) signals is proposed, which allows the determination of extinction and the lidar ratio (i.e. extinction to backscatter ratio) of the cirrus clouds without any assumption. The retrieval of contrails' optical properties and preliminary calculations of its microphysics based on Mie theory in the approximation of spherical particles is illustrated by an example. The typical profiles of UT aerosol and cirrus optical properties were obtained for 30 min integration time, and 75 m vertical resolution up to the lower stratosphere. The depolarization analysis at 532 nm was also operational and it was proven its worth in distinguishing between water and ice content cirrus clouds.

- The nighttime water vapor mixing ratio profiles were derived using the ratio of the lidar signals corresponding to Raman rotational -vibrational backscatter at 407 nm from the water vapor and at 387 nm from the nitrogen molecules. A complete procedure including corrections, error calculations and a preliminary method for calibration is proposed. Regular measurements in different seasons were taken. The integrated profiles are in good agreement with co-located related measurements obtained from GPS and sun-photometer instruments. The typical vertical profiling of the UT nighttime water vapor mixing ratio is obtained within 1h integrated time and 150 m up 8 - 10 km ASL. The detection limit is about $\sim 1 \times 10^{-2}$ g_{water} $kg^{-1}{}_{dry\ air}$ (i.e. ~15 ppm). The use of simultaneous temperature profiles (e.g. from model or measurements) makes it possible to estimate the relative humidity and in particular to identify the upper troposphere super-saturated regions. The Raman backscatter at 387 nm was used to determine the cirrus absolute extinction coefficient and their lidar ratio. The Raman lidar is the only technique at JFJ that is capable of estimating the water vapor profiles above the station in the nighttime.

- In May 2002, a double grating polychromator (DGP) was implemented, allowing us to record parts of the Stokes and anti-Stokes pure rotational Raman backscatter excited at 532 nm. The ratio of lidar signals, corresponding to low and to high quantum numbers' in the pure rotational spectra, was used to derive the UTLS temperature profile. The DGP

module proves its stability (i.e. weak variation in time of calibration constants). The best result obtained was a temperature profile for 30 min acquisition time and a vertical gliding smoothing of 500 m, up to 18 km ASL using 400 mJ emission energy at 1064 nm. Statistical errors (1σ) reach some ~ 4 - 6 °C at the 18 km ASL. The temperature profiles are in good agreement both with atmospheric models and with the closest regional radiosonde measurements. The sum of the lidar signals, corresponding of pure rotational backscatter radiation, is used to retrieve the aerosol-cirrus extinction and lidar ratio absolute values of cirrus clouds.

Two case studies are also included in this work due to their climate related relevance.

(i) The first concerns the optical characterization of the mineral dust that often blows over the Alps from the Saharan desert (SDO),

(ii) The second involves lidar and complementary measurements taken during the Western Europe heat wave that occurred between 1 and 15 August 2003.

(i) The Saharan dust extended up to 5500 - 6000 m ASL and it was found optically thick (i.e. 0.2-03 aerosols optical depth) and formed by relatively large particles (i.e. > 1 μm and low Angstrom exponent ~ 0.14) of quasi-spherical shapes (i.e. ~10 % depolarization ratio). The ambient average extinction estimated from lidar data is ~ 0.1 km^{-1} and is almost not wavelength dependent in the UV-VIS-NIR. The slight dependency is due to the absorption contribution which is estimated for in *situ* measurements at ~10 % in UV and less than ~ 5 % in VIS and NIR. Results from different related co-located observations are presented.

(ii) The horizontal and vertical lidar measurements of water vapor and aerosols backscatter coefficient were analyzed together with simultaneous sonic anemometer wind and temperature measurements at the Aletsch glacier surface from April to August 2003. Using the aerosols and water vapor as tracers of the planetary boundary layer it was noticed a relatively unusual daytime high convection of the planetary boundary layer (i.e. PBL $\rightarrow$ 5000 m ASL). The persistence of PBL residual air masses above the Alps during the nighttime was also observed. These results, confirmed by the regional radiosoundings, may be of importance for future work concerning the consequences of the August 2003 heatwave extreme event.

Perspectives

These promising results encourage the continuation of regular operation of the JFJ lidar with an emphasis on maintaining the data series with as few breaks as possible towards a long-term monitoring. At the same time, more precise calibration procedures and comparisons with co-located measurements are still needed. For this, the regular launching at JFJ of radiosondes equipped with temperature, water vapor, pressure, ozone and aerosol measurements specific detectors will allow determination of more precise calibration constants and the checking of their in time stability. Improvements and changes are also necessary for obtaining daytime temperature and water vapor profiles and in general, the increase in the SNR of Raman signals is suitable. For this purpose additional optical device as Fabry-Perrot interferometer that could perform better filtering of the pure rotational may be a solution. The operation in the Fraunhofer regions may also reduce the solar induced noise on the water vapor Raman detection channels. One big step in the further developments will be the extension to the stratosphere of these observations using the Cassegrain former astronomic telescope (0.76 m diameter collector mirror; focal length F ~11.4 m) coupled with a new more powerful laser source. The use of the Cassegrain will increase the sensitivity by ~ 15 times while the new Nd: YAG laser source may be used with ~3 times more energy (i.e. 1600 mJ at 1064 nm). In principle, stratospheric aerosols (e.g. volcanic ash, sub-visible stratospheric clouds), and nighttime stratospheric water vapor could be retrieved. In order to avoid the problems associated with the mechanical stability of the Cassegrain telescope, and thus the sensitivity of the alignment, the emission of the laser may use the path of the Coudé optical layout. An additional steering mirror mounted on the telescope structure will finally send the laser beam into the atmosphere. This layout will avoid the problem of misalignment, as the emission will be mechanically coupled with the telescope movements. Based on these system developments, the measurement of stratospheric ozone may be performed by DIAL technique. The ozone OFF/ON appropriate wavelengths pair, situated in the ozone absorption spectra (Hartley band), may be generated as Raman stimulated radiations from a nitrogen high pressure cell pumped by the 4^{th} harmonic (e.g. 266 nm) of the new Nd: YAG laser source. Obviously the new system will be able to be used for determining stratosphere temperature profiles based on Rayleigh molecular scattering, which can be coupled with the pure rotational-based determination in the troposphere to get a complete profile up to the mesosphere. The troposphere-stratosphere folding and exchanges may be also addressed. This will enhance the other measuring techniques at JFJ making multi-technique atmospheric complex investigations possible. On the horizon as a long-term goal is a plan to provide remote control of the JFJ-LIDAR operation, which is still a challenge due to the complex technical and meteorological conditions involved.

A resuming scheme…

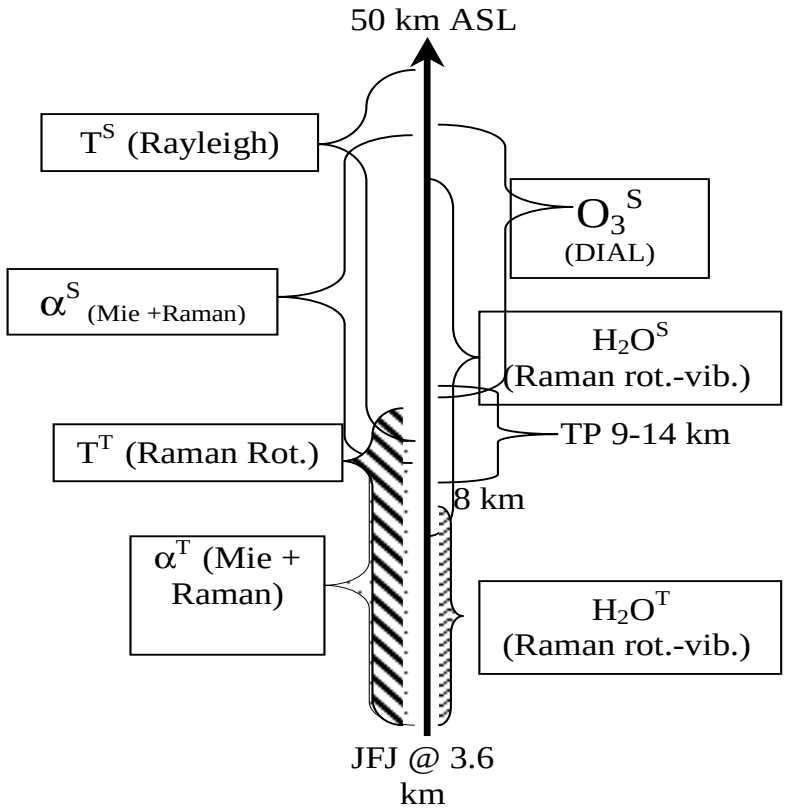

Summarizing, the main achievement of this research is the implementation and the regular operation of the JFJ-LIDAR, which allows the high-resolution retrieval of aerosols-cirrus-contrails extinction and backscatter coefficients, temperature and water vapor mixing ratio, both vertically (up to the tropopause) and horizontally (above the Aletsch glacier). The analysis of these measurements brings more knowledge in the general effort to reduce the present uncertainties in quantifying the contribution of various atmospheric compounds as water vapor, cirrus clouds and aerosols to the radiative budget of the Earth-Atmosphere-Sun system.

Hatched accolades ↔ past and present (i.e. conclusions)
Non hatched accolades → future (i.e. perspectives)
T (troposphere)
S (stratosphere)

Chapter IX

ANNEXES

A 1 Earth Atmosphere Characterization

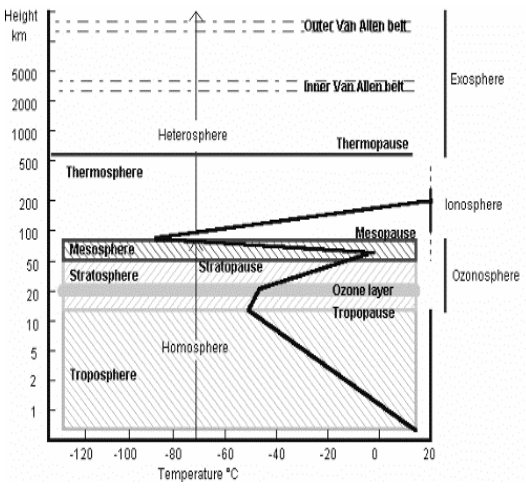

Terrestrial atmosphere has been slowly but radically transformed since the formation of our planet, about 4,6 billion years ago. Reductive (strongly or weakly according to the earth accretion theories) at the beginning, the atmosphere is oxidant nowadays knowing that the current oxygen concentration (20,95 % in volume) was reached 400 million years ago. But, since a few decades, atmosphere composition has been evolving relatively rapidly irrespective to the two major constituent N_2 (78.08 % in volume) and O_2 whose concentrations stay stable, but with the trace components having a mixing ratio less than 100 ppm (N_2O, NO, NO_2, O_3, CO, CH_4, VOC, CFC, …) and the minor component like CO_2. These trace and minor components play an important role in tropospheric (NO_2, VOC,….) and stratospheric chemistry (N_2O, CFC,….), and in the global warming of our planet (CO_2, CFC, O_3, N_2O, CH_4). This change is due in a large part to human activities (fossil gas combustion, farming practices, CFC use, …) that lead to massive, gases or particular, emissions of primary pollutants like SO_2, NO, VOC, CO. Those ones are susceptible to react in the atmosphere to generate secondary pollutants, like photochemical oxidants, which are often more harmful than the initial ones. Air pollution effects are multiple: decrease of the visibility (especially for particles in suspension which diameter is included between 0,1 and 1 µm), lakes acidification, attack or corrosion of numerous non-biological material like historic monuments, injuries to plants, animals and human health (growth of mortality and morbidity). Additionally to the potential effects on health of an increase on earth surface of the sun UV-B radiation, due to the decrease of the stratospheric ozone layer, this radiation increase could also generate higher ozone concentration in the troposphere, created by photolysis, this being the main component of the problematic photochemical smog. In the other hand O_3, N_2O, CFC, CO_2 and CH_4 whose concentrations are also growing (except the water vapor that seems stable) are all greenhouse gases. So they could contribute to a temperature elevation on earth and bring potential effects more dangerous than those that would result from the solely increase of the UV-B radiation.

The Earth *atmosphere* describes the layer, essentially gaseous, that envelopes the earth. The atmosphere can be seen as a fluid in movement, so all the theories related to it will try to explain its behavior and among this its vertical structure, the winds and more generally the meteorology, and the pollution related problems. Several classifications can be defined, but the most commonly used is based on the vertical stratification of the temperature as proposed and accepted in 1960, after it had given rise to much controversy, by the Geodesy and Geophysics International Union in Helsinki then in 1962 by the executive committee of the World Meteorological Organization (WMO).

The *troposphere*, the first layer, starts from the ground and is characterized by a negative temperature gradient.

The *stratosphere* starts from the tropopause and is characterized by an increase of the temperature with the altitude. It ends with the *stratopause* at an altitude of approximately 50 km where the temperature reaches a maximum at about 270 K (the highest temperature at the stratopause is reached in the polar regions during their "local" summer, when the insolation is permanent). This temperature increase is the result of the solar UV absorption, mainly due to the ozone which reaches a maximal concentration in the stratosphere. This creates a temperature gradient inversion, with warmer stratospheric air above the colder air of the top of troposphere. Consequently, this restricts considerably the vertical mixing both in the stratosphere itself and between the troposphere and the stratosphere. Due to the low tropopause temperature and this temperature inversion, a water vapor trap is created that explains the low level of water vapor content in the stratosphere. Beyond the stratopause the infrared emission by CO_2, which is a minor constituent, is sufficient to induce a temperature decrease. This region, named *mesosphere*, extends from 50 km till the *mesopause* at an altitude of about 85 km where the temperature reaches a minimum. Unlike what occurs in the stratopause, the mesopause temperature reaches its highest value (about 210 K) in the polar regions during their "local" winter, and the lowest value (150 K) in the polar regions during their "local" summer. This strange behavior is contradictory with the insolation conditions but can be explained by the existence of a meridian circulation that permits an energy transport from the "summer" polar mesopause to the "winter" polar mesopause.
The last region is the *thermosphere* which extends after the mesopause, and where the atmosphere is warmed by the UV solar radiation with wavelength lower than 175 nm. The temperature constantly increases (855 K at 200 km, 1000 K at 750 km) till the *thermopause* where the temperature gradient starts to become negligible and gives a quite constant temperature value. The altitude of the thermopause is strongly linked to the solar activity.
In term of the chemical composition and the dynamic state we speak about the *homosphere* which is the atmospheric region where the mixing phenomenons like winds, convection and turbulence are rapid and important enough to allow a constant volume composition of the main constituents (like O_2, N_2, Ar, but not for minor constituents like O_3 for example) according to the altitude. This homogeneity stops at approximately 80 km, with the *homopause* or *turbopause*, which is a transitional region with the *heterosphere* where turbulence starts to be weak and then does not allow a perfect mixing. In this region the earth gravity induces a molecular diffusion of the main constituents (in the homosphere too, but hidden by the "turbulence-mixing") and then it gives a variable volume composition of the main constituents. At a certain altitude, depending on the solar activity and the geomagnetism, is the *heteropause* or *exobase* where the particle concentrations start to be very low and where each particle can be approximated to a single one. Beyond in the *exosphere*, rules can be quite different than our usual ones. The radio physicists often use the second one. It begins with the *neutrosphere*, a region characterized by a very low concentration in free electrons and ending at about 60-70 km with the *neutropause* which makes a separation with the *ionosphere* where the free electron concentration start to be important. Above 750 km the molecular mean free pass starts to be so high that each molecule can be considered as a ballistic particle and then the normal gas physic law is no more valid. This region is called *exosphere* and extends till approximately 2000 km. In the last region the terrestrial magnetism supplants the terrestrial gravity and ions and protons are in majority. It is called *magnetosphere* or *protosphere.*

A 2 LIDAR: brief historic

The use of the lasers has the basis already in 1917 when Albert Einstein studied the quantum transitions between two energy levels and explained the spontaneous emission and predicted the stimulated emission phenomenon. Later, in the 50's, the physicist Alfred Kastler obtained

the first inversion of population by optical pumping. In 1954, Townes built the first MASER (Microwave Amplifier by Stimulated Emission of Radiation), based on a transition of the ammoniac molecule, the precursor of the laser. After further theoretical investigation, Townes and Schawlow concluded, in 1958, that it was possible to build such a MASER system at higher frequency, i.e. in the visible spectral range [*Schawlow and Townes*, 1958] and Maiman was the first in 1960 to build an optical maser with ruby [*Maiman*, 1960]. Then there was an exponential increasing of the research and applications in this field, and the name changed to LASER for Light Amplifier by Stimulated Emission of Radiation. As the "laser sounding" era did not start because of the unavailability of lasers, some attempts were made by means of searchlight probing technique in 1952 [*Elterman*, 1954], to retrieve temperature, density and pressure in the atmosphere, followed in 1962 by experiments with a similar giant pulse technique [*Mc Clung and Hellworth*, 1962]. First laser soundings on aerosols with a ruby laser were made in the stratosphere [*Fiocco and Smullin*, 1963], to study volcanic compounds. A similar system for the troposphere was made [*Ligda*, 1963]. This so called lidar technique has then expanded and stimulated research into many fields: laser sources, optics, electronics, atmospheric chemistry, and more. The main advantage of this technique is the ability for range resolved probing of the atmosphere at distance in real time. No other systems, even today, can compete with this feature. This system has also some limitations due to the optical concept, the most commonly known are clouds or big aerosol loading. From the 60's different techniques were investigated for detecting, with higher resolution, more and more types of molecules, pollutants, clouds or physical process like wind. Among all one may cite: Rayleigh lidar, which is usually used for determining temperature above 30 km [*Hauchecorne et al.*, 1991]. The feasibility of atmospheric temperature measurement down to 1 km has been also shown [She et al, 1992]. The DIAL is based on a different absorption, by the molecule studied, of the pump beam. This technology is classic but the emitting system is complicate. It permits the measurement of various constituents [*Uchiumi et al.*, 1994], but the most classical use is for the ozone concentration retrieval [*Browell et al.*, 1985], [*Calpini et al.*, 1997]. The water vapor case is quite difficult with this method, and numerous problems occur [*Browell et al.*, 1979]. Shot per shot lidar is tested to retrieve wind and ozone fluxes [*Fiorani et al.*, 1998]. The Raman lidar vibrational [*Renaut and Capitini*, 1988] (water vapor in the boundary layer), rotational [*Arshinov et al.*, 1983] (temperature under 1 km), or resonant form [*Rosen et al.*, 1975] (SO_2 and NO_2 concentrations under 1 km, with eyes safety considerations), [*Hochenbleicher et al.*, 1976] (conditions of application) are some examples. Fluorescence lidar, used for mesospheric temperature measurement, where quenching is small [*She et al.*, 1992] or a pump and probe lidar to estimate the OH radical concentration [*Jeanneret et al.*, 2000] are quite unique applications. The idea of using the Raman effect for lidar, came in 1967 [*Leonard*, 1967], when the first Raman shifts from the atmospheric oxygen and nitrogen were observed, and the advantage of this novel technique was pointed out. Several pioneering groups then worked in this promising way: Cooney [*Cooney*, 1968] measured atmospheric density profiles from N_2, Inaba [*Inaba and Kobayashi*, 1969] theoretically showed that it was possible to monitor atmospheric gases or pollutants and proposed a diagram for the lidar to be built. The first observation of the water vapor mixing ratio with a Raman technique was reported by Melfi [*Melfi et al.*, 1969].

A 3 US-Standard-Atmosphere 1976

The US-Standard-Atmosphere 1976 is an idealized, steady state representation of the earth's atmosphere from the surface to 100 km, as it is assumed to exist in a period of moderate solar activity. The air is assumed to be dry, and below 86 km homogeneously mixed with a relative-volume composition leading to a mean molecular weight. The temperature and the

pressure at a given altitude z [m] above the Jungfraujoch station[1] (3580 m ASL) may be thus calculated by the following equations:

$$T(z) = T(3580m)\left(\frac{1-\frac{dT}{dz}}{T(3580m)(z-3580)}\right)$$

$$P(z) = P(3580)\left(\frac{1-\frac{dT}{dr}}{T(3580m)(r-3580)}\right)^{R\frac{g}{\frac{dT}{dr}}}$$

$$n_{air}(z) = \frac{P(z)}{K_B T(z)}$$

The standard atmosphere is divided in five layers: from 0 to the altitude of the tropopause, from this altitude to 20km, from 20 to 35km and from 35 to 50km with gradients of temperature dT/dz of -0.65K/100m, +0.0K/100m0.1K/100m and +0.24K/100m, respectively.

Example of calculation:

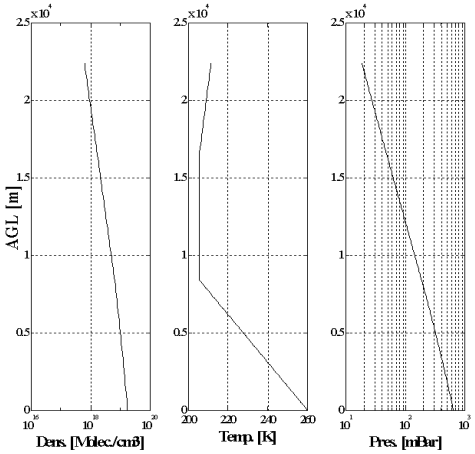

T (3580m) = 260 K (-13°C)
P (3580m) = 660 hPa

R = 8.3143 x 10^3 J K^{-1}
g(z) ~ 9.81 ms^{-2}
K_B=1.381 x 10^{-23} J K^{-1} $molecule^{-1}$

[1] Observation: the local P and T at Jungfraujoch station may vary during the year from: -30°C to 12°C and 650-675 hPa, from personal observations during the lidar operation time.

A 4 Lidar system related pictures

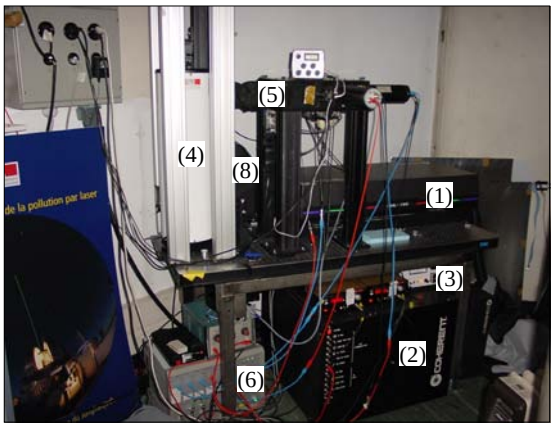

(1) Nd: YAG laser head

(2) Laser power suppy

(3) PMTs power supply

(4) Newtonian telescope

(5) Filter polychromator

(6) LICEL (Tr. Recorders)

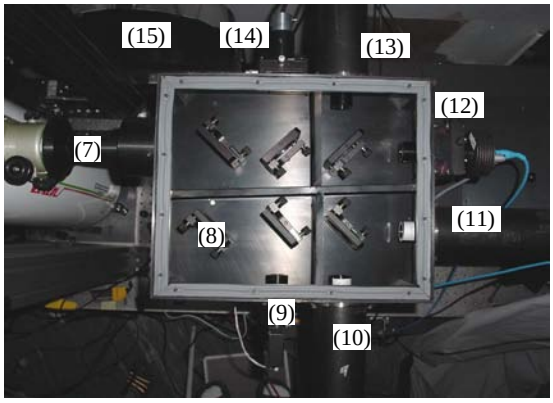

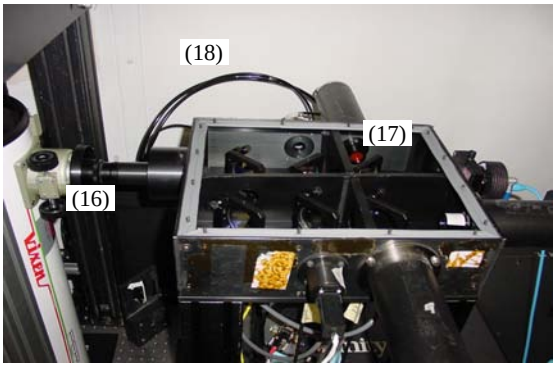

(7) Diaphragm

(8) Dichroic beam splitters

(9) Hamamatsu PMT355nm

(10)ThornEmi PMT387nm

(11)ThornEmi PMT407nm

(12) APD 1064 nm

(13) ThornEmi 607nm

(14) Optical fiber head for 532 nm → DGP

(15) DGP optical fiber bending protection

(16) Optical coupling (polychromator - telescope)

(17) Filters Combinations

(18) Optical fibers→ DGP

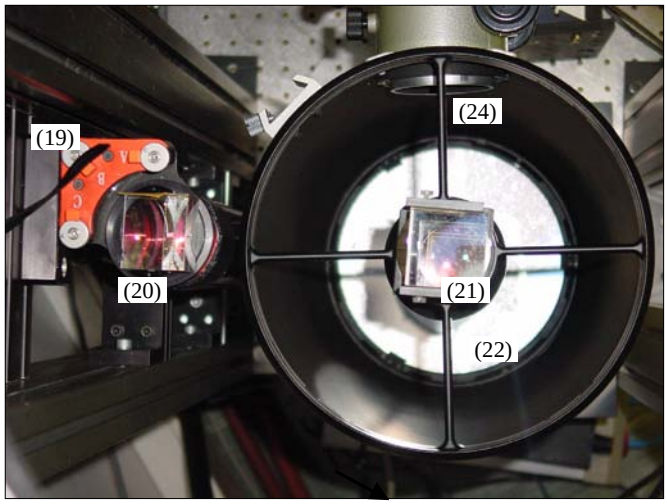

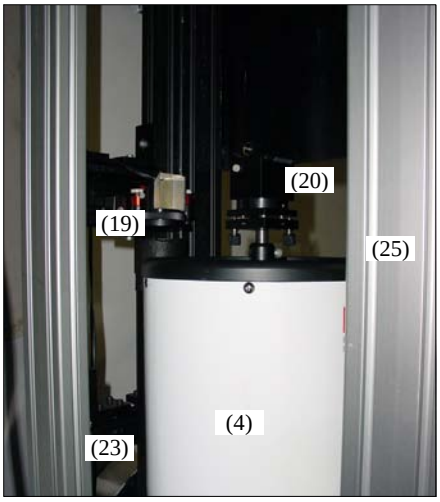

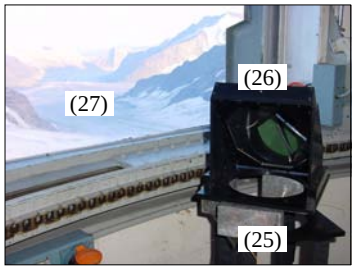

(19) Piezoelectric controlled stage

(20) Fine alignment prism

(21) Coarse alignment prism

(22) Collector mirror (20cm)

(23) Beam expander

(24) To the FPM

(25) Support horizontal mirror

(26) Steering mirror for horizontal observations

(27) Open cupola-a view on the Aletsch glacier

A 5 Laser (Nd:YAG Infinity 40-100) related schemas

(a) Laser main optical layout

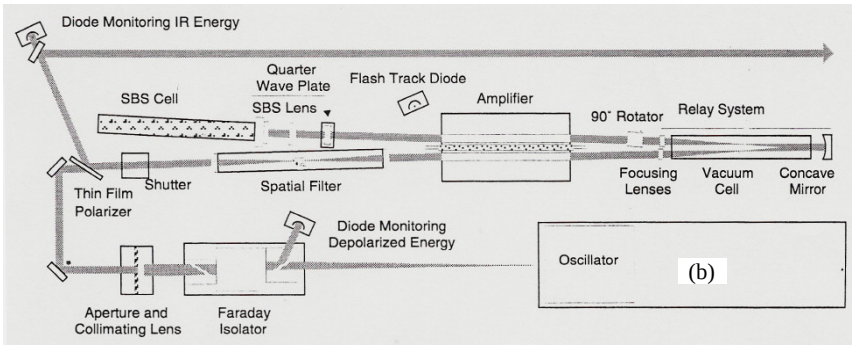

(b) Oscillator optical layout

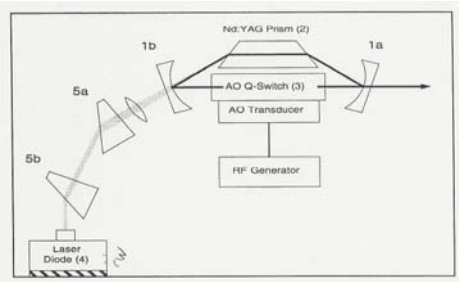

(1a,b) concave mirrors

(2) Trapezoidal Nd:YAG prism

(3) Acusto-optic modulator

(4) Pump laser diode at 810 nm

(5a,b) Shape light prisms

(c) Nd: YAG Energy levels scheme

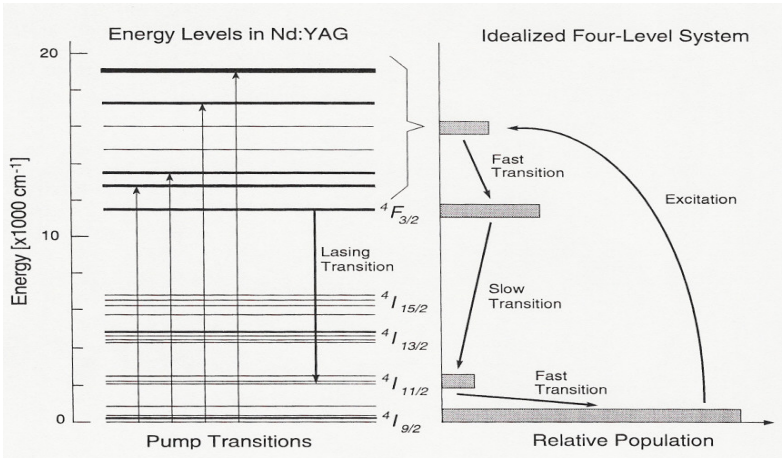

(d) Nd: YAG laser head controls and indicators location

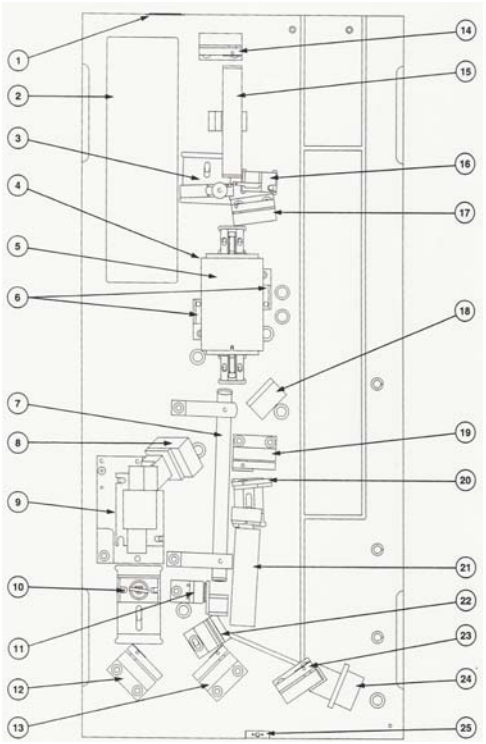

CALLOUT	NAME
1	Laser emission indicator
2	DPMO, Diode Pumped Master Oscillator
3	Relay system lens 1
4	Amplifier assembly, POT
5	Flash lamp terminal box (above amplifier assembly)
6	Safety interlock dowel pin
7	Vacuum spatial filter
8	Photo-diode monitoring depolarized energy
9	Faraday isolator
10	Collimating lens
11	Mechanical shutter
12	Folding mirror, M1
13	Folding mirror, M2
14	Concave mirror, relay system
15	Relay system vacuum cell
16	Relay system lens 2
17	90° Polarization rotation prism
18	Flash track photo-diode
19	Quarter wave plate
20	SBS lens
21	SBS cell
22	Thin film polarizer
23	Folding mirror, M3
24	Photo-diode monitoring IR energy
25	Head cover interlock

(e) Principles of 2nd and 3rd harmonic generations

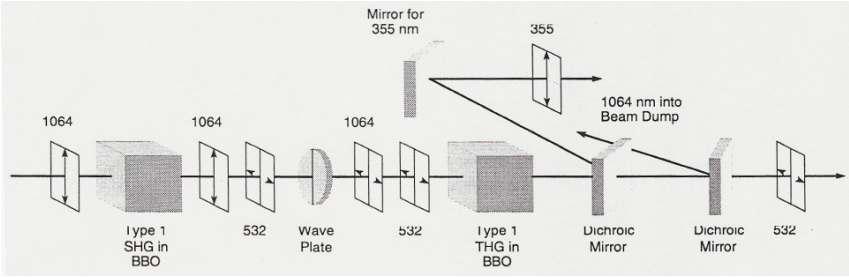

A 6 Hamamatsu Photosensor module Type H5773-6780

Metal Package PMT

Photosensor Modules H5773/H5783/H6779/H6780 Series

The H5773/H5783/H6779/H6780 series are photosensor modules housing a metal package PMT and high-voltage power supply circuit. The metal package PMTs have a metallic package with the same diameter as a TO-8 package used for semiconductor photodetectors, and deliver high gain, wide dynamic range and high-speed response while maintaining small dimensions identical to those of photodiodes. The internal high-voltage power supply circuit is also compact, making the module easy to use.

Considering the mounting methods, a cable output type and a pin output type are provided, and a total of 7 types are available according to the wavelength range to be measured. A P-type is also available with selected gain and dark count ideal for photon counting under extremely low light conditions.

Product Variations

Type No. \ Suffix	None	-01	-02	-03	-04	-06	-20	Output Type	Features
H5773	yes	yes	yes	yes	yes	yes	yes	On-board	Low power consumption
H5783	yes	yes	yes	yes	yes	yes	yes	Cable output	
H5773P	yes	no	no	no	no	no	no	On-board	For photon counting
H5783P	yes	no	no	no	no	no	no	Cable output	Low power consumption
H6779	yes	yes	yes	yes	yes	yes	yes	On-board	Low ripple noise
H6780	yes	yes	yes	yes	yes	yes	yes	Cable output	Fast settling time

Suffix	Spectral Response
None	300 nm to 650 nm
-01	300 nm to 850 nm
-02	300 nm to 880 nm
-03	185 nm to 650 nm
-04	185 nm to 850 nm
-06	185 nm to 650 nm
-20	300 nm to 900 nm

The suffix -06 type (synthetic silica window) has higher sensitivity than the -03 type below 300 nm in wavelength range.

Specifications

Parameter			H5773 / H5783 / H6779 / H6780 Series					Unit
Suffix			None	-03, -06	-01, -04	-02	-20	—
Input Voltage			+11.5 to +15.5					V
Max. Input Voltage			+18					V
Max. Input Current			H5773 / H5783 Series: 9 H6779 / H6780 Series: 30					mA
Max. Output Signal Current			100					µA
Max. Control Voltage			+1.0 (Input impedance 100 kΩ)					V
Recommended Control Voltage Adjustment Range			+0.25 to +0.9					V
Effective Area			φ8					mm
Sensitivity Adjustment Range			1: 10^4					—
Peak Sensitivity Wavelength			420	420	400	500	630	nm
Cathode	Luminous Sensitivity	Min.	40	40	80	200	350	µA/lm
		Typ.	70	70	150	250	500	
	Blue Sensitivity Index (CS 5-58)		8	8	—	—	—	—
	Red/White Ratio		—	—	0.2	0.25	0.45	—
	Radiant Sensitivity *1		62	62	60	58	78	mA/W
Anode (Standard Type)	Luminous Sensitivity	Min.	10	10	15	25	35	A/lm
		Typ.	50	50	75	125	250	
	Radiant Sensitivity *1 *2		4.3×10^4	4.3×10^4	3.0×10^4	2.9×10^4	3.9×10^4	A/W
	Dark Current *2 *3	Typ.	0.2	0.2	0.4	2	2	nA
		Max.	2	2	4	20	20	
Anode (P Type)	Gain *2	Min.	7.5×10^5	—				—
		Typ.	1×10^6	—				
	Radiant Sensitivity *1 *2		6.2×10^4	—				A/W
	Dark Count *2 *3	Typ.	80	—				s^{-1}
		Max.	400	—				
Rise Time *2			0.78					ns
			H5773 Series	H5783 Series	H6779 Series	H6780 Series		
Ripple Noise *2 *4 (peak to peak)		Max.	1.2		0.6			mV
Settling Time *5			2		0.2			s
Operating Ambient Temperature			+5 to +50		+5 to +45			°C
Storage Temperature			-20 to +50					°C
Weight			60	80	60	80		g

*1: Measured at the peak sensitivity wavelength *2: Control voltage = +0.8 V *3: After 30 minute storage in darkness
*4: Cable RG-174/U, Cable length 450 mm, Load resistance = 1 MΩ, Load capacitance = 22 pF
*5: The time required for the output to reach a stable level following a change in the control voltage from +1.0 V to +0.5 V.

16

Current Output Type Photosensor Modules

Characteristics (Cathode radiant sensitivity, Gain)

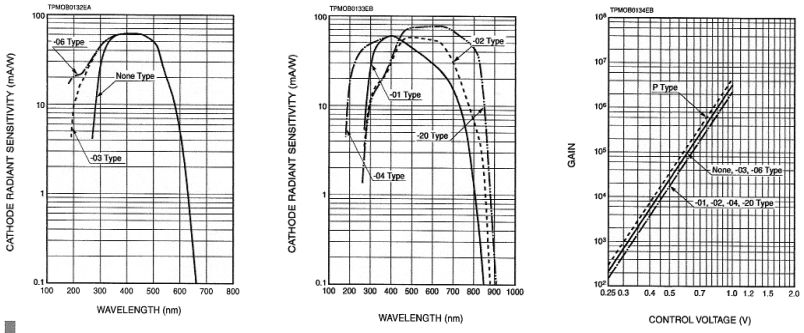

Sensitivity Adjustment Method

Voltage Programming

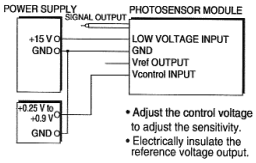

- Adjust the control voltage to adjust the sensitivity.
- Electrically insulate the reference voltage output.

Resistance Programming

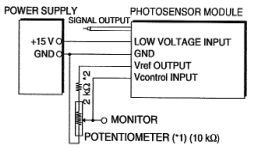

*1: When using a potentiometer to adjust sensitivity, monitor the control voltage so it does not exceed +1.0 V.

*2: H6779/H6780 series has this 2 kΩ resistor. No external resistor is needed.

TPMOC0131EC

Dimensional Outlines (Unit: mm)

H5773/H6779 Series

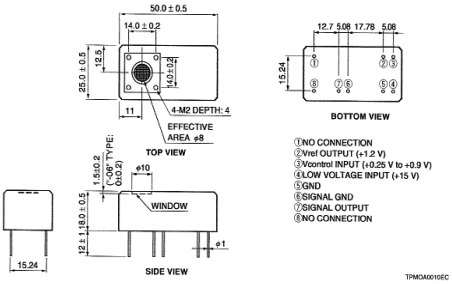

①NO CONNECTION
②Vref OUTPUT (+1.2 V)
③Vcontrol INPUT (+0.25 V to +0.9 V)
④LOW VOLTAGE INPUT (+15 V)
⑤GND
⑥SIGNAL GND
⑦SIGNAL OUTPUT
⑧NO CONNECTION

TPMOA0010EC

H5783/H6780 Series

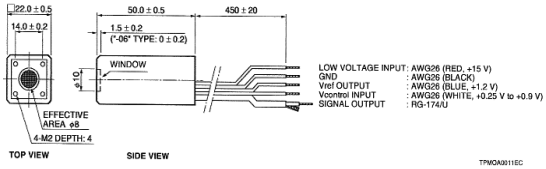

LOW VOLTAGE INPUT: AWG26 (RED, +15 V)
GND : AWG26 (BLACK)
Vref OUTPUT : AWG26 (BLUE, +1.2 V)
Vcontrol INPUT : AWG26 (WHITE, +0.25 V to +0.9 V)
SIGNAL OUTPUT : RG-174/U

TPMOA0011EC

Option (Optical Fiber Adapter) (Unit: mm)

E5776 (FC Type)

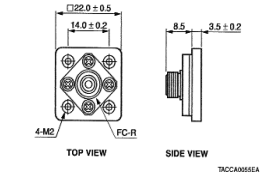

TACCA0055EA

E5776-51 (SMA Type)

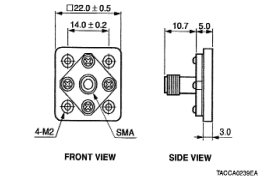

TACCA0236EA

A 7 Thorn Emi Type QA9829B series technical specifications

52 mm (2″) photomultiplier 9829B series data sheet

electron tubes

1 description

The 9829B is a 52 mm (2") diameter, end window photomultiplier with a thin domed window, sandblasted for enhanced cathode sensitivity, blue-green sensitive bialkali photocathode and 12 BeCu dynodes of linear focused design for good linearity and timing. The 9829WB and 9829QB are variants for applications requiring uv sensitivity.

2 applications

- liquid scintillation counting
- photon counting of bio- and chemi-luminescent samples
- low light level detection

3 features

- good SER

4 window characteristics

	9829B borosilicate	9829WB uv glass	9829QB* fused silica
spectral range** (nm)	290 - 630	185 - 630	160 - 630
refractive index (n_d)	1.49	1.48	1.46
K (ppm)	300	8500	<10
Th (ppb)	250	30	<10
U (ppb)	100	30	<10

*note that the sidewall contains graded seals of high K content
**wavelength range over which quantum efficiency exceeds 1 % of peak

5 typical spectral response curves

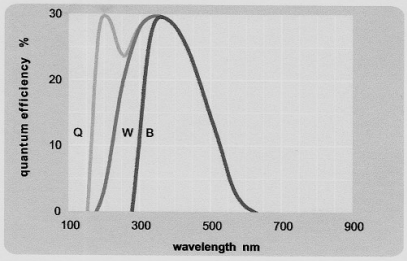

6 characteristics

	unit	min	typ	max
photocathode: bialkali				
active diameter	mm		46	
quantum efficiency at peak	%		30	
luminous sensitivity	µA/lm		85	
with CB filter		9.5	12.5	
with CR filter			2	
dynodes: 12LFBeCu				
anode sensitivity in divider A:				
nominal anode sensitivity	A/lm		500	
max. rated anode sensitivity	A/lm		2000	
overall V for nominal A/lm	V		1600	1900
overall V for max. rated A/lm	V		1800	
gain at nominal A/lm	x 10^6		6	
dark current at 20 °C:				
dc at nominal A/lm	nA		3	10
dc at max. rated A/lm	nA		12	
dark count rate	s^{-1}		300	
pulsed linearity (-5% deviation):				
divider A	mA		50	
divider B	mA		150	
rate effect (I_a for Δg/g=1%):	µA		1	
magnetic field sensitivity: the field for which the output decreases by 50 %				
most sensitive direction	T x 10^{-4}		1	
temperature coefficient:	% $°C^{-1}$		± 0.5	
timing:				
single electron rise time	ns		2	
single electron fwhm	ns		3	
single electron jitter (fwhm)	ns		2.2	
multi electron rise time	ns		3.2	
multi electron fwhm	ns		4.5	
transit time	ns		41	
weight:	g		130	
maximum ratings:				
anode current	µA			100
cathode current	nA			100
gain	x 10^6			25
sensitivity	A/lm			2000
temperature	°C	-30		60
V (k-a)(1)	V			2800
V (k-d1)	V			500
V (d-d)(2)	V			450
ambient pressure (absolute)	kPa			202

(1) subject to not exceeding max. rated sensitivity (2) subject to not exceeding max rated V(k-a)

7 typical voltage gain characteristics

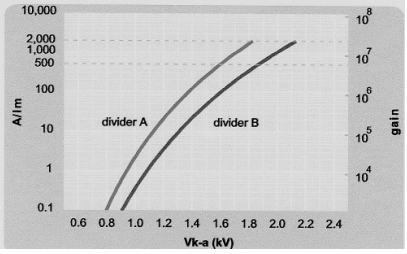

8 voltage divider distribution

	k	d_1	d_2	.....	d_8	d_9	d_{10}	d_{11}	d_{12}	a	
A	300V	R		.....	R	R	R	R	R	R	Standard
B	300V	R		.....	R	1.25R	1.5R	1.5R	2R	3R	High Pulsed Linearity

note: focus connected to d_1

Characteristics contained in this data sheet refer to divider A unless stated otherwise.

9 external dimensions mm

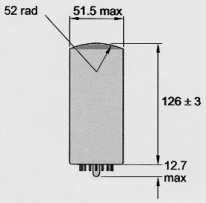

10 base configuration (viewed from below)

'ic' indicates an internal connection

note: connect f to d_1

Our range of B21 sockets, available for this series, includes versions with or without a mounting flange, and versions with contacts for mounting directly onto printed circuit boards.

11 handling instructions

The window of this pmt has been specially cleaned to give maximum efficiency. It should not be touched with fingers or allowed to come into contact with oil or grease. The window can be cleaned with isopropyl alcohol to remove oil deposits.

12 ordering information

The 9829B meets the specification given in this data sheet. You may order **options** by adding a suffix to the type number. You may order product with **specification options** by discussing your requirements with us. If your selection option is for one-off order, then the product will be referred to as 9829A. For a repeat order, Electron Tubes will give the product a two digit suffix after the letter B, for example B21. This identifies your specific requirement.

9829 ☐ ☐ ☐

window variants
W uv glass
Q fused silica

options
E electrostatic shielding see drawing below
S electromagnetic shielding see drawing below
M supplied with spectral response calibration

specification options
B as given in data sheet
A single order to selected specification
Bnn repeat order to selected specification

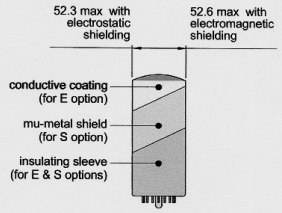

13 voltage dividers

The standard voltage dividers available for these pmts are tabulated below:

	k	d_1	d_2	d_3	.....	d_8	d_9	d_{10}	d_{11}	d_{12}	a
C676A	3R	R	R	.....	R	R	R	R	R		
C676B	3R	R	R	.....	R	1.25R	1.5R	2R	3R		

note: focus connected to d_1
R = 330 kΩ

Electron Tubes Limited
Bury Street, Ruislip
Middx HA4 7TA, UK
tel: +44 (0) 1895 630771
fax: +44 (0) 1895 635953
e-mail:
info@electron-tubes.co.uk

Electron Tubes Inc.
100 Forge Way, Unit F
Rockaway, NJ 07866, USA
tel: (973) 586 9594
toll Free: (800) 521 8382
fax: (973) 586 9771
e-mail: sales@electrontubes.com

an ISO 9001 registered company

www.electrontubes.com

DS_ 9829B Series Issue 1
07 January 2002

A 8 Avalanche Photodiode (NIR-Si-APD) series technical specifications

Si-Avalanche Photodiode module

licel
lidar computing and electronics

Low noise - high speed detector @ 400 nm-1100nm

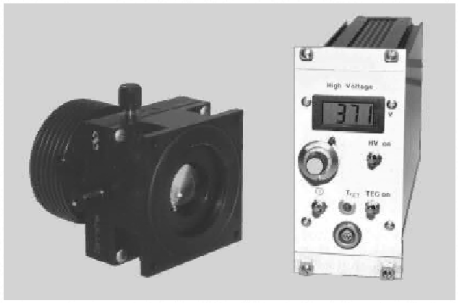

High NIR Quantum Efficiency

Now you can measure optical signals in the near IR with high quantum efficiency, comparable to UV-Vis detectors. Our Si-APD Module consists of a TE-cooled detector, a high-speed low-noise preamplifier and HV supply. Signals can be acquired using analog detection as well as single photon counting mode.
Integrated focussing optics and alignment mechanics allow easy integration into your optical setup.The increased sensitivity in the near infrared is a major advantage compared to photomultipliers.

Features:

- 0.8,1.5 or 3 mm dia. detector size
- thermoelectric cooled up to -20° C
- low noise, high gain preamplifier
- easy system integration with integrated alignment optics and mechanics
- integrated HV- and AC-power supply

Applications:

- LIDAR (Light Detection and Ranging)
- fluorescence detection
- replacement for photomultipliers >800nm

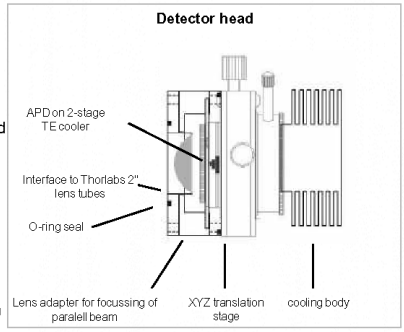

LICEL GbR, Chausseestr. 34/35, D-10115 Berlin, phone/fax +49.30.283.917.37/38, info@licel.com

Specifications

Detector:

detector size:	0.8, 1.5 or 3 mm dia.
QE @650 nm:	> 80%
QE @ 900 nm:	85%
responsivity @ 1060 nm:	34 A/W typ., QE=38%
dark current @22° C:	50 nA (0.8 mm dia), 100 nA (1.5 & 3 mm dia.)
spectral noise current: @10kHz	1 pA/√Hz typ., 2 pA/√Hz max.

Mechanics:

The compact APD/preamp/TEC controller unit is mounted in a XYZ translation stage for easy integration and alignment in detection systems.

XY axis travel:	5 mm
Z-axis travel:	6 mm
precision:	4µm

Preamplifier for analog detection:

bandwidth:	DC-10 MHz
gain:	11mV/µA into 50 Ω
spectral noise current:	
DC...1MHz	2 pA/√Hz
DC...10 MHz	7.2 pA/√Hz
output polarity:	negative
output signal:	0...-1V (max), 0...-100mV (typ. operation) into 50 Ω

Integrated TE cooler and temp. controller:

Detector temperature:	+0°C (+25°C for 3mm APD)
Temperature stability:	<0.5 K

Power supply:

input:	230V/50 or 110V/60 Hz
output:	+5V, -5V, +15 V, linear regulated.

HV supply:

voltage range:	0...+450V
max. current:	0.6 mA
voltage ripple:	<0.005%

Environmental conditions:

Operating temperature:	0°C to 30°C (non condens.)
Storage temperature:	-40°C to 70°C

Signals

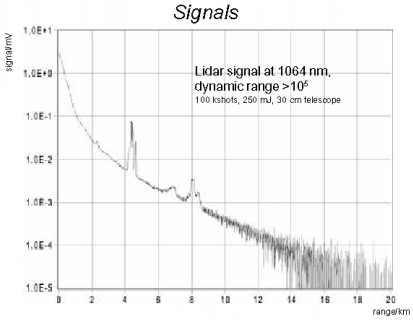

International distribution:

USA:
Boston Electronics Corp.
91 Boylston Street
Brookline MA 02445
phone (800)347-5445
fax (617)731-0935

e-mail: boselec@world.std.com
www.boselec.com

Pacific Rim:
Electronics Optics Res., Ltd.
3-fl., Onoda Building,
4-26-19, Koenzi-Minami-Ku
Tokyo 166, Japan
phone 03-3314-5699
fax 03-3314-2333
email eor@tkd.att.ne.jp

United Kingdom:
Photonic Solutions PLC
Gracemount Business Pavillons,
40 Captains Road,
Unit A2/A3, Edinburgh, EH17 8QF
phone: 0131 664 8122
fax: 0131 664 8144
email: sales@psplc.com
www.psplc.com

other countries:
Licel GbR
Chausseestr. 34/35
D-10115 Berlin
phone +49.30.283 917 37
fax +49.30.283 917 38

e-mail: info@licel.com
www.licel.com

A 9 JFJ –LIDAR system: list of technical specifications

TRANSMITTER

Nd:YAG solid state laser

Manufacturer and model: Coherent Infinity 40-100
Wavelength: 1064nm (fundamental
532nm (second harmonic)
355nm (third harmonic)
Repetition rate: up to 100Hz
Max. pulse energy @100Hz: 400mJ @1064nm, 200mJ @532nm and 160mJ @355nm
Pulse to pulse stability @100Hz:1.7% @1064nm, 2.5% @532nm and 2.5% @355nm
Pulse width (typical): 3.5ns @1064nm and 3.0ns @532, 355nm
Line width (typical): < 250MHz (single shot)
Beam diameter (near-field): > 95% of pulse energy into 5.5mm diameter at SHG crystal plane
Beam diameter (far-field): > 84% of pulse energy into 0.7mrad divergence
Divergence (full-angle): < 0.7mrad
Timing jitter (rms): < 500 psec rms

Glan-Thompsom prism

Manufacturer: Optics for Research, Aperture: 10mm, T:95%, Ext. ratio: $5x10^{-5}$

Beam Expander

Manufacturer: ET «D & D», Sofia, Material:Fussed silica with antireflection coatings, Wavelength: 355, 532 and 1064nm, Magnification: 5, Input aperture diameter: 6mm

Motorized optical mount

Manufacturer and model: New Focus, model #8852, Style: Corner, Optics diameter: 2 inches
Motorized axes: 3, Angular resolution: 0.7mrad, Driver: New Focus economical multi-axes driver model #8801

RECEIVER

Telescope (for upper tropospheric observations)

Manufacturer and model: Vixen, model R200SS, Configuration: Newton, Primary mirror: 200 mm, parabolic multi-coated, Focal length: 800mm

Telescope (for stratospheric observations)

Manufacturer: Grubb Parsons & Co. Ltd., Configuration: Cassegrain, Primary mirror: 760 mm, paraboloidal, glass type Duran 50, aluminized, Cassegrain convex mirror: 7.0 inches, hyperboloid, fused quartz type Herasil special, aluminized, Focal length: 11400 mm

Beamsplitter (BS1)

Manufacturer: Barr Associates Inc., Diameter: 2 inches, Angle of incidence: 45, Transmission: 88% @532nm, 90% @607,1064nm, Reflection: 95% @355, 387, 408nm

Beamplitter (BS2), Manufacturer: Omega Optical, Diameter: 2 inches, Angle of incidence: 45, Transmission: 70% @387nm, 85% @408nm, Reflection: 97% @355nm

Beamsplitter (BS3), Manufacturer: Barr Associates Inc., Diameter: 2 inches, Angle of incidence: 45, Transmission: 97% @408nm, Reflection: 99% @387nm

Beamsplitter (BS4), Manufacturer: Barr Associates Inc., Diameter: 2 inches, Angle of incidence: 45, Transmission: 90% @607,1064nm, Reflection: 95% @532nm

Beamsplitter (BS5), Manufacturer: Barr Associates Inc., Diameter: 2 inches
Angle of incidence: 45, Transmission: 90% @1064nm, Reflection: 95% @607nm

Bandpass filter (F1)
Manufacturer: Barr Associates Inc., Diameter: 1 inch, Center wavelength: 354.67nm,
Bandwidth FWHM: 0.97nm, Transmission: 58% @355nm
Out-of-band transmission: OD > 4

Bandpass filter (F2)
Manufacturer: BarrAssociates Inc., Diameter:1 inch, Center wavelength: 386.4nm,
Bandwidth FWHM: 3.0nm, Transmission: 78.5% @387nm, Out-of-band transmission :OD>5
Manufacturer: Barr Associates Inc., Diameter:1 inch, Center wavelength: 386.65nm
Bandwidth FWHM: 0.50nm, Transmission: 66%@387nm, Out-of-band transmission :OD>5

Bandpass filter (F3)
Manufacturer: Barr Associates Inc., Diameter: 1 inch, Center wavelength: 408.55nm
Bandwidth FWHM: 3.80nm, Transmission: 66%@408nm, Out-of-band transmission:OD>5

Manufacturer: Barr Associates Inc., Diameter: 1 inch, Center wavelength: 407.49nm, Bandwidth FWHM: 0.5nm, Transmission: 53% @408nm, Out-of-band transmission: OD>5

Bandpass filter (F4)
Manufacturer:L.O.T.-Oriel GmbH, Diameter:1 inch, Center wavelength 532.16nm, Bandwidth FWHM:0.93nm,Transmission:73%@532nmOut-of-band transmission: OD>4
Manufacturer: Andover Corporation, Diameter:1 inch, Center wavelength: 532.05nm,
Bandwidth FWHM: 1.2nm, Transmission: 41% @532nm, Out-of-band transmission: OD>4

Bandpass filter (F5)
Manufacturer: Barr Associates Inc., Diameter:1 inch, Center wavelength: 607.28nm,
Bandwidth FWHM: 0.9nm, Transmission: 69% @607nm, Out-of-band transmission: OD>5
Manufacturer: Barr Associates Inc.Diameter: 1 inch, Center wavelength: 607.3nm, Bandwidth FWHM:0.9nm, Transmission:61% @607nm, Out-of-band transmission: OD>4

Bandpass filter (F6),
Manufacturer: Barr Associates Inc., Diameter: 1 inch, Center wavelength: 1063.89nm, Bandwidth FWHM:1.1nm, Transmission:81% @1064nm, Out-of-band transmission: OD>4

Manufacturer: Barr Associates Inc., Diameter:1 inch, Center wavelength: 1064.07nm,
Bandwidth FWHM:1.0nm, Transmission:72% @1064nm, Out-of-band transmission: OD>4

Wollaston prism (WP)
Manufacturer: Casix PWT5010, Material: Calcite with Single layer MgF2 AR Coating @633nm, Extinction ratio: $<5x10^{-5}$, Angular separation: 15 – 20°, Diameter: 10mm

Photomultiplier (PMT_1)

Manufacturer and reference Hamamatsu photosensor module, H6780-06 series,
Type:End-on photomultiplier with built-in high voltage power supply, Effective area:8mm, Spectral response range:185-650nm, Time response: 0.78ns @0.8V on control voltage, Gain:6.0 105, Radiant sensitivity: 43mA/nW @0.8V on control voltage, Dark current: Typ. 0.2nA @0.8V on control voltage, Max. 10nA @0.8V on control voltage

Photomultiplier (PMT_2)

Manufacturer and reference Thorn EMI, QA9829B series
Type: End-on photomultiplier, Effective area:45mm, Spectral response range:320-650nm, Time response:3ns, Anode sensitivity:500A/lm, Gain: 6.7 106, Dark current:0.4nA

Photomultiplier (PMT_3)

Manufacturer and reference Thorn EMI, B9202 series
Type: End-on photomultiplier, Effective area: 45mm, Spectral response range: 320-850nm, Time response: 5ns, Anode sensitivity: 200A/lm, Gain: 0.8 106, Dark current: 1.0nA

Si-Avalanche Photodiode (APD)

Manufacturer and reference EG&G, C30954/5e
Type: Integrated TE cooler and temperature controller, Effective area: 1.5mm, QE @650nm: >80%, Responsivity @1060nm: 34A/W typ., QE=38%, Dark current @22oC: 100nA, Spectral noise current:0.5 pA/sqrt(Hz) max.
Preamplifier: bandwidth: DC-200MHz gain: 11mV/mA into 50W, output polarity:negative
output signal: 0...-1V max.
Geiger mode operation: single photon rise time:< 5ns

Transient recorder

Manufacturer and model: Licel
General description: Built in analog and photon counting acquisition device
Analog acquisition:
- Signal input range: 0-20, 0-100, 0-500 mV @ 50 W load
- A/D resolution: 12 bit
- Sampling rate: 20 MHz, giving a lidar spatial resolution of 7.5 m
- Summation memory: 4094 acquisitions for the two channels together
- SNR single shot: 66 dB @ 100 mV
- Memory depth: 8192 or 16384 bins (i.e. 61440 m or 122880 m)
- Max repetition rate: 150 Hz @ 400 ms signals, 75 Hz @ 800 ms signals
- Trigger delay and jitter: 50 ± 12.5 ns

Photon counting acquisition:
- Signal input range: 0-20, 0-100 mV @ 50 W load
- Discriminator: 64 levels software controlled
- Bandwidth: 10 - 250 MHz
- Summation memory: 4094 acquisitions for the two channels together
- Memory depth: 8192 or 16384 bins (i.e. 61440 m or 122880 m)

Trigger: Two trigger inputs to acquire signals in two separate memories
Threshold and slope 2.5 V, positive, 50 W load
Delay and jitter: 50 ± 12.5 ns

A 10 Inter-comparison with the Neuchatel Observatory lidar

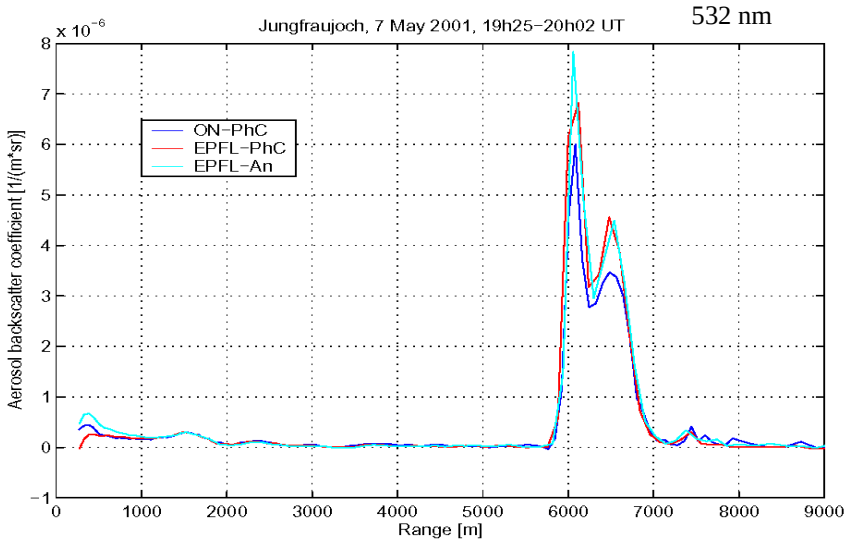

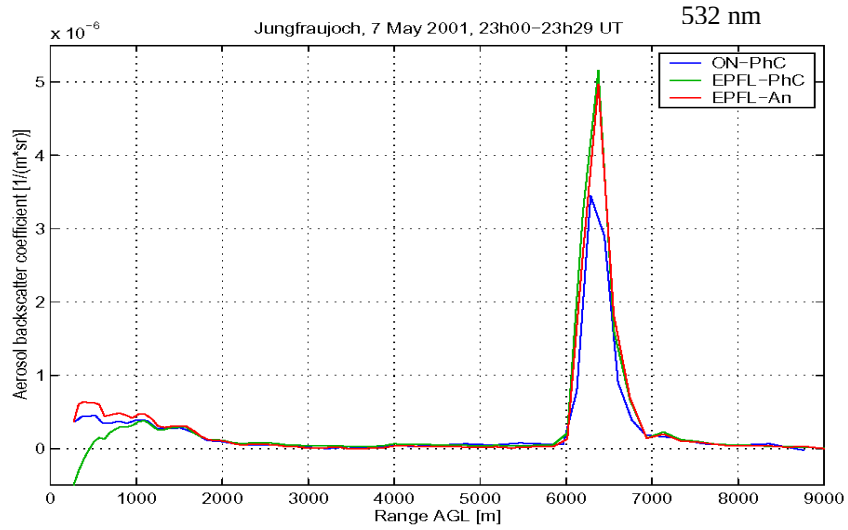

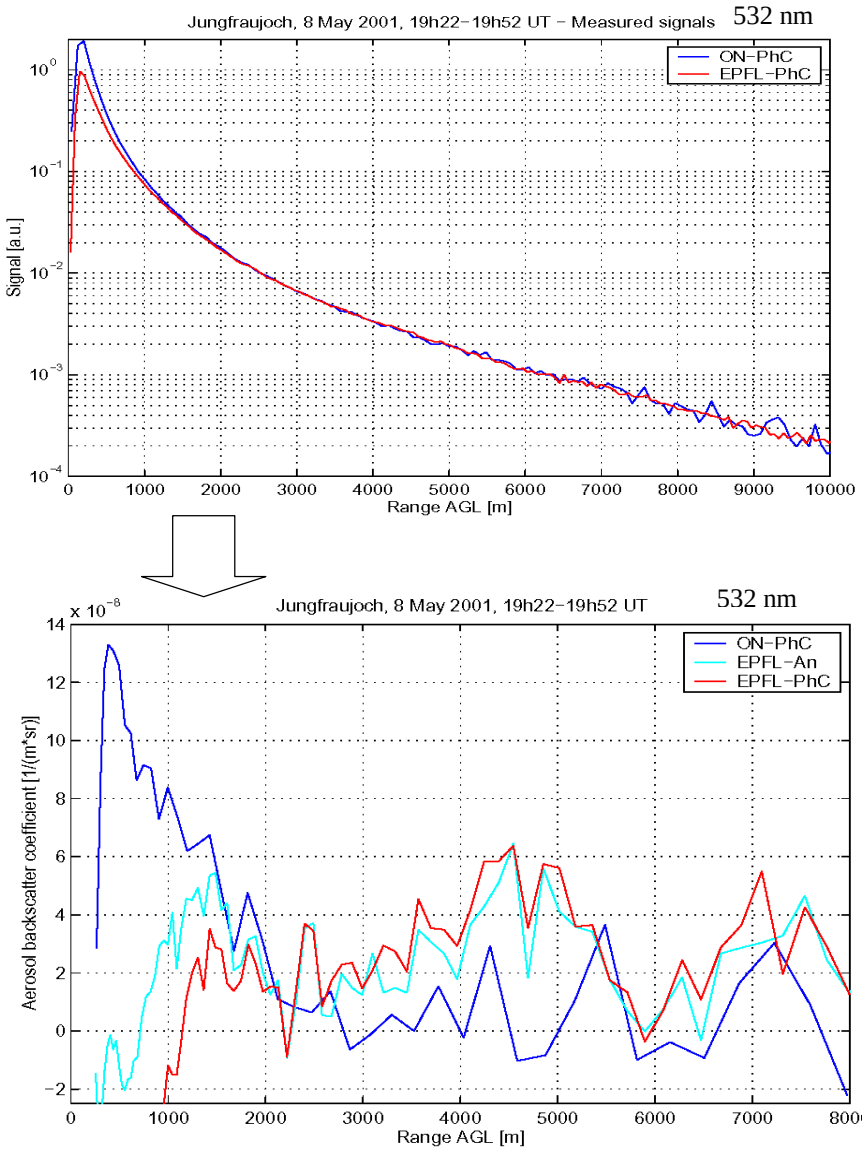
Jungfraujoch, 8 May 2001, 19h22–19h52 UT – Measured signals
532 nm
ON–PhC
EPFL–PhC
Signal [a.u.]
Range AGL [m]
Jungfraujoch, 8 May 2001, 19h22–19h52 UT
532 nm
x 10^-8
ON–PhC
EPFL–An
EPFL–PhC
Aerosol backscatter coefficient [1/(m*sr)]
Range AGL [m]

A 11 Inter-comparison with the Johns Hopkins University lidar

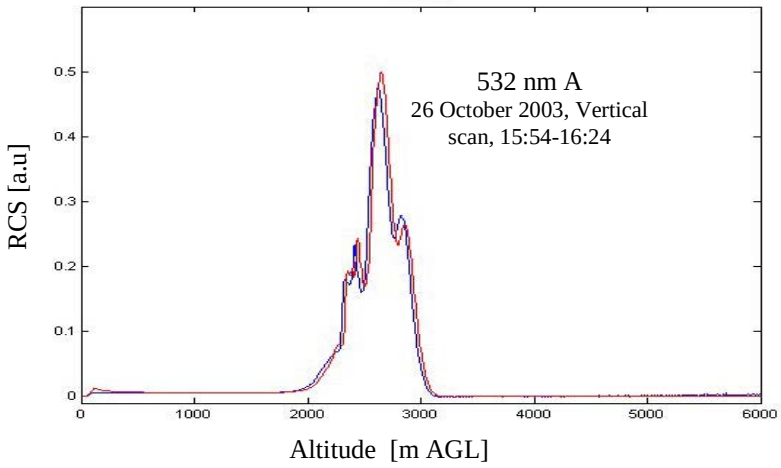

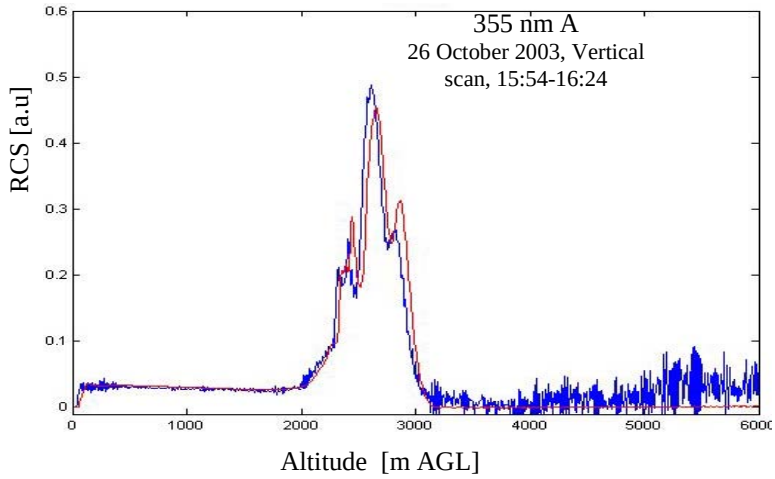

A 12 Aerosols typology

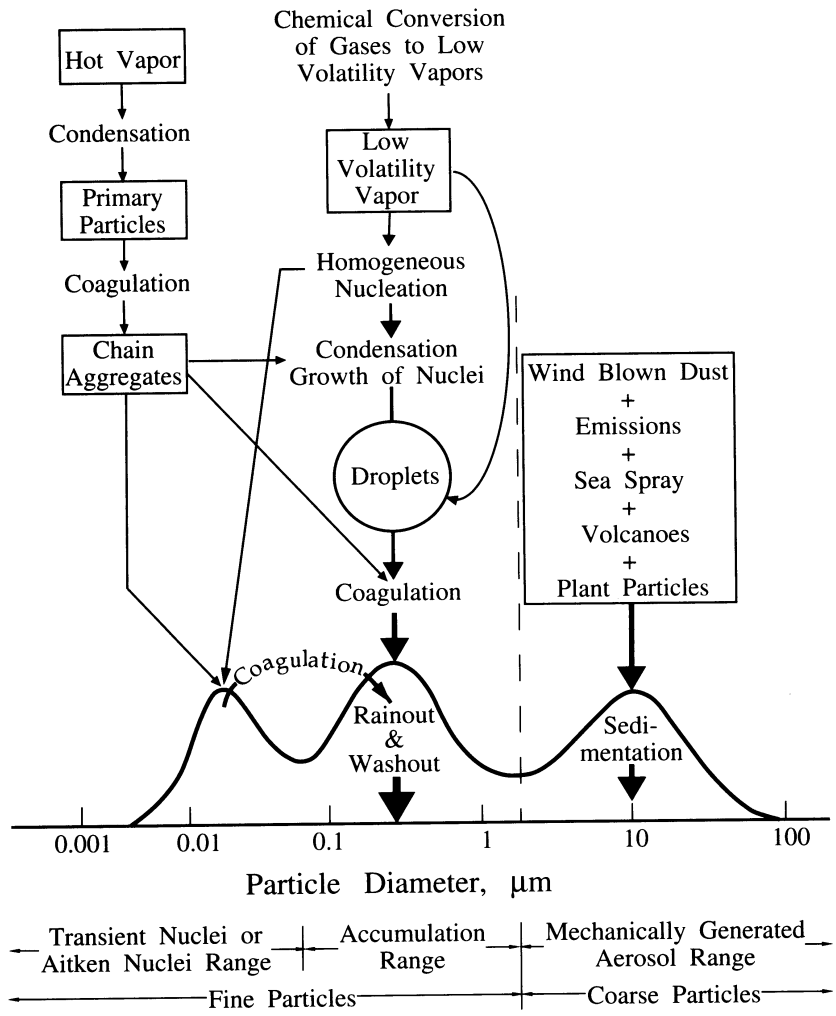

A 13 JFJ-LIDAR: 2000-2003 measurements series

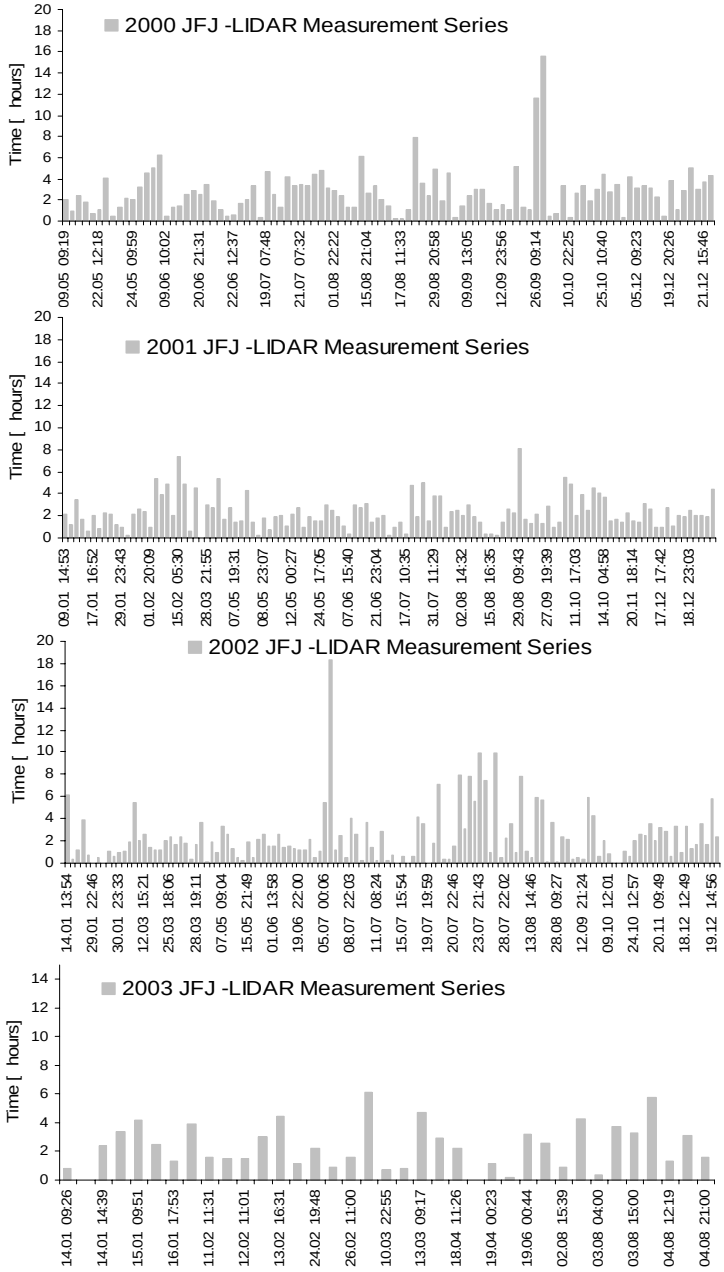

A 14 Poisson statistics and the photon - counting detection mode

At lower backscatter intensities (e.g. Raman processes) the detection is possible only in photon-counting mode. The photon counting detection may be described by the Poisson statistics, which is given by: $P(N) = \frac{\mu^N e^{-\mu}}{N!}$, where P(N) is the probability to record N counts in a single measurement, with the property that its standard deviation $\sigma_N = \sqrt{\mu} \sim \sqrt{N}$, where μ is the average. The counting precision $\frac{\sigma_N}{N}[\%] = \frac{100\%}{\sqrt{N}}$ and is improving with the increasing of counts number.

A 15 MatLab front panel of the main sub-routine

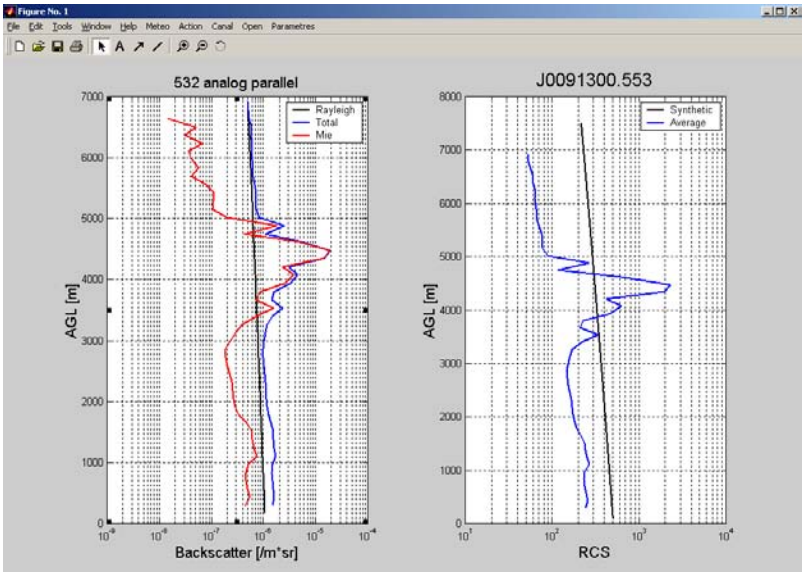

(Rayleigh, Mie and Total backscatter coefficient in the left panel and simulated Rayleigh and Elastic RCS signals on the right panel)

A 16 Clouds texture: sky black and white pictures

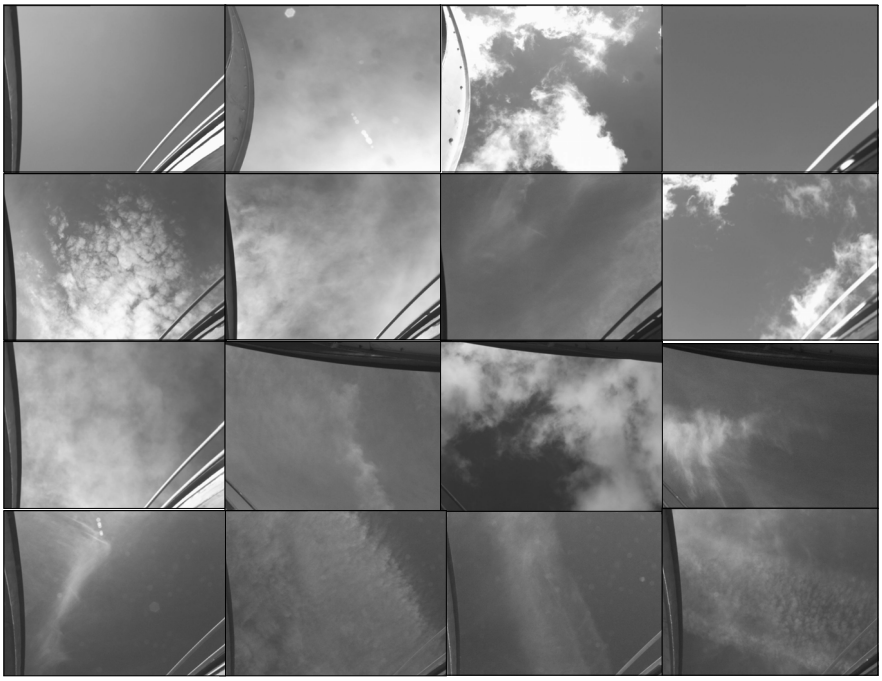

A 17 LabView front panel for RCS, Rayleigh, TMR and Depolarization calculus

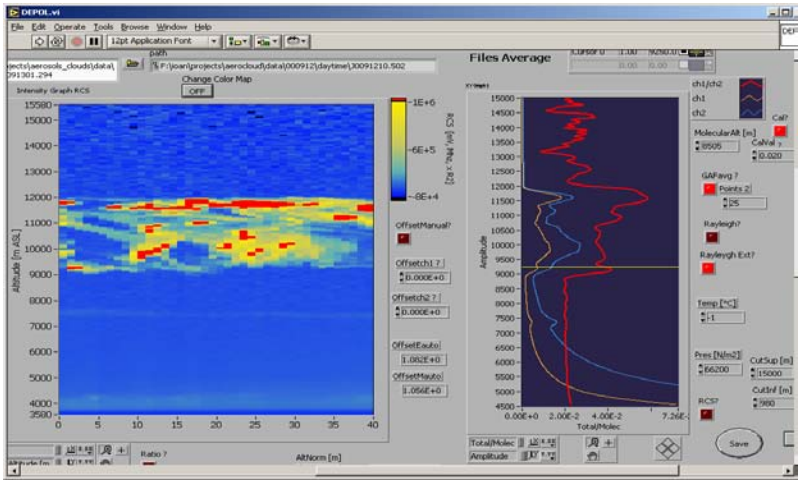

A 18 LabView: Raman 387 – Elastic 355 nm inversion combined method

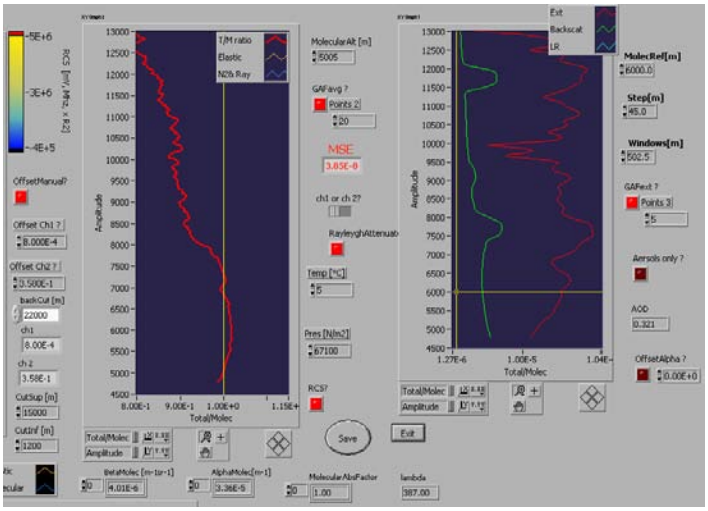

A 19 LabView: for Raman 532 – Elastic 532 nm inversion combined method

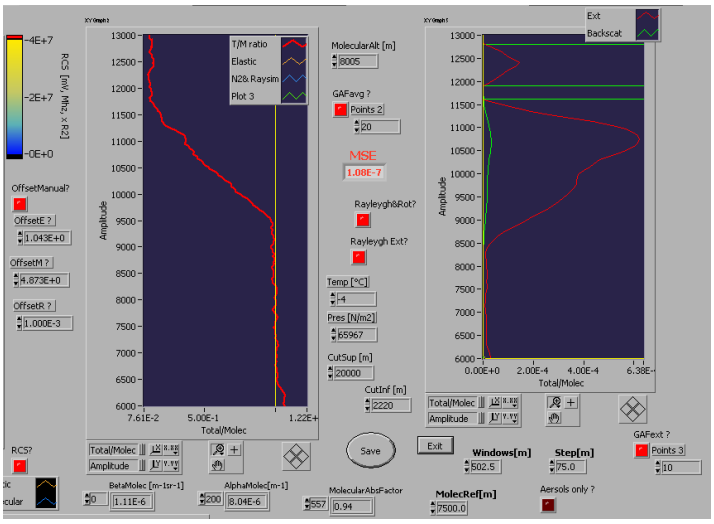

A 20 RSL Suphotometer specifications

RSL Remote Sensing Laboratories
Department of Geography
University of Zurich

Sunphotometer

"University of Arizona Auto Sun-Tracking 10-Channel Solar Radiometer Instrument"

Manufactured by the Department for Electrical Engineering, University of Tuscon, Arizona, 1995 (Serial Number 14)

Purpose

The Reagan Sunphotometer is a sun-looking ground based instrument for atmospheric measurements. In Remote Sensing applications it is mainly used for atmospheric measurements in order to improve atmospheric correction algorithms. It therefore is used as atmospheric ground truthing instrument in field campaigns. It's continuous monitoring of the state of the atmosphere allows furthermore conclusions on atmospheric stability and daily developments of aerosol contents. Cross calibration with other instruments will help to evaluate their performance.

Abilities

- Observation of atmospheric aerosol optical thickness
- Retrieval of atmospheric aerosols particle size distribution
- Measurement of columnar atmospheric water vapor contents
- Measurement of columnar atmospheric ozone contents

Specifications

- 10-channel parallel co-alligned FOV tube with FOV ≈ 3.2°
- Channels at 382, 410, 501, 611, 669, 721, 780, 872, 940, and 1033 nm.
- Narrow band three-cavity Interference Filters with FWHM of ≈ 8 to 12 nm
- Digitzation 16 bits
- RS-232 line driver/receiver
- Temperature Stability at ≈ 43 ± 0.5 °C by heater control
- Data logger for 2-3 days of data acquisition (32 K byte non volatile RAM)
- Automatic Sun tracking with four quadrant detector technology, ± 17° Tracking capability

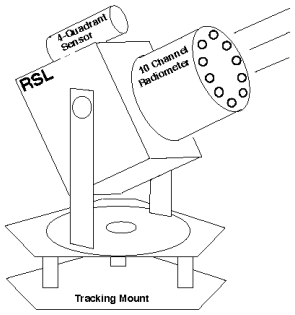

- 12 V Power supply or battery for one day of independent usage
- Average Power Consumption 15W
- Fully transportable (Total Weight: ca. 13.5 kg + boxes)

For more information please contact dschlapf@geo.unizh.ch.

A 21 Atmospheric -TOD - sun-photometer measurements on May 2001

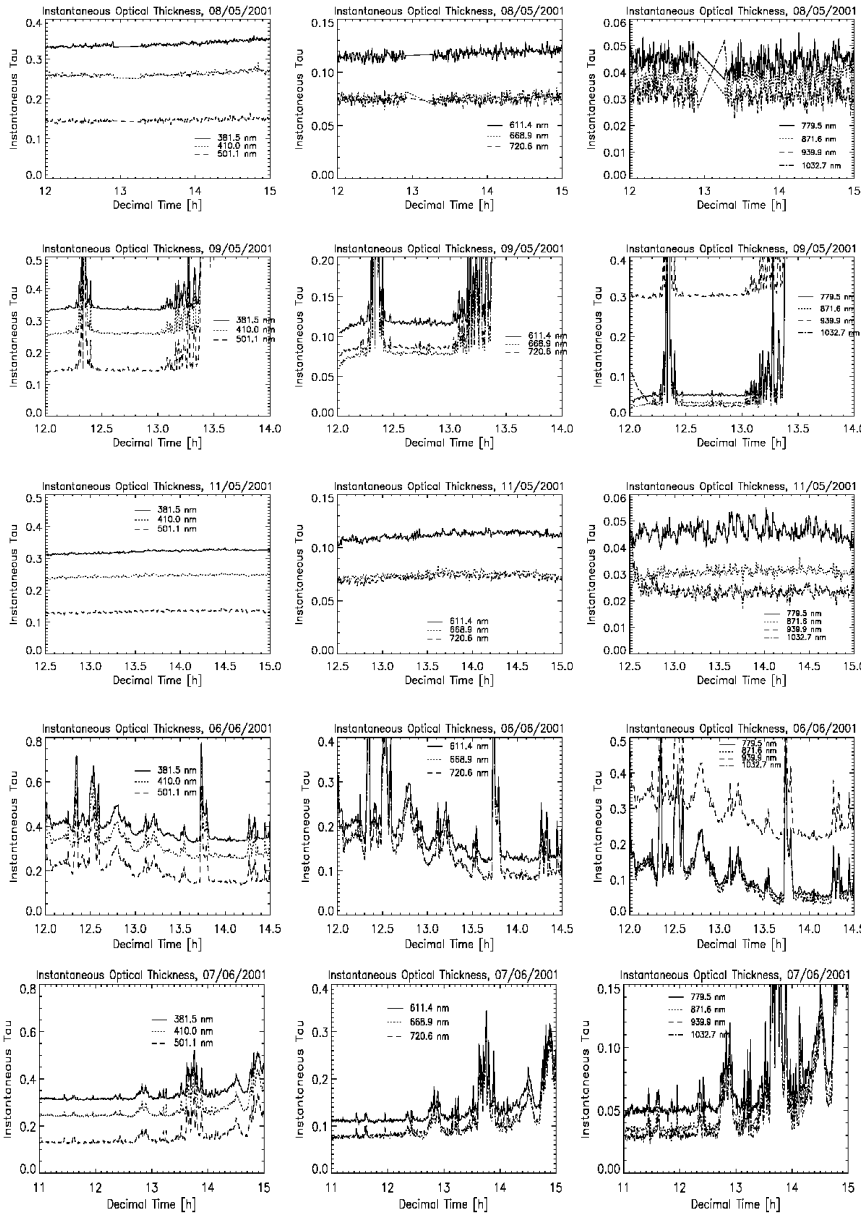

A 22 Water vapor definitions and transformation equations

$n_{H_2O}[\#molec/cm^3] = \frac{N_{H2O}[\#molec]}{V[cm^3]}$, water vapor molecular concentration

$\rho_{H_2O}[\mu g/m^3] = \frac{m_{H2O}[\mu g]}{V[m^3]}$, water vapor density (or mass concentration)

$\xi_{H_2O}[ppmv] = \frac{V_{H2O}[m^3]}{V[m^3]}$, water vapor volume mixing ratio, 1ppm = 10^{-6}

$q_{H_2O}[g/kg_{dry\ air}] = \frac{m_{H2O}[g]}{m_{dry\ air}[kg]}$, water vapor mixing ratio (q)

$q_{H_2O}[g/kg_{air}] = \frac{m_{H2O}[g]}{m_{air}[kg]}$, specific humidity (SH)

$RH_{H_2O}[\%] = 100\frac{P_{H_2O}[hPa]}{P_{sat}[hPa]} = 100\frac{e}{e_s} = 100\frac{q_{H_2O}}{q^{sat}_{H_2O}}$, relative humidity (RH)

$P_{sat}[hPa] = 6.1086\ \exp\left(\frac{17.856\ T_{air}[°C]}{245.52 + T_{air}[°C]}\right)$, saturation pressure used formula

$q_{H_2O}[g/Kg_{dry\ air}] = \frac{M_{H_2O}[g]}{M_{dry\ air}[g]}\frac{RH\ [\%]\cdot P_{sat}}{100\cdot\left(P_{air} - 0.01\ RH\cdot P_{sat}\right)}$, RH → q

$q_{H_2O}[g/Kg_{dry\ air}] = \frac{M_{H_2O}[g]P_{H_2O}[hPa]}{M_{dry\ air}[g]\left(P_{air}[hPa] - P_{H_2O}[hPa]\right)}$, $P_{H2O} \rightarrow q$

$P_{H_2O}[hPa]V[m^3] = \frac{m_{H_2O}[g]}{M_{H_2O}[g]}R[J\ K^{-1}molec^{-1}]\ T[K]$, $m_{H2O} \rightarrow P_{H2O}$

$n_{H_2O}[molec.m^{-3}] = \frac{N_{H_2O}[molec]}{V[m^{-3}]} = \frac{P_{H_2O}[hPa]}{k_B[J\ K^{-1}]T[K]}$, $P_{H2O} \rightarrow n_{H2O}$

$1[ppm] = 10^{-6}\times\frac{P}{k_BT}[molec.m^{-3}]$; $1[ppm]_{H_2O} = 1608\times q_{H_2O}[g/kg_{dry\ air}]$, q→ξ

$\xi_{H_2O}[ppm] = \frac{R[J.mol^{-1}.K^{-1}]T_{air}[K]}{M_{H_2O}[g.mol^{-1}]P_{air}[Pa]}\rho_{H_2O}[\mu g.m^{-3}]$, $\rho_{H2O} \rightarrow \xi$

$P_{H_2O}\,V_{H_2O} = N_{H_2O}R\,T \xrightarrow{\times M_{H_2O}} M_{H_2O}P_{H_2O} = \underbrace{\frac{N_{H_2O}M_{H_2O}}{V_{H_2O}}}_{\rho_{H_2O}}R\,T$, ideal gas law for water vapor

$\rho_{H_2O} = \frac{M_{H_2O}P_{H_2O}}{R\,T}$, $\rho_{dry\ air} = \frac{M_{dry\ air}P_{dry\ air}}{R\,T} = \frac{M_{dry\ air}\left(P_{tot} - P_{H_2O}\right)}{R\,T}$, $q_{H_2O}(Z) = \frac{\rho_{H_2O}(Z)}{\rho_{dry\ air}(Z)}$,

$IWV_{H_2O}[mm] = \int_{Zo}^{Z}\rho_{H_2O}(z)dz$

A 23 Main routine for water vapor mixing ratio retrieval

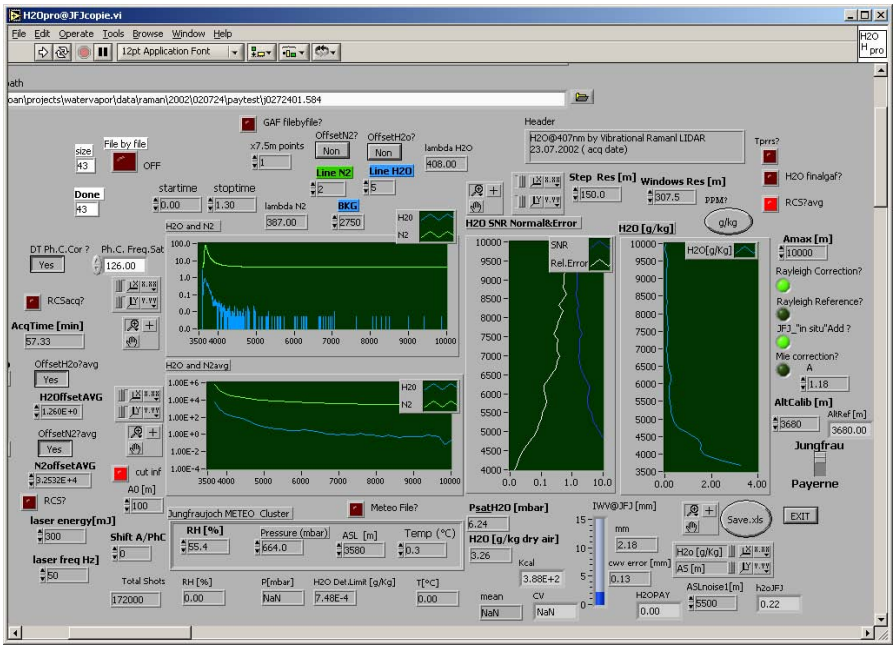

H2O@407nm by Vibrational Ramanl LIDAR
24.07.2002 (acq date)

Startime [h.min]	Stoptime [h.min]	AcqTime [min]	LaserFreq [Hz]	SatFreq [Counts]	LaserEnerg [mJ]	Shots [#]	Windows [m]	Step [m]	Tavg [°K]	Pavg [mbar]	RHavg [%]	AltCal [m]	Psat [mbar]	H2O [g/kg]	H2Odl (3580)	H2Odl(snr1)	JFJcwv [mm]
0.00	2.00	117.33	50.00	125.00	400.00	352000.00	300.00	75.00	-0.41	663.58	69.83	3630.00	5.93	3.90	0.00	1.32	7.88

ASL [m]	N2 [mV/Mhz]	H2O [Mhz]	H2O [g/kg]	SNR	ErH2O [g/Kg]	Ph2o [N/m2]	Dens [g/m3]	Psat [N/m2]	RH [%]	Raycor	Pay [g/Kg]	T [K]
3630.00	276624.33	4154.47	3.90	1331.20	0.01	414.71	3.29	592.83	69.95	1.00	2.27	272.74
3705.00	132619.54	1959.74	3.84	628.48	0.01	404.47	3.22	572.07	70.70	1.00	2.45	272.25
3780.00	63234.19	1030.50	4.23	330.95	0.02	441.62	3.52	551.96	80.01	1.00	2.40	271.76
3855.00	37982.90	593.81	4.06	191.13	0.03	419.80	3.35	532.48	78.84	1.00	2.35	271.28
3930.00	25545.42	371.85	3.78	120.06	0.03	387.39	3.10	513.61	75.43	1.00	2.30	270.79
4005.00	18381.66	244.88	3.46	79.41	0.04	351.40	2.81	495.34	70.94	1.00	2.25	270.30
4080.00	13819.32	181.76	3.41	59.20	0.04	343.70	2.76	477.65	71.96	1.00	2.21	269.81
4155.00	10738.20	151.57	3.66	49.53	0.05	365.22	2.94	460.53	79.31	1.00	2.11	269.33
4230.00	8561.64	130.02	3.93	42.63	0.06	389.07	3.13	443.95	87.64	1.00	1.98	268.84
4305.00	6964.12	113.27	4.21	37.27	0.06	412.60	3.33	427.91	96.42	1.00	1.91	268.35
4380.00	5750.75	97.37	4.38	32.18	0.07	425.35	3.44	412.38	103.15	1.00	1.95	267.86
4455.00	4806.22	84.15	4.53	27.94	0.08	435.56	3.53	397.36	109.61	1.00	1.91	267.38
4530.00	4058.02	67.35	4.29	22.56	0.09	409.13	3.32	382.83	106.87	1.00	1.84	266.89
4605.00	3458.54	50.10	3.74	17.04	0.09	354.02	2.88	368.77	96.00	0.99	1.78	266.40
4680.00	2974.54	36.60	3.18	12.72	0.09	298.13	2.43	355.17	83.94	0.99	1.72	265.91
4755.00	2581.57	26.62	2.66	9.52	0.09	247.72	2.02	342.03	72.43	0.99	1.65	265.43
4830.00	2259.01	18.25	2.09	6.84	0.09	192.39	1.57	329.31	58.42	0.99	1.53	264.94
4905.00	1993.31	14.55	1.88	5.66	0.09	172.23	1.41	317.03	54.33	0.99	1.41	264.45
4980.00	1769.50	12.20	1.78	4.91	0.10	161.16	1.32	305.15	52.81	0.99	1.29	263.96
5055.00	1579.99	10.20	1.66	4.27	0.10	149.49	1.23	293.67	50.90	0.99	1.24	263.48
5130.00	1416.93	8.80	1.60	3.82	0.11	142.46	1.17	282.58	50.41	0.99	1.55	262.99
5205.00	1276.12	7.85	1.59	3.51	0.12	139.76	1.15	271.86	51.41	0.99	1.85	262.50
5280.00	1154.19	6.58	1.47	3.11	0.13	128.21	1.06	261.51	49.03	0.99	2.15	262.01
5355.00	1045.94	5.75	1.42	2.84	0.13	122.55	1.01	251.51	48.73	0.99	2.34	261.53
5430.00	953.71	5.43	1.46	2.74	0.15	125.58	1.04	241.85	51.92	0.99	2.20	261.04
5505.00	875.15	5.13	1.51	2.64	0.16	128.04	1.06	232.53	55.06	0.99	2.04	260.55
5580.00	803.43	4.98	1.59	2.59	0.17	134.06	1.12	223.53	59.97	0.99	1.94	260.06
5655.00	741.12	3.73	1.29	2.19	0.17	107.83	0.90	214.84	50.19	0.99	1.84	259.58
5730.00	684.52	3.70	1.39	2.19	0.19	114.82	0.96	206.46	55.61	0.99	1.76	259.09
5805.00	630.16	3.50	1.43	2.12	0.20	116.83	0.98	198.37	58.90	0.99	1.69	258.60

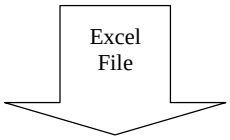

A 24 Dead time photon counting correction sub-routine

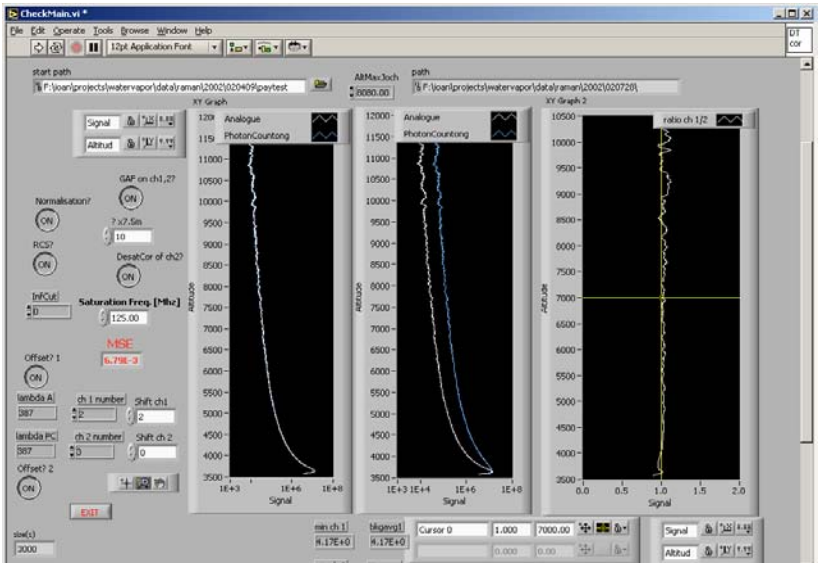

A 25 Payerne radiosoundings data treatment sub-routine

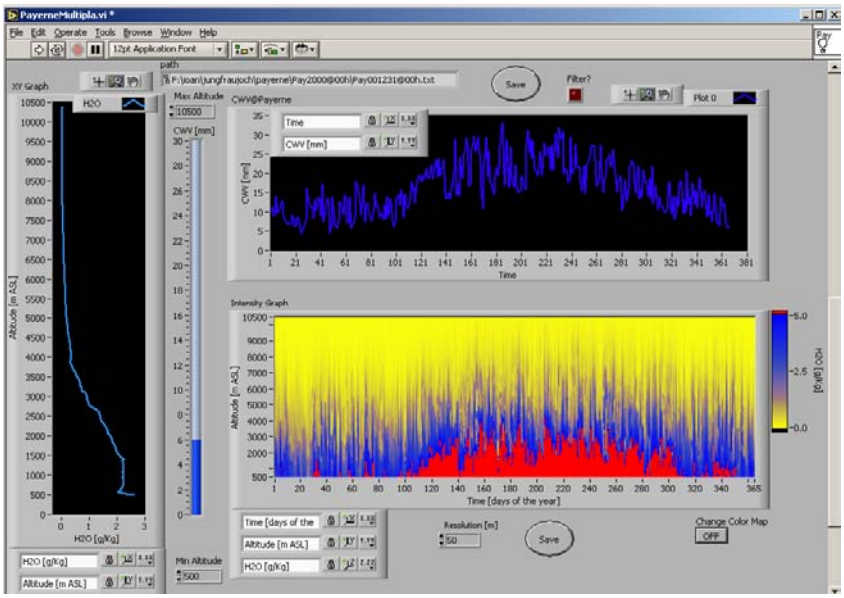

A 26 GPS principle for water vapor column retrieval [2]

As the GPS signals propagate from the GPS satellites to the receivers on the ground, the atmosphere delays them. There is a dispersive effect of the ionosphere due to the free charge (i.e. electrons concentrations) and a non-dispersive effect of the troposphere. The ionosphere effects are largely removed by the use of linear combination of dual frequency data. The remaining atmospheric delay is due to the electrically neutral atmosphere, which is non-dispersive to GPS frequencies. The troposphere constitutes most of the neutral atmosphere. The tropospheric delay consists of two components: the hydrostatic (or "dry" by induced dipole moment) accounts for approximately 90% of the delay and the "wet" (due to the permanent water vapor dipole) component proportional with the moisture delay. Because the effects of water vapor can be indistinguishable from the effects of background variations in temperature and pressure, the Total Zenith Delay (TZD) will be estimated and the wet component extracted later

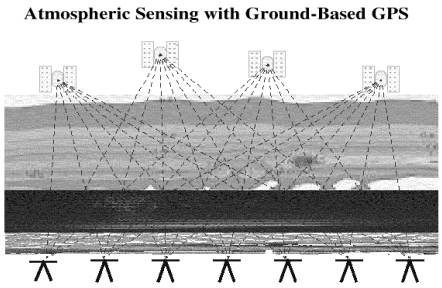

In 1993, the first GPS remote sensing experiment for probing the earth's atmosphere was created and called GPS/MET. The phase delay along the zenith direction is called the “zenith total delay” and is related to the atmospheric refractivity, N(z) by:

$ZTD = 10^{-6} \int_{Zantena}^{Zsat \cdot \cos\theta} N(z)dz$, where the atmospheric refractivity is expressed by:

$N(z) = \underbrace{77.6\frac{P}{T}}_{dry\cdot delay} + \underbrace{3.73\cdot 10^5 \frac{q}{T^2}}_{wet\cdot delay}$, with P dry air pressure, T the air temperature and q specific humidity . The dry term contributes up to 240 cm to the total zenith delay while the wet term contributes up to 40 cm.

Using the hydrostatic approximation and the ideal gas state equation the dray delay may be expressed as: $ZDD = -7.76\cdot 10^{-6}\frac{R}{g}\times P$ and in fact a simple measurement of the pressure at the location of the antenna receiver is allowing the calculation of the ZDD. As the ZTD is GPS measured the ZWD = ZTD-ZDD, and finally the precipitable water vapor column (IWV) is given by: IWV = 0.15 * ZWD

[2] http://apollo.lsc.vsc.edu/classes/remote/lecture_notes/gps/theory/theoryhtml.htm

A 27 Details of the DGP optical combinations[3]

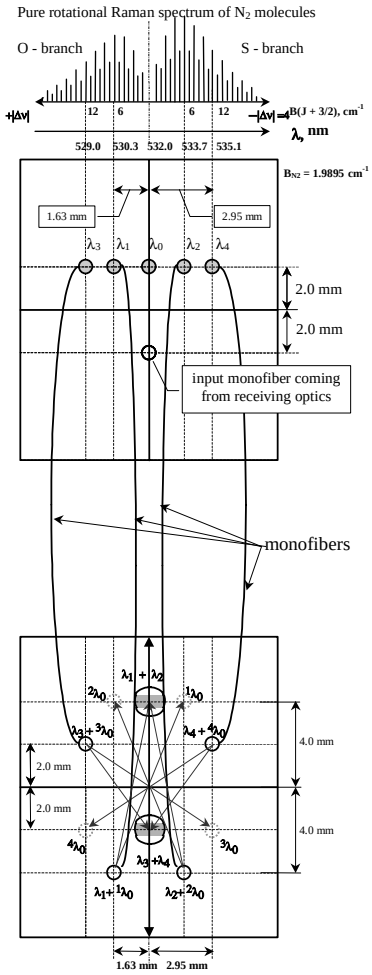

Arrangement of the monofiber ends in the input and output monofiber blocks of the DGRM.

The diagram on top of this figure shows schematically the PRRS of nitrogen molecules. The white light of the lidar backscatter plus sky background comes, being transmitted through the input monofiber from the lidar receiver towards the lens in the first monochromator that collimates the flux and directs it to the grating No.1. Then the portion of radiation reflected back by the grating, within the spectral region desired, is focused in the focal plane of this same lens thus making up the spectral image of the entrance monofiber end or, in other words, the spectrum of radiation received with the lidar optical antenna from the atmosphere. The spots marked with the letters λ_1 to λ_4 (Fig.2, the top block) show the monofiber ends that isolate four spectral portions (λ_1 to λ_4) in the S and O branches of the PRRS of nitrogen and oxygen molecules symmetric relative to the line of exciting radiation at λ_0. The radiation within the spectral intervals at λ_1 to λ_4 is contaminated with the radiation of the wavelength λ_0 due to spurious signal from Mie+Rayleigh scattering line. Normally, the gratings provide for a contrast on the order of 10^4. So, in the atmosphere the contribution coming from the line of unshifted scattering at λ_0, as a spurious light noise, into the intensity of PRRS of nitrogen and oxygen may be compared with the intensity of PRRS portions isolated. The symbols ${}^i\lambda_0$ are for spurious radiation component at λ_0 that must be removed or suppressed down to an acceptable level. The cross points at the centers of this blocks are the positions of the corresponding monochromators' optical axes, the vertical solid line being parallel to the grating's grooves and the horizontal one being perpendicular to them. The lenses in both chambers of the DGRM construct the spectral images of the input ends of the monofibers along the lines that are parallel to the horizontal solid line and at exactly the same distance on the opposite side from it because of the specular reflection from the grating in the plane that is parallel to the grooves. The spots with the nearby indices (λ_i + ${}^i\lambda_0$) show the position of the monofiber ends from which radiation of the corresponding PRRS portions isolated by the first monochromator comes out toward the grating 2 through the lens in the second monochromator. The arrows drawn in the scheme of the monofiber block of the second monochromator (bottom) show the position where the corresponding images of the input ends of monofibers are to be formed by the light of the wavelengths λ_0 and λ_i at the DGRM exit after being reflected (and dispersed) from the grating 2 and focused back by the lens. In this particular arrangement the diffraction grating 2, in the second monochromator, works in the dispersion subtraction mode. The radiation of pairs of symmetric, with respect to λ_0 line, portions of the PRRS is being optically summed within the shaded stripes of the bigger circles at the exit of the second monochromator. The length of these stripes equals to a doubled diameter of the monofiber end used to isolate the corresponding PRRS portion, provided that all the λ_i monofibers have the same diameter and the lenses and gratings in both monochromators are identical. This is simply because it equals the width of the instrumental contour of the first monochromator at the base line. On the contrary, the spots ${}^i\lambda_0$ have the size that is exactly the size of the monofiber end because these are the images formed by the monochromatic spurious light of λ_0 wavelength.

[3] (from Ansmann, A., et al. *Double-grating monochromator for a pure rotational Raman lidar*. in *Fifth International Symposium on Atmospheric and Ocean Optics*. 1998: Proc. SPIE.

A 28 LabView routine for temperature retrveal using PRRS lidar signals

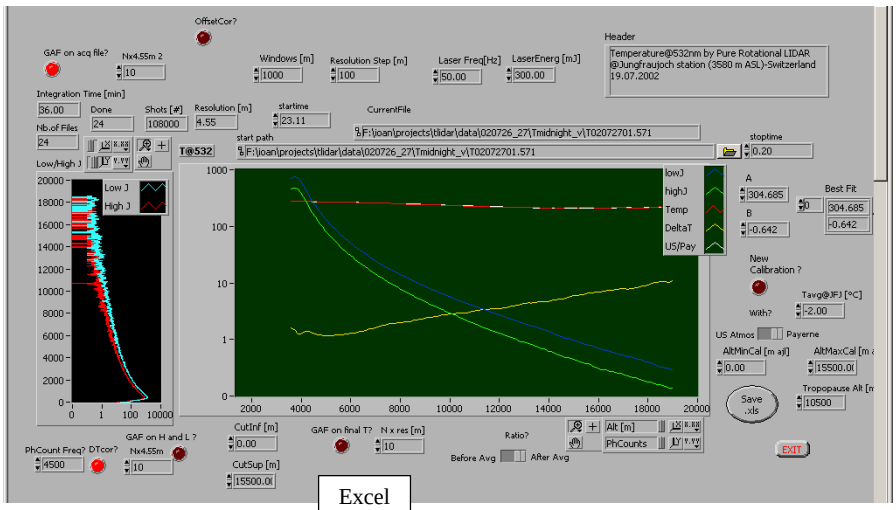

Excel File

Temperature@532nm by Pure Rotational LIDAR
@Jungfraujoch station (3580 m ASL)-Switzerland
27.07.2002

Startime [h.min]	Stoptime [h	AcqTime [m	LaserFreq	SatFreq [C	LaserEnerg	Shots [#]	
23.11	0.2	58.5	50	5000	300	175500	
Windows [m]	Step [m]	Tavg [°K]	Tropo [m]	inf [m]	sup [m]	A	B
998.64	100	274.15	12500	4780	14780	300.3646	-0.627164

ASL [m]	Low J [#]	High J [#]	T [K]	dT/T [%]	Tpay/us [°K]
3780	914.9212	581.3288	277.939	3.210645	275.2189
3880	737.3776	467.1188	277.1708	3.299506	274.9233
3980	561.4926	354.9139	276.6076	3.301537	274.3
4080	421.2259	265.3955	275.7885	3.214821	273.6757
4180	320.6062	201.5285	275.1986	3.113791	272.6439
4280	249.7797	156.5635	274.4857	3.032592	271.8427
4380	199.1631	124.6146	274.0398	2.970072	271.1454
4480	162.0131	101.1184	273.4195	2.919823	270.8038
4580	134.2507	83.53115	272.6489	2.88715	270.3
4680	113.0963	70.04822	271.5234	2.867931	269.6726
4780	96.42304	59.47288	270.5041	2.852636	269.4233
4880	83.03048	51.15146	270.214	2.858983	269.4018
4980	72.2264	44.35142	269.4277	2.861766	268.7633
5080	63.35271	38.81029	268.8557	2.869817	268.0355
5180	55.94214	34.14071	267.9455	2.879291	267.238
5280	49.73545	30.27173	267.3074	2.902475	266.6685
5380	44.45442	26.98238	266.6485	2.921268	265.8555

A 29 Sonics anemometers technical specifications

3-D Sonic Anemometer

Model CSAT3

Campbell Scientific, Inc.'s model CSAT3 3-D Sonic Anemometer has a 10 cm vertical measurement path, operates in a pulsed acoustic mode, and withstands exposure to harsh weather conditions. Three orthogonal wind components (u_x, u_y, u_z) and the speed of sound (c) are measured and output at a maximum rate of 60 Hz. Analog outputs and two types of digital outputs are provided. Measurements can be triggered from three sources: the CSAT3's internal clock, a PC-generated RS-232 command, or our datalogger's SDM command. The SDM protocol supports a group trigger for synchronizing multiple CSAT3s. The model FW05 fine wire thermocouple (12.7 µm diameter) is available as an option for fast response temperature measurements.

The CSAT3, shown making measurements over a fallow field in Minnesota, provides precision turbulence measurements with minimal flow distortion.

Specifications*

Measurements:

Outputs: u_x, u_y, u_z, c (u_x, u_y, u_z are wind components referenced to the anemometer axes; c is speed of sound)

Speed of Sound: determined from 3 acoustic paths; corrected for crosswind effects

Measurement Rate: programmable from 1 to 60 Hz, instantaneous measurements; two oversampled modes are block averaged to either 20 Hz or 10 Hz

Measurement Resolution: u_x, u_y is 1 mm s^{-1} rms; u_z is 0.5 mm s^{-1} rms; c is 1 mm s^{-1} (0.002°C) rms; values are for instantaneous measurements

Accuracy (-30° to +50°C operating range; wind speeds < 30 m s^{-1}; wind angles between ±170°):

Offset error:

u_x, u_y:	<±4.0 cm s^{-1}
u_z:	<±2.0 cm s^{-1}

Gain error:

Wind vector within ±5° of horizontal	<±2 percent of reading
Wind vector within ±10° of horizontal	<±3 percent of reading
Wind vector within ±20° of horizontal	<±6 percent of reading

Output Signals:

Digital SDM: CSI 33.3 k baud serial interface for datalogger/sensor communication
Data type: 2-byte integer per output plus 2-byte diagnostic

Digital RS-232: Baud rate: 9600, 19200 bps
Data type: 2-byte integer per output plus 2-byte diagnostic

Analog: Number of outputs: 4
Voltage range: ±5 V
Number of bits: 12

CAMPBELL SCIENTIFIC, INC.
815 W. 1800 N. • Logan, Utah 84321-1784 • (435) 753-2342 • FAX (435) 750-9540 • www.campbellsci.com

Specifications (cont.)

Reporting Range

SDM and RS-232 Digital Outputs:

Full scale wind: ±65.535 m s^{-1} autoranging between four ranges; least significant bit is 0.25 to 2 mm s^{-1}

Speed of sound: 300 to 366 m s^{-1} (-50° to +60°C); least significant bit is 1 mm s^{-1} (0.002°C)

Analog Outputs:

Output	Range	LSB
u_x, u_y	±30 m s^{-1}	15 mm s^{-1}
	±60 m s^{-1}	30 mm s^{-1}
u_z	±8 m s^{-1}	4 mm s^{-1}
c	300 to 366 m s^{-1}	16 mm s^{-1}
	(-50° to +60°C)	(0.026°C)

Physical Description

Measurement Path Length: 10.0 cm vertical; 5.8 cm horizontal

Path Angle from Horizontal: 60 degrees

Transducer: 0.64 cm diameter

Transducer Mounting Arms: 0.84 cm diameter

Support Arms: 1.59 cm diameter

Dimensions:

Anemometer head: 47.3 cm (l) x 42.4 cm (h)

Electronics box: 26 cm x 16 cm x 9 cm

Weight:

Anemometer head: 1.7 kg (3.7 lb)

Electronics box: 3.8 kg (8.4 lb)

Materials:

Sealed sonic transducers and electronics:

Anemometer head: stainless steel tubing

Electronics box: cast aluminum

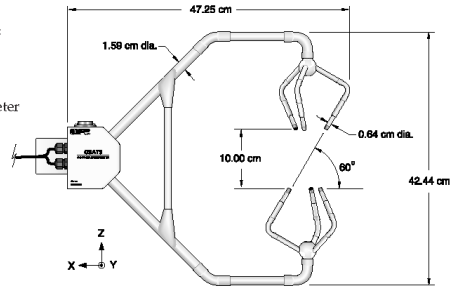

Anemometer Head

Environmental

Operating Temperature Range: -30° to +50°C

Power Requirements

Voltage Supply: 10 to 16 Vdc

Current: 200 mA @ 60 Hz measurement rate; 100 mA @ 20 Hz measurement rate

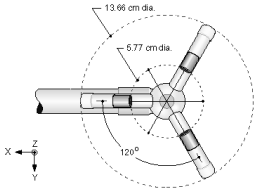

Lower Transducer Assembly Top View

* Specifications are subject to change

CAMPBELL SCIENTIFIC, INC.
815 W. 1800 N. • Logan, Utah 84321-1784 • (435) 753-2342 • FAX (435) 750-9540
Offices also located in: Australia • Brazil • Canada • England • France • South Africa • Spain

A 30 Overview of ultrasonic anemometers measurements

(a) Vertical sensitivity of the 4xSonics anemometers arrow (April 2003 *afternoon*)
Distance above glacier surface: (4) at ~0.6 m; (3) ~1.1m; (2) ~1.6 m and (1) ~ 2.1 m

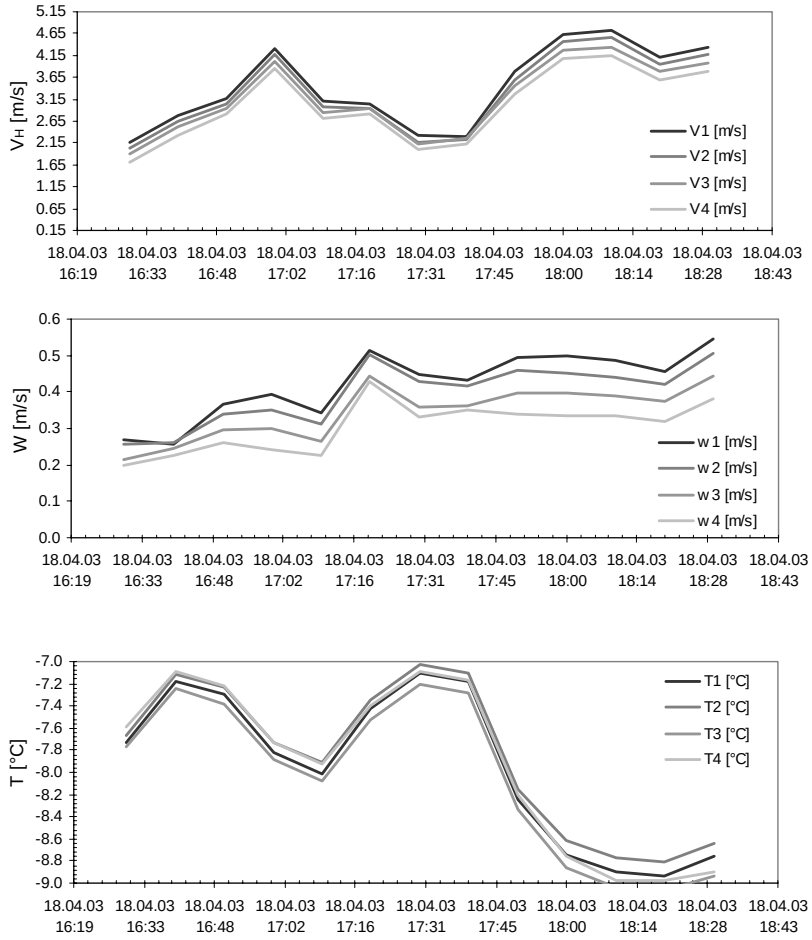

(b) Vertical sensitivity of the 4xSonics anemometers arrow (May 2003 *sunset* transition)

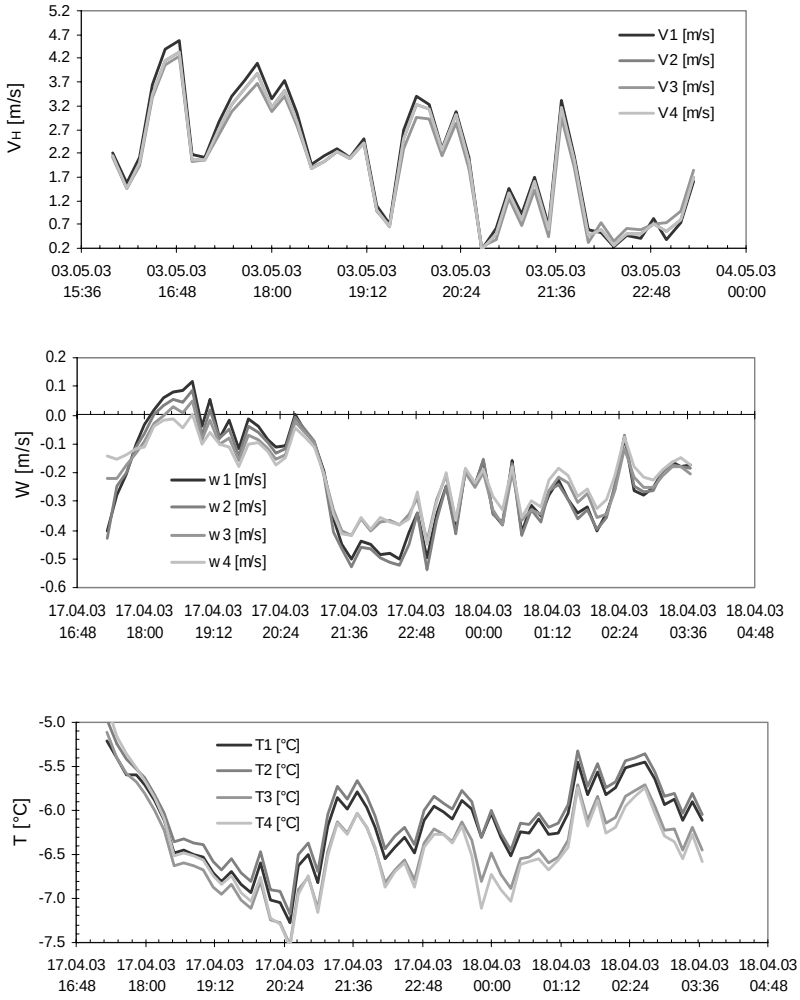

(c) Data series (June 2003)

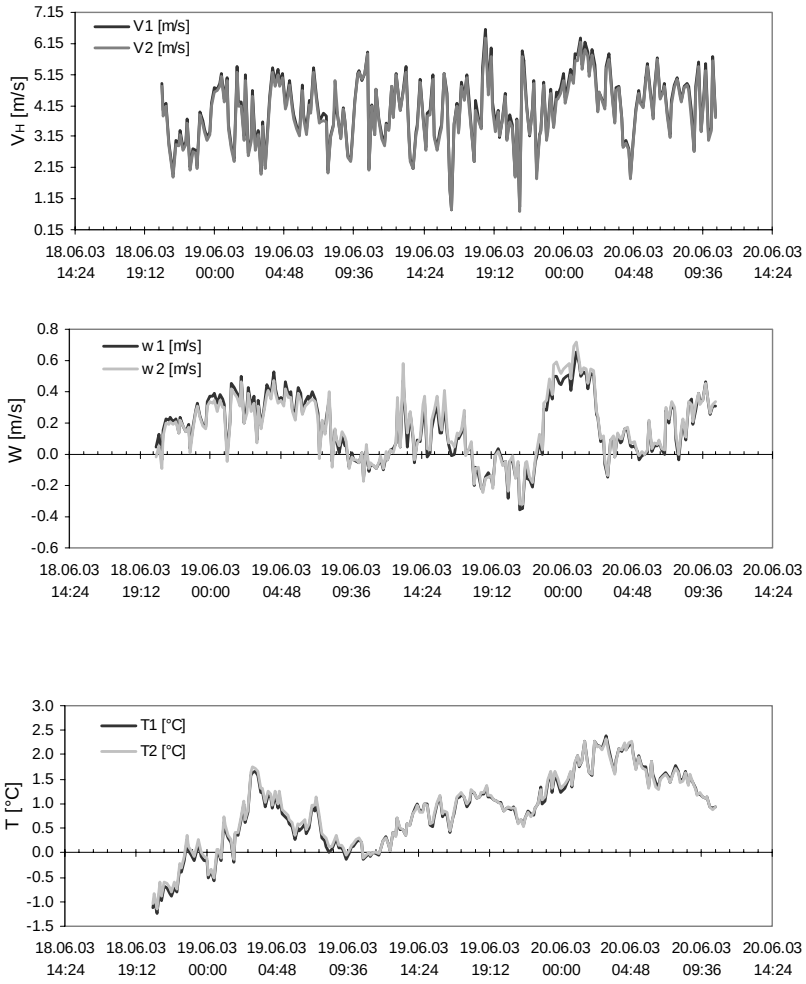

(d) May-June 2003 data series

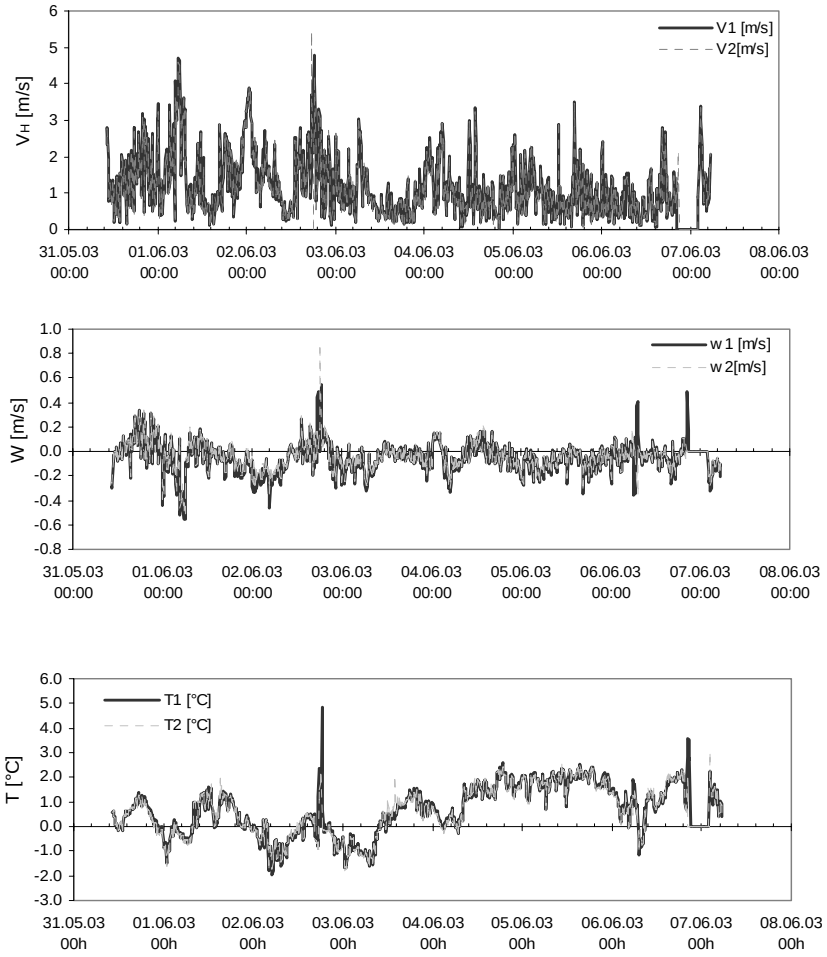

(e) August heat-wave period data series

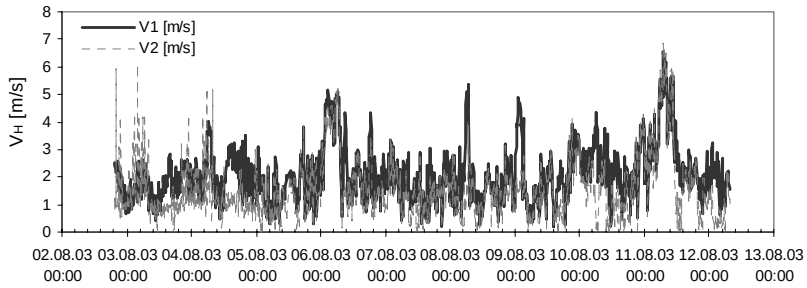

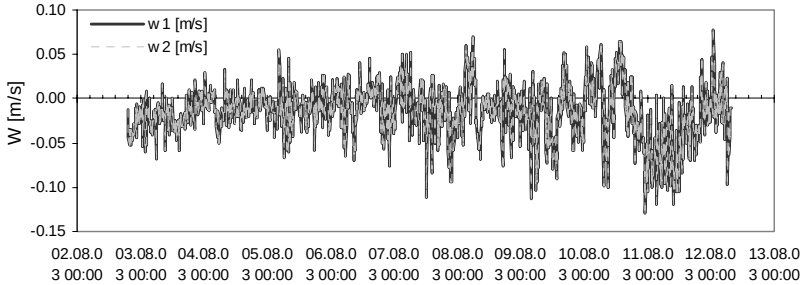

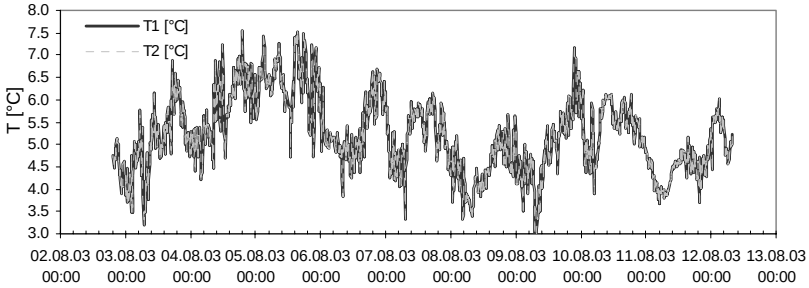

A 31 Jungfraujoch project: puzzle of pictures

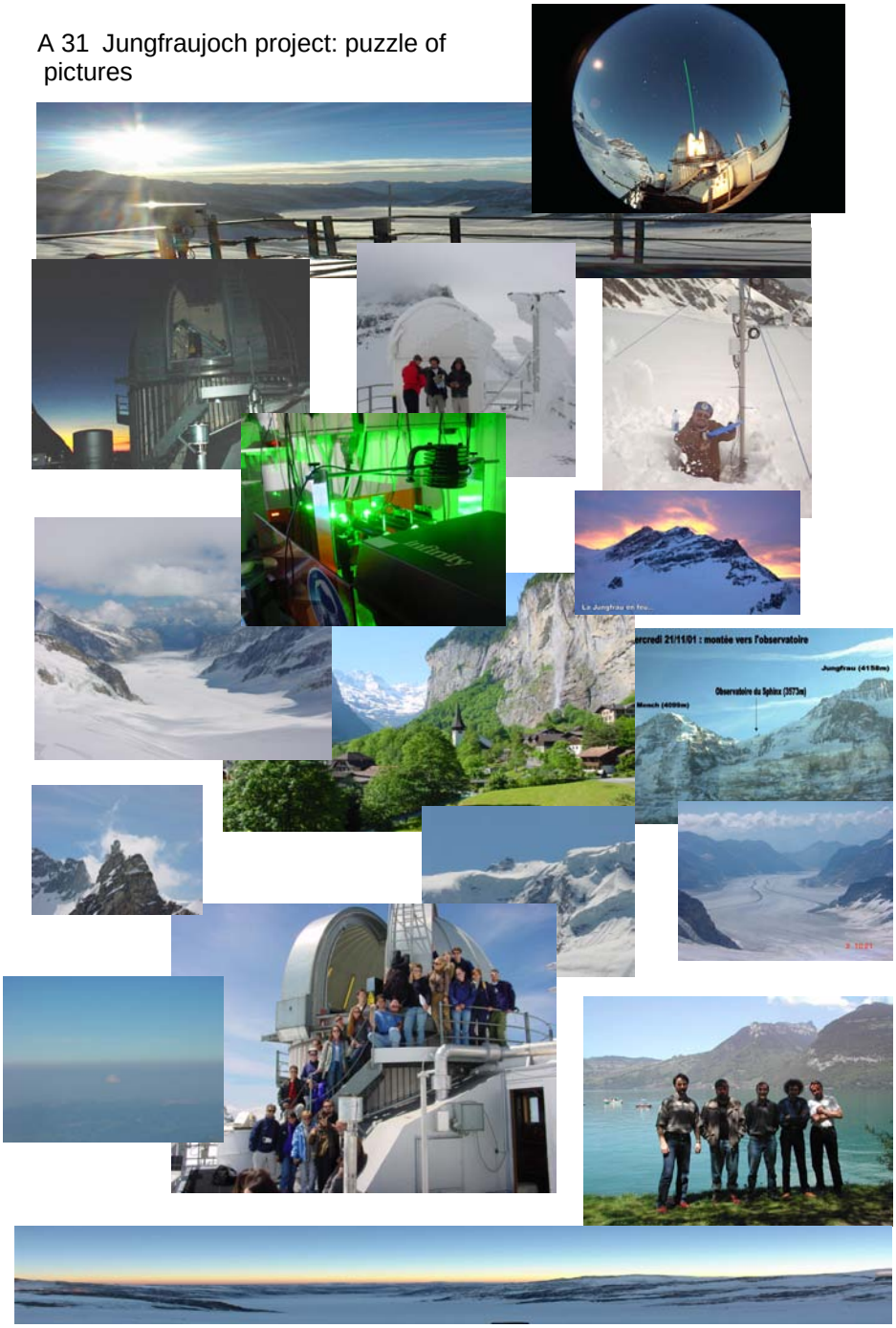


JUNGFRAU

A 32 Constants

Stefan-Boltzmann constant: $\sigma = 5.6704 \times 10^{-8}$ W m^{-2} K^{-4}

Universal gas constant: R = 8.3143 x 10^{3} J K^{-1} $molecule^{-1}$

Boltzmann's Constant: K_B=1.381 x 10^{-23} J K^{-1} $molecule^{-1}$

Avogadro's number: N_A=6.022 x 10^{23} mol^{-1}

Average Molecular Weight of Dry Air: $M_{dry\ air}$ = 28.97 g mol^{-1}

Gas Constant of Dry Air: $R_{dry\ air}$ =287 J K^{-1} kg^{-2}

Density of Dry Air at 0°C and 101325 Nm-2: $\rho_{dry\ air}$ = 1.275 kg m^{-3}

Specific Heat of Dry Air at Constant Pressure: $Cp_{dry\ air}$ = 1004 J K^{-1} kg^{-1}

Specific Heat of Dry Air at Constant Volume: $Cpv_{dry\ air}$ = 717 J K^{-1} kg-1

Thermal Conductivity of Dry Air at 0° C: k = 2.40-2 J m^{-1} s^{-1} K^{-1}

Molecular Weight of Water: M_{H2O} = 18.016 g mol-$^{-1}$

Gas Constant for Water Vapor: R_{H2O} = 461 J K^{-1} kg^{-1}

Density of Liquid Water at 0°C: ρ_{H2O} = 1 x 10^{3} kg m^{-3}

Density of Ice at 0°: ρ_{ice} = 0.917 x 10^{3} kg m^{-3}

Specific Heat of Water Vapor at Constant Pressure: Cp_{H2O} = 1952 J K^{-1} kg^{-1}

Specific Heat of Water Vapor at Constant Volume: Cv_{H2O} = 1463 J K^{-1} kg^{-1}

Specific Heat of Water Vapor at 0° C: C_{H2O} = 4218 J K^{-1} kg^{-1}

Specific Heat of Ice at 0°C: C_{ice} = 2106 J K^{-1} kg^{-1}

Enthalpy (Latent Heat) of Vaporization of Water at 0°C: L_v = 2.50 x 106 J kg^{-1}

Enthalpy (Latent Heat) of Vaporization of Water at 100°C: L_f = 2.25 x 106 J kg^{-1}

Enthalpy (Latent Heat) of Fusion of Water at 0°C: L_f = 3.34 x 105 J kg^{-1}

Enthalpy (Latent Heat) of Sublimation of Water at 0°C: L_f = 2.83 x 106 J kg^{-1}

Ioan BALIN
Ch. des Pyramides, 14, 1007 Lausanne
Phone: 004176/5733949
Email: ioan.balin@epfl.ch
Weblink: http://lpas.epfl.ch/lidar

37 years
physicist
Romanian
married
no children

Professional Objective
Academic Career on Applied Physics in Environmental Sciences

Competences & expertise

- Analytic techniques[1] applied to environmental studies
- Atmospheric local, regional and remote sensing measurements[2] and interpretation [3]
- Data handling: acquisition, analysis and interpretation[4]
- Training and formation[5]
- Scientific communication[6]

Professional experiences

- Lidar (development, measurements, interpretation) at Jungfraujoch observatory, (2000-2003)
- Teaching and research assistant at EPFL/LPAS on atmospheric sciences, (1999-2003)
- Teaching and research assistant on Physics, (optics and spectroscopy), UAIC/Ro, (1992-1997)
- Teaching (Thin Films) and research (FTIR) assistant, Paris-Sud Univ. (1994-1995)

Informatics: LabView, MatLab, MSOffice, DOS, Windows 3.1 at XP Pro TurboBasic, Webmaster, PC helpdesk, …

Languages: Romanian (native), English (fluent), French (fluent), German (basics)

[1] Familiar with different laboratory and field techniques measuring various environmental parameters
[2] Air pollution measurements (pollutants and meteorology) at Milano (1998), Grenoble (1999), Crete (1999), Marseille (2001), Switzerland (1998-2003) using mobile point monitors, DOAS and LIDARs systems.
[3] Ozone and PBL dynamics based on measurements and modelisation, valleys photochemistry, transboundary pollution, urban air quality, etc
[4] Creation of the digital database system of the FEI (Fédération Equestre Internationale, Lausanne 1999)
[5] Seminars, laboratory work, conferences and courses (~11 years at academic level in Romania, France and Switzerland); organisation and coordination of the environmental EPFL student air pollution campaigns since 1998
[6] Scientific community, public and various mass medias

Education

Ph. D. in atmospheric sciences field - lidar applications (*Measurement and analysis of aerosols-cirrus-contrails, water vapor and temperature in the upper troposphere with the Jungfraujoch-LIDAR system*: June 2000 - March 2004), at EPFL/LPAS-Lausanne-Switzerland

M. Sc. in Environmental Sciences EPFL (*DOAS air quality measurements*) (1997-99), EPFL

Physicist (optics and spectroscopy: *Fluorescence of the complex organic molecules*), at Faculty of Physics of the "Al.I.Cuza" University, of Iasi-Romania, (1987-1992)

Continuous formation
- Radioprotection expert, IRA/EPFL, 1998
- Scientific Investigations of the Cultural Heritage[7], UNESCO/ICCROM, Paris, 1997

Membership: American Geophysical Union, European Geophysical Society, ..

Voluntary work: staff in foreigner students sky camp in Switzerland (Engelberg) since 1998

Hobbies: Music, Dance, Cooking, Communication, Diplomatic Affairs, Ski, Mountains and Forests Hiking, Research&Education Politics, Cultural Heritage Preservation, the Humor, …

RESEARCH Publications [8]

In preparation

- I. Balin, M. Parlange, C. Higgins, R. Nessler, B. Calpini, V. Simeonov and H. van den Bergh, Aerosols and water vapor dynamics at the interface of the Free Troposphere (FT) with the Planetary Boundary Layer (PBL) under a persistent stationary anticyclone over Western Europe

- I. Balin, R. Nessler, B. Calpini, V. Simeonov and H. van den Bergh, *Raman lidar high resolution monitoring of the upper troposphere water vapor above the Swiss Alps*

- I. Balin, M. Collaud, R. Nessler, S. Nyeki E. Weingartner, D. Shaub, B. Calpini, V. Simeonov, U. Baltensperger and H. van den Bergh, *Optical properties of a free*

[7] Creation of a new course in " Analytic methods for investigations of the cultural heritage", devoted to the last year students from Theology Faculty , section Cultural Heritage Restoration and Preservation, Iasi-Romania

[8] Only related to thesis period (i.e.2000-2004) at EPFL-LPAS (with the LIDAR group)

troposphere Saharan dust from in situ integrated and vertical resolved collocated observations

- I. Balin, I. Serikov , R. Nessler , Y. Bobrovnikov, V. Simeonov, B. Calpini, Y. Arshinov and H. Van den Bergh, *Pure rotational Raman-lidar technique on the Jungfraujoch multi-wavelength lidar system: implementation and new atmospheric retrievals,* to be submitted to Applied Physics B

Submitted and/or accepted

- I. Balin, M. Parlange, B. Calpini, V. Simeonov and H. van den Bergh, Elevated atmospheric boundary layer over the Swiss Alps during the August 2003 heat wave, accepted to 22nd International Lidar Radar Conference, (ILRC 2004), Matera-Italy

- I. Balin, V.Simeonov, I. Serikov , S. Bobrovnikov, B. Calpini, Y. Arshinov and H. van den Bergh, Simultaneous measurement of temperature, water vapor, aersol extinction and backscatter by Raman lidar, accepted to 22nd International Lidar Radar Conferenc, (ILRC 2004), Matera-Italy

- R. Jiménez, O. Couach, F. Kirchner, I. Balin, V. Simeonov, B. Calpini and H. Van den Bergh, Sources and sinks of HCHO in the Grenoble area experimental and modelling investigation, Atmos. Env. Submitted, 2002 (submitted)

- Papayannis, V. Amiridis, J. Baldasano, I. Balin, D. Balis, A. Boselli, A. Chaikovsky, B. Chatenet, G. Chourdakis, V. Freudenthaler, M. Frioux, J. Herman, M. Iarlori, S. Kreipl, G. Larcheveque, R. Matthey, I. Mattis, D. Müller, M. Pandolfi, G. Papalardo, J. Pelon, M.R. Perrone, V. Rizi, A. Rodrigues, L. Sauvage, P. Sobolewski, N. Spinelli, F. Tomasi de, T. Trickl, M. Wiegner, A.D.A. Castanho, N. Chrysoulakis, Y. Balkanski, J.P. Leon, and a. et, Continental-scale vertical profile measurements of free tropospheric Saharan dust particles performed by a coordinated ground-based European Aerosol Research Lidar Network (EARLINET project), submitted to Atmospheric Physics and Chemistry, Nov. 2003).

Peer reviewed publications

- Matthias, V.; Freudenthaler, V.; Amodeo, A.; Balin, I.; Balis, D.; Bosenberg, J.; Chaikovsky, A.; Chourdakis, G.; Comeron, A.; de Tomasi, F.; Eixmann, R.; Hagard, A.; Komguem, L.; Kreipl, S.; Matthey, R.; Rizi, V.; Rodrigues, J.A.; Wandinger, U.; Wang, X., Aerosol lidar intercomparaison in the framework of EARLINET: Part I – instruments, in Applied Optics, 43, 4, 961-976, 2004

- O. Couach, F. Kirchner, R. Jimenez, I. Balin, S. Perego and H. van den Bergh, A development of ozone abatement strategies for the Grenoble area using modeling and indicators, Atmospheric Environment Volume 38, Issue 10, Pages 1425-1436, 2004

- D. Gerber, I. Balin, D. Feist, N. Kämpfer, V. Simeonov, B. Calpini and H. van den Bergh, Ground-based water vapour soundings by microwave radiometry and

Raman lidar on Jungfraujoch (Swiss Alps), Atmospheric Chemistry and Physics 3, 4833-4856, 2003

- O. Couach, I. Balin, R. Jimenez, P. Ristori, S. Perego, F. Kirchner, V. Simeonov, B. Calpini and H. van den Bergh, An investigation of ozone and planetary boundary layer dynamics over the complex topography of Grenoble combining measurements and modeling, Atmospheric Chemistry and Physics 3, 549-562, 2003

- G. Larcheveque, I. Balin, R. Nessler, P. Quaglia, V. Simeonov, H. van den Bergh and B. Calpini, Development of a multiwavelength aerosol and water-vapor lidar at the Jungfraujoch Alpine Station (3580 m above sea level) in Switzerland, Applied Optics 41(15), 2781-2790, 2002

- O. Couach, I. Balin, R. Jiménez, S. Perego, F. Kirchner, P. Ristori, V. Simeonov, P. Quaglia, V. Vestri, A. Clappier, B. Calpini and H. Van den Bergh, Study of a photochemical episode over the Grenoble area using a mesoscale model and intensive measurements, Pollution Atmosphérique 174, 2002

- I. Balin, Larchevêque G., Quaglia P., Simeonov P., H. van den Bergh, and Calpini B., Water vapor vertical profile by Raman lidar in the free troposphere from the Jungfraujoch Alpine Station, in: Advances in Global Change Research, M.e. Beniston, Climatic Changes: Implications for the Hydrological Cycle and Water Management, ed. 9, pp. 123-138, Kluwer Academic Publisher, Dordrecht and Boston, 2002

- O. Couach, I. Balin and M.B. Personnaz, GRENOPHOT project - Summer photochemical smog study over the Grenoble area, Lettre PIGB-PMRC 14 (www.cnrs.fr/dossiers/dosclim/biblio/pigb14/), 2002

- L. Sesana, Milesi M., Benigni S., Facchini U., Dommen J., Prevot A., Quaglia P., Balin I., Lanzani G., Bosio C., Radon and pollutants in the Milan area: May and June 1998, The Pipapo Campaign, I.L. Rendiconti, Academia Di Scienze E Lettere, ed. 133, Milano, 2001

Conferences peer reviewed proceedings

- M. Adam, M. Pahlow, V. Kovalev, J. Ondov, I. Balin, V. Simeonov, H. van den Bergh and M. Parlange, Determination of the Vertical Extinction Coefficient Profile in the Atmospheric Boundary Layer and the Free Troposphere, in: EGS-AGU-EUG, E.G. Society, ed., Geophysical Research Abstracts 5, pp. 07663, Nice France, 2003

- Balin, R. Nessler, V. Simeonov, B. Calpini, M. Parlange, Y. Arshinov, H. Van den Bergh, I. Serikov, G. Larcheveque and S. Bobrovnikov, Simultaneous water vapor and temperature nighttime observations above the Aletsch Glacier - Switzerland with a Raman lidar, in: EGS-AGU-EUG, E.G. Society, ed., Geophysical Research Abstracts 5, pp. 07920, Nice France, 2003

- V. Simeonov, B. Calpini, I. Balin, P. Ristori, R. Jimenez and H. van den Bergh, UV ozone DIAL based on a N2 Raman converter, design and results during ESCOPMTE field campaign, in: 21st International Laser Radar Conference Quebec Canada, Lidar remote sensing in atmospheric and Earth Sciences, pp. 403-406, Quebec Canada, 2002

- G. Larchevêque, Balin I., Quaglia P., Nessler R., Simeonov V., H. van den Bergh and Calpini B., Optical properties of aerosols-clouds-contrails and water vapor mixing ratio by lidar from Jungfraujoch Research Station (3580 m ASL), in: EGS (European Geophysical Assembly), Nice-France, 2002

- O. Couach, Balin I., Jimenez R., Quaglia P., Ristori P., Simeonov V., Clappier A., Calpini B. and Hubert van den Bergh, Measurements and Modelling of the air pollution and the meteorology on a complex topography region: Case study Grenoble 1998/1999, in: EGS (European Geophysical Assembly), Nice-France, 2002

- B. Calpini, I. Balin, O. Couach, R. Jimenez, P. Ristori, P. Quaglia, H. Van den Bergh and V. Simeonov, Air pollution study over Grenoble-France in summer 1999 : lidar measurements and model predictions, in: International Lidar Radar Conference (ILRC), Quebec, Canada, 2002

- I. Balin, G. Larchvêque, R. Nessler, P. Quaglia, V. Simeonov, H. van den Bergh and B. Calpini, Monitoring of water vapor, aerosols and clouds/contrails in the free troposphere by lidar from Jungfraujoch station (3580 m ASL), in: 21st International Laser Radar Conference, Lidar remote sensing in atmospheric and Earth Sciences, pp. 685-688, Quebec Canada, 2002

- R. Nessler, Larchevêque G., Balin I., Quaglia P., Simeonov V., Weingartner E., Baltensperger U., H. Van Den Bergh and Calpini B., LIDAR and in situ aerosol measurements at the Jungfraujoch Alpine Station, in: AGS, Lausanne-EPFL, 2001

- R. Nessler, Larchevêque G., Balin I., Bukowiecki N., Weingartner E., Baltensperger U., H.van den Bergh and Calpini B., Study of the tropospheric aerosol at the Jungfraujoch alpine station by mean of simultaneous lidar and in-situ measurements, in: European Aerosol Conference, Leipzig, Germany, 2001

- P. Quaglia, Couach O., Balin I., Simeonov V., Lazzarotto B., H. van den Bergh, and Calpini B., Air pollution measurements during the Grenoble 1999 campaign, in: 20th International Laser Radar Conference, pp. 435-438, Vichy-France, 2000

- P. Quaglia, Jiménez R., Simeonov V., Larchevêque G., Lazzarotto B., Balin I., Besson C. and Calpini C., The EPFL contribution to the PIPAPO experiment, in: Photochemical Oxidants and Aerosols in Lombardy Region, pp. 45-50, Milano, Italy, 1999

- P. Quaglia, Balin I., Jeanneret F., Jimenez R., Larchevèque G., Lazzaraotto B., Simeonov V. and Calpini B., Development of new optical methods for tropospheric ozone studies, in: International Ozone Symposium, Basel - Switzerland, 1999

- Balin, M. Parlange, R. Nessler, C. Higgins, B. Calpini, V. Simeonov and H. van den Bergh, The atmospheric boundary layer above Aletsch glacier (3580 m - Switzerland), in: AGU Fall Meeting, San Francisco, US, 2003

- O. Couach, F. Kirchner, R. Jiménez, I. Balin, S. Perego and A. Clappier, Grenoble region : test and application od different indicators in order to develop ozone abatement strategies, in: Eurotrac Symposium, Garmish-Partenkirchen, 2002

- O. Coach, Kirchner F., Jimenez R., Balin I., Quaglia P., Perego S., Clappier A. and H. van den Bergh, Grenoble region: Test and Application of different Indicators in order to develop ozone abatement strategies, in: EUROTRAC symposium, Garmich-Partenkirchen, 2002

- I. Balin, Jimenez R., Navarette M., Nessler R., Ristori P., Simeonov V., Kirchner F., Hubert van den Bergh and Calpini B., The ESCOMPTE - Marseille 2001 international field experiment: Ground based and lidar results obtained at St Chamas by the EPFL mobile laboratory, in: EUROTRAC symposium, Garmich-Partenkirchen, 2002

- I. Balin, Larchevêque G., Nessler R., Simeonov V., Quaglia P., H. van den Bergh and Calpini B., Retrieval of the water vapor content in the free troposphere by a Raman lidar technique: implementation, measurements results and present limitations, in: National Physics Conference, Iasi-Romania, 2001

- I. Balin, Jimenez R., H. van den Bergh and Calpini B., Air pollution measurement campaign for student training: technical and pedagogical aspects, in: National Physics Conference, Iasi-Romania, 2001

- I. Balin, Larcheveque G., Nessler R., H.van den Bergh, and Calpini B., Aerosols and water vapor by lidar from the Jungfraujoch research station, in: NDSC meeting (Network for Detecting of Stratospheric Changes), Arcachon - France, 2001

- I. Balin, Larcheveque G., Quaglia P., Simeonov V., Nessler R., Van den Bergh H. and Calpini B., Water vapor measurements in the free troposphere by RAMAN Lidar technique from Jungfraujoch Alpine Station, in: AGS, Lausanne-EPFL, 2001

- O. Couach, R. Jiménez, I. Balin, P. Quaglia, F. Kirchner, S. Perego, A. Clappier and H. Van den Bergh, Mesoscale photochemical modeling of GRENOPHOT 1999 data - Studying the air pollution over Grenoble's complex topography, in: A Changing Atmosphere 8th European Symposium on the physical-chemical behaviour of atmospheric pollutants, Torino, 2001

- R. Jimenez, A. Martilli, I. Balin, H. Van den Bergh, B. Calpini, B. Larsen, G. Favaro and D. Kita, Measurement of formaldehyde (HCHO) by DOAS : Intercomparison to DNPH measurements and interpretation from Eulerian model calculations, Proceedings of A&WMA 93rd Annual Conference, Salt Lake City (UT), Paper # 829, 2000.

- P. Quaglia, Jiménez R., Simeonov V., Larchevêque G., Lazzarotto B., Balin I., Besson C. and Calpini C., The EPFL contribution to the PIPAPO experiment, in: Photochemical Oxidants and Aerosols in Lombardy Region, pp. 45-50, Milano, Italy, 1999

- Balin, R. Jimenez, B. Calpini and H. van den Bergh, Contribution to the development of a new DOAS system for Air Pollution Measurements, in: Physical national Conference, Fundamental and Applicative Physics Research, Iasi-Romania, 1999.

Reports

- ✓ O. Couach, I. Balin, P. Quaglia, R. Jimenez, V. Simeonov, G. Larchevêque, B. Lazzarotto, J. Kuebler, V. Sathya, A. Martilli, M. Junier, Y.A. Roulet, F. Kirchner, A. Clappier, B. Calpini and H. Van den Bergh, Campagne de mesures intensives 1999 sur la région grenobloise, ensemble des résultats et analyse des Périodes d'Observations Intensives (POI), LPAS-EPFL, Lausanne, 2000

- ✓ R. Jimenez, Balin, I., Calpini, B., Van den Bergh, H, TE DOAS 2000 Characterisation, Calibration and Development, LPA-EPFL, for Thermo Environmental Instruments, Inc. (TEI), Franklin, MA 02038, USA, 1998

- ✓ I. Balin, Jimenez R., H. van den Bergh and Calpini B., DOAS: Differential Optical Absorption Spectroscopy Technique for Air Pollution Measurements, 1999 (M.Sc. Thesis)

STUDENTS TRAINING [9]

Air pollution & climate changes: laboratory works

(a) Ozone: generation by oxygen photo-dissociation and Hartley band UV absorption
(b) UV-VIS absorption spectroscopy for gas concentrations measurements
(c) Kinetics of titration reaction NO+O3

Air quality and atmospheric dynamics: student field campaigns

[9] Only related to the Swiss - EPFL experience 1998-2003.
From 1992 to 1997 the teaching activities included various seminars and laboratory works for students as teaching assistant in Analytic Spectroscopy, Fundamental Optics, Atomic and Nuclear Physics, at "Al.I.Cuza" University in Iasi-Romania and Thin Films: deposition techniques and their electric, elipsometric and RBS analysis (1994-1995) at IUT of Paris-Sud University as well a new course and laboratory work of "Scientific Investigations of the Cultural Heritage" addressed the last year students section work of art preservation and restoration at Theology Faculty of Iasi -Romania

(a) Air quality and regional meteorology: (Pays d'Enhaut 2003, ongoing)
(b) Rhone (industrial) and Anniviers (alpine) valleys: air quality study (2002)
(c) Circulation and air quality in an alpine topography (Val d'Anniviers, 2001)
(d) Trans-boundary air pollution study (Geneva -France 2000)
(e) Urban and regional air pollution in the Geneva area (1999)
(f) Urban air quality in Jura (Le Locle, 1998)

Reference: http://lpas.epfl.ch/lidar/didactic/student_campaigns.html

Informatics

(a) Software developments in LabView, occasionally MatLab, Windows user
(b) PCs configurations and maintenance at EPFL, Jungfraujoch and field campaigns
(c) LIDAR group web site webmaster http://lpas.epfl.ch/lidar/

Scientific communication: conferences, public, scientific communities, medias

(a) Organization of regular visits at Jungfraujoch observatory for LIDAR project presentation to scientific communities, students and medias
(b) Medias interventions the measurements usefulness for air quality studies and of atmospheric parameters related to the climate change topics (Radio Suisse Romande, TVR1, Arte, ...
(c) Regular presentations for the ISTE department and for EPFL public vulgarization projects

…and the natural cycles?!